

CRANFIELD UNIVERSITY

David H Johnson

Department of Engineering and Applied Science

Lüders bands in RPV steel

Submitted for the degree of Doctor of Philosophy

Academic year of submission: 2012

Supervisor: Dr Michael Edwards

©Crown copyright, 2012. All rights reserved. No part of this publication may be reproduced without the written permission of the copyright holder.

## Abstract

The R6 procedure is used for the prevention and prediction of crack behaviour and other defects in the reactor pressure vessel(RPV). The RPV material is an upper-bainitic, low alloy steel structure, which deforms inhomogeneously when yielding. The current codes that are used to design and calculate the fracture, within an RPV, assume that the material yields continuously as the size of the Lüders strain is less than 2%. However, the work of Wenman et al[1] has shown that the inclusion of a Lüders band during calculations can reduce the residual stress in a material, when compared to standard work-hardening models and, consequently, reduces the amount of conservatism.

The objective of the research was to determine whether Wenman's finding could be generalised and therefore initiate a re-evaluation of R6 procedure, when looking into materials that yield discontinuously. This required further investigation into Lüders bands, such as using failure assessment diagrams (FADs). The findings from FADs showed that at the temperature range for an RPV steel at -155°C for different micro-structures (assuming that the material deforms homogeneously), this reduced the amount of conservatism. However, at fracture toughness values more representative of room temperature behaviour, the converse was true. That is, assuming a discontinuous yield point reduced the amount of conservatism. It was also shown that the tempered martensite structure could be used as an alternative to the current upper bainitic, low alloy steel that is used in RPVs.

Further insight is gained into the nature of a Lüders band, by developing a theoretical model that showed explicit relations between Lüders strain and the mean free-path(ferrite path), dislocation density and the grain-size.

It was also shown that an explicit relation between the Lüders strain and carbon content was possible from known data, which a new parameter  $\phi$  was derived, and is the derivative of the work-hardening exponent with respect to the lower yield stress.

## Acknowledgements

Firstly, I would like to thank Dr Ian Giles of the Ministry of Defence for the generous funding that enabled the project to come about.

I would also like to thank Dr Michael Edwards for his great encouragement, input, guidance, patience and insistence on clarity that has enabled this thesis to come about; Dr Paul Chard-Tuckey for his support and guidance throughout and Dr Mark Wenman, although not directly involved, has nonetheless offered guidance that has been invaluable in terms of the direction of research.

For technical assistance I would like to thank Sean and Terry ,who taught me that not everything can be answered through theoretical work alone.

I would also like to thank my family and friends, especially D.P and J.K for their continual support.

Finally, a special thanks to my girlfriend Chiaki san for being there throughout and showing me that, “Saru mo ki kara ochiru ne”. Arigatou gozaimashita, watashi ni itsumo ite, “Saru mo ki kara ochiru ne”tte iu no wo oshite imashita.

# Contents

<b>1</b>	<b>Introduction to Problem</b>	<b>1</b>
1.1	Structure of thesis . . . . .	4
1.2	Statement of originality . . . . .	5
<b>2</b>	<b>Literature Review</b>	<b>8</b>
2.1	Lüders bands . . . . .	8
2.2	Static Pinning . . . . .	8
2.3	Dislocation multiplication . . . . .	15
2.4	Carbon content . . . . .	22
2.4.1	Pearlitic and Spheroidal structures . . . . .	22
2.5	Temperature . . . . .	29
2.6	Grain size . . . . .	41
2.7	Strain-rate . . . . .	48
2.7.1	Low strain-rates . . . . .	48
2.7.2	High strain-rates . . . . .	52
2.8	Irradiation . . . . .	54
2.9	Cold working . . . . .	54
2.10	Summary . . . . .	56
<b>3</b>	<b>Theoretical</b>	<b>58</b>
3.1	Lüders strain as a function of carbon content . . . . .	58
3.2	Summary . . . . .	64
3.3	Dynamics of Sun's model . . . . .	64
3.4	Profile of the Lüders band . . . . .	77
3.5	Zhang model . . . . .	80
3.6	Summary . . . . .	82
3.7	Conclusion . . . . .	83
<b>4</b>	<b>Tensile testing</b>	<b>84</b>
4.1	Introduction . . . . .	84
4.2	Materials and methods . . . . .	84
4.2.1	Specimen geometry . . . . .	86
4.2.2	Hardness . . . . .	86
4.3	Procedure . . . . .	87
4.4	Exponents . . . . .	89
4.5	Results . . . . .	90

4.6	Discussion . . . . .	101
4.7	Conclusion . . . . .	108
<b>5</b>	<b>Tensile experiment with defect</b>	<b>112</b>
5.1	Method . . . . .	112
5.2	Results . . . . .	113
5.3	Discussion . . . . .	120
5.4	Conclusion . . . . .	124
<b>6</b>	<b>Failure Assessment Diagrams(FAD) using R6 code</b>	<b>125</b>
6.1	Introduction . . . . .	125
6.2	R6 code . . . . .	125
6.3	Generating FADs . . . . .	142
6.4	Method . . . . .	142
6.5	Geometry . . . . .	145
6.6	Results . . . . .	148
6.7	Discussion . . . . .	155
6.8	Conclusion to FADs . . . . .	156
<b>7</b>	<b>Modelling Analysis</b>	<b>158</b>
7.1	Method . . . . .	158
7.2	Results . . . . .	159
7.3	Discussion . . . . .	161
7.4	Conclusion . . . . .	171
<b>8</b>	<b>Modelling of the tensile and hole defect</b>	<b>173</b>
8.1	Method . . . . .	173
8.2	Results . . . . .	174
8.3	Discussion . . . . .	185
8.4	Conclusion . . . . .	187
<b>9</b>	<b>General discussion</b>	<b>188</b>
9.1	Theoretical . . . . .	188
9.2	Experimental . . . . .	190
9.2.1	FAD . . . . .	192
9.3	Modelling . . . . .	193
<b>10</b>	<b>Conclusion</b>	<b>196</b>

<b>11 Future work</b>	<b>199</b>
<b>A Appendix-Data from tensile tests</b>	<b>202</b>
A.1 Additional results . . . . .	206
<b>B Optical micrographs</b>	<b>207</b>
<b>C Appendix-Time dependent yield prediction</b>	<b>210</b>
C.1 Method . . . . .	211
C.2 Results . . . . .	212
C.3 Conclusion . . . . .	212
<b>D Appendix-Digital Image Correlation.</b>	<b>213</b>
D.1 Obtaining image . . . . .	213
D.2 Correlation Algorithm . . . . .	215
<b>E Appendix-J-integral</b>	<b>219</b>
<b>F Appendix Lüders strain carbon content</b>	<b>222</b>
F.1 Theory . . . . .	222
F.2 Method . . . . .	226
F.3 Results . . . . .	227
F.4 Summary . . . . .	231
F.5 Conclusion . . . . .	231
<b>G Subroutine</b>	<b>232</b>

## List of tables

Table 1:The data on yield point against temperature.

Table 2:Carbon contents with different grain-sizes( $1.6\text{-}60.2\mu\text{m}$ ), illustrating the dependence of the Lüders strain with grain-size. That is the smaller the grain-size for a given carbon content, the larger the Lüders strain.  $C(\%)$  is the carbon content,  $d(\mu\text{m})$  is the grain-size,  $\varepsilon_L(\%)$  is the Lüders strain,  $K'(\text{MPa})$  is a parameter and  $u$  is an exponent.

Table 3: Chemical composition of elements in % wt of the RPV steel, mild steel with manganese sulphide particles and the ultra low carbon steel.

Table 4:A summary of the materials and expected micro-structures.

Table 5:The hardness of AR FP and TM at 650C.

Table 6:Strain-rate sensitivity and stress-rate exponents of AR, TM-5H, TM-120H, TM-144H, TM-168H, UL and AL.

Table 7:Two band nucleation for the AR, TM-144H and structure at  $\dot{\varepsilon}=1\times10^{-2}\text{ s}^{-1}$  with  $\varepsilon_f = \frac{\varepsilon_L}{2}$ .

Table 8:Predicted yield and actual yield time in seconds.

Table 9:Predicted and observed failure modes of A533B.

Table 10:Structural conditions for significant influence of yield plateau.

Table 11:Values of the parameters used for modelling with the blanks indicating dimensionless quantities.

Table 12:Failure of AR, FP and TM-168H.

Table 13:Failure of AR and TM-168H with Lüders strain( $a_{dis}$ ) and without( $a_{con}$ ).

Table 14:Failure of TM-168H for varying fracture toughness(57-800) $\text{MPa m}^{\frac{1}{2}}$ .

Table 15:The calculated values of parameters  $\Omega$ ,  $\gamma$ ,  $\lambda$ ,  $\rho_{max}$ ,  $S_0$ ,  $\varepsilon_L$ ,  $\dot{\varepsilon}_{max}$ ,  $v_l$ ,  $v_d$ ,  $\tau$  and  $\tau_{acc}$ .

Table 16:Values of the parameters used for AR and TM-28H modelling with the blanks indicating dimensionless quantities.

Table 17:The results for the as-received or AR, upper bainitic structure.

Table 18:The results of FP, ferrite-pearlite structure.

Table 19:The results of TM-5H(for 5hours), tempered martensitic structure.

Table 20:The results of TM-120H(for 120hours), tempered martensitic structure.

Table 21:The results of TM-144H(for 144hours), tempered martensitic structure.

Table 22:The results of TM-168H(for 168hours), tempered martensitic structure.

Table 23:The results of UL(0.007% C).

Table 24:The results of AL(0.07% C).

Table 25:The results of TM-120H(for 120hours), tempered martensitic structure.

Table 26:The results of TM-192H(for 192hours), tempered martensitic structure.

## List of Figures

Fig.1:Stress-strain curve Hastelloy N.

Fig.2:Stress-strain curve of tempered martensite. Where  $\sigma_{uy}$  is the upper yield point,  $\sigma_{ly}$  is the lower yield point and  $\varepsilon_l$  is the Lüders strain.

Fig.3:Equ.(6) curve fitted to some data from McAdams et al.

Fig.4:Shows a plot of  $S_{dis}$  vs time the contrast between Cottrell's model in dotted lines and the modified models with the continuous lines with the experimental data. The material was pre-strained by 0.02% The crosses are aged at 414 K, triangles at 349K and squares at 324 K.

Fig.5:Shows a linear plot of Equ.(16) plot of the dislocation velocity with  $\frac{1}{T}$ .

Fig.6:Shows Equ.(19) for different dislocation populations.

Fig.7:Shows the formation of pearlite at the grain boundaries during cooling.

Fig.8:Stress-strain curve of varying carbon content.

Fig.9:SEM images of 0.15%, 0.20% and 0.3% C.

Fig.10:Elongation of the Lüders strain vs the carbon content at the same strain-rate:  $8 \times 10^{-5} s^{-1}$ .

Fig.11:Shows Yield stress vs temperature of Equ.(29) against data from Table 1.

Fig.12:Pulled at a strain rate of  $\dot{\varepsilon} = 0.52 \times 10^{-4} s^{-1}$ .

Fig.13:A plot of the Lüders strain( $\circ$ ) and temperature, with upper yield point( $\bullet$ ).

Fig.14:Shows  $v$  vs  $\frac{1}{\sigma T}$ .

Fig.15:Lüders strain vs lower yield stress at strain-rate= $3.3 \times 10^{-4}$  with grain-sizes 1.1, 1.5, 3.6, 9.8 and 46.2  $\mu\text{m}$  respectfully. The Lüders strain in the aforementioned grain-sizes reduces as the temperature increases, albeit less evidently at the largest grain-size(46.2 $\mu\text{m}$ ).

Fig.16: $(\ln(\varepsilon_L))$  vs  $(\frac{1}{\sigma_L T})$  with regressions lines(Equ.(31)). Plotted at different grain-sizes with constant strain-rate  $3.3 \times 10^{-4}\text{s}^{-1}$ , showing good correlation between Equ.(31) and the data.

Fig.17:Plot of data with Equ.(33) curve fitted through the data. . Note that  $n$  in the above figure is termed  $u$  as  $n$  has already been defined as the stress-rate exponent and  $K$  is  $K'$  as  $K$  is defined as Kelvin. Also, the data was taken from many sources, which had different grain-sizes and strain-rate, therefore the above correlation should be view with caution.

Fig.18:Equ.(34) against plotted data for temperatures: (1)213, (2) 296, (3) 400, (4) 500 and (6) 700 K . For strain less than 0.1 where serrations are most prominent, the constitutive model predicts the trend but not the serrations.

Fig.19:(a)Work-hardening(work-hardening rate) and stress(in the same axis) as a function of Lüders strain, at grain sizes  $d_1$  and  $d_2$ , where  $d_1 > d_2$  with the corresponding lower yield stresses and work-hardening values at those points. (b)Work-hardening(work-hardening rate) and stress(in the same axis) as a function of grain-size( $d^{-\frac{1}{2}}$ ), at Lüders strain values  $\varepsilon_1$  and  $\varepsilon_2$ , where  $\varepsilon_2 > \varepsilon_1$  with the corresponding stress and work-hardening values at those points. It is evident that the work-hardening decreases and the yield point decreases as a function of grain-size.

Fig.20:Pole diagrams of material strain at 1% in Lüders band region. (a) {200} (b) {211} (c){100} planes. The {200} is the direction the uniaxial direction and therefore shows greatest strain.

Fig.21:Pole diagrams strain at 20%, after Lüders band has propagated. (a) {200} (b) {211} (c){100} planes. The strain distribution in the three planes is more intense version of Fig.20, indicating the strain in the planes during inhomogeneous deformation resolves in a similar manner to homogeneous de-

formation.

Fig.22:Plot of Lüders strain vs strain-rate and band velocity vs strain-rate of 0.07% C(steel sheet) at strain-rates:  $4.17 \times 10^{-6}$ - $8.37 \times 10^{-4} \text{ s}^{-1}$ .

Fig.23:Shows the effect of irradiated material on the yield point.

Fig.24: 0.025, 0.05, 0.13 and 0.16% C. Though the data points from the 0.05%C and 0.13%C have only 3 points, assuming a linear trend is substantiated by fitting the materials with more data points.

Fig.25:Plot of  $\phi$  vs carbon content, showing negative gradient between  $\phi$  and carbon content.

Fig.26:Plot of Equ.(71)(black line) with only  $\kappa$  free with Equ.(71)(red line) with  $a$ ,  $b$  and  $\kappa$  free.

Fig.27:Lüders strain( $\varepsilon_L$ ) against grain-size(d) at 296 K, with the model line(Equ.(127)).

Fig.28:x-axis is perpendicular to the gauge length and the y-axis is parallel or in the direction of the gauge length. This orientation has been chosen, because the DIC's axis are set in this way.

Fig.29:Profile of Lüders band propagating at shearing angle of  $45^\circ$  with the direction of propagation along the gauge length.

Fig.30:Picture of double-shoulder specimen with a 35mm gauge length.

Fig.31:Speckled specimen superimposed over the image generated from the DIC.

Fig.32:Effect of carbon content on Lüders strain(UL,AL,FP).

Fig.33:Effect of carbon content on lower yield strength(UL,AL,FP).

Fig.34:Effect of heat treatment of RPV steel on Lüders strain(AR,FP,TM-5H,TM-168H).

Fig.35:Effect of heat treatment of RPV steel on lower yield stress(AR,FP,TM-

5H,TM-168H).

Fig.36:Plot showing the spread of data of the lower yield stress at strain-rates:  $1 \times 10^{-2}$ ,  $1 \times 10^{-3}$  and  $1 \times 10^{-4} \text{ s}^{-1}$  of TM-168H structure.

Fig.37:Plot showing the spread of data of the Lüders strain at strain-rates:  $1 \times 10^{-2}$ ,  $1 \times 10^{-3}$  and  $1 \times 10^{-4} \text{ s}^{-1}$  of TM-168H structure.

Fig.38:Plot showing the spread of data of the lower yield stress at strain-rates:  $1 \times 10^{-2}$ ,  $1 \times 10^{-3}$  and  $1 \times 10^{-4} \text{ s}^{-1}$  of UL structure.

Fig.39:Plot showing the spread of data of Lüders strain at strain-rates:  $1 \times 10^{-2}$ ,  $1 \times 10^{-3}$  and  $1 \times 10^{-4} \text{ s}^{-1}$  of UL structure.

Fig.40:Plot showing the spread of data of the stress at strain-rates:  $1 \times 10^{-3}$ ,  $7.14 \times 10^{-4}$  and  $2.28 \times 10^{-4} \text{ s}^{-1}$  of AL structure.

Fig.41:Plot showing the spread of data of the Lüders strain at strain-rates:  $1 \times 10^{-3}$ ,  $7.14 \times 10^{-4}$  and  $2.28 \times 10^{-4} \text{ s}^{-1}$  of AL structure.

Fig.42:2 band nucleation using D.I.C software on UL specimen, with the bottom band nucleating first followed by the top band. The local Lüders strain on the top and bottom band are 6.5% and 7%, respectfully.

Fig.43:Lüders strain against the tempering time at strain-rates  $1 \times 10^{-2}$ - $1 \times 10^{-4} \text{ s}^{-1}$ , where the lines are there purely for illustration to show the trend of the data for each tempering time and are not regression lines.

Fig.44:1.5mm TM-28H hole of tensile specimen taken from the DIC. Points 1, 2, 3 and 4 are clockwise from on the top right.

Fig.45:Strain vs Frame number taken from point1(top right of circle surrounding the hole of Fig.44) indicating no Lüders band.

Fig.46:Strain vs Frame number taken from point2(bottom right of circle surrounding the hole of Fig.44), indicating no Lüders band.

Fig.47:True stress( $\sigma$ ) vs True strain( $\varepsilon$ ) curve of TM-28H(black) and TM-

168H(red) at strain-rates  $1 \times 10^{-3}$  and  $1 \times 10^{-4} \text{ s}^{-1}$  respectfully.

Fig.48:The spatial distribution of the total displacement of TM-168H, showing greater displacement on the left and than right. Because the hole is located more to the left than right.

Fig.49:Strain displacement in the y-axis with the point of nucleation location on the tensile specimen of UL-05. Taken from DIC.

Fig.50:DIC with corresponding strain displacement in the x-axis with dot on compressive specimen(point of nucleation) of UL-05. The maximum strain in the compressive axis is less than the strain in the uniaxial direction or y-axis, see Fig.49. This confirms the prediction of Equ.(132)(chapter 3) that is  $\varepsilon_y > \varepsilon_x$ .

Fig.51:Integration path around the crack tip.

Fig.52:Specimen geometry.

Fig.53:Development of mesh during compression and tension.

Fig.54: $J$  as function the distance  $a$  from the crack tip.

Fig.55:FAD curves for A533B specimens at -150° C under primary and secondary stresses by in-plane compression.

Fig.56:Compositions of all steels used by SINTAP.

Fig.57:A comparison between the Zhang model with modifying hardening models and experimental data.

Fig.58:CT test specimen using DIC of (a) loading and (b) unloading, showing the shear strains around the crack tip, with the spatial dependence across the line A-B taken.

Fig.59:The residual stress distribution predicted from the FE model from the crack tip. Fig.a shows the stress distribution for the Zhang model and Fig.b show the stress distribution for the standard work-hardening models

at strain-rate  $1 \times 10^{-2} \text{ s}^{-1}$ . Lines 1-4 can be seen in Fig.61.

Fig.60:Load vs CMOD or Crack mouth opening displacement plot, in order to determine the type of work-hardening model to use. The hysteresis curve from the Zhang model is smaller than the curve from the data. However the shape is approximately congruent, illustrating that the Zhang model or yield drop model is qualitatively correct. This is also true for the standard work-hardening models, showing that the material does not purely obey a kinematic or isotropic work hardening model, but rather a combination of the former and the latter, as shown for reactor pressure vessel steel.

Fig.61:The residual stresses predicted by each model in the x-direction-along the face of the CT specimen. The serrated lines of the Zhang model in plot (a) and (b) are evidence of yield points and, therefore, inhomogeneous deformation(Lüders bands) around the crack region during the loading and unloading of the CT specimen. It is evident that the residual stresses predicted by the Zhang model are consistently less than the other work hardening models, supporting the consensus that a yield drop model will predict lower residual stresses and, therefore, reduce the degree of conservatism.

Fig.62:Geometry chosen with constraint choice on geometry.

Fig.63:Selected parameters for the plastic behaviour.

Fig.64:Assumed stress distribution of secondary/residual stress in plate.

Fig.65:Failure assessment diagram of AR structure at strain-rate  $1 \times 10^{-3} \text{ s}^{-1}$ , where  $a$  is the crack length. Measured at  $K_{frac} = 57 \text{ MPa m}^{\frac{1}{2}}$  at  $\varepsilon_L = 0.82\%$ .

Fig.66:Failure assessment diagram of ferrite/pearlite structure at strain-rate  $1 \times 10^{-3} \text{ s}^{-1}$ , where  $a$  is the crack length. Measured  $K_{frac} = 57 \text{ MPa m}^{\frac{1}{2}}$  at  $\varepsilon_L = 0.6\%$ .

Fig.67:Failure assessment diagram of TM-168H structure at strain-rate  $1 \times 10^{-3} \text{ s}^{-1}$ , where  $a$  is the crack length. Measured  $K_{frac} = 57 \text{ MPa m}^{\frac{1}{2}}$  at  $\varepsilon_L = 3.54\%$ .

Fig.68:Failure assessment diagram of AR structure with Lüders strain(24.5 mm) without Lüders strain(25.5mm).

Fig.69:Failure assessment diagram of TM-168H structure at strain-rate $1 \times 10^{-3} s^{-1}$  varying fracture toughness values and FAD of TM-168H without Lüders strain(dotted line).

Fig.70:The value of  $K_{frac}$  for 57, 400 and 800 MPa m $^{\frac{1}{2}}$ .

Fig.71:Strain-time curve of AR with model curve in red and data in black at strain-rate  $1 \times 10^{-3} s^{-1}$ .

Fig.72:Strain-time curve of TM-168H with model curve in red and data in black at strain-rate  $1 \times 10^{-3} s^{-1}$ .

Fig.73:Strain-time curve of AL with model curve in red and data in black at strain-rate  $1 \times 10^{-3} s^{-1}$ .

Fig.74:Strain-time curve of UL with model curve in red and data in black at strain-rate  $1 \times 10^{-3} s^{-1}$ .

Fig.75:Tensile specimen taken from DIC software, showing points 1-5 of the first band,starting from the bottom and ending at the top of the first band(the longest band) and points 1-3 of the second band(starting from the top of the second band and ending end at the bottom of the second band(the smallest band) of UL-05 at strain-rate  $1 \times 10^{-2} s^{-1}$ .

Fig.76:Points 1-5 of the first Lüders band nucleated at the bottom of the tensile specimen, see Fig.75 with point 1 starting from the bottom, shows a reduction in the Lüders strain as it propagates to the last point on the first band. This characteristic of dampening.

Fig.77:Points 1-3 of the second Lüders band(nucleated at the top) of UL-05 have strains that are less than the first band, because nucleation occurred later and therefore at a lower stress. However, dampening is evident in the second band, too.

Fig.78:Comparison of the Zhang model with AR at strain-rate  $1 \times 10^{-2} s^{-1}$

with parameter  $D_1 = 500\text{ MPa}$ .

Fig.78:Comparison of the Zhang model with AR at strain-rate  $1 \times 10^{-2}\text{s}^{-1}$  and  $1 \times 10^{-3}\text{s}^{-1}$  with parameter  $D_1 = 500\text{ MPa}$  compared with the model data at the same strain-rates.

Fig.79:Zhang model at point of necking, showing key feature of dislocation pile up on grain-boundary.

Fig.80:Point of yield of 1.5mm hold with  $D_1 = 635$  at time at point of yielding.

Fig.81:Calculated stress-strain-curve of Fig.80.

Fig.82:Elements taken from top of hole of TM-28H model plotted in Fig.83.

Fig.83:Strain vs time(in seconds) for approximately 18 elements around the elements in Fig.82 at strain-rate  $1 \times 10^{-3}\text{s}^{-1}$  on the top.

Fig.84:Elements taken from the left of hole of TM-28H model plotted in Fig.85.

Fig.85:Strain vs time(in seconds) for approximately 10 elements around the elements in Fig.84 at strain-rate  $1 \times 10^{-3}\text{s}^{-1}$ .

Fig.86:Magnification of Fig.85 indicating no evidence of a Lüders band or sigmoidal strain-time curve.

Fig.87:Point of nucleation for TM-28H.

Fig.88:Grain structure of TM-120H at 500 magnification.

Fig.89:Grain structure of TM-144H at 500 magnification.

Fig.90:Grain structure of TM-168H at 500 magnification.

Fig.91:Load vs frame number of 0.007%C ferritic steel, pulled at strain-rate  $2.85 \times 10^{-6}\text{s}^{-1}$ .

Fig.92:Stochastic technique with the red crosses indicating displacement, while the blue crosses represent non-displaced elements.

Fig.93:Aluminium calibration target with the green dots are the tracking dots.

Fig.94:Two 5-mega-pixel camera mounted on a tripod facing the object of interest.

Fig.95:Curve fitting of Equ.(261) for the carbon content vs Lüders strain at different strain-rates.

Fig.96:Curve fitting of Equ.(262) of the lower yield stress vs carbon content at different strain-rates.

Fig.97:Curve fitting of Equ.(263) for the carbon content vs Lüders strain at different strain-rates, with combined values calculating from Fig.95 and Fig.96.

## List of Symbols

### Chapter 2

$\beta$  - the coefficient of compression.

$\dot{\gamma}_r$  - a constant of proportionality.

$\Delta$  - a universal material constant.

$\dot{\epsilon}_e$  - the strain rate of the elastic contribution.

$\varepsilon_{hkl}$  - the plane strain with Miller indices  $h, k, l$ .

$\dot{\epsilon}_p$  - the strain rate of the plastic contribution.

$\varepsilon_T$  - the true strain.

$\dot{\varepsilon}$  - the strain-rate and strain-rate tensor.

$\dot{\varepsilon}_M$  - the strain-rate of the machine.

$\lambda$  - the slip plane distance.

$\rho_0$  - the density of the material.

$\rho_M$  - the mobile dislocation density.

$\dot{\Sigma}$  - a parameter determined from neutron diffraction.

$\sigma_{ave}$  - the average stress of the material.

$\sigma_{cri}$  - the stress required to move a dislocation from a carbon atmosphere.

$\sigma_{ly}$  - the lower yield stress.

$\sigma_{uy}$  - the upper yield point.

$\sigma_T$  - the true stress.

$\sigma_0$  - a constant of integration.

$\sigma'_0$  - a constant which can be regarded as the sum of the internal friction.

$\dot{\sigma}$  - the grain stress tensor and general stress-rate.

$\tau_0$  - the internal shearing or frictional stress on the glide plane.

$\Upsilon$  - a constant

$B$  - the interacting parameter.

$b$ - the Burger's vector.

$C$  - a constant.

$C_b(t)$  - the atomic fraction of carbon in the grain.

$c_0$  - a constant.

$D$  - a constant.

$D_\gamma$  - the diffusion coefficient within the  $\gamma_{fcc}$ -iron.

$D_{car}$  - the diffusion coefficient of carbon.

$d_{grain}$  - the grain-size.

$d_{hkl}$  - the spacing between atomic planes after deformation.

$d_{hkl(ref)}$  - the spacing taking from a reference point after annealing.

$E$  - Young's modulus

$F(\varepsilon_i^p)$  - the fraction of dislocation.

$f_r$  - the volume fraction of particles(precipitates).

$f$  - a fixed fraction of the dislocation length.

$G$  - the shear modulus.

$G_0$  - the thermal activation energy.

$H_{work}$  - the work-hardening.

$K$  - kelvin.

$K'$  - a constant.

$k_r$  - a constant that is slightly dependent on temperature.

$L$  - the total length of the dislocation.

$L_d$  - the initial number of unpinned dislocations.

$l_0$  - the gauge length.

$m$  - the strain-rate sensitivity.

$N$  - the number of bands formed.

$N_p$  - the pit density per  $\text{cm}^2$ .

$N(t)$  - the number of carbon atoms available to pin the dislocations.

$n$  - the stress-rate sensitivity exponent.

$n_0$  - the initial solute density.

$O$  - the Elshier tensor.

$Q$  - the activation energy of the carbon or the force required(energy) to segregate the carbon atoms to the grain-boundaries.

$q$  - the macroscopic work hardening.

$R$  - the rate of formation.

$R_{grain}$  - the radius of the grain.

$r$  - the average particle radius.

$r_{cri}$  - the equilibrium distance from the carbon atmosphere.

$S$  - the distance between the lamellae.

$T$  - the temperature.

$T_c$  - defined as the temperature before serration or blue brittle failure.

$T_{max}$  - the maximum temperature that serrations can appear.

$U_{max}$  - the maximum potential.

$u$  - the strain-hardening exponent.

$v_d$  - the dislocation velocity.

$v_L$  - the velocity of the Lüders band.

$v_m$  - the cross-head velocity.

$W$  - the overall stiffness tensor.

$\dot{X}$  - a parameter determined from neutron diffraction.

$Z$  - Zener-Holloman parameter.

## Chapter 3

$\alpha$  - a dimensional parameter.

$\Gamma$  - a constant.

$\gamma$  - the frequency.

$\varepsilon_L$  - the Lüders strain.

$\varepsilon_{x,y}$  - the strain in the x or y-direction.

$\kappa$  - a constant.

$\nu$  - Poisson's ratio

$\rho_0$  - the free-dislocation density.

$\rho_{max}$  is the maximum dislocation density.

$\sigma_{uy}$  - the upper yield point.

$\sigma_{ly}$  - the lower yield stress.

$\phi$  - the work hardening rate.

$\Omega$  - the dislocation remobilization parameter.

$\omega$  - a parameter related to the micro-structure of the material.

$A$  - a constant dependent on the grain-size.

$A_{cross}$  - the cross-sectional area.

$a$  - the acceleration of a dislocation.

$B$  - a constant dependent on the grain-size.

$b$  - the dislocation length or Burger's vector.

$b_{fri}$  - a constant of friction.

$C$  - amount of carbon content.

$d_{grain}$  - the grain-size.

$E$  - Young's modulus.

$F_{drive}$  - the driving force.

$F_{drag}$  - a frictional force.

$K$  - universal material constant.

$k_e$  - a constant derived from the Hall-Petch relation.

$L_0$  - the gauge length.

$m$  - the strain-rate sensitivity.

$n$  - the stress-rate sensitivity.

$S_0$  - the mean free path of the dislocation.

$U(\varepsilon)$  - an immobilization term.

$u$  - the strain-hardening exponent.

$v_d$  - the dislocation velocity.

## Zhang model parameters

$\alpha$ -constant.

$\beta$ -constant.

$\varepsilon_{eq}^e, \varepsilon_{eq}^p$ -elastic and plastic strain.

$\dot{\varepsilon}$ -strain-rate.

$\sigma_y$ -yield stress.

$\Omega$ -effective strain during interaction.

$\omega_1, \omega_2$ -constants.

$C_M$ -maximum solute concentration.

$C_S$ -pinning solute concentration.

$D_1$ ,  $D_2$ ,  $D_3$ -constants.

$P_1$ ,  $P_2$ -constants.

$S_1$ ,  $S_2$ -constants.

$T_A$ -ageing time.

$T_W$ -time taken for dislocation to traverse an obstacle.

$t$ -time.

## Chapter 4

$\sigma_{uy}$  - the upper yield point.

$\sigma_{ly}$  - the lower yield stress.

$\varepsilon_f$  - the total Lüders strain after multiple banding.

$\varepsilon_L$  - the Lüders strain

$m$  - the strain-rate sensitivity.

$n$  - the stress-rate sensitivity.

$u$  - the strain-hardening exponent.

## Chapter 5

$A$  - the cross-sectional areas of the tensile specimen.

$E$  - Young's modulus.

$k_1$  - the spring constant of the Hydraulic machine.

$k_2$  - the spring constant on DIC.

$t_y$  - the time taken for the material to yield.

## Chapter 6

$\varepsilon_{ref}$  - a reference strain.

$\varepsilon_L$  - the Lüders strain.

$\nu$  - Poissons ratio.

$\sigma_{ij}$  components of stress.

$\sigma_{lyp}$  - the lower yield stress.

$\sigma_{UTS}$  - the ultimate tensile stress.

$a$  - the crack length.

$K$  - the stress intensity factor

$K_{frac}$  - the fracture toughness.

$J_{mod}$ - modified form of  $J$  that accounts for residual stress.

$L_r$  - the proximity of plastic collapse.

$N$  - an exponent.

## Chapter 7

$\alpha$  - a dimensional parameter.

$\gamma$  - the frequency.

$\varepsilon_L$  - the Lüders strain.

$\varepsilon_c$  - localised maximum strain.

$\dot{\varepsilon}_{max}$  - the maximum strain-rate in Lüders band.

$\Lambda$  - A constant.

$\rho_0$  - the free-dislocation density.

$\rho_{max}$  - the maximum dislocation density.

$\Omega$  - the dislocation remobilization parameter.

$\tau$  - the average time Lüders band

$\tau_{acc}$  - the actual measured time of the Lüders band.

$b$  - the dislocation length or Burger's vector.

$d_{grain}$  - the grain-size.

$S_0$  - the mean free path of the dislocation.

$v_d$  - the dislocation velocity.

$v_l$  - the velocity of the Lüders band.

# 1 Introduction to Problem

A Reactor Pressure Vessel or RPV is a low alloy steel body that surrounds the fuel assemblies and constitutes part of the primary circuit in a nuclear reactor. During a reactor's life time, which can be up to 60 years, the RPV undergoes stresses induced by pressure and temperature gradients, lateral stresses due to the cylindrical symmetry and prolonged exposure to radiation from the fission process. Therefore, it is imperative that the correct structural safety assessment codes are used to ensure structural integrity is maintained, during the life time of the reactor. These codes collectively are known as the R-code[2], which consist of R6 for low temperature and R5 for high temperatures <sup>1</sup>. The R6 code is assessment of the integrity of structures containing a procedure for defects that is an industrial standard in the nuclear industry. Although it is one of the most robust and frequently updated safety procedures in the nuclear industry, whose success is reflected in the design of current RPVs, it assumes that for RPV steel, which has an upper bainitic structure, the transition from elastic to plastic, under tensile dominated stresses, is continuous. This is true for face centred cubic or f.c.c structures, such as Hastelloy N. Hastelloy N is a nickel based alloy with 16% Mo and 7 % Cr and 5% Iron(max), which was used in molten salt reactors[3](see Fig.(1)). However, RPV steel yields discontinuously under tensile dominated stresses and the result of this is a Lüders band(see Fig.(2)). Consequently, the residual stresses predicted by the R6-code, when contrasted with calculations that include discontinuous yielding, can be over-conservative<sup>2</sup>[4].

An over-conservative design results in thicker walls and, therefore, more material. This results in additional costs, due to pessimistic calculations and not using the full potential of the material. A more detailed understanding of how the material responds under primary and residual stresses could result in less pessimistic predictions and, therefore, less costly designs.

It is the objective of this work is to identify the amount of conservatism that is employed in the standard R6 procedure by developing a model that

---

<sup>1</sup>The temperature ranges in this thesis deal primarily in low temperature region, therefore only R6 code will be discussed.

<sup>2</sup>Conservatism is defined as the amount of pessimism added to a material(by assuming that the material will fail prematurely) to avoid either the three modes of failure(ductile, brittle and fatigue). This is manifested as a smaller fracture toughness value relative to the actual fracture toughness value.

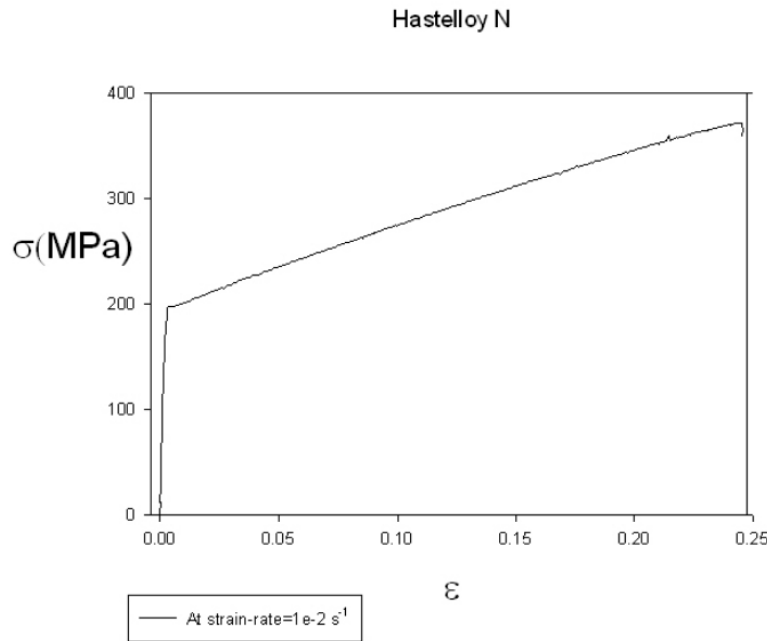


Figure 1: Stress-strain curve Hastelloy N with no definite yield point and therefore, no Lüders band present.

uses the fundamental parameters that define a Lüders band.

This leads to the question: Does a model that represents Lüders bands when compared to the R6 procedure, produce less conservative values for tensile dominated stress and, additionally, is this difference significant enough to warrant an alternative approach when employing this type of steel in RPVs or the design of RPVs

In order to investigate the proposed problem, the above question has been broken down into several questions or objectives that will be answered in the thesis:

1. What dictates the magnitude of the Lüders strain?
2. How does the micro-structure affect Lüders bands?
3. How does the Failure Assessment Diagram determine how the magnitude of the Lüders strain affect component design. That is, is a larger Lüders strain more beneficial than a Lüders strain of less magnitude?
4. What is the best method of integrating the model into the standard R6

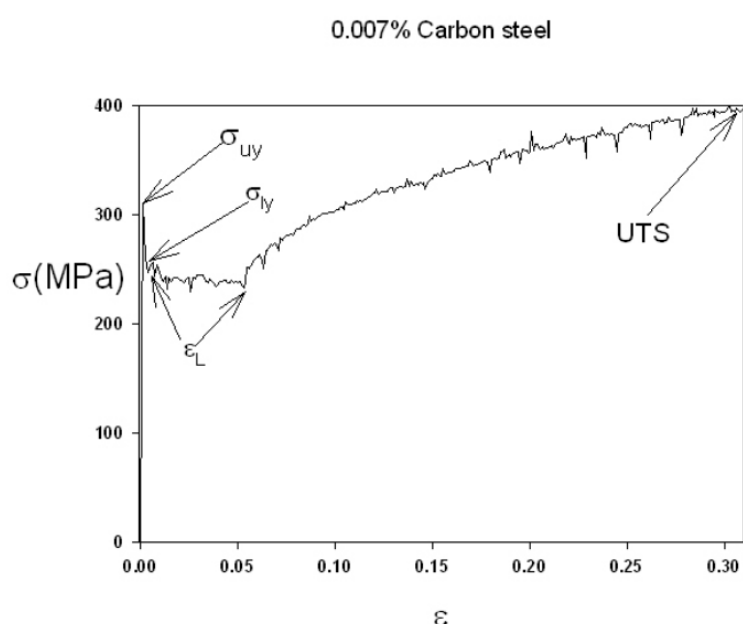


Figure 2: Stress-strain curve of ultra low carbon steel(0.007% C).  $\sigma_{uy}$  is the upper yield point,  $\sigma_{ly}$  is the lower yield point and  $\varepsilon_L$  is the Lüders strain and UTS the ultimate tensile stress.

procedure? For example, as an extension: adding a yield drop model to the standard work hardening models or using an independent model that accounts for the yield drop behaviour.

The explicit answers to the above questions will contribute to the statement of originality.

The next section will comprise of the structure of the thesis.

## 1.1 Structure of thesis

- Chapter 2 presents the literature review section. This contains a comprehensive review of the current theories and experiments on Lüders band development and, subsequently, what warrants further investigation.
- Chapter 3 presents the theoretical section. This consists of the main model used to describe Lüders bands. A further model using the Bergstrom equation[5], which was originally developed to describe homogeneous plastic deformation up to necking, will also be presented and modified to account for inhomogeneous deformation and, therefore with the intention of calculating the localised dislocation density, Lüders strain and band velocity from given data.
- Chapter 4 presents experimental section on tensile data of 0.17% C low alloy reactor pressure vessel steel with an upper-bainite structure, a tempered martensite structure and ferrite-pearlite structure of the same composition. A low carbon steel of 0.07% C and an ultra low carbon steel of 0.007% C are also presented. The methodology and description of experiments are followed with discussion and conclusion.
- Chapter 5 presents the tensile experiment with a defect. This chapter uses similar techniques in chapter 4 on tensile specimens, but with a circular defect for tempered martensite steel abbreviated to TM-28H and TM-168H, which indicates that the material was tempered for 28 and 168 hours, respectively. This is followed by discussion and conclusion
- Chapter 6 presents the application of FADs in conjunction with the R6 procedure. FADs are constructed for an RPV steel with 0.17% C with an upper-bainitic micro-structure abbreviated to AR. Through

heat treatments of the AR micro-structure, two other micro-structures were created and compared with the AR. These were a ferrite-pearlite structure and a tempered martensite structure, abbreviated to FP and TM, respectively.

- Chapter 7 presents the application of the theoretical model, derived in chapter 3, and is applied to some of the tensile data namely, upper-bainite structure(AR), tempered martensite structure(TM-168H), the mild steel with manganese sulphide particles(AL) and an ultra-low carbon steel with trace carbon(UL) at a constant strain-rate of  $1 \times 10^{-3} \text{ s}^{-1}$ .
- Chapter 8 presents the Zhang's model[6] to the AR structure at strain-rate  $1 \times 10^{-3} \text{ s}^{-1}$  for uniaxial test and TM-28H the model for biaxial freedom at the same strain-rate.
- Chapter 9 presents the main discussion consisting of the main points from which it is determined to what extent the thesis has addressed and answered the questions presented.
- Chapter 10 presents the main conclusions drawn from Chapter 9. The conclusions that warrant further investigation are identified in future work.

## 1.2 Statement of originality

The following is a list of what is original in this thesis.

- a) The amalgamation of the Tsuchida model[7] and the model due to Sun et al[8] that is Equ.(55) and adding further insight into the constant  $\Delta$  by improving Equ.(33) to produce Equ.(58). The plot of Fig.(15) using the data of Tsuchida et al[7] to plot Equ.(31). Equ.(31) that relates the Lüders strain to the stress and temperature, before serrations begin on the Lüders plateau is also original, as an explicit equation that relates the Lüders strain to the temperature that fits the data as shown in Fig.(16) has thus far alluded the author in the literature search.
- b) All the work in the theoretical section apart from the equations and data that has been used and acknowledged, is original. The relation of the Lüders strain to the grain-size or Equ.(127) has been mentioned

and shown by Conrad[9] and Tsuchida et al[7], however a full theory where the equations fall out naturally and the exact form are original. It has been possible to therefore describe qualitatively how a Lüders band could vary with the same composition, but with different micro-structure.

- c) The use of digital image correlation or DIC to specifically look at the Lüders band on an RPV steel, comparing an upper-bainite structure, tempered martensite and a ferrite-pearlite structure, with similar tensile properties. The objective was to quantify the micro-structural effects by keeping other factors as constant as practically as possible, such as the yield point and hardness, although it was shown that two materials can not have the same hardness and same yield point for the same composition. New insight has been added by showing specifically that a Lüders strain varies significantly in an RPV steel with the same composition but different micro-structures. Therefore, showing that simply correlating the Lüders strain to carbon content is incorrect or is only valid for the micro-structures and grains of similar sizes.
- d) An application of the theoretical model to the strain-time curves taken from DIC, giving insight into how precipitates can affect the propagation of the band such as the manganese sulphide clusters that were evident in the 0.07 % C steel. Also, as a result of the theory a compressive band was also predicted and this was verified through DIC(see Fig.(50)). This has wider implications for band nucleation as most research is focussed on the tensile and not on the compressive component.
- e) The use of the FADs to specifically look at the upper-bainite, ferrite-pearlite and tempered martensite structure and at -155°C and above, by increasing the fracture toughness. To show conclusively that the micro-structure does not significantly affect the initiation of failure by crack-propagation. Therefore, the tempered martensite structure could be as beneficial as an upper-banitic structure, as the degree of conservatism is similar.
- f) The use of DIC on specifically TM-28H and TM-168H that is a material that has been tempered for 28 hour and a material that has been tempered for 168 hours. By looking at the effect of a hole defect and also the modelling of the problem using the Zhang model[6], showing

that if the tensile component during nucleation is less dominant, then a Lüders band will not nucleate.

- g) In Appendix E the proposition of a J-integral that factors in a Lüders strain has been proposed, using the gauge invariance of the J-integral.
- h) The work in Appendix F, relating the Lüders strain to the carbon content, without assuming the form of the stress-strain relationship between the lower yield stress and the Lüders strain(see chapter 3). The derivation of the lower yield stress as a function of carbon content is also original, with the final result similar to more sophisticated models. Finally, from knowing how the Lüders strain and lower yield stress vary as a function of carbon content, it was possible to derive the corresponding stress-strain relationship, which is also original in its form.

## 2 Literature Review

To understand what factors contribute to the nucleation and propagation of a Lüders band, a comprehensive literature review is required to determine which areas need investigating. The elements identified from this investigation will form the basis of research and, therefore, a working, realistic model can be developed.

### 2.1 Lüders bands

Lüders bands have been observed since the mid-19th century. However, it was Lüders in 1860 who first realised the importance of this phenomenon which bears his name[10]. Lüders bands occur in body centred cubic ferritic and mild steel, but can occur in non-ferrous material, such as copper alloys. They are observed in uniaxial tensile tests, although uniaxial stress is not essential for nucleation. A Lüders band nucleates when the material reaches its elastic limit and the following condition is satisfied:

$$\sigma_{uy} > \sigma_{ave} \quad (1)$$

where  $\sigma_{uy}$  is the upper yield stress and  $\sigma_{ave}$  is the average stress in the material.

Equ.(1) is due to static pinning, which will be discussed in the next section. This process is analogous to necking and is a condition of instability. For the process to continue, a second condition is satisfied. That is:

$$\sigma_{ly} > \tau_0 \quad (2)$$

where  $\sigma_{ly}$  is the lower yield stress and  $\tau_0$  is the internal shearing or frictional stress on the glide plane.

When Equ.(2) is satisfied, the type of deformation occurring, which is defined as the propagation of dislocations, is known as inhomogeneous deformation.

The process has several key features that define the Lüders band. They are: upper yield stress( $\sigma_{uy}$ ), lower yield( $\sigma_{ly}$ ) stress and the Lüders strain( $\varepsilon_L$ ).

### 2.2 Static Pinning

Steel is an alloy mainly composed of iron and carbon, the chosen composition is usually dependent on the application. Carbon can exist, because of its

size compared to iron, both interstitially within the iron matrix and as a compound i.e as carbide. An interstitial atom is known as a solute. A solute atom has the ability to move around the iron matrix to regions of high potential<sup>3</sup>, through thermal diffusion. These regions mainly consist of dislocations.

Cottrell and Bilby [11] on their seminal work on yield stress phenomena proposed that the solute or carbon atoms would interact and pin the dislocations. This resulted in the relaxation of the surrounding lattice and a decrease in the stored energy of the dislocation. Consequently, deformation occurred when the dislocations were released from the elastic potential of the carbon atoms or the carbon atmospheres. Although the analysis henceforth will be for carbon atoms as they are the most abundant solute in steel, nitrogen can also pin dislocations.

For this interaction to occur, it was assumed that carbon atoms would interact with dislocations through hydrostatic pressure or elastic interaction. However, this is only true for edge dislocations, as screw dislocations interact through sheering only and not through the principal or planar stresses. Consequently, their model was only valid for edge dislocation dominated materials. The final results of Cottrell's model that predicted the yield stress and strain-ageing relationship, which will now be provided.

Cottrell showed that the stress required to move a dislocation from a carbon atmosphere, without thermal contributions(athermal interactions)is[11]:

$$\sigma_{cri} = \frac{3\sqrt{3}B}{4\lambda^2 r_{cri}^2} \times 10^{-2} \quad Nm^{-2} \quad (3)$$

where  $\sigma_{cri}$  is the stress required to move a dislocation from a carbon atmosphere,  $B$  is the interacting parameter,  $\lambda$  is the slip plane distance and  $r_{cri}$  is the equilibrium distance from the carbon atmosphere.

Equ.(3) is interpreted as the yield stress at 0 K.

Quantum mechanics shows that 0 K is not possible, as there is always a ground state energy thus making it impossible to validate Equ.(3) directly. Therefore, Cottrell used an extrapolation method to show that as the amount of thermal energy available to the dislocations decreases, the ratio of the measured yield stress( $\sigma_y$ ) and  $\sigma_{cri}$  increased, as shown in Table 1 taken from McAdams et al[12].

---

<sup>3</sup>Regions of high potential refer to regions where there is considerable high strain and stress on the lattice.

If the limit is taken between the ratio of  $\sigma_y$  and  $\sigma_{cri}$ , the following result is expected:

$$\lim_{T \rightarrow 0} \frac{\sigma_y}{\sigma_{cri}} \approx 1 \quad (4)$$

The  $\approx$  has been added due to the quantum mechanical limit i.e. ground state energy.

Table 1: Data taken from [12]

Temperature(K)	$\sigma_y$ (MPa)	$\frac{\sigma_y}{\sigma_{cri}}$
85	607	0.485
144	414	0.330
195	283	0.225
303	145	0.115
373	110	0.0009

The equilibrium distance calculated between the carbon atmosphere and the dislocation is as follows:

$$r_{cri} \approx 7\text{\AA} \quad (5)$$

The second result presented and predicted by the static pinning model is the time taken for the percentage population of carbon atoms migrating to the dislocations, after pre-straining the material in order to free the dislocations. It was shown that the number of carbon atoms available to pin the dislocations  $N(t)$  is proportional to  $(t^{\frac{2}{3}})$ . In its full form:

$$\frac{N(t)}{N_s} = 3 \left( \frac{\pi}{2} \right)^{\frac{1}{3}} n_0 L_d \left( \frac{BD_{car} t}{k_b T} \right)^{\frac{2}{3}} \quad (6)$$

where  $\frac{N(t)}{N_s}$  is the fraction of the total dissolved carbon to migrate in time  $t$  at temperature  $T$ ,  $n_0$  is the initial solute density,  $B$  is the interacting parameter,  $D_{car}$  is the diffusion coefficient of carbon,  $L_d$  is the initial number of unpinned dislocations and  $k_b$  is Boltzmann's constant.

In Fig.(3) it is evident that there is a strong correlation between Equ.(6) and the strain-ageing data. For small  $t$ , when the distance of the carbon atoms from the dislocations, on average, are greater than or equal to  $r_{cri}$ , Equ.(6) and the data are in agreement. This is to be expected, as distances greater than or equal to  $r_{cri}$ , are in the regions where elastic theory are valid. As  $t$  increases and the distance of the carbon atoms is now less than  $r_{cri}$ ,

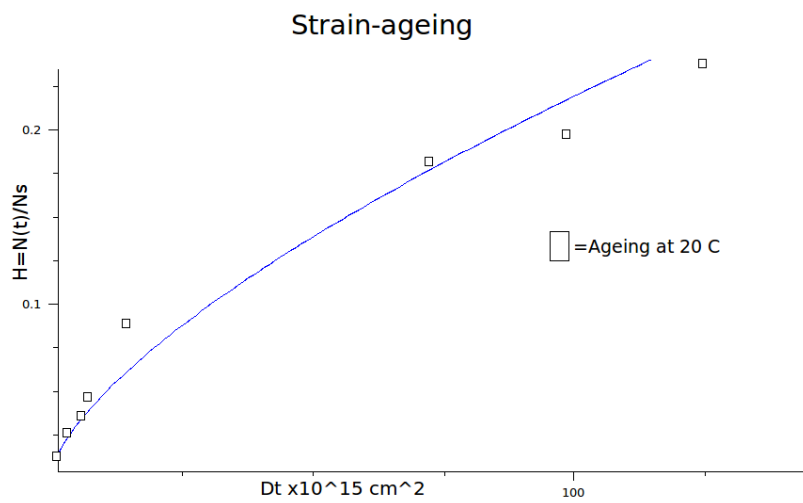


Figure 3: Equ.(6) curve fitted to strain-ageing data, with the squares representing the fraction of carbon atoms migrating and pinning the dislocations, in units of  $Dt$  ( where  $D = D_{car}$  is the diffusion coefficient and  $t$  is the time taken for the fraction of carbon atoms to pin the dislocations.). Taken from McAdams et al[12].

Equ.(6) and the data begin to diverge. This is due to local effects that were not included into the atmosphere model, such as chemical bonding, dislocation dipole interaction and asymmetric distortions. The disagreement between Equ.(6) and Fig.(3) for large  $t$  illustrates the complexity of solute-dislocation interactions.

Modern theories have modified the atmosphere model by incorporating more detailed interactions with the carbon atoms and the grains. This was done by Zhao et al[13], with the additional assumption that: the rate of carbon atmosphere formation to dislocations, during strain-ageing, was proportional to the active number of carbon atoms. That is:

$$\frac{dN(t)}{dt} = L_d(t)n(t)v_{dis}\frac{1}{t^{1/3}} \quad (7)$$

where  $N(t)$  has its same meaning,  $v_{dis} = 2(\pi/2)^{1/3}(AD_{car}/kT)^2/3$ ,  $n(t)$  is the local active carbon, and  $L_d(t)$  is the density of the dislocations unpinned, defined as:

$$L_d(t) = L_d - \Upsilon N(t) \quad (8)$$

where  $L_d$  is the initial number of dislocations unpinned per length and  $\Upsilon$  is a constant.

Additionally, it was assumed that the grains were circular, with radius  $R_{grain}$  and that the carbon solute atoms migrated to grain boundaries, during strain ageing, to minimise the free energy of the material. Equ.(7) together with the following diffusion equation:

$$\frac{1}{r^2} \frac{\partial(D_{car}r^2\frac{\partial n}{\partial r})}{\partial r} - v_{dis}\frac{F}{t^{1/3}} = \frac{\partial n}{\partial t} \quad (9)$$

where  $F = L_d(t)n(t,r)$  for the general model,  $D_{car}$  is the diffusion path coefficient of carbon.

$$C(t, R_{grain}) = \frac{C_b(t)}{B \exp(\frac{Q}{k_b T})(1 - C_b(t))} \quad (10)$$

where  $C(t, R_{grain})$  is the fraction of the distorted positions in the grain boundaries by the carbon atoms,  $Q$  is the activation energy or the work required to segregate the carbon atoms to the grain boundaries with value 62700 J/mol and  $C_b(t)$  is the atomic fraction of carbon in the grain.

With boundary conditions:

$$n(t=0, r) = n_o \quad (11)$$

$$L(t = 0, r) = L_d \quad (12)$$

formed the entire equations necessary to describe carbon atmosphere dislocation interaction.

Cottrell's model assumed that the initial active dislocation length and the initial number of carbon solutes remains constant during ageing i.e. Equ.(11) and Equ.(12). This is in contrast with the Zhao model, which factors the evolution of the number of carbon and dislocation lengths available for the interaction-time. Zhao compared the modified model to their experimental data on strain-ageing: Steel sheets with the following chemical composition in ppm 20 C, 900 Mn, 450 P, 30 S, 490 Al, 70 Ti and 16N; with the titanium added to bond with all the nitrogen atoms. This ensured that the only solutes taking part in the strain-ageing process were the carbon atoms. The sheets were annealed at 850°C for 60 seconds and over aged for 180 seconds at 400°C on a 80 mm gauge length.

The contrast between the original Cottrell-Bilby model and the Zhao model is shown by solving the following equation:

$$S_{dis}(t) = \frac{\int_0^R N(r, t) dr}{R_{grain} N_s} \quad (13)$$

where  $S_{dis}$  is the average saturation level of the dislocations.

When Equ.(13) is solved for the Cottrell-Bilby model and the Zhao model, the result is shown in Fig.(4). It is evident that the Cottrell-Bilby model accounts for early strain-ageing, which was also shown in Fig(3). However, instead of showing the average number of available carbon atoms, Fig.(4) shows the corresponding average distance of the number of available carbon atoms to pin the dislocations or the saturation level of dislocations, similar to Fig.(3). As the carbon atoms or dislocations move closer to each other, the Cottrell-Bilby model begins to diverge away from the data. The Zhao model fits the trend of the data satisfactorily, because of Equ.(8). That is the number of mobile dislocations decreases with time, due to other forms of pinning during strain-ageing, such as back diffusion and segregation on the grain-boundaries. This is reflected in the trend of the ratio of  $\frac{\sigma_{applied}}{\sigma_{yield}}$  converging to 1 or when the distance between the dislocation and carbon atom( $r_{cri}$ ) have reached a minimum, where  $\sigma_{applied}$  is the stress required to move a dislocation from a carbon atmosphere for a given distance. As the Cottroll-Bilby model does not converge with the data at 1, the Zhao model

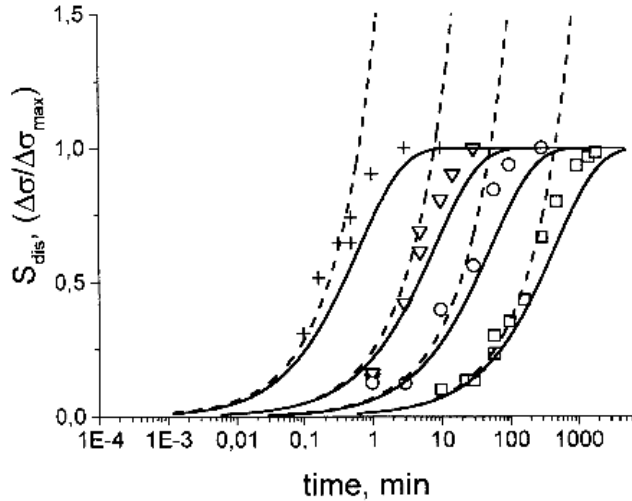


Figure 4: Plot fraction increase in yield stress and  $S_{dis}$  vs time, showing the contrast between Cottrell's model in dotted lines and the modified models with the continuous lines with the experimental data. The material was pre-strained by 0.02% and the ageing temperatures are represented as follows: 140°C(+), 100°C(▽), 75°C(○) and 50°C(□). Specifically, the Zhao model and the data converge at  $\frac{\Delta\sigma}{\Delta\sigma_{max}} = \frac{\sigma_{applied}}{\sigma_{yield}} = 1$ , which is representative of the distance at the equilibrium point from the dislocation core or  $r_{cri}$ . Taken from [13]

gives a better representation and is therefore an improvement to the original atmosphere model.

To summarise: the static pinning model has been presented. It was shown that carbon atoms exist interstitially in the iron lattice and migrate to regions of high potential(dislocations), by thermal diffusion and dilate the lattice which, subsequently, pin the dislocation. This gave a simple, intuitive picture of yield stress; the stress required to remove a dislocation from a carbon atmosphere. It was also demonstrated that the atmosphere model can be used to explain strain-ageing. However, strain-ageing also illustrated the limitation in the atmosphere model when compared to Fig.(3), but this was rectified by Zhao et al[13], who has improved the model.

The next section will present the Johnston-Gillman model for rapid multiplication of the dislocations. A dynamic model was warranted, because the Cottrell/Bilby model, although it described nucleation of a Lüders band,

could not account for the propagation of a Lüders band. There were also some anomalies that could not be explained by the pinning model alone.

It was shown that pure ionic solids such as LiF exhibited a stress-strain curve similar to Fig.(2), by Johnston et al[14]. Therefore, a yield stress could exist without interstitials. It was also observed by Conrad et al[9] that at temperatures where the diffusion of carbon is negligible and, consequently, no solutes can pin the dislocations, a yield stress was still observed.

### 2.3 Dislocation multiplication

Johnston and Gilman[14] investigated the ionic material LiF(lithium fluoride) to look at the dynamics of dislocations. LiF was chosen because stress analysis can be done in an as-grown condition and also, when the crystals are grown, there is a notably low dislocation density which makes it ideal for studying dislocation movement.

The methodology of preparation was as follows: LiF was cleaved from a bigger crystal, chemically polished to remove any dislocations formed from the cutting process, polished again and rolled with an 8mm diameter sphere to add the dislocations on the surface(on the  $\langle 100 \rangle$  slip-planes). The initial position of the dislocations were noted(with etchant) and stress pulses, with varying times, were sent through the surface. The specimens were then etched again to reveal the final positions of the dislocations. The speeds measured were in the range 4m/s to 103m/s-depending on frequency of pulse.

The etching technique used to reveal the dislocations was a technique known as etch pitting<sup>4</sup>. Etch pitting reveals imperfections on a polished surface. Johnston and Gilman's key observations can be summarised as follows:

1. The yield stress had a direct dependence on the dislocation density and the number of dislocations increased after initiation.
2. The velocities of the dislocations were dependent on the strain rate of the material and temperature.
3. Angle of pits slopes, on the etched surface, did not have a dominant affect on the dislocations, which was reflective in the dislocation distribution.

---

<sup>4</sup>A detailed explanation of etch pitting can be found in most materials science books[15].

4. Distribution of the dislocations affected the formation of plastic flow, although not essential for plasticity.
5. The number of dislocations increased exponentially, with strain rate(during plasticity).
6. Dislocations formed loops on the slip plane.
7. Edge dislocations moved faster than screw dislocations, although they converged to the same maximum speed, which for a material is the speed of sound in a medium.
8. Dislocations at low velocities did not have uniform motion.
9. Irradiation pins dislocations.
10. Crystals with higher hardness at low temperature, formed higher multiplications of dislocations during plasticity than softer crystals at the same temperatures.

These observations give an insight into how the dynamics of dislocations behave with the application of stress.

The most significant of these observations is the multiplication of the dislocations, when the yield stress is applied. This occurred when dislocations saturated the glide-plane, forming dislocation loops and multiplying in the process at an exponential-rate. The distribution of the original dislocations affected how the material would plastically deform. This, coupled with the viscous stress, gave a picture of plasticity in terms of dislocations alone.

To eliminate the effect of static pinning, the material was strain-aged to allow time for the impurities to lock the dislocations(presumably by diffusion) and free-dislocation loops were created on the slip-planes. A sufficient stress was then induced to produce dislocation movement, with magnitudes less than the stress required to move the pinned dislocations. However, the type of pinning or locking of the sessile dislocations was unclear as the source of the pinning was not stated explicitly. Therefore, Johnston and Gilman's analysis is treated with caution, as additional analysis, such as quantifying the number of free and pinned dislocations with electron back scattering techniques before and after the experiment was necessary to fully eliminate any contribution from the immobilized or sessile dislocations.

The type of interactions of the dislocations with the slip-plane was interpreted differently to others. Johnston and Gilman's analysis is based on the tacit assumption that the dislocation motion, during plasticity, is purely glide interaction and not dislocation-precipitate interaction. This is inconsistent with the findings of Hassen et al[16] with face centred cubic pure NaCl. The inconsistency comes from the relationship of the sheer stress to pit density count. It was stated previously that etch pitting was used because it reveals most of the dislocations on the surface, therefore the number density of pits per unit area can be representative of the dislocation density per unit area. In LiF, this relationship was shown to be[14]:

$$\tau_0 \propto N_p \quad (14)$$

where  $\tau_0$  is the sheering stress and is  $N_p$  is the pit density per  $\text{cm}^2$ .

For NaCl this was shown to be:

$$\tau_0 \propto N_p^{\frac{1}{2}} \quad (15)$$

Hassen's data for NaCl when fitted to Equ.(15), had good correlation and went through the origin. Hassen pointed out that this result was indicative of no friction in the glide plane and any deviation from the Equ.(15) i.e. not through the origin, would indicate frictional loss. Johnston and Gilman's line did not agree with Equ.(15) and thus constituted to dislocation-precipitate interactions, although it could be due to the different crystal lattice structure. The former reason is further substantiated by Johnston[17], on further studies into LiF. In their original investigations, Johnston and Gilman used precipitation hardening on LiF which would contribute to dislocation-precipitate interactions. This was in contrast to Hassen et al[16] who avoided precipitating hardening by air-cooling the specimens.

Another important observation in Johnston and Gilman's findings was the velocity dependence of the dislocations as function of temperature. It was shown that it varied in the temperature range( $224 \text{ K} \leq T \leq 294 \text{ K}$ ) with the fraction  $\frac{1}{T}$ . Or:

$$v_d = f(\sigma) \exp\left(\frac{Q}{k_b T}\right) \quad (16)$$

where  $v_d$  is the dislocation velocity,  $Q$  is the activation energy  $\approx 0.7 \text{ eV}$  and  $f(\sigma)$  is some function of the stress, fitted to the data(Fig.5).

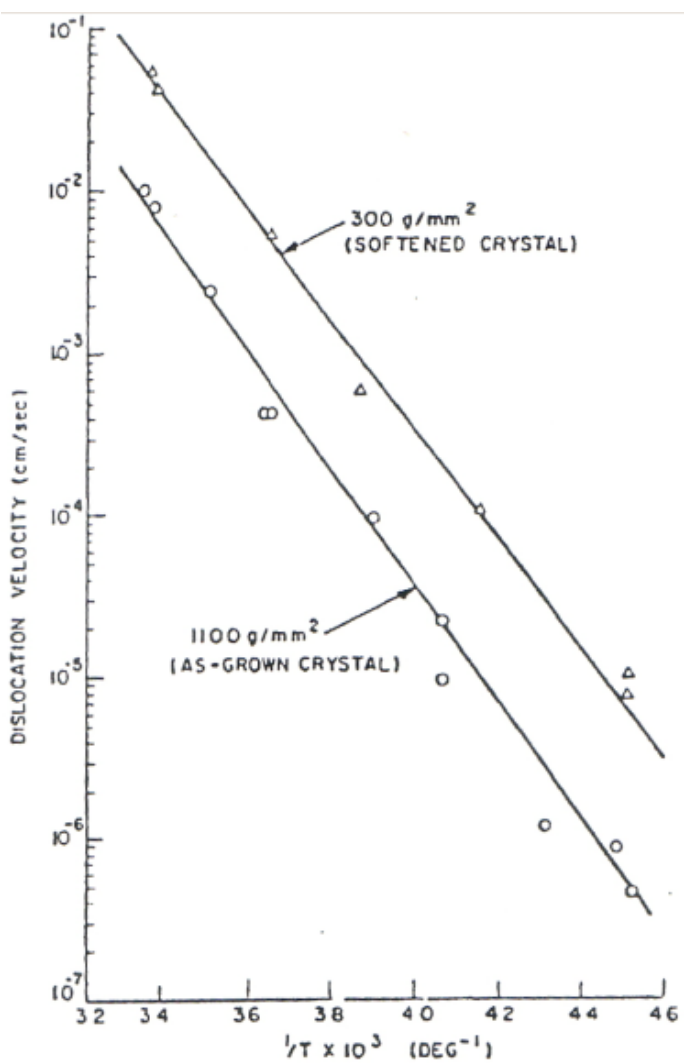


Figure 5: Dislocation velocity( $\text{cm s}^{-1}$ ) vs  $(\frac{1}{T})$  of LiF plotted with Equ.(16) with a softened crystal(highest line) and as grown in crystal(lowest line). The plot is linear because the velocity axis has been logged. Taken from Johnston et al[14].

For temperatures below this range(78 K) the data dependence seemed to shift from the predicted values of Equ.(16). This was due to the limitation of the model and understanding of dislocation-thermal interaction. For example, mechanisms such as twinning can occur at low temperatures[9].

To summarise: Johnston and Gilman used a simple model that illustrated the dynamics of dislocations in regions where atmospheres are not prevalent. The use of an ionic compound is ideal for dislocation analysis, as the experiments are simplified to single crystal structures and clear observations, such as the dislocation dynamics as a function of stress and temperature, can be quantified. The phenomenon of dislocation multiplication was also shown, illustrating the observation of a yield stress without the inclusion of the static pinning model. However, the use of a single crystal compound is not reflective of steel, which is a polycrystal material. It was Hahn[18] who applied Johnston and Gilman's model to b.c.c ferritic steel that eventually cemented the Johnston and Gilman model, as an alternative to the static pinning model.

## Hahn model

Although Johnston and Gilman showed that a Lüders type yield stress is possible without the inclusion of static pinning, their analysis had not been extended to poly-crystal structures. Therefore, an extension to poly-crystalline structures was required to substantiate their findings and rival Cottrell and Bilby's model, as the static pinning model is valid for poly-crystalline structures. It was Hahn who first applied the Johnston-Gilman model to poly-crystalline structures, such as steel.

Hahn proceeded as follows: The total strain-rate on a body can be written as the sum of the elastic and plastic contribution. That is:

$$\dot{\varepsilon}_T = \dot{\varepsilon}_e + \dot{\varepsilon}_p = \frac{1}{E} \frac{d\sigma}{dt} + 0.5bLv_d \quad (17)$$

where  $\dot{\varepsilon}_T$  is the total strain rate,  $\dot{\varepsilon}_e$  is the elastic and  $\dot{\varepsilon}_p$  is plastic strain-rate contribution, respectively,  $E$  is Young's modulus,  $b$  is the Burger's vector,  $L$  is the total length of the dislocation and  $v_d$  is the average velocity.

Hahn used Johnson and Gilman values  $v_d$  of  $L$  to produce an equation of state that described the whole strain-rate. That is:

$$\dot{\varepsilon}_T = \frac{1}{E} \frac{d\sigma}{dt} + 0.5bf(\rho_M + C\varepsilon_p^a)(2\tau_o)^{-n}(\sigma_{mises} - q\varepsilon_p)^n \quad (18)$$

where  $f$  is a fixed fraction of the dislocation length,  $\tau_0$  is the resolved sheer stress,  $q$  is the macroscopic work hardening,  $\rho_M + C\varepsilon_p^a$  corresponds to a modification of the dislocation density and  $n$  is the stress-rate sensitivity exponent.

In the region of interest where Lüders bands occur, the stress is approximately constant or time independent, assuming a flat plateau Equ.(18) becomes:

$$\dot{\varepsilon}_p = 0.5bf(\rho_M + C\varepsilon_p^a)(2\tau_0)^{-n}(\sigma - q\varepsilon_p)^n \quad (19)$$

The findings of Hahn's analysis can be summarised as follows.

1. The most dominant mechanism in Lüders band propagation is rapid dislocation multiplication, after the yield stress.
2. The velocity of the Lüders band is dependent on the injection of dislocations within the vicinity of the Lüders band.
3. The velocity of a Lüders band is considered constant throughout the specimen.
4. A description of Lüders band behaviour can be derived from an equation of state without considering static pinning, whose stress-strain curve is plotted for different dislocation populations, see Fig.(6).

The model accounts for the basic features, such as the yield stress and Lüders strain, without the use of the static pinning model.

In conclusion Hahn's model has shown that the propagation of a Lüders band can be described from the dislocation dynamics alone, by using the equations developed by Johnston and Gilman. Hahn's model was able to account for the main features of a Lüders band such as the upper and lower yield stress and Lüders strain, while also illustrating how the yield stress can vary as a function of the initial free dislocation density and strain-rate. However, Lüders bands are not only dependent on the aforementioned variables, as Hahn's model assumes, it also depends upon other factors such as the grain size, amount of solute, micro-structure and temperature.

Despite the success of Hahn's model, the work of Wilson et al[19] showed incontrovertible evidence that static pinning plays a vital role in the nucleation of a Lüders band. Therefore, Hahn concluded that a more complete model would involve both static pinning and rapid dislocation multiplication, although it is the latter of the two which is the more dominant. An

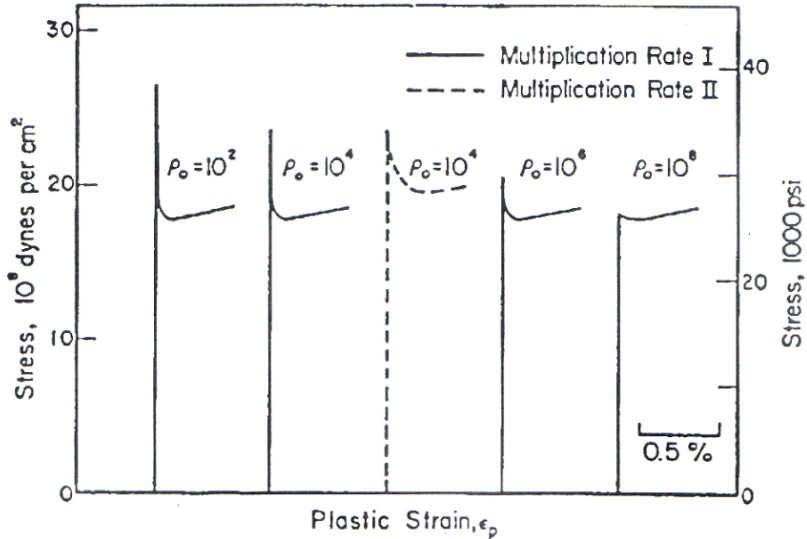


Figure 6: Equ.(19) for different free dislocation densities. Taken from Hahn[18].

illustration of the magnitude of the multiplication of the free dislocations on the yield stress is shown in Fig.(6), for different dislocation populations.

To summarise: The main theories of Lüders bands has been shown. The Cottrell and Bilby model showed that the yield stress or nucleation of a Lüders band can be treated as the work done or stress required to release a dislocation from the carbon atmosphere. However, the limitations of the model were shown in the strain-ageing data of McAdams et al[12].

The Johnston and Gilman model is also presented, showing that it is possible to have a Lüders type curve without the inclusion of the static pinning model. Although their analysis was restricted to ionic compounds, their model was extended by Hahn to include poly-crystalline materials. Subsequently, a model that accounted for the main features of a Lüders band was developed independently of the atmosphere model, giving credence to the Johnston and Gilman model, as an alternative to the static pinning model. However, despite the success of Hahn's model, it failed to factor in variables such as the carbon content, grain size and micro-structure, as it assumed that the only variables affecting Lüders bands were the strain-rate and the

dislocation density.

The factors that are neglected in the Hahn model will be researched further, in order to obtain a more realistic model, such as the Zhang model[6].

According to the literature, the following factors affect Lüders bands and will be covered as part of the literature review. They are: The carbon content, strain-rate, temperature, grain size, irradiation and nucleation.

## 2.4 Carbon content

Dalby[20] showed that the yield drop, which is the discontinuous stress drop between the upper and lower yield stress(see Fig.(2)), was observed in mild steel, but not in bronze or brass alloys. He suggested that carbon was responsible for the yield drop. Kuroda[21] did similar experiments to Dalby, with the exception of proposing how the carbon was responsible for the yield drop. He proposed that the carbide present at the grain boundary was the cause of the yield drop. This was refuted by Cottrell[11] who showed that the yield drop was seen in very low carbon  $\approx 0.012\%$  C steels where no carbide was present. Cottrell's solution, as covered in section 2.2 , was that the carbide in the iron did affect the yield stress, as it shortened the ferrite path, but it was the interstitial carbon that was essential for the characteristic yield drop.

The form of carbon in iron takes on two forms: interstitial, as discussed previously and in carbide form. The role of interstitial carbon has already been discussed in detail with Cottrell's atmosphere model and Zhao's modification of the atmosphere model, therefore only the carbide form of carbon will be discussed in this section.

### 2.4.1 Pearlitic and Spheroidal structures

When carbon in iron has passed the point of saturation, the excess carbon that has not formed in solution in the  $\alpha_{bcc}$ -iron becomes cementite or  $Fe_3C$ -iron carbide. Lamellae form on the grain boundaries, becoming denser with increasing carbon content.

Fig.(7) shows the formation of iron carbide around the grain, at the eutectoid(997 K) point, when the  $\gamma_{fcc}$ (f.c.c) iron changes to the  $\alpha_{bcc}$  ferrite and iron carbide or cementite begins to form. The following relationship describes the main variables in the diffusion process to determine the type of lamellae

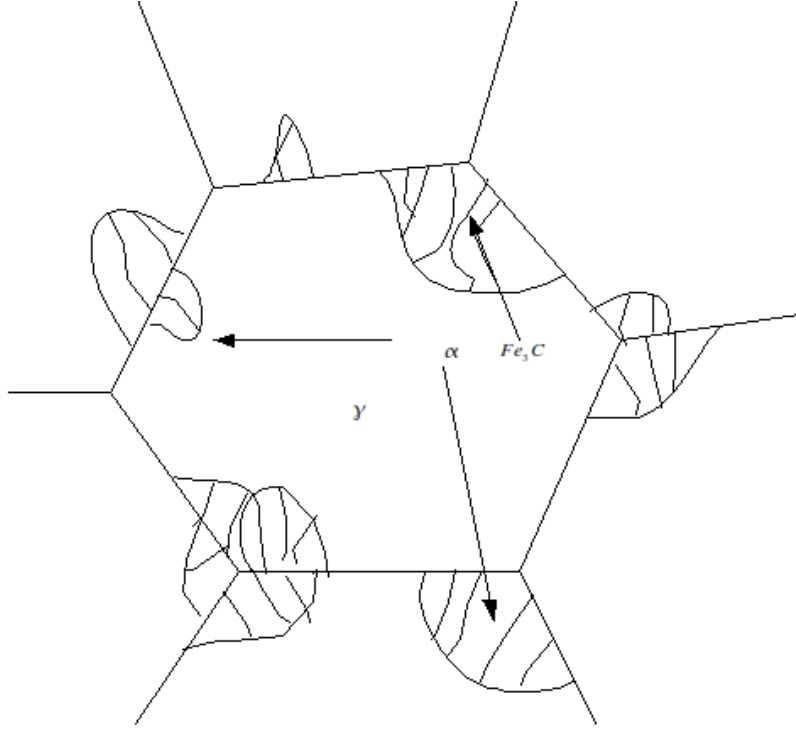


Figure 7: The formation of pearlite at the grain boundaries during cooling from the process  $\gamma_{fcc} \rightarrow \alpha_{bcc} + Fe_3C$ .

formed i.e. continuous or discontinuous from. That is[22]:

$$SR \propto D_\gamma \quad (20)$$

more fittingly:

$$R \propto \frac{D_\gamma}{S} \quad (21)$$

where  $S$  is the distance between the lamellae,  $R$  is the rate of formation and  $D_\gamma$  is the diffusion coefficient within the  $\gamma_{fcc}$ -iron.

The rate( $R$ ) can be separated into two types of formation: discontinuous nucleation:  $\gamma_{fcc} \rightarrow \alpha_{bcc} + Fe_3C$  and bulk diffusion: which is the excess carbon being pushed as a wave front to form the lamellae.

When iron carbides are formed on the grain, they displace longitudinally and perpendicular to the crystal plane. This nucleation produces the leaf effect which is common in pearlitic structures. Equ.(21) shows that for a fixed  $D_\gamma$  the rate of nucleation can determine the type of lamellae formed:

- Rapid varying  $R$  constitutes to a small  $S$  or continuous lamellae.

- Slow varying  $R$  constitutes high  $S$  and thus more spread or peppered lamellae

The size of the ferrite path is ultimately related to the above conditions, which will affect the Lüders band.

The effect of carbon on a Lüders band was shown by Winlock[23] using several carbon steels in the range of 1.03% C-0.06% on 50mm gauge length, at strain-rates  $1.72\text{-}1.75 \times 10^{-5} \text{ s}^{-1}$ , with one of the results shown in Fig.(8).

It is evident in Fig(8) that the Lüders strain decreases as a function of carbon content for constant strain-rate.

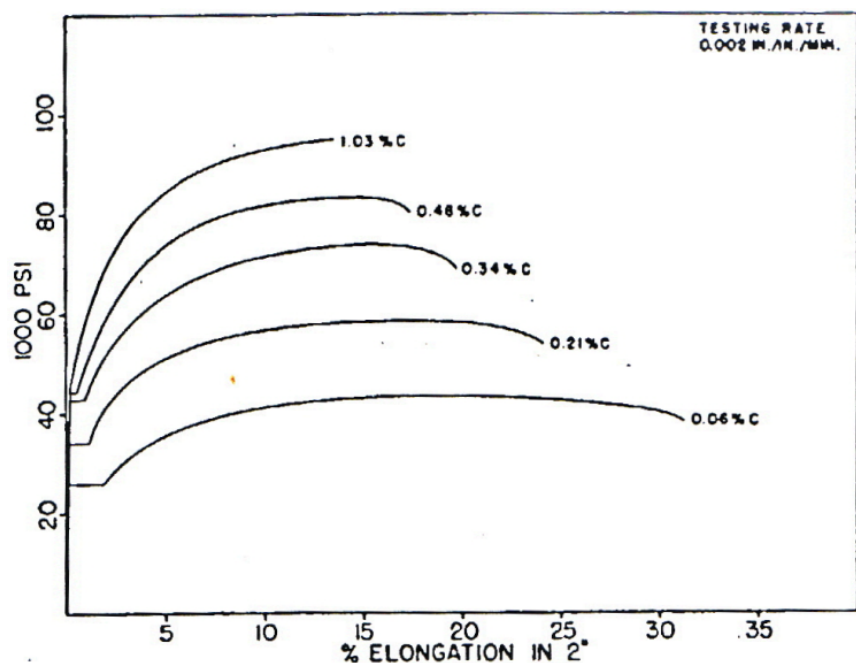


Figure 8: Stress-strain curve of varying carbon content at strain-rate  $1.75 s^{-1}$  in SI units. The Lüders strain decreases until it becomes almost indistinguishable from homogeneous deformation. Taken from Winlock[23].

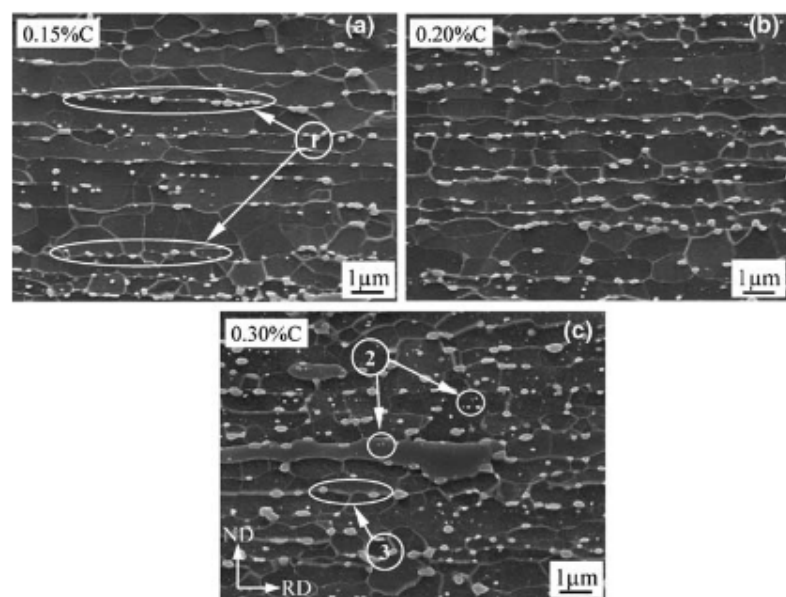


Figure 9: SEM images of 0.15%, 0.20% and 0.3% C, with increasing precipitate density starting clockwise (top left). Taken from [24].

The velocity variation was explained by Song et al[24], although not quantitatively. The dependency of the Lüders strain against carbon content from 0.15, 0.2% and 0.3% C was shown, while investigating the work hardening rate of ultra fine grained steels. A description of the heat treatment can be found in the paper to show how they produced the fine cementite structure as shown in Fig.(9).

The aim of the heat treatment was to achieve a bainitic free, ferrite-pearlite structure and improve the work hardening of each steel by having cementite particles homogeneously distributed in the ferrite matrix, both inter-granular and on the grain boundary as shown in Fig.(9). It was shown that as the amount of carbon content increased, due to the amount of extra carbon available during the transformation discussed above, the Lüders strain decreased as shown in Fig.(10). This was attributed to increased work hardening as a result of the increased pinning of the dislocations, such as Zener pinning; which is the pinning or prevention of new boundaries being formed by the precipitated particles[24]. The larger the particles, due to spheroidisation, the larger the impeding force on new boundaries being formed. This coupled with the Orowan mechanism increased the amount of pinning and, consequently, the work hardening rate of the Lüders band as it propagates through the material. Consequently, the velocity of a Lüders band increases as a function of carbon content, as a greater stress is required to free the dislocation.

It was also shown that the work hardening or  $\frac{d\sigma_T}{d\varepsilon_T}$  ( $\sigma_T$  is the true stress and  $\varepsilon_T$  is the true strain) increased with carbon content. This is due to several factors including; the rapid multiplication of the dislocations and the increase in dislocation pinning due to the number of precipitates present, which required a higher stress for dislocation propagation and resulted in shorter  $\varepsilon_L$ . Based on these observations, Song et al explained, qualitatively, that the above made for rapid Lüders band propagation. As precipitates are difficult to model, no theoretical model for band propagation or strain was proposed. However, the following equation for the additional work hardening due to the accumulation of dislocations at particles or precipitates was defined as[24]:

$$\Delta\sigma_H = \hat{m}^{3/2} FG \left( \frac{bf\varepsilon_t}{2r} \right)^{1/2} \quad (22)$$

where  $\Delta\sigma_H$  is the extra work hardening,  $\hat{m}$  is the Taylor factor, which is a measure of the lattice rotation to sheer stress response,  $G$  is the sheer

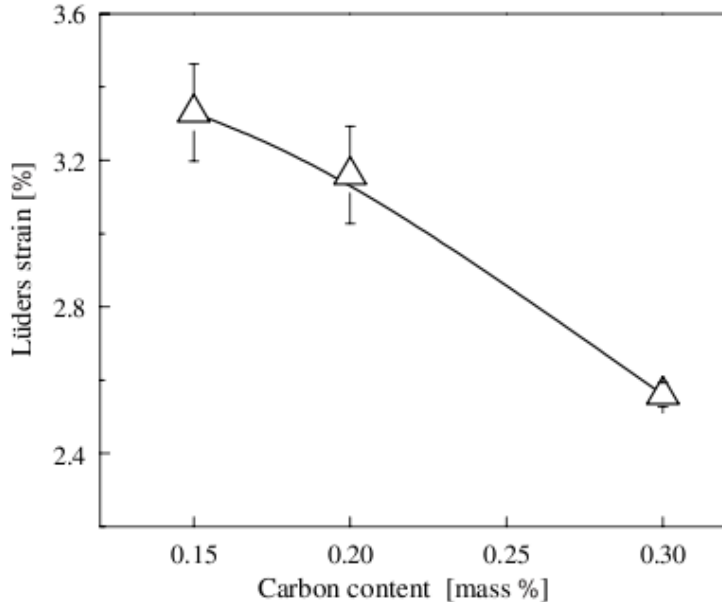


Figure 10: Elongation of the Lüders strain vs the carbon content at the same strain-rate:  $8 \times 10^{-5} \text{ s}^{-1}$ [24]

modulus,  $f_r$  is the volume fraction of particles(precipitates),  $r$  is the average particle radius,  $\varepsilon_t$  is the true strain and  $F$  is a constant.

In Song's analysis, the difference in micro-structures at different carbon contents was discussed, however the relationship between the Lüders strain and carbon content as shown in Fig.(10) assumed that work hardening was the primary mechanism for the dependency of the Lüders strain and carbon content. Although work hardening can be considered a dominant mechanism that propagates the Lüders front, variables such as the yield strength and the micro-structural dependence were neglected. These factors are important because the hardness and the yield stress between materials will be different. Therefore, until the same experiments can be done with constant carbon content with similar yield stress, the full dependency of Lüders strain with carbon content can not be fully explained by Fig.(10).

It has not been demonstrated that the Lüders strain and carbon content are uniquely correlated as implied by Fig.(10). This will be investigated further in this work with the intention studying the Lüders strain dependence with micro-structure, with constant carbon content and composition.

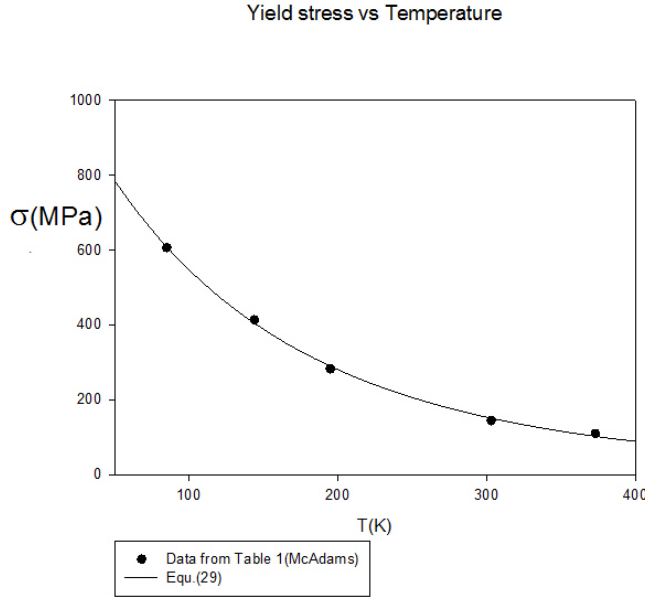


Figure 11: Yield stress vs temperature of Equ.(29) against data from table 1.

To summarise: A section on carbon content has been presented. It was shown that the process of precipitate formation is governed by the temperature dominated formation  $\gamma_{fcc} \rightarrow \alpha_{bcc} + Fe_3C$ . Depending on the amount of thermal energy available, the form of the laths can vary from continuous to discontinuous, sporadic lamellae.

It was shown that from the work of Winlock, the Lüders strain decreased as a function of carbon content, although it was not apparent from Winlock's analysis the cause of this trend. Further insight was added by Song et al[24], by looking at the effects of homogeneous grain-refinement through the formation of fine cementite precipitates, both on the grain and grain boundary. It was explained that the decrease in Lüders strain with increase carbon content was due to the increase in work hardening as a result of the increased amount of pinning.

## 2.5 Temperature

The data from Table 1 shows that as the temperature increases the yield stress decreases, showing a clear dependency between the yield stress and the temperature. The standard relationship between the yield stress and temperature is quoted in most materials books, however the derivation was

either complicated or a simple derivation has eluded the author thus far. Therefore, the author has came up with a simple way of deriving the relationship between the yield stress and temperature.

Taking the relationship from Hahn[18]:

$$\sigma_y = C\dot{\varepsilon}^m \quad (23)$$

where  $C$  is a constant,  $m$  is the strain-rate sensitivity and  $\dot{\varepsilon}$  is the strain-rate.

To find how the stress varies with the temperature, one can express the temperature dependency as follows:

$$\frac{d \ln \sigma}{dT} = \frac{d \ln \sigma}{d \ln \dot{\varepsilon}} \frac{d \ln \dot{\varepsilon}}{dT} \quad (24)$$

using Zener-Holloman parameter, which is the temperature modified strain-rate:

$$Z = \dot{\varepsilon} \exp \left( \frac{\Delta H}{RT} \right) \quad (25)$$

where  $Z$  is Zener-Holloman parameter,  $\Delta H$  is the change in enthalpy in joules,  $R$  is the molar gas constant in and  $T$  is the temperature in Kelvin.

Taking the natural log of  $Z$ , differentiating w.r.t to  $T$  and setting  $\frac{d \ln(Z)}{dT} = 0$ , one obtains:

$$\frac{d \ln \dot{\varepsilon}}{dT} = -\frac{\Delta H}{RT^2} \quad (26)$$

Equ.(26) can be thought of as  $T+dT$  for yield temperature only and not for temperatures outside the domain of yield stress.

Recognising that:

$$\frac{d \ln \sigma}{d \ln \dot{\varepsilon}} = m \quad (27)$$

Equ.(24) becomes:

$$\frac{d \ln \sigma}{dT} = -m \frac{\Delta H}{RT^2} = \frac{Q}{RT^2} \quad (28)$$

as  $\Delta H = \frac{Q}{m}$ [25] and  $Q$  is the activation energy in joules/mol.

Upon integration gives:

$$\sigma_y = \sigma_0 \exp \left( \frac{Q}{RT} \right) \quad (29)$$

where  $\sigma_y$  is the yield stress and  $\sigma_0$  is a constant of integration.

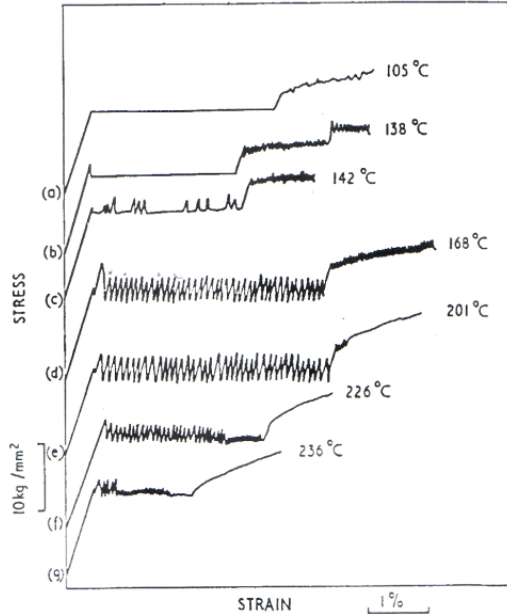


Figure 12: 0.06%C at a strain rate of  $\dot{\varepsilon} = 0.52 \times 10^{-4} s^{-1}$  of a material with 0.06%C. It shows that the Lüders strain and the yield stress decrease as a function of temperature. For the Lüders strain, it is the average strain between serrations that is taken as the Lüders strain at temperature  $T$ . Taken from Blakemore [26].

Equ.(29) when plotted against the data of table 1 shows good correlation, illustrating that b.c.c materials upon heating obey this equation.

This trend is further illustrated in Fig.(12), taken from Blakemore et al[26] in the temperature range 374-524 K, as the yield stress decreases as a function of temperature. The carbon content of the steel was 0.06% wt C with 0.0022 % wt Nitrogen, there was no vanadium or titanium present in the material, which would affect the amount of solute interacting with the dislocations. It was pickled and annealed in a vacuum in an unspecified time; ranging from strain-rates:  $0.052\text{--}5.210 \times 10^{-4} s^{-1}$  with several grain sizes. It was shown that above 424 K or  $T_c$  serration began to form. The effect of a serrated plateau is shown in Fig.(13) with Lüders strain vs temperature. The serrated behaviour will be discussed shortly. At temperatures less than  $T_c$ , where  $T_c$  is defined as the temperature before serration or blue brittle failure<sup>5</sup>, the relationship between the velocity and Lüders strain with temperature was investigated by Fischer et al[28]. Using the time delay model or Cottrell-Bilby model, which takes into account the time taken for the dislocation to become unlocked, it was shown that the velocity of the band was described as:

---

<sup>5</sup>Blue brittle failure refers to the interference colour of steel, when it oxidises at serrated temperatures[27]

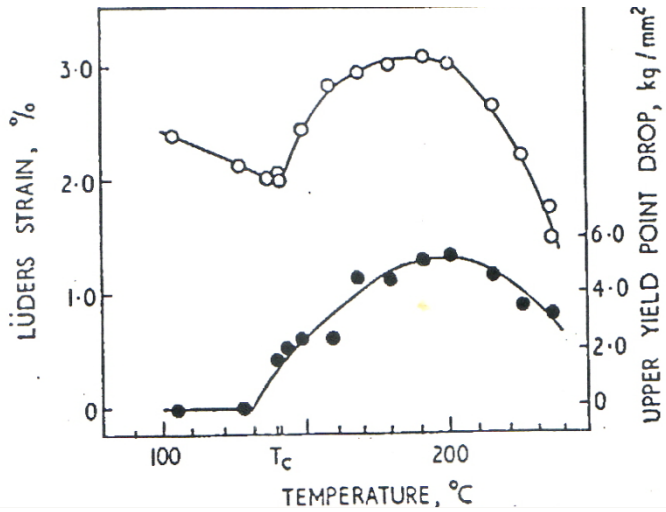


Figure 13: A plot of the Lüders strain( $\circ$ ) and temperature, with upper yield stress( $\bullet$ ). Taken from Blakemore[26]

$$\ln(v_L) = C - \left( \frac{D}{\sigma_{ly}T} \right) \quad (30)$$

where  $v_L$  is the velocity of the band measured in inch per second,  $C$  and  $D$  are constants dependant on the grain size and  $\sigma_{ly}$  is the lower yield stress in psi at a temperature  $T$  in Kelvin.

According to Hall<sup>6</sup> the conventional relationship between velocity and strain-rate i.e.  $v_L = \frac{\varepsilon_M l_0}{\varepsilon_L}$  was shown to hold at all temperatures, therefore to obtain the strain dependence with the temperature one can substitute  $v_L$  coupled with the Lüders strain into Equ.(30) to obtain:

$$\ln(\varepsilon_L) = \ln(v_m) - C + \frac{D}{\sigma_{ly}T} \quad (31)$$

or:

$$\ln(\varepsilon_L) \propto \frac{1}{\sigma_{ly}T} \quad (32)$$

where  $\varepsilon_L$  is the Lüders strain and  $v_m$  is the cross-head velocity.

Thus both the natural log of velocity and the Lüders strain are inversely proportional to the product  $\sigma_{ly}T$ . The decrease in Lüders strain with in-

---

<sup>6</sup>Hall, E.O(1970). "Yield Point Phenomena in Metals and Alloys" Page 34

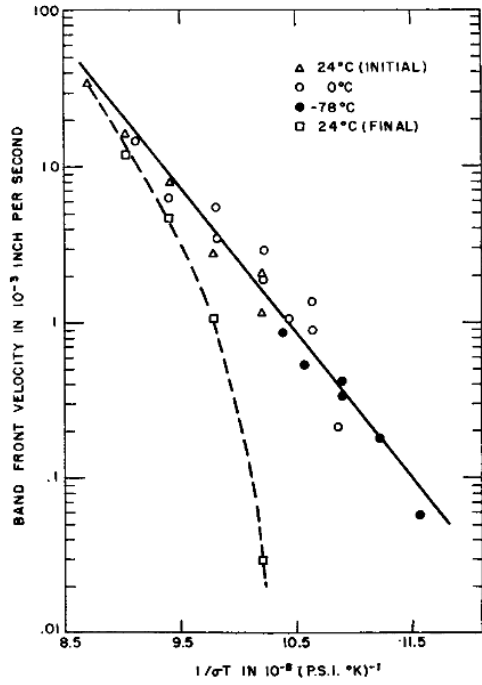


Figure 14: Dislocation velocity(inch  $s^{-1}$ ) vs  $\frac{1}{\sigma_y T}$ (PSI K) $^{-1}$  plotted with Equ.(30)) on SAE-1010(0.13-0.08%C). The plot is linear because the velocity axis has been logged, with the data diverging away from the trend at low temperatures. Taken from Fischer et al[28].

creasing temperature is apparent in Fig.(13) before the serrated temperature  $T_c$  is reached and then the Lüders strain begins to increase.

The material used by Fischer et al was an SAE-1010 steel wire, with a composition between 0.013-0.08% C, 0.3-0.6 Mn, 0.04% P and 0.05% S<sup>7</sup>. It was dry hydrogen heated up to 1000°C for ten minutes then cooled in water jacket chambers. The temperatures ranged: -70,0 and 24°C with the results shown in Fig.(14). At temperatures below room temperatures 24°C the data points fit a linear trend of Equ.(30). However, at room temperature the data takes a non-linear trend and diverges away from the predictions of Equ.(30). This was possibly due to over-ageing of the material. The effect of this, as the Lüders band was propagating through the material, was strain-ageing occurring in front of the band, which resulted in the deceleration of the Lüders band.

Although Equ.(31) was not derived by Fischer and, therefore, not investigated in his work, the verification of the linear trend with the reciprocal of the product of the lower yield stress and the temperature can be shown from the data of Tsuchida et al[7], who investigated the Lüders strain and work hardening-rate as a function of lower yield stress and temperature.

A mild steel with the following composition was used: 0.15%C, 0.4%Si, 1.5%Mn, 0.014%P, 0.0004%S, at a strain-rate of  $3.3 \times 10^{-4} s^{-1}$ , and the details

---

<sup>7</sup>Composition taken from [www.postdiluvian.org/mason/materials/carbon-steels.html](http://www.postdiluvian.org/mason/materials/carbon-steels.html)

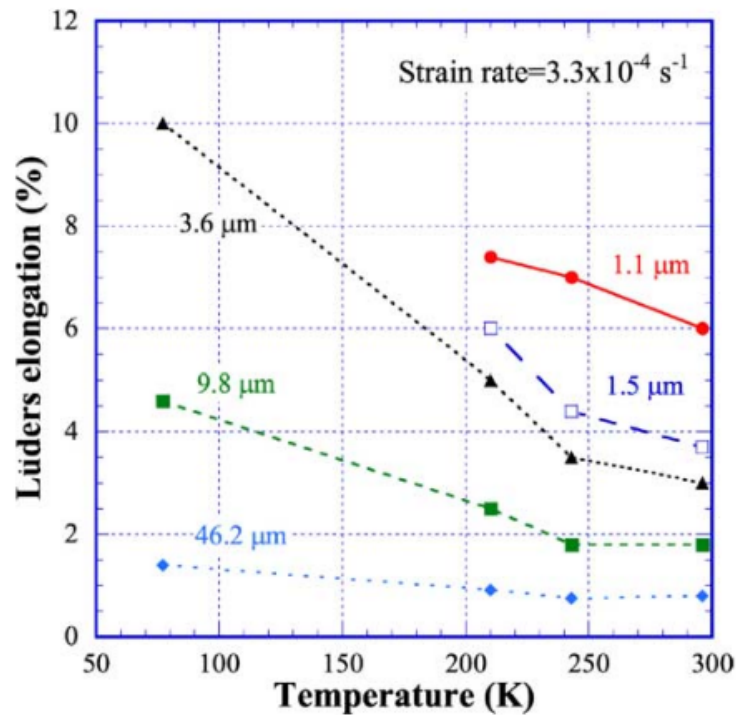


Figure 15: Lüders strain vs lower yield stress at strain-rate= $3.3 \times 10^{-4}$  with grain-sizes 1.1, 1.5, 3.6, 9.8 and 46.2  $\mu\text{m}$ , respectively. The Lüders strain in the aforementioned grain-sizes reduces as the temperature increases, albeit less evidently at the largest grain-size(46.2 $\mu\text{m}$ ). Taken from Tsuchida et al[7].

of the heat treatment were not given. The tests were performed at 77K in liquid nitrogen, 210K in liquid methanol and 296K in air. The Lüders strain as a function of temperature and the lower yield stress, for different grain-sizes, is shown in Fig.(15). If the data of these is combined, the graph produced is Fig.(16) shows good correlation between the data at different grain-sizes and at constant strain-rate and Equ.(31).

The main objective of the Tsuchida's work was to show that a simple equation relating the Lüders strain as follows:

$$\varepsilon_L^u = \left( \frac{\Delta}{K'u} \right) \quad (33)$$

where  $\Delta$  a universal constant,  $u$  is an exponent and  $K'$  is a parameter dependent on stress-strain data (see Fig.(17)).

According to Equ.(33) the plot between the left side of the equation and the right side should be linear. However, as shown in Fig.(17), although there is a linear correlation, there is a lot of scatter between points; this is attributed to the source of the data. They were taken mainly from Winlock[23], Butler[29] and other sources of tensile data that were done at different strain-rates, grain-sizes and micro-structure. However, a positive trend is evident.

For the serrated region(see Fig.(12) and Fig.(13)) after  $T_c$ , the strain increases until it reaches a maximum at approximately 474 K(201 °C), after which the same trend is repeated. The increase in Lüders strain, above  $T_c$  is due to the appearance of the serrations or multiple yield points. This phenomena, known as dynamic strain ageing or blue-brittle failure, is due to the carbon atoms pinning the dislocations, similar to strain-ageing, but for dislocations in motion. This repeated locking produces negative strain-sensitivities[30] which causes the serrations and results in the termination of Lüders bands, resulting in the formation of secondary or even tertiary bands.

The serrated behaviour is dependent on two factors:

1. A stress gradient in the Lüders plateau.
2. Discontinuities in the strain, causing bands to terminate.

The model presented in this report is from Balohonooov et al[31] who applied conservation and continuity equations for the stresses. The details of the model can be found in the paper, however the equation of state used is

0.15%C with constant strain-rate  $3.3 \times 10^{-4} \text{ s}^{-1}$

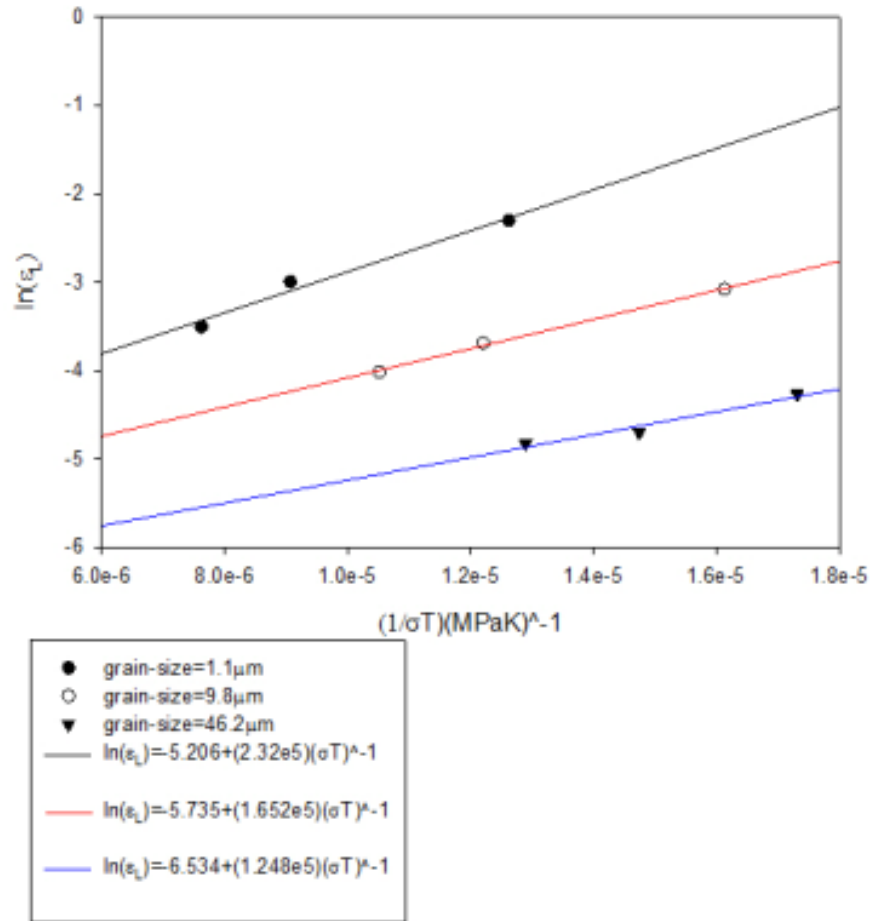


Figure 16:  $(\ln(\varepsilon_L))$  vs  $(\frac{1}{\sigma_T})$  with regressions lines(Equ.(31)). Plotted at different grain-sizes with constant strain-rate  $3.3 \times 10^{-4} \text{ s}^{-1}$ , showing good correlation between Equ.(31) and the data. Taken from Tsuchida et al[7]

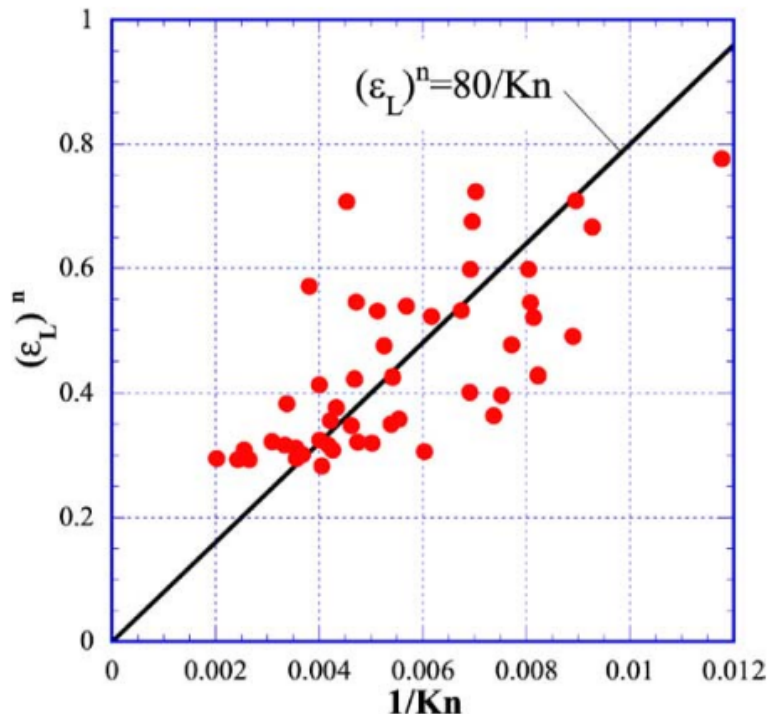


Figure 17: Plot of data with Equ.(33) curve fitted through the data. Note that  $n$  in the above figure is termed  $u$  as  $n$  has already been defined as the stress-rate exponent and  $K$  is  $K'$  as  $K$  is defined as Kelvin. Also, the data was taken from many sources, which had different grain-sizes and strain-rate. Therefore the above correlation should be viewed with caution. Taken from [7]

shown. That is:

$$\dot{\varepsilon}_i^p = \dot{\gamma}_r F(\varepsilon_i^p) \exp \left\{ -\frac{G_0}{kT} \left[ 1 - \left( \frac{\sigma_i - \tau_n(\varepsilon_i^p)}{\tilde{\tau}} \right)^d \right]^q \right\} \quad (34)$$

where  $q$  is the macroscopic work hardening,  $d$  is a material constants,  $G_0$  is the thermal activation energy,  $\dot{\gamma}_r$  is a constant of proportionality and  $F(\varepsilon_i^p)$  is the fraction of dislocation, defined as:

$$F(\varepsilon_i^p) = F^* + (1 - F^*) \exp(-B\varepsilon_i^p / (|g|)b) \quad (35)$$

where  $|g|$  is the orientation multiplier and  $b$  is the Burgers vector,  $F^*$  is a dimensionless number related to the population of the dislocations and  $B = \frac{2}{d_{grain}\rho_M}$ .

This equation coupled with:

$$T = T_0 + \int_0^{\varepsilon_p} \frac{\beta}{\rho_0 C_V} \sigma d\varepsilon_i^p \quad (36)$$

where  $T$  is the temperature,  $\beta$  is the coefficient of compression,  $\rho_0$  and  $C_v$  are the specific heat capacities.

Equ.(34) plotted in Fig.(18) against experimental data, shows good agreement; especially at temperatures when serrations are not prevalent(above 700K). The model and the data also converge at all temperatures and strains greater than 0.1-0.2. This suggests that the model described, works well for continuous deformation or plasticity within the temperature range 213-700 K. However, at temperatures below 500 K and strains less than 0.1 where serrations are prevalent, although the model predicts the initial trend, it fails to model the serrated behaviour. This is due to the fact that, in the serrated region, the transfer of stress is discontinuous. Therefore models that assume continuous stress and strain transfer through each volume element of Lüders band propagation, such as Balohonoov et al, will not produce serrations.

It was shown in Fig.(18) that above a certain temperature(700K) the serrations began to diminish.

A theoretical limit of when serrations are expected to finish can be calculated by considering the interstitial concentration[27].

$$c = c_0^{\frac{U}{k_b T}} \quad (37)$$

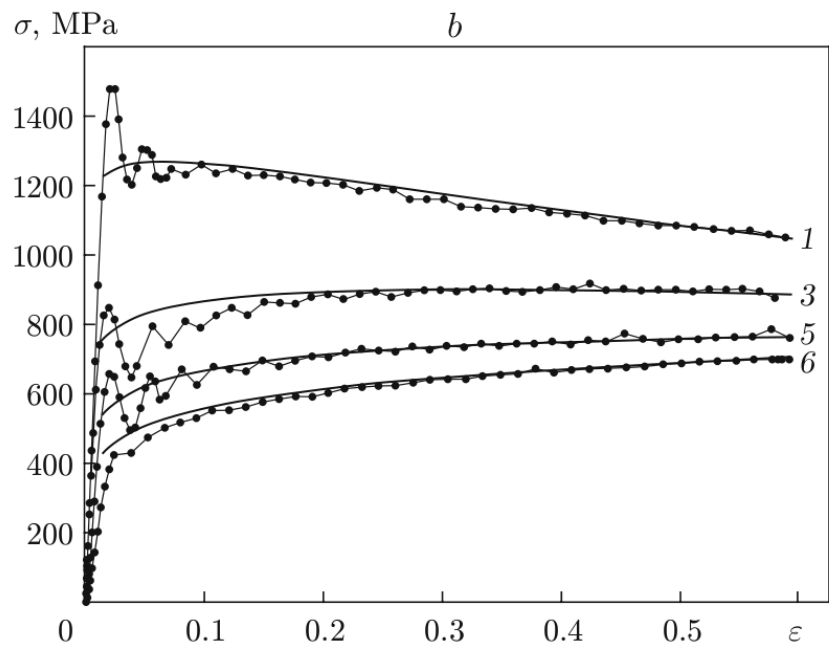


Figure 18: Equ.(34) against plotted data for temperatures: (1) 213, (2) 296, (3) 400, (4) 500 and (6) 700 K . For strain less than 0.1 where serrations are most prominent, the constitutive model predicts the trend but not the serrations. Taken from Balokhonov[31]

where  $c$  is the interstitial concentration,  $c_0$  is the average concentration,  $U$  is the binding energy and  $T$  is the temperature.

According to Bhedesia[27] dynamic strain-ageing stops when the carbon atmospheres have condensed, such that  $c=1$  and  $U = U_{max}$ . Rearranging Equ.(37) for  $T$  gives:

$$T_{cri} = \frac{U_{max}}{k_b \ln(\frac{1}{c_0})} \quad (38)$$

where  $T_{cri}$  is the maximum temperature and  $U_{max}$  is the maximum binding energy that serrated behaviour can occur.

Taking  $c_0 = 1 \times 10^{-4}$  and  $U_{max} = 10^{-19} \text{ J}$  gives a value for the maximum temperature  $T_{cri} = 700K(423^\circ\text{C})$ .

Although the value for  $T_{cri}$  is a simplistic calculation, it is evident in Fig.(13) and Fig.(18) that as the temperature increases up until the theoretical limit, the serrations become less prominent.

To summarise: For low temperatures less than  $T_c$ , it was shown that the natural log of the Lüders strain was inversely related to the product of the yield stress and the temperature. This relation was further substantiated Fig.(12) and Fig.(13), which shows, explicitly, that the Lüders strain decreased as a function of temperature. This trend continues until a threshold temperature  $T_c$  is reached and then dynamic strain-ageing begins. This is shown as serrations in the plateau.

A clear dependency Equ.(31) was derived from the standard relationship between band velocity and Lüders strain whose verification was shown in Tsuchida's work(Fig.(16)). It was also shown, when equating Lüders strain or the speed of Lüders band to only stress or temperature, according to Equ.(33), that either it is assumed that the stress is constant or the temperature is constant.

Temperature at approximately  $T_c$  resulted in serrations being formed. An adequate model was presented, which predicted the true stress-strain curve for varying temperatures. However, the model relied on conservation equations, such as conservation of mass, which is used for continuous phenomena such as fluid flow or homogeneous deformation, and as the serrated behaviour is discontinuous, the model could not fully describe the stress-strain curve.

## 2.6 Grain size

The work of Butler[29] and more recently by Tsuchida et al[32] reported that the Lüders strain decreased as a function of grain-size. This is shown further in table 2 taken from Tsuchida et al[7].

The Lüders strain decreases a function of grain-size, because the work-hardening or work-hardening rate increases a function of grain-size, according to Tsuchida[32]. This is shown by looking at the equation below:

$$\varepsilon_L \frac{d\sigma_L}{d\varepsilon_L} = \Delta \quad (39)$$

the term  $\Delta$  in the equation (according to the work of Tsuchida et al) must remain constant for all materials. Therefore, as work-hardening increases, for the term on the right side of Equ.(39) to remain constant, the Lüders strain must decrease and conversely if the Lüders strain increases. The variable that is responsible for the above process is the grain-size, which is shown on Fig.(19). The lower yield stress will vary as[33]:

$$\sigma_{ly} = \sigma'_0 + \frac{k_r}{d_{grain}^{\frac{1}{2}}} \quad (40)$$

where  $\sigma_{ly}$  is the lower yield stress,  $\sigma'_0$  is a constant which can be regarded as the sum of the internal friction[34],  $d_{grain}$  is the average distance of the grains and  $k_r$  is a constant that is slightly dependent on temperature.

The work of Tsuchida neglected to account for the presence of the dislocation density. Therefore, in the process, failing to explain how the lower yield stress decreases as a function of grain-size, as the lower yield stress inextricably linked to the dislocation density.

The dislocation density as a function of grain-size was studied by Conrad et al[9] when he was looking at b.c.c niobium based alloys. It was shown that as the grain-size decreased, the dislocation density increased, because the dislocations made small cellular networks, which became more dense. The Lüders strain according to the Cottrell model is the strain displaced after the pinned dislocations are released. Therefore the larger the dislocation density for a given region, the smaller grain-size, which gives a larger proportion of pined dislocations and, consequently, a greater Lüders strain, when released. In other words, the Lüders strain decreases a function of grain-size, because the dislocation density is inversely proportional to the grain-size, which results in a lower yield stress.

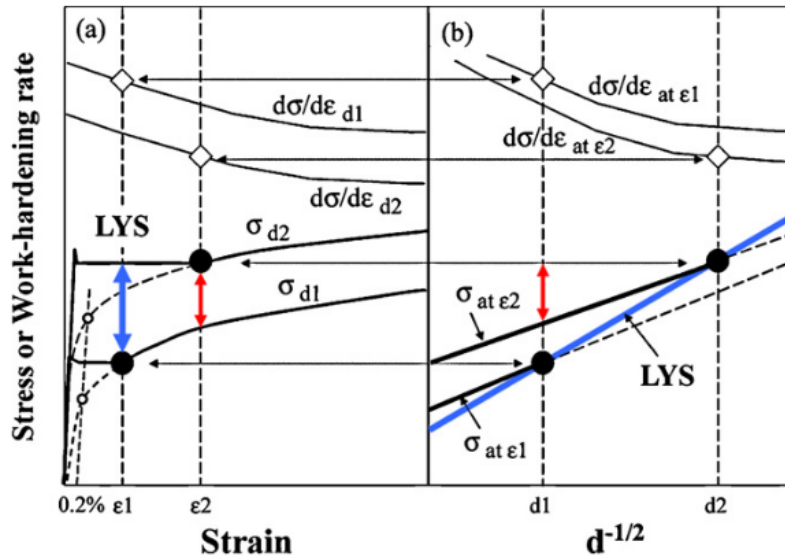


Figure 19: (a) Work-hardening(work-hardening rate) and stress(in the same axis) as a function of Lüders strain, at grain sizes  $d_1$  and  $d_2$ , where  $d_1 > d_2$  with the corresponding lower yield stresses and work-hardening values at those points. (b)Work-hardening(work-hardening rate) and stress(in the same axis) as a function of grain-size( $d^{-\frac{1}{2}}$ ), at Lüders strain values  $\varepsilon_1$  and  $\varepsilon_2$ , where  $\varepsilon_2 > \varepsilon_1$  with the corresponding stress and work-hardening values at those points. It is evident that the work-hardening decreases and the yield stress decreases as a function of grain-size. Taken from Tsuchida et al [32].

Table 2: Carbon contents with different grain-sizes( $1.6\text{-}60.2\mu\text{m}$ ), illustrating the dependence of the Lüders strain with grain-size. That is the smaller the grain-size for a given carbon content, the larger the Lüders strain.  $C(\%)$  is the carbon content,  $d(\mu\text{m})$  is the grain-size,  $\varepsilon_L(\%)$  is the Lüders strain,  $K'(\text{MPa})$  is a parameter and  $u$  is an exponent. Taken from Tsuchida et al[7]

$C(\% \text{ mass})$	$d(\mu\text{m})$	$\varepsilon_L(\%)$	$\sigma_L(\text{MPa})$	$K'(\text{MPa})$	$u$
0.025	14.5	13.7	274	482	0.258
	17.3	9.6	259	478	0.259
	24.8	8.6	240	462	0.266
	40	6.6	210	429	0.262
	62.5	4.4	179	449	0.296
0.05	4.5	9	399	679	0.213
	7.2	7	327	626	0.237
	21	3.5	203	590	0.306
0.13	1.6	8	577	821	0.136
	2.8	5	461	854	0.206
	30	1	191	645	0.257
0.16	1.1	6	723	944	0.08
	1.5	3.7	570	877	0.123
	3.6	3	443	877	0.185
	9.8	1.8	321	951	0.243
	46.2	0.8	262	898	0.235

It was also noted that the difference in upper and lower yield stress increased with decreasing grain-size. This was also observed by Imamura et al[33] when looking at the shape of the Lüders wave front with different grain-sizes.

The dynamics of the granular scale have been discussed. The question now arises, how does this affect the shape or definition of the Lüders band front?

The work of Imamura et al[33] observed that the smaller the grain-size, the sharper or more defined the front of the Lüders band seemed. This was due to rapid yielding. The above observations by Imamura et al[33], gave credence to the notion that a Lüders band is a time dependent mechanism that occurs on each grain-boundary i.e. where the dislocations are restricted. If the grains have a large surface area, yielding will occur more quickly as the

dislocation unlocking occurs on a wider surface area. This leads to a more diffuse band and less cohesive process between the grains or less defined band shape. Conversely, if the grain-size is small, where the band front becomes more defined, the process takes place on a smaller surface area and, therefore, maintains the shape of the band. This coupled with the dislocation dependence of the grain-size suffices for a description of Lüders band with grain-size dependence.

Innovations in neutron and X-ray diffraction, make it possible to look at the texture and crystal orientation of the grain structure. This is done via pole diagrams, which are figures or diagrams generated from neutron and X-ray diffraction and can be used to determine the texture of a material. This approach was adopted by Huntanu et al[35], who was looking at the effect a Lüders band had on the grain structure.

The method was as follows; mild steel with unknown carbon content and no heat treatments, and strained between 1%-20%, was cut in cubes, using an electron-discharge machine or EDM and neutron diffraction techniques were used to look at the direction of stress in each crystal plane. The results of these were then compared to elasto-plastic self consistent model or EPSC, which was developed by Turner et al[36]. The method assumed the grains were elliptical in shape and used a numerical code based on the formula:

$$\dot{\sigma} - \dot{\Sigma} = -W^{-1} : (O^{-1} - I) : (\dot{\varepsilon} - \dot{X}) \quad (41)$$

where  $\dot{\sigma}$  and  $\dot{\varepsilon}$  are the grain stress and strain rate tensors,  $\dot{\Sigma}$  and  $\dot{X}$  are the homogeneous effective medium or HEM overall stress and strain rate tensors,  $O$  is the Elshel tensor which is a function of the stiffness tensor  $W$ , and  $W$  is the overall stiffness tensor describing the mechanical properties of the electro-plastic model, and according to Huntanu et al, the boundary conditions stipulate that  $\dot{\Sigma}$  and  $\dot{X}$  are specified from neutron diffraction.

Pang et al[37] noted that EPSC model only worked when the elastic strain in the grain was comparable to the plastic contribution, otherwise the modified visco-plastic model is used.

The sections of material were resolved into sample reference directions:

1. RD-rolling direction.
2. ND-through thickness direction.
3. TD-Width direction.

The orientations were {220}, {200} and {112} directions and the strain was obtained from the neutron diffraction texture:

$$\varepsilon_{hkl} = \frac{d_{hkl} - d_{hkl(\text{ref})}}{d_{hkl}} \quad (42)$$

where  $\varepsilon_{hkl}$  is the plane stress with Miller indices  $h, k, l$ ,  $d_{hkl}$  is the spacing between atomic planes after deformation and  $d_{hkl(\text{ref})}$  is the spacing taking from a reference point after annealing.

After straining the material, the cubes were annealed at 874 K for 1 hour. It was shown that, after Lüders band a band had propagated, the largest tensile strains were present in the {200} plane than the {220} or {112} planes(see Fig.(20) and Fig.(21)).

There seemed to be weaker texture dependence on samples from thicker specimens. This indicated that a thicker specimen gave a dispersive profile as confirmed from other observations(see Imamura et al[33]).

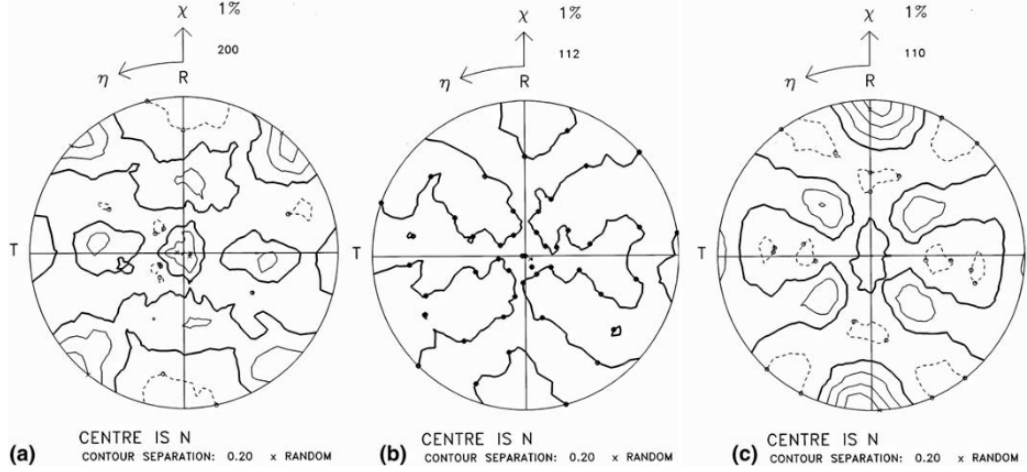


Figure 20: Pole diagrams of material strain at 1% in Lüders band region. (a) {200} (b) {211} (c){100} planes. The {200} is the direction the uniaxial direction and therefore shows greatest strain. Taken from Huntanu et al[35].

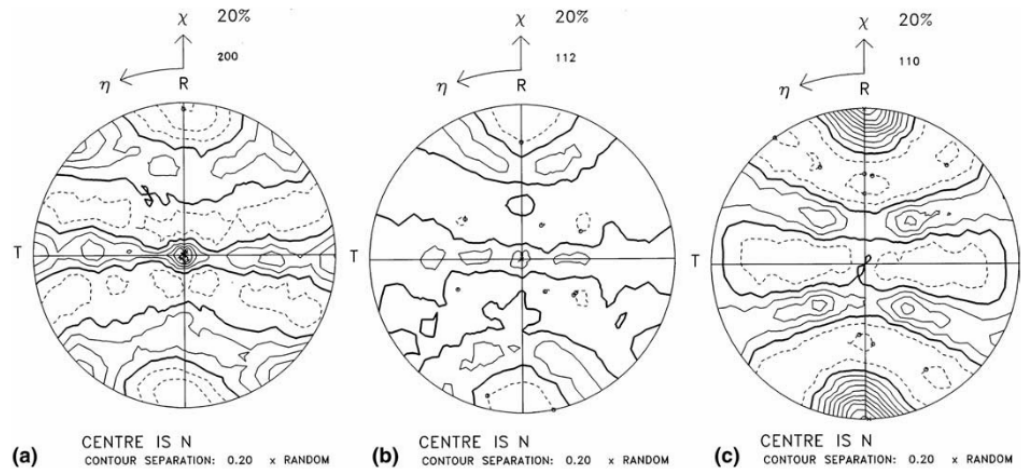


Figure 21: Pole diagrams strain at 20%, after Lüders band has propagated. (a) {200} (b) {211} (c){100} planes. The strain distribution in the three planes is more intense version of Fig.(20), indicating the strain in the planes during inhomogeneous deformation resolves in a similar manner to homogeneous deformation. Taken from Huntanu et al[35].

As the material was unspecified it is uncertain to what extent substitutional alloying affected the texture of the material. It is likely that the material was of low alloy; following Pang[37]. However, as it is not known, the results could be over or under exaggerated depending of the type of alloy substitution.

Hutatu noted that the thickness gave a weak texture, although it was still apparent that there was a dependence. However, this dependence has to be viewed with caution as the amount of experimental error was not shown. This lack of information is unusual, as Pang et al, whose paper Hutatu refers to consistently, shows the experimental error and is thus more rigorous, which is essential in Pole graph analysis.

There is also a limitation as to the interpretation of the pole figures as they cannot add insight into the dynamics of the dislocations, which are vital in the understanding of dislocation interaction on the grains and therefore Lüders bands. Thus a more thorough model and dynamic description is needed.

Dunne et al[38] applied the dynamics of dislocations to numerical models approach to model H.C.P. structures or hexagonal closed packed on cold-dwell fatigue in titanium alloy. Up until the time of writing, to the authors knowledge, this approach has not been applied to bcc structures. An application of Dunne's model in tandem with the EPSC model for b.c.c may add more insight into grain-dislocation dynamics.

To summarise: It was shown that the relationship between Lüders strain and the grain-size, almost follows a Hall-Petch type relationship. The result of such a dependence was an increase in work hardening-rate within the grain and a larger Lüders strain. It was shown that the dependence shown in Fig.(19) was explained two-fold. A mathematical description that looked at the work-hardening rate, provided by Tsuhida et al[32] and a mechanical version that looked at the dislocation density as a function of the grain-size, provided by Conrad and later Imamura et al[33].

It was also shown that the grain-size dictated the shape of the band front: The smaller the grain-size the sharper and more defined the band front. Conversely, the larger the grain-size the more diffused and less pronounced the band front.

Further work using pole diagrams and neutron/X-ray diffraction techniques are warranted, to give a better understanding and deeper insight into the inner workings of a grain during plastic deformation. It was shown that the axis parallel to the direction of uniaxial stress experienced the most strain,

during band propagation.

## 2.7 Strain-rate

In the previous subsections it was shown that the strain-rate plays a fundamental role in Lüders behaviour and plasticity in general. Strain-rate can be broken in to two sections: Low strain-rate, which would be nominal strains less than  $\dot{\varepsilon} < 10^3 \text{ s}^{-1}$ ; and high-strain-rates greater than  $\dot{\varepsilon} > 10^3 \text{ s}^{-1}$ .

### 2.7.1 Low strain-rates

For Lüders bands, the strain-rate dependence is expressed as follows:

$$v_L = \frac{\dot{\varepsilon}_M l_0}{\varepsilon_L N} \quad (43)$$

where  $v_L$  is the speed of the band,  $\dot{\varepsilon}_M$  is the strain-rate of the machine, approximated as the strain-rate of the material,  $l_0$  is the gauge length,  $\varepsilon_L$  is the Lüders strain and  $N$  is the number of bands formed.

The velocity of the Lüders band in Equ.(43) is also dependent on the magnitude of the Lüders strain. In order to obtain the velocity the Lüders strain as a function of strain rate separately, the velocity of the band and the Lüders strain in Equ.(43) must be decoupled. This was done by Sun et al[39] to produce the following equations:

$$v_L = k D C^n \dot{\varepsilon}^{mn} \quad (44)$$

in terms of log derivative:

$$\frac{d \ln(v_L)}{d \ln(\dot{\varepsilon})} = mn \quad (45)$$

where  $v_L$  is the velocity,  $k$ ,  $D$  and  $C$  are constants,  $m$  is the strain-rate exponent and  $n$  is the stress-rate sensitivity exponent.

The Lüders strain is then found by substituting Equ.(43) into Equ.(44):

$$\varepsilon_L = \frac{L_0}{k D C^n} \dot{\varepsilon}^{1-mn} \quad (46)$$

in terms of logs:

$$\frac{d \ln \varepsilon_L}{d \ln \dot{\varepsilon}} = 1 - mn \quad (47)$$

where  $\varepsilon_L$  is the Lüders strain.

The above equations show that the Lüders strain and band velocity both increase with strain-rate.

The experimental method: a flat sheet of low carbon steel(0.07% C) and a 0.036% C steel wire, were annealed at 970 K and 1023 K for one hour respectively, then furnace cooled. This produced an average grain-size of  $11.5\mu m$ .

Fig.(22) shows that Equ.(44) and Equ.(46) correlate well for the carbon steel and strain-rate. Further insight can be added into the equations proposed by Sun, by deriving the corresponding stress-strain curve and combining the model with the curve derived by Tsuchida et al[7]. If Equ.(43) is combined with Equ.(23) then the relationship between stress and strain is as follows.

Realising that the work-hardening can be written as:

$$\frac{d\sigma_{lyp}}{d\varepsilon_L} = \frac{d\sigma_{lyp}}{d\ln(\sigma_{lyp})} \frac{d\ln(\sigma_{lyp})}{d\ln(\dot{\varepsilon})} \frac{d\ln(\dot{\varepsilon})}{d\ln(\varepsilon_L)} \frac{d\ln(\varepsilon_L)}{d\varepsilon} \quad (48)$$

which gives:

$$\frac{d\sigma_{lyp}}{d\varepsilon_L} = \frac{\sigma}{\varepsilon_L} \frac{m}{1 - mn} \quad (49)$$

with solution:

$$\sigma_{lyp} = W \varepsilon_L^{\frac{m}{1-mn}} \quad (50)$$

or logged form

$$\frac{d\ln(\sigma_{lyp})}{d\ln(\varepsilon_L)} = \frac{m}{1 - mn} \quad (51)$$

where  $\sigma_{ly}$  is the lower yield stress and  $W = \frac{kDC^n}{l_0}$ .

It is straight forward to show that Equ.(51) is equivalent to Equ.(23) by substituting Equ.(47) into Equ.(51) for  $d\ln(\varepsilon_L) = (1 - mn)d\ln(\dot{\varepsilon})$ , to give:

$$\frac{d\ln(\sigma_{lyp})}{d\ln(\dot{\varepsilon})} = \frac{m}{1 - mn}(1 - mn) = m \quad (52)$$

with solution:

$$\ln(\sigma_{lyp}) = \Theta + m \ln(\dot{\varepsilon}) \quad (53)$$

where  $\Theta$  is a constant of integration.

Comparing Equ.(50) with standard models of plasticity, the power indices on the strain are usually associated with the stress-rate sensitivity.

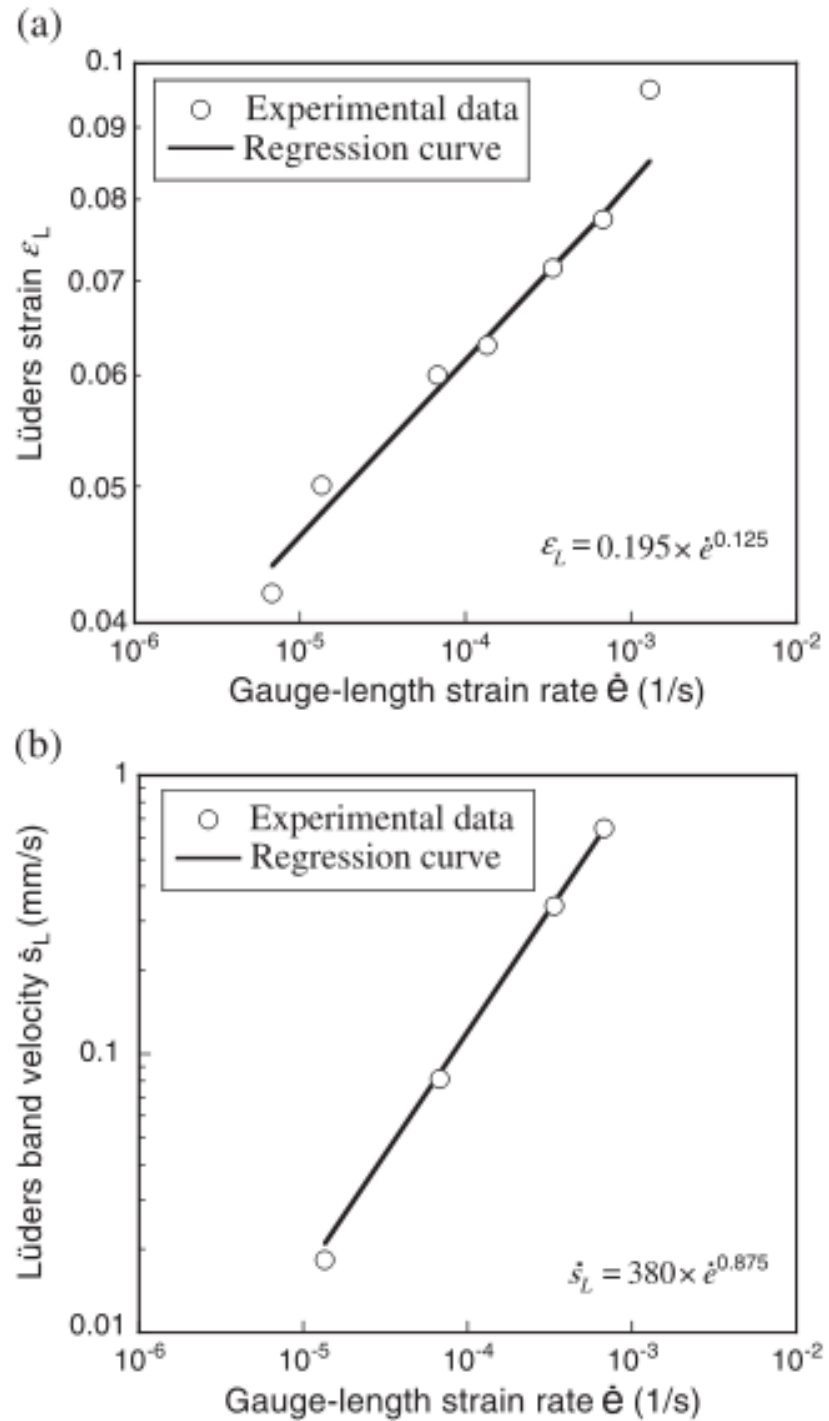


Figure 22: Plot of Lüders vs strain-rate and band velocity vs strain-rate of 0.07% C(steel sheet) at strain-rates:  $4.17 \times 10^{-6}$ - $8.37 \times 10^{-4}$  s $^{-1}$ . Taken from Sun et al[39]

If Equ.(50) is compared to a similar equation used by Tsuchida et al[7] to correlate the  $\sigma_{ly}$  with  $\varepsilon_L$ . That is:

$$\sigma_{lyp} = K' \varepsilon^u \quad (54)$$

where  $K'$  and  $u$  are Hollomon parameters ( $u$  is defined as the strain-hardening exponent).

Comparing Equ.(54) and Equ(50) it can be shown that:

$$u = \frac{m}{1 - mn} \quad (55)$$

A simple relationship has been derived that relates the three parameters, namely strain-rate sensitivity( $m$ ), stress-rate sensitivity( $n$ ) and strain-hardening exponent( $u$ ).

Taking the values measured from Sun et al's original work, that is  $n = 17.5$  and  $m = 0.046$ , the value of  $u$  is :

$$u = \frac{0.046}{1 - 17.5 \times 0.046} = 0.235(3dp) \quad (56)$$

The value calculated was for a grain-size of  $11.5\mu\text{m}$ . If this value is compared to the nearest grain-size from Tsuchida et al's data, which is approximately  $9.8\mu\text{m}$ , the value calculated was  $u=0.26$  at room temperature. Equ.(55) can be seen as an extension of Sun et al[8], with the additional parameter  $u$ . The constant  $K'$  can be expressed in more fundamental constants. That is :

$$K' = \left( \frac{kDC^n}{l_0} \right) \quad (57)$$

Equ.(33) can be re-written as:

$$\varepsilon_L = \left( \frac{l_0 \Delta (1 - mn)}{kDC^n m} \right)^{\frac{1-mn}{m}} \quad (58)$$

The constant  $\Delta$  is considered as a universal constant according to Tsuchida et al[7], therefore with the aid of Equ.(58) this could add further insight into the nature of  $\Delta$ .

The equations above illustrates the dependency between Lüders strain and velocity with strain-rate. Further analysis showed that key relationships

can be derived, which are useful when understanding the constants derived from experiment.

Equ.(44) and Equ.(46) do not give a description of the dynamics of dislocations within the Lüders band. A theoretical model presented in chapter 3 will show which type of dislocation dynamics lead to Equ.(44) and Equ.(46).

The equations presented for low strain-rate imply that as the strain-rate goes to infinity, then the speed of the band must also go to infinity. This is clearly incorrect and will be rectified under the section of higher strain-rates.

### 2.7.2 High strain-rates

Higher strain-rates are defined, according to Magd[40] as  $\dot{\varepsilon} > 10^3 s^{-1}$ , which is comparable to a car crash[41]. Strain-rates at this magnitude correspond to high temperature gradients in the material, which are accompanied by the adiabatic nature of the strain-rates. Therefore, the equations that have been used hitherto this section are only valid for low strain-rates as they assume no temperature change in the material. An adiabatic process assumes there is no heat exchange between the material and the surroundings. This implies that the condition for yielding or instability, with the adiabatic assumption becomes, according to [25]:

$$\frac{\partial \sigma}{\partial \varepsilon} - \sigma \leq \frac{\partial \sigma}{\partial T} \frac{\sigma}{c\rho_0} + \frac{d\dot{\varepsilon}}{d\varepsilon} \quad (59)$$

where  $\rho_0$  is the density of the material,  $c_v$  is the specific heat capacity and the other symbols have their usual meaning.

At low temperatures and strain-rates, the strain becomes less dependent on the strain-rate. Thus  $\frac{d\dot{\varepsilon}}{d\varepsilon} \approx 0$ . Equ.(59) reduces to:

$$\frac{\partial \sigma}{\partial \varepsilon} - \sigma \leq \frac{\partial \sigma}{\partial T} \frac{\sigma}{c\rho} \quad (60)$$

Equ.(60) illustrates why the yield stress at low temperatures is more pronounced than at room temperatures. This is because the specific heat  $c$  decreases at low temperatures, resulting in  $(c\rho)^{-1} \gg 1$ .

For high strain-rate, the difference between the upper and lower yield increases[40]. This is because, as the strain-rate increases, the mass inertia stress increases such that an energy balance must be constructed to overcome the dislocation blocking by the solute atoms. This results in an increase in

absorption energy per unit volume, such that the logarithmic relationship between the strain-rate and the stress deviates.

The simple interaction between dislocation and solute atom becomes more complicated at high strain-rates. The velocity and the strain of the Lüders band are modified accordingly. That is[40]:

$$v_L = \frac{v_M}{\sqrt{\varepsilon_{L0}^2 + (v_M/c)^2}} \quad (61)$$

where  $\varepsilon_{L0}$  is the strain at low strain-rates  $c = \sqrt{H_{work}/\rho}$ ,  $H_{work}$  is the work hardening defined as:

$$H_{work} = \frac{\partial \sigma}{\partial \varepsilon} \quad (62)$$

correspondingly, the strain is defined as:

$$\varepsilon_L = \sqrt{\varepsilon_{L0}^2 + (v_M/c)^2} \quad (63)$$

where  $\varepsilon_L$  is the Lüders strain at high strain-rate.

Contrasting with the model proposed by Sun et al[8], Hahn[18] and the conventional equation for the propagation of a band, the speed of the Lüders band does converge to a maximum with increasing strain-rate. This is to be expected as the fastest speed dislocations can go is at the speed of sound in the medium, as verified by Johnston et al[14].

Research into this area has recently been done by Itabashi et al[41] and Lee et al[42] with the application of structural failure to car accidents. In their experiments, using high velocity slip shot machines, it was possible for them to look at the resultant effects of high-impact/high strain-rate tests, with varying carbon content. The common points were the increase in flow stress, increase in adiabatic process and the validity of the adiabatic assumption at high strain-rates.

To summarise: when the band velocity( $v_L$ ) and the Lüders strain( $\varepsilon_L$ ) are separated, they both are functions of the strain-rate, strain-rate sensitivity and stress-sensitivity exponents. It was also shown that the derived stress-strain of these relations were similar with the stress-strain relation of Tsuchida et al[7](Equ(33)). This enabled a more descriptive model of Lüders strain, as there is now explicit relations for quantities of  $u$  and  $K'$ .

It was also shown that at higher strain-rates, the speed of the band had a limit as its velocity was ultimately related to the dislocation speed, which

has a maximum velocity of the speed of sound in the medium. This corresponded to prominent adiabatic processes that deviated from the standard stress-strain relationship for low strain-rates. Therefore, new equations were required. This gave new equations for both the  $v_L$  and  $\varepsilon_L$ . Confirmation of the adiabatic assumption came from Lee et al[42] and Itabashi et al[41].

## 2.8 Irradiation

When the RPV is exposed to gamma and neutron radiation, the material within the RPV will become irradiated. The effect of irradiation is to pin the dislocations due to the bombardment of fast neutrons on the material. The material becomes less ductile and more brittle, resulting in a higher yield point.

The bombardment of neutrons on the material can cause the crystal lattice to have more voids and defects, resulting in the creation of jogs, which pin the dislocations. This will result in a reduction in Lüders strain as seen in Fig.(23), which is analogous to the Lüders strain decreasing as a function of carbon content (see Fig.(8)). The increase in neutron bombardment decreases the Lüders strain. This similarity provides the possibility of modelling precipitate dislocation interaction, by applying irradiation models.

In conclusion, it was shown that the effect of irradiation was similar to increasing carbon content, in terms of the effects on dislocation motion and ductility. This symmetry has implications for modelling possibilities.

## 2.9 Cold working

Cold working refers to materials that have been deformed without the presence of heat treatment. The effect of this is to elongate the grains and produce further defects in the material. This increases the dislocation population.

Fig.(6) shows the result of an increase in dislocation population, according to Hahn's model. It shows that an increase in dislocation population, increases the chances of homogeneous deformation. This was further observed by Itoh et al[43] who showed that further increases in dislocation population, increased work hardening and the plastic zone around the yield stress.

In conclusion, it has been shown that the processing of a material, if no heat treatment is done prior to tensile testing, then the yield stress becomes less defined as more dislocations are free to deform homogeneously. It was

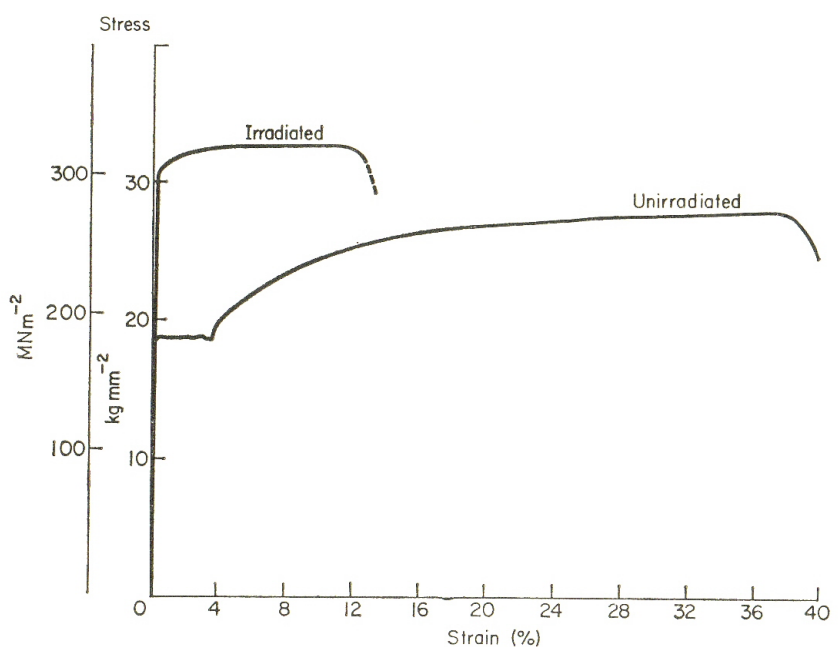


Figure 23: The effect of irradiated material on the yield stress. Taken from Hall E.O Yield point Phenomena in Metal and Alloys. Page-110

also shown how, with increasing dislocation density, the magnitude of the plastic zone increases.

## 2.10 Summary

It has been shown that the nucleation of a Lüders band can be thought of in terms of the work or stress required to remove a dislocation from the carbon atmosphere. The release of a dislocation was not enough to fully describe the Lüders band holistically, therefore a more dynamic model was required that could account for the band velocity, yield stress and Lüders strain. This was due to Hahn[18] who applied the Johnston and Gilman model to polycrystalline materials, such as bcc steel.

Although the models accounted for the main features of a Lüders band (upper and lower yield stress and Lüders stain), they were largely strain-dependent and did not factor in other quantities such as the carbon content, grain-size and temperature. Therefore, further investigation was required in order to understand and determine how the other factors affected the Lüders band.

It was shown that the Lüders strain reduces as the carbon content increases and as a result of the additional work-hardening between adjacent carbon contents, the band velocity became faster as shown by Song et al[24]. However, it was not determined precisely how the Lüders strain depended on the carbon content as the micro-structure and, consequently, the morphology were not taken into account. In other words, until it is known how the form of the carbides affect the Lüders strain for a given composition, it is incorrect to correlate Lüders strain with carbon content as Winlock[23] and Song et al[24] did, as it is tacitly assumed that the form of the micro-structure and the grain-size are the same for each percentage carbon. This was identified as a potential area of research by looking at materials with the same composition with different micro-structures, in order to determine how the morphology and the micro-structure of the carbides affects the Lüders strain.

The Lüders stain decreases as a function of grain-size. This was due to the dislocation density increasing as the grain-size decreased shown through Tsuchida et al[7] and Conrad[9].

The Lüders strain decreased as the temperature increased. This relation only applies to temperatures before serrations begin. When the serrations have initiated the relationship between the Lüders strain and temperature is difficult to quantify as the Lüders strain is serrated.

In conclusion it is apparent that the Lüders strain is dependent on many variables and therefore to build a model that factors all of them can be complicated; for example, the Lüders strain is inversely related to the grain-size, however in order to observe a Lüders band the material must be stretched which is dependent on the strain-rate and is ultimately related to the carbon content.

The subsequent chapters will look further into the explicit dependence on the Lüders strain with carbon content and the micro-structure for the same composition. Further investigation will also go into the nature of the shape of the band itself, which has not been mentioned in the literature review. It is hoped that insight will be gained from looking at the profile of the band, such as the shape at each carbon content and how that is related to the micro-structure.

### 3 Theoretical

This chapter will consist of two parts: The relationship of Lüders strain to carbon content and the sigmoidal strain displacement of a Lüders band. The first section will elaborate on observations made in the carbon content section, by Song et al[24], where it was stated that a method of modelling the Lüders strain with carbon content was to quantify the additional work-hardening that is required with the precipitates. It followed that the higher the carbon content, the larger  $\Delta\sigma$  would become. However, as it will be shown further in this chapter that the work-hardening alone does not uniquely identify with the carbon content, if other variables such as the grain-size are not constant. Therefore, a quantity will be pursued based on data from Tsuchida et al[7] and to a lesser extent Song et al[24] that is unique to amount of carbon content, from which an equation that relates the Lüders strain to the carbon content will be derived.

The second section consists of the type of deformation occurring in the model derived by Sun et al[8], by looking at the equation of motion of a Lüders band or group of dislocations. This will be followed by the corresponding strain-time curve derived from the Bergstrom equation[5] and the Orowan equation. Predictions will be made from the solutions and tested against the experimental data, which will be shown in chapter 7.

#### 3.1 Lüders strain as a function of carbon content

Fig.(24) shows the work-hardening behaviour ( $\frac{d\sigma_{LY}}{d\varepsilon_L}$ ) as a function of lower yield stress ( $\sigma_{LY}$ ) from which it is evident that the gradient of each line fitted has a unique value for each carbon content. The gradients of each line are defined as:

$$\phi = \frac{\frac{d\sigma_{LY}}{d\varepsilon_L}}{d\sigma_{LY}} \quad (64)$$

where  $\phi$  is a dimensionless parameter.

Plotting  $\phi$  against carbon content gives a linear trend to a first approximation in Fig.(25). Therefore, the following equation can be derived from the linear relation. That is:

$$\phi = \Phi C + \Gamma \quad (65)$$

where  $\Phi$  is the gradient and  $\Gamma$  is the intercept, yet to be determined.

or

$$\frac{d\sigma_{LY}}{d\varepsilon_L} = \sigma_{LY}(\Phi C + \Gamma) \quad (66)$$

Equ.(66) shows that for a chosen work hardening rate a relationship between the strain and carbon content can be derived. However, there is still the stress term on the right side of Equ.(66). Therefore, an explicit relation between the stress-strain must be defined<sup>8</sup>. This is done by considering the trend of lower yield stress against the Lüders strain as the carbon content increases.

---

<sup>8</sup>The  $\sigma_{lp}$  on the right of the equation come from integrating Equ.(65) with boundary condition  $\sigma_{lp} = C = 0$ . In other words, when the lower yield stress is zero, the material deforms homogeneously.

### Work hardening vs Lower yield stress

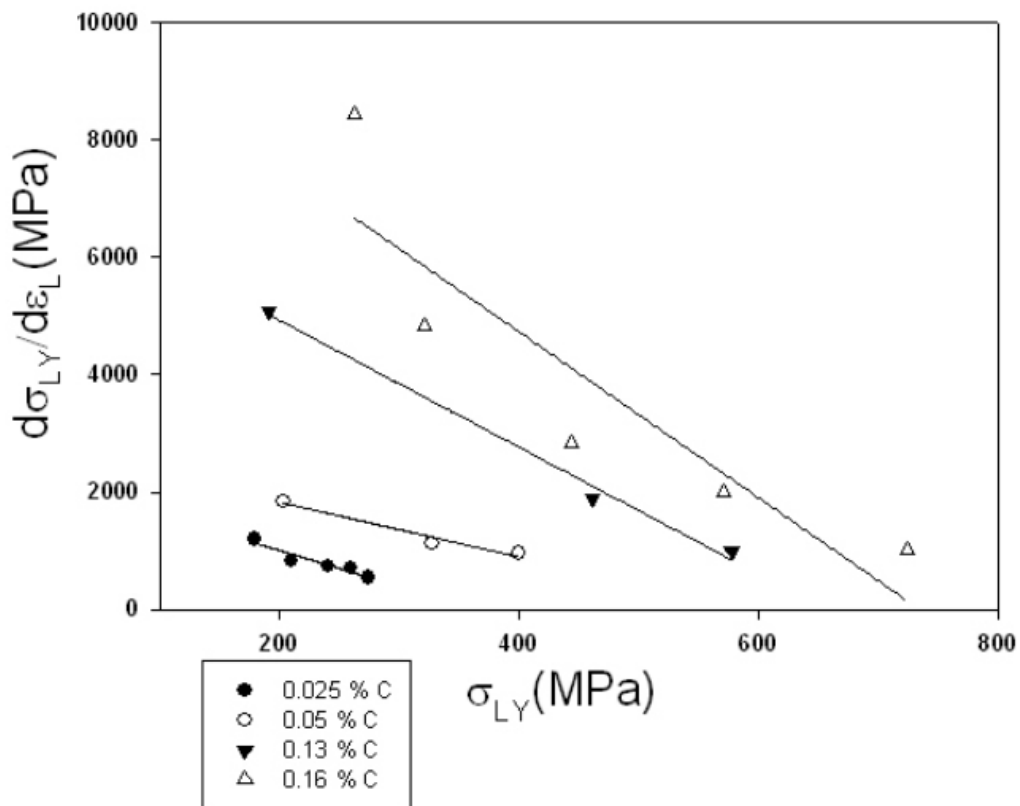


Figure 24: Data taken from Tsuchida et al[7] for 0.025, 0.05, 0.13 and 0.16% C. Although the data points from the 0.05%C and 0.13%C have only 3 points, assuming a linear trend is substantiated by fitting the materials(0.025 and 0.16%C) with more data points.

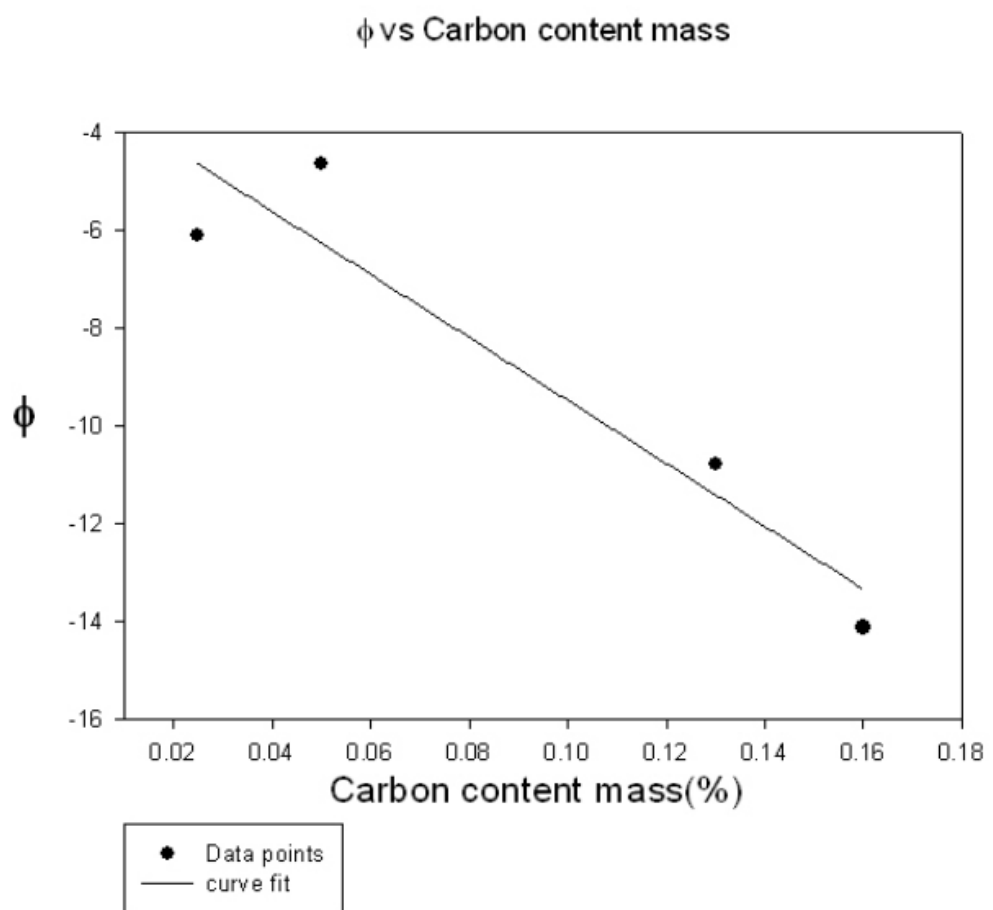


Figure 25: Plot of  $\phi$  vs carbon content, showing negative gradient between  $\phi$  and carbon content

Looking as Fig.(8) it is clear the Lüders strain and lower yield stress are inversely related, therefore let us assume that the stress and strain are related to each other as a power law:

$$\sigma_{LY} = M\varepsilon_L^{-\kappa} \quad (67)$$

where  $M$  and  $\kappa$  are constant.

Taking the derivative:

$$\frac{d\sigma_{LY}}{d\varepsilon_L} = -M\kappa\varepsilon_L^{-\kappa-1} = -\frac{\kappa\sigma_L}{\varepsilon_L} \quad (68)$$

substituting Equ.(68) into Equ.(66) gives

$$-\frac{\kappa\sigma_{LY}}{\varepsilon_L} = \sigma_{LY}(\Phi C + \Gamma) \quad (69)$$

or

$$\varepsilon_L = -\frac{\kappa}{(\Phi C + \Gamma)} \quad (70)$$

Although at first it seems Equ.(70) produces negative strain, the value of  $\Phi$  and  $\Gamma$  according Fig(25) are negative or less than zero with values  $\Phi = -64.4$  and  $\Gamma = -3.05$  respectively and as they are considered constant for all materials of different carbon contents,  $\varepsilon_L$  will remain positive.

Re-writing Equ.(70) gives:

$$\varepsilon_L = \frac{a}{1 + bC} \quad (71)$$

where  $a = \frac{\kappa}{3.05}$  and  $b = 21$ .

It is apparent that the Lüders strain decreases as the carbon content increases which is observed in Winlock[23] and Song et al[24].

Choosing a Lüders strain that is unique for each carbon content is difficult, because of the inevitable difference in grain-sizes, as shown in table 2( see chapter 2). Therefore, in order to obtain a value that is representative of the Lüders strain for each carbon content, the average was taken. The values of these were then plotted against carbon content, including the data of Song et al[24], with the result shown in Fig.(26).

The black line on Fig.(26) is plotted with  $b$  and the denominator of  $a$  constant i.e. 21 and 3.05, allowing only  $\kappa$  to vary. This is feasible as  $\kappa$  was originally an exponent in Equ.(67) and therefore depends entirely on the carbon content.

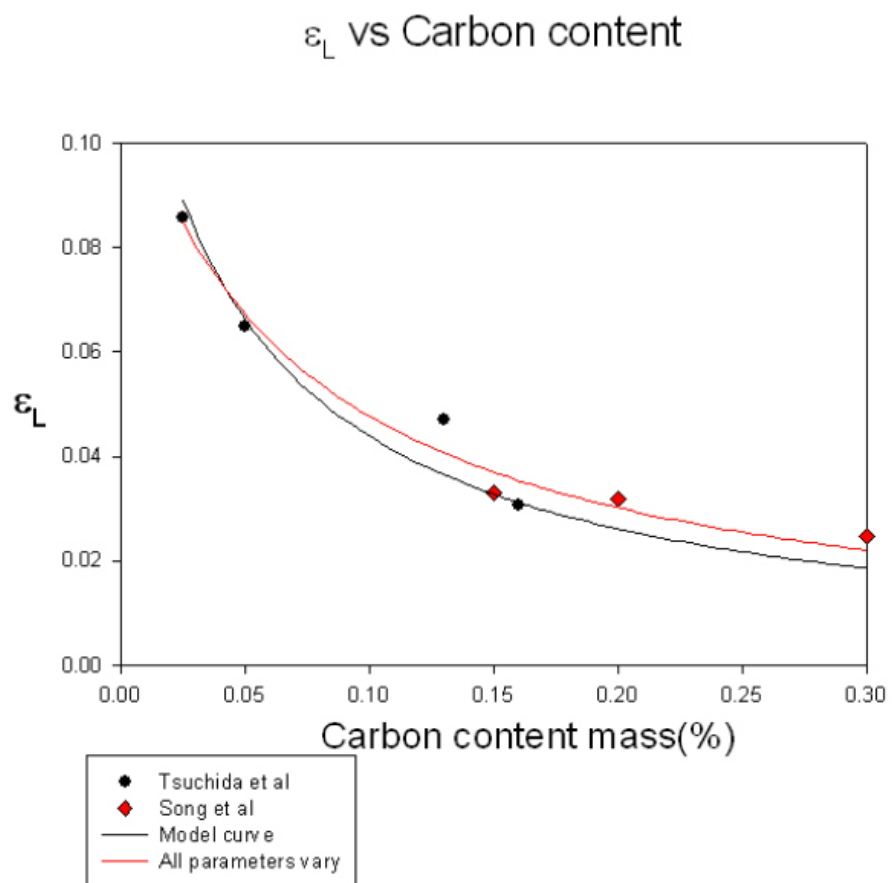


Figure 26: Plot of Equ.(71)(black line) with only  $\kappa$  free. Equ.(71)(red line) with  $a$ ,  $b$  and  $\kappa$  are free and the data Tsuchida et al[7](black circles) and Song et al[24](red diamonds).

The second curve in Fig.(26) shows the same curve but allowing  $a$  and  $b$  to vary. When this occurs, the value of  $b = 13.94$  and  $a = 0.1141$ .

Equ.(71) is in good correlation with the data points in general and extends to the values of Song et al[24], although the Lüders strain measured was at different micro-structures and strain-rates.

### 3.2 Summary

An equation based upon the data of Tsuichida et al[7] has been derived. It is shown that the parameter  $\phi$  gives a unique value for each percentage mass of carbon. When this was equated to the carbon content and solved for the Lüders strain, it is shown that the Lüders strain decreased as a function of increasing carbon content. Although the method of derivation is simplistic and lacked a theoretical basis, the curve of Equ.(71) predicted, approximately, where the data Song et al[24] should lie. The equation only had one free parameter,  $\kappa$  and therefore showed that the numbers 21 and 3.05 can be considered as constants in this model.

It was assumed that the Lüders strain entirely depended on the carbon content and thus implicitly assumed that the form of the carbides between materials of different carbon content were the same. In the case of Fig.(26), Equ.(71) predicted the expected Lüders strain of Song et al[24], because the form of the carbides were similar to Tsuichida et al[7] i.e. ferrite-pearlite dominant, although with fine cementite particles on the grains as shown in Fig.(9). This highlights the limitation of the model.

It is, however, hoped that further work can ascertain certain relationships between  $\phi$  and the micro-structure of the carbon content. This would then produce a relationship between the Lüders strain and carbon content that factors in the morphology of the carbides for different carbon contents.

The next section in this chapter will be on the strain-time curve of the Lüders band.

### 3.3 Dynamics of Sun's model

In section 2.7 (under strain-rate effect) it was shown that the Lüders strain and velocity can be decoupled and written separately as Equ.(44) and Equ.(46). Although the equations were successful in correlating the Lüders strain and velocity with the applied strain-rate, the equations were empirically based and, therefore, did not reveal the internal dynamics of the Lüders band, such

as the strain displacement before the Lüders strain and velocity variation within the Lüders band.

This section is dedicated to producing a model that encompasses Equ.(44) and Equ.(46) by showing that the equations are a natural consequence of steady state motion and, subsequently, when substituted into the Orowan equation, produces the correct strain-time profile of the Lüders band. In uniaxial tensile tests for one dimension, the following equation of motion is assumed to hold:

$$F_{drive} - F_{drag} = ma \quad (72)$$

where  $F_{drive}$  is the driving force,  $F_{drag}$  is a frictional force, which is assumed to follow a power law<sup>9</sup>, and  $m$  is the mass and  $a$  is the acceleration.

In a steady state or when the  $a = 0$ , Equ.(72) simplifies to:

$$F_{drive} = b_{fric}v^k \quad (73)$$

where  $v$  is the band velocity and  $b_{fric}$  is a constant of friction, dependent on the geometry of the object and  $k$  is a constant.

To determine the value of  $k$ , using the definition of stress and substituting into Equ.(73):

$$v = \left( \frac{\sigma A_{cross}}{b_{fric}} \right)^{\frac{1}{k}} \quad (74)$$

To find the value of  $k$ , comparing to the Johnson-Gilman equation that relates the velocity and stress:

$$v \propto \sigma^n \quad (75)$$

where  $n$  is the stress-rate sensitivity.

Comparing Equ.(74) to Equ.(75), it is evident that  $k = \frac{1}{n}$ . Using Equ.(23) to relate the velocity to the strain-rate and substituting into Equ.(74):

$$v = \frac{C^n A_{cross}^n}{b_{fric}^n} \dot{\varepsilon}^{mn} \quad (76)$$

For the strain using  $v = \frac{\dot{\varepsilon}l_0}{\varepsilon_L}$ :

$$\varepsilon_L = \left( \frac{C^n A_{cross}^n}{l_0 b_{fric}^n} \right)^{-1} \dot{\varepsilon}^{1-mn} \quad (77)$$

---

<sup>9</sup>As the dislocation movement is defined as the viscous stress according to Schlipf[44], it is therefore approximated as a continuous medium (such as a fluid), which obey a power law.

which are equations of the same form as shown in Sun et al[8]. That is:

$$v_L = kDC^n \dot{\varepsilon}^{mn} \quad (78)$$

$$\varepsilon_L = \frac{L_0}{kDC^n} \dot{\varepsilon}^{1-mn} \quad (79)$$

Therefore it has been shown that when the strain value has reached the Lüders strain, the dislocation density is in a steady state or  $\frac{d\rho}{dt} = 0$ .

It has been shown that in the Lüders band or when the strain has achieved a value of  $\varepsilon_L$ , the band velocity is constant. It follows that as the dislocations are constituents of the Lüders band, the average velocity of the dislocation is also constant. Therefore, the velocity term in the Orowan equation, which has the dislocation velocity, will remain constant.

The Orowan equation is defined as[45]:

$$\frac{d\varepsilon}{dt} = b\rho(\varepsilon(t))v_d \quad (80)$$

where  $v_d$  is the dislocation velocity,  $\rho$  is the dislocation density and  $b$  is the Burger's vector.

The solution to Equ.(80) is dependent on the form of dislocation density chosen. This is achieved with the aid of the Bergstrom model that was originally derived to describe homogeneous deformations[5]. That is:

$$\frac{d\rho}{d\varepsilon} = U(\varepsilon) - \Omega\rho \quad (81)$$

where  $U(\varepsilon)$  is an immobilization term and  $\Omega$  is the dislocation remobilization constant.

It will be shown that Equ.(81) can describe any type of deformation provided that the correct immobilization term is used. According to Bergstrom et al[5] the form of the  $U(\varepsilon)$  is written as:

$$U = \frac{\hat{m}}{bS(\varepsilon)} \quad (82)$$

where  $\hat{m}$  is the Taylor factor,  $b$  is the dislocation length and  $S(\varepsilon)$  is the length of the mean free path of the dislocation, as a function of strain.

For homogeneous deformation it was shown that the following relation described the mean free path up to necking[5]:

$$S(\varepsilon) \propto \exp(-\omega\varepsilon) \quad (83)$$

where  $\omega$  is a constant related to the micro-structure of the material.

Consequently, the mean free path of the dislocations becomes smaller as the strain increases, until there is dislocation build up within the grain and necking occurs.

According to Schlipf[44] Lüders bands can be considered as the reverse process of necking, although the mechanism of nucleation is different.

Mathematically, this is described by simply reversing the relations of Equ.(83) to produce:

$$S = S_0 \exp(\omega\varepsilon) \quad (84)$$

where  $S_0$  is a constant interpreted as the mean free-path.

Substituting Equ.(84) into Equ.(82) and then into Equ.(81), producing the following differential equation:

$$\frac{d\rho}{d\varepsilon} = \frac{\hat{m}}{bS_0} \exp(-\omega\varepsilon) - \Omega\rho \quad (85)$$

For the special case, which is the one under consideration,  $\Omega = \omega$ , Equ.(85) becomes:

$$\frac{d}{d\varepsilon}(\rho \exp(\Omega\varepsilon)) = \frac{\hat{m}}{bS_0} \quad (86)$$

or

$$\rho(\varepsilon) = \left( \frac{\hat{m}}{bS_0}\varepsilon + \rho_0 \right) \exp(-\Omega\varepsilon) \quad (87)$$

where  $\rho_0$  is a constant of integration interpreted as the number of free dislocations with in the ferrite matrix.

Equ.(87) is similar to the equation derived by Gilman[45], although some of the constants within Gilman's original equation were archaic and therefore redundant. Equ.(87) is an actual improvement to Gilman's original equation as it is expressed in terms of modern parameters<sup>10</sup>.

Gilman derived the exponential factor within Equ.(87) by assuming that the friction term within the glide plane was proportional to the number

---

<sup>10</sup>For example Gilman's original equation read as follows:  $\rho(\varepsilon) = (\rho_0 + M\varepsilon) \exp(-\phi\varepsilon)$ , where  $M = \frac{\delta}{b}$  and  $\phi$  is a coefficient;  $\delta$  and  $\phi$  are considered archaic as they are not measured in current literature. However, contrasting with Equ.(87),  $\delta$  is expressed as  $\delta = \frac{\hat{m}}{S_0}$  and  $\phi = \Omega$ . Thus, the original form of the Gilman's equation is modified to allow the archaic coefficients to be expressed in terms of more modern, fundamental parameters.

of dislocations, similar to a decay rate relation<sup>11</sup>. There is, however, no theoretical basis to the relation.

It is interesting to note Equ.(84) (in the case where  $\Omega = \omega$ ) in the process of producing Gilman's original equation (Equ.(87)), has given credence to Gilman's original assumption that the friction on the glide plane is first order.

Substituting Equ.(87) into the Orowan equation gives:

$$\int_o^\varepsilon \left( \frac{\exp(-\Omega\varepsilon)}{\frac{\hat{m}}{bS_0}\varepsilon + \rho_0} \right) d\varepsilon = \int_o^t \Omega v b dt \quad (88)$$

The integral on the left side of the above equation can not be expressed in terms of standard functions. Therefore, Equ.(87) is Taylor expanded with only terms of  $\varepsilon^2$  and any terms of higher are ignored. This expansion is justified as the strain in most Lüders bands range between 1-8% at nominal strain-rate, therefore the strain in the Lüders region will be small enough to ignore the higher terms.

Equ.(88) becomes:

$$\int_0^x \frac{dx}{(1 + \xi x - \eta x^2)} = \int_0^t \zeta dt \quad (89)$$

where  $x = \Omega\varepsilon$  is a free variable,  $\xi = \left(\frac{\hat{m}}{bS_0\Omega\rho_0} - 1\right)$ ,  $\eta = \left(\frac{\hat{m}}{bS_0\Omega\rho_0} - \frac{1}{2}\right)$  and  $\zeta = \Omega b v \rho_0$ .

The solution to the integral equation is of the form:

$$x(t) = \frac{\xi + (\xi^2 + 4\eta)^{\frac{1}{2}} \tanh(\frac{\varsigma t - q}{2})}{2\eta} \quad (90)$$

where  $\varsigma = \zeta(\xi^2 + 4\eta)^{\frac{1}{2}}$  and  $q = 2 \tanh^{-1} \left( -\frac{\xi}{(\xi^2 + 4\eta)^{\frac{1}{2}}} \right)$ .

When Equ.(90) was derived from the Taylor expansion, it was assumed that the constants  $\eta > 0$  and  $\xi > 0$ . This is easily shown by simply looking at the maximum of Equ.(87):

$$\rho_0 = \frac{\hat{m}}{bS_0} \left( \frac{1}{\Omega} - \varepsilon_L \right) \quad (91)$$

---

<sup>11</sup>Friction, in the sense of dislocation motion, is the reduction of dislocations from the Lüders band. Therefore, the higher the friction on the glide plane, the more dislocations are taken away from the Lüders band.

Dividing by  $\rho_0$  rearranging to get the same expression as  $\xi$ :

$$\frac{\hat{m}}{bS_0\Omega\rho_0} - 1 = \frac{m\varepsilon_{max}}{bS_0\rho_0} \quad (92)$$

where  $\varepsilon_{max}$  is where maximum deformation occurs.

It is evident that the left hand side of Equ.(92) is equal to  $\xi$  and as the terms on the right of the equation are positive, it follows that:

$$\xi > 0 \quad (93)$$

or

$$\frac{\hat{m}}{bS_0\Omega} > \rho_0 \quad (94)$$

As  $\rho_0 > \frac{\rho_0}{2}$  therefore  $\frac{\hat{m}}{bS_0\Omega} > \frac{\rho_0}{2}$  and thus  $\eta > 0$ .

Although it has been demonstrated that the  $\xi$  and  $\eta$  are greater than zero in the original equation, the equation used for integration was the Taylor expanded form. However, as will be shown shortly, the values when integrated, although give the correct curve, do not give positive values.

This was shown through physical argument with the aid of Equ.(90) and looking at the Taylor expanded form of the dislocation density as a function of strain.

Taylor expanded form:

$$\rho(x) = \rho_0(1 + \xi x - \eta x^2) \quad (95)$$

with the following maximum, substituting  $x = \Omega\varepsilon$ :

$$\varepsilon_{max} = \frac{\xi}{2\eta\Omega} \quad (96)$$

this is where deformation is a maximum in the Lüders band.

The initial strain and the strain where the bands exist, or Lüders strain, is calculated when the multiplication of the dislocation is zero such that:

$$\eta x^2 - \xi + 1 = 0 \quad (97)$$

with the following roots:

$$\varepsilon = \frac{\xi}{2\Omega\eta} \pm \frac{\sqrt{\xi^2 + 4\eta}}{2\Omega\eta} \quad (98)$$

where  $x = \Omega\varepsilon$  has been substituted.

Taking the limit of Equ.(90) which physically means that the Lüders band has passed and inhomogeneous deformation has ceased:

$$\varepsilon_L = \lim_{t \rightarrow \infty} \varepsilon(t) = \frac{\xi}{2\Omega\eta} + \frac{\sqrt{\xi^2 + 4\eta}}{2\Omega\eta} \quad (99)$$

Therefore, from Equ.(98) the Lüders strain is the sum of the maximum strain and the additional strain after the maximum. Consequently, let the additional strain be denoted as  $\varepsilon_{add}$ , then one can equate the terms on the right hand side of Equ.(99) to  $\varepsilon_{max}$  and  $\varepsilon_{add}$  as follows:

$$\varepsilon_{max} = \frac{\xi}{2\Omega\eta} \quad (100)$$

and

$$\varepsilon_{add} = \frac{\sqrt{\xi^2 + 4\eta}}{2\Omega\eta} \quad (101)$$

when solved for  $\eta$  gives:

$$\eta = -\frac{1}{\Omega^2(\varepsilon_{max}^2 - \varepsilon_{add}^2)} \quad (102)$$

and with the aid of Equ.(98), which shows that the solutions of the quadratic for  $\varepsilon$  have to be positive that is:

$$\varepsilon_i = \frac{\xi}{2\Omega\eta} - \frac{\sqrt{\xi^2 + 4\eta}}{2\Omega\eta} \quad (103)$$

and

$$\varepsilon_L = \frac{\xi}{2\Omega\eta} + \frac{\sqrt{\xi^2 + 4\eta}}{2\Omega\eta} \quad (104)$$

where  $\varepsilon_i$  is the initial strain and  $\varepsilon_L$  is the Lüders strain.

As  $\varepsilon_L > \varepsilon_i$  it follows that  $\varepsilon_{max} > \varepsilon_{add}$ . Therefore,  $\eta < 0$  and  $\xi < 0$  as  $\Omega$  by definition is positive.

If  $\eta$  and  $\xi$  are then re-substituted back into Equ.(89) the result is an equation with different signs and, therefore, when integrated, does not produce the appropriate solution, as the integral of the reciprocal of quadratics, in general, are sensitive to the signs of the coefficients.

A solution to this problem is solved by assuming that  $\rho_0 = 0$ . As result, Equ.(87) from the original equation derived from the Bergstrom equation becomes:

$$\rho(\varepsilon) = \frac{\hat{m}}{bS_0} \varepsilon \exp(-\Omega\varepsilon) \quad (105)$$

Taylor expanding the above equation and ignoring higher than  $O(\varepsilon^2)$  becomes<sup>12</sup>:

$$\rho(x) \approx \frac{\hat{m}}{bS_0\Omega} x(1-x) \quad (106)$$

where  $x = \Omega\varepsilon$ .

Substituting into back in to the Orowan equation produces the following integral:

$$\int \frac{1}{x(x-1)} = \int \gamma dt \quad (107)$$

where  $\gamma = \frac{v_d \hat{m}}{S_0}$ .

the corresponding solution of:

$$x(t) = \frac{1}{1 + \Lambda \exp(-\gamma t)} \quad (108)$$

where  $\Lambda$  is a constant of integration yet to be determined.

Equ.(106) and Equ.(108) refer to only the release of the pinned or immobilized dislocations. As a result, the dislocation density calculated in Equ.(106) up until  $\rho_{max}$ , where  $\rho_{max}$  is the maximum number of dislocations, represents the dislocations density of the number of dislocations freed from the Cottrell atmospheres and from the other sources of pinning.

The physical interpretation of Equ.(106) and Equ.(108) can be further substantiated by calculating the average time for the immobilized dislocations to move from the Cottrell atmosphere. According to Bergstrom[46] this is calculated by time averaging the dislocation density. That is:

$$\tau = \frac{\int_0^\infty t \rho(t) dt}{\int_0^\infty \rho(t) dt} \quad (109)$$

---

<sup>12</sup>Equ.(105) was Taylor expanded, because when it is substituted into the Orowan equation, the solution is still expressed in terms of non-standard functions. Therefore, the same procedure is applied again, in order to obtain a solution that is expressed terms of standard functions.

where  $\tau$  is defined as the average time taken for the dislocations to release from the carbon atmospheres and  $t$  is the time.

The above equation can be simplified by using the Orowan equation that relates the strain-rate to the dislocation density. Therefore, Equ.(109) becomes:

$$\tau = \frac{\int_0^\infty t\dot{\varepsilon}dt}{\int_0^\infty \dot{\varepsilon}dt} \quad (110)$$

which becomes:

$$\tau = \frac{[\varepsilon]_0^\infty - \int_0^\infty \varepsilon(t)dt}{[\varepsilon(t)]_0^\infty} \quad (111)$$

substituting Equ.(108) (recalling  $x = \Omega\varepsilon$ ) for  $\varepsilon$  gives:

$$\tau = \frac{(\Lambda + 1) \ln(\Lambda + 1)}{\Lambda\gamma} \quad (112)$$

where  $\Lambda$  and  $\gamma$  are parameters that will be determined from curve fitting the data.

It is better to express  $\tau$  in terms of more familiar variables.

Using Equ.(116) to relate  $\gamma$  to the maximum strain-rate gives:

$$\tau = \frac{(\Lambda + 1) \ln(\Lambda + 1)}{4\Omega\Lambda\dot{\varepsilon}_{max}} \quad (113)$$

If  $\tau$  is comparable to the time taken for the band to traverse a given region, which is calculated through the width of the trough of the strain-time curve, the mechanism responsible for this is the freeing of the dislocations and, additionally, the number dislocations freed.  $\tau$  will be calculated from the data in the Chapter (7).

Equ.(108) with its derivative makes several predictions how the band behaves, from which properties such as the maximum strain-rate within the band can be calculated. The derivative of Equ.(108) is simply the Equ.(107). The maximum of Equ.(107) or maximum strain-rate is calculated from taking its derivative, which is, in terms of  $x$ :

$$\frac{d^2x}{dt^2} = \gamma \left( \frac{dx}{dt}(1-x) - \frac{dx}{dt}x \right) \quad (114)$$

equating the left side of the above equation gives  $x = \frac{1}{2}$ . Substituting back into Equ.(107) gives a maximum strain-rate of:

$$\left( \frac{dx}{dt} \right)_{max} = \frac{\gamma}{4} \quad (115)$$

substituting  $x = \Omega\varepsilon$ :

$$\left(\frac{d\varepsilon}{dt}\right)_{max} = \frac{\gamma}{4\Omega} \quad (116)$$

Another prediction due to the nature of the sigmoidal function in Equ.(108) is taking the limit of the function, similar to the hyperbolic function in Equ.(90).

$$\lim_{t \rightarrow \infty} x(t) = 1 \quad (117)$$

this is interpreted as discussed above as the maximum strain or Lüders strain, therefore:

$$x_{max} = \Omega\varepsilon_L = 1 \quad (118)$$

or

$$\varepsilon_L = \frac{1}{\Omega} \quad (119)$$

Therefore the strength of the Lüders strain is determined by the re-immobilization parameter or rather the re-immobilisation parameter is determined by the Lüders strain.

It is interesting to note that the Lüders strain is twice that value of the strain that corresponds to the point of maximum strain-rate.

The maximum dislocation density or  $\rho_{max}$  occurs when  $x = \frac{1}{2}$ , therefore when substituted into Equ.(108) gives:

$$\rho_{max} = \frac{\hat{m}}{4bS_0\Omega} \quad (120)$$

But  $\Omega = \frac{1}{\varepsilon_L}$  therefore:

$$\rho_{max} = \frac{\hat{m}\varepsilon_L}{4bS_0} \quad (121)$$

Consequently, there is an explicit dependence between the dislocation density of the dislocations released and the Lüders strain.

One can go further and relate the dislocation mean free path to the dislocation density. It was mentioned by Vetter[47] that the dislocation mean free path can be related to the dislocation density by:

$$S \propto \rho^{-\frac{1}{2}} \quad (122)$$

Bergstrom[46] went one further and showed that this relationship can be applied to most steels and found that the constant of proportionality is that related  $S_0$  and the corresponding  $\rho$  for  $S_0$  was:

$$S_0 = \frac{\hat{m}}{bK} \rho^{-\frac{1}{2}} \quad (123)$$

where K is a material constant with dimension of  $m^{-1}(\text{length})^{-1}$  and is considered universal for all steels.

Relating Equ.(123) to Equ.(121) gives:

$$\varepsilon_L = 4 \frac{\rho_{max}^{\frac{1}{2}}}{K} \quad (124)$$

and for the Lüders strain dependence on the mean free-path:

$$\varepsilon_L = \frac{4\hat{m}}{S_0 b K^2} \quad (125)$$

Equ.(124) and Equ.(125) show direct relations between the Lüders strain and the dislocation density and the Lüders strain density and mean free path.

The work of Bailon et al[48] related the dislocation density at the end of the Lüders strain to the grain-size with the following relation:

$$\rho = \frac{1}{d_{grain}} \left( \frac{k_e}{\alpha b E} \right)^2 \quad (126)$$

where  $\alpha$  is a dimensionless constant,  $k_e$  is a constant derived from the Hall-Petch relation,  $E$  is Young's modulus,  $b$  is the Burger's vector and  $d_{grain}$  is the grain size.

Substituting Equ.(126) into Equ.(124), as  $\rho_{max}$  is interpreted as the number of dislocations at the end of the band gives:

$$\varepsilon_L = \frac{4}{K d_{grain}^{\frac{1}{2}}} \left( \frac{k_e}{\alpha b E} \right) \quad (127)$$

or

$$\varepsilon_L \propto d_{grain}^{-\frac{1}{2}} \quad (128)$$

Equ.(127) shows an explicit Hall-Petch type relation between the Lüders strain and the grain-size. Therefore, the Lüders strain is related to the dislocation

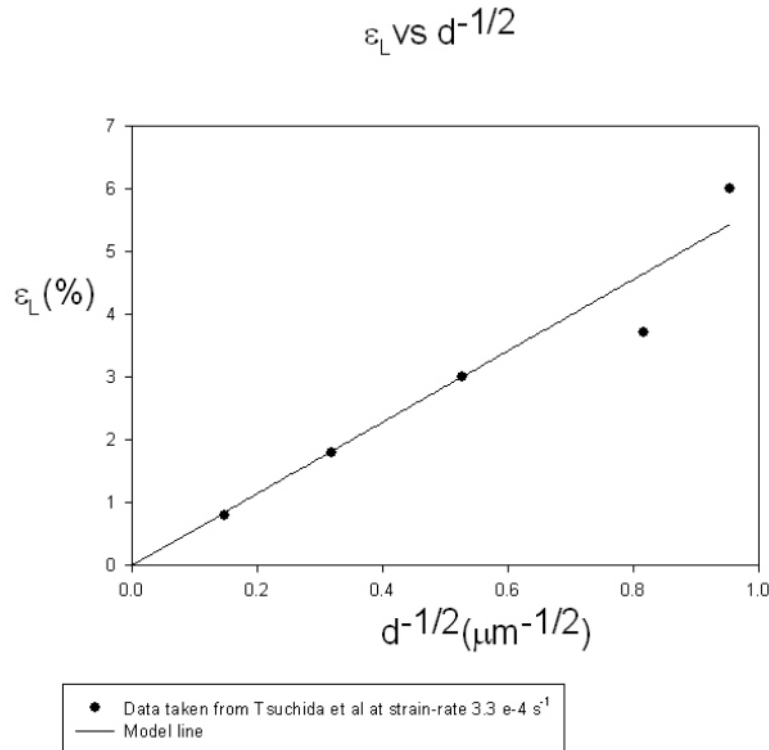


Figure 27: Lüders strain( $\varepsilon_L$ ) against grain-size(d) at 296 K taken Tsuchida et al[7], with the model line(Equ.(127))

density through the grain-size. In other words the smaller the grain-size, the larger the number of dislocations unpinned during band propagation and , therefore, the larger the Lüders strain.

The relationship is verified by taking the data from Tsuchida et al[7] that shows the Lüders strain for each grain-size of the same material 0.15%C steel and plotted in Fig.(27).

It was identified in the literature review that there was no explicit explanation how a Lüders strain with the same composition would depend as a function of micro-structure. Or in other words, what is the micro-structural dependence of the Lüders strain for the same composition of material.

The answer to the question forms a large part of the thesis, however using Equ.(125) it is possible to give an explanation with the additional work due to Song et al[24], as discussed in the literature review chapter.

Song et al[24] showed that the amount of precipitates on the ferrite matrix can be quantified by calculating the difference between the work-hardening stress required to move dislocations through the precipitates and the work-hardening stress required to move a dislocation on a ferrite matrix, with no precipitates. In other words, let  $\sigma_{prep}$  be the stress required to move dislocations through or around precipitates and let  $\sigma_{ferr}$  be the stress required to move dislocations on the ferrite matrix. The larger  $\frac{\sigma_{prep} - \sigma_{ferr}}{d\varepsilon}$ , the larger the number of precipitates or obstacles. The effect of a larger  $\frac{\sigma_{prep} - \sigma_{ferr}}{d\varepsilon}$  is a reduction in the mean free path of the dislocations. According to Equ.(125) this increases the Lüders strain. Consequently, materials with the same composition but with different micro-structure, due to heat-treatment for example, will differ in Lüders strain if the mean free path of the dislocations( $S_0$ ) is reduced or increased relative to non-heat treated or as-received micro-structure.

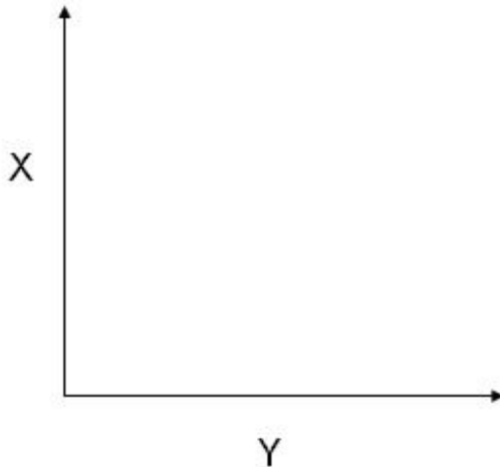


Figure 28: x-axis is perpendicular to the gauge length and the y-axis is parallel or in the direction of the gauge length. This orientation has been chosen, because the DIC's axis are set in this way.

### 3.4 Profile of the Lüders band

Having calculated how the Lüders strain varies with time, it is possible to calculate how the strain varies with distance and, consequently, the spatial profile of the Lüders band, from which the angle of the profile can be calculated.

The strain dependence on the distance is calculated using the chain rule. That is:

$$\frac{d\varepsilon_y}{dy} = \frac{d\varepsilon_y}{dt} \frac{dt}{dy} = \dot{\varepsilon}_y \frac{1}{v_{yl}} \quad (129)$$

where  $y$  is the y-direction and  $v_{yl}$  is the Lüders band velocity in the y-direction, which is assumed to be constant.

It is assumed that the change in cross-sectional area is small such that the elastic limit is still dominant and, therefore, the strains in the x and y direction are related via Poissons's ratio. That is:

$$\frac{\varepsilon_x}{\varepsilon_y} = -\nu \quad (130)$$

where  $\varepsilon_x$  and  $\varepsilon_y$  are the strain in the  $y$  and  $x$  direction, respectively, and  $\nu$  is Poisson's ratio.

Using Equ.(130) it is possible to show how the band would look in the compressive, x-direction. Substituting Equ.(130) into Equ.(108) one obtains:

$$\varepsilon_x = -\frac{\nu}{\Omega(1 + \Lambda \exp(-\gamma t))} \quad (131)$$

with the corresponding magnitude of Lüders strain in the x-direction:

$$\varepsilon_x = -\frac{\nu}{\Omega} \quad (132)$$

Now that the strain dependence is known for both directions, to find  $x(y)$  the following formula is used:

$$\frac{dx}{dy} = \frac{dx}{d\varepsilon_x} \frac{\varepsilon_x}{\varepsilon_y} \frac{d\varepsilon_y}{dy} = \frac{v_x}{v_y} \quad (133)$$

using the formula for band velocity:

$$v_i = \frac{\dot{\varepsilon} \Delta z_i}{\varepsilon_i} \quad (134)$$

where  $v_i$  is the velocity,  $\Delta z_i$  change in spatial direction,  $\varepsilon_i$  is the strain in the  $i^{th}$  direction and  $\dot{\varepsilon}$  is the strain-rate.

Therefore Equ.(133) becomes:

$$\frac{dx}{dy} = \frac{\dot{\varepsilon} \Delta x}{\varepsilon_x} \times \frac{\varepsilon_y}{\dot{\varepsilon} \Delta y} \quad (135)$$

Assuming the strain-rate in both of the directions is approximately equal and using Equ.(131), upon integration Equ.(135) becomes:

$$x(y) = -\frac{\Delta x}{\Delta y \nu} y + x_0 \quad (136)$$

where  $x_0$  is the initial length of the band and  $\Delta x$  and  $\Delta y$  are the width and length of the Lüders band, respectively.

With the corresponding sheering angle:

$$\frac{dx}{dy} = \tan(\theta) = -\frac{\Delta x}{\Delta y \nu} \quad (137)$$

Taking the special case where the sheering angle is at  $\theta = 45^\circ$  in terms of the angle orientation this would be -1:

$$\Delta x = \Delta y \nu \quad (138)$$

Fig.(29) shows what the band would look like travelling in the y-direction at a sheering angle of  $45^\circ$ .

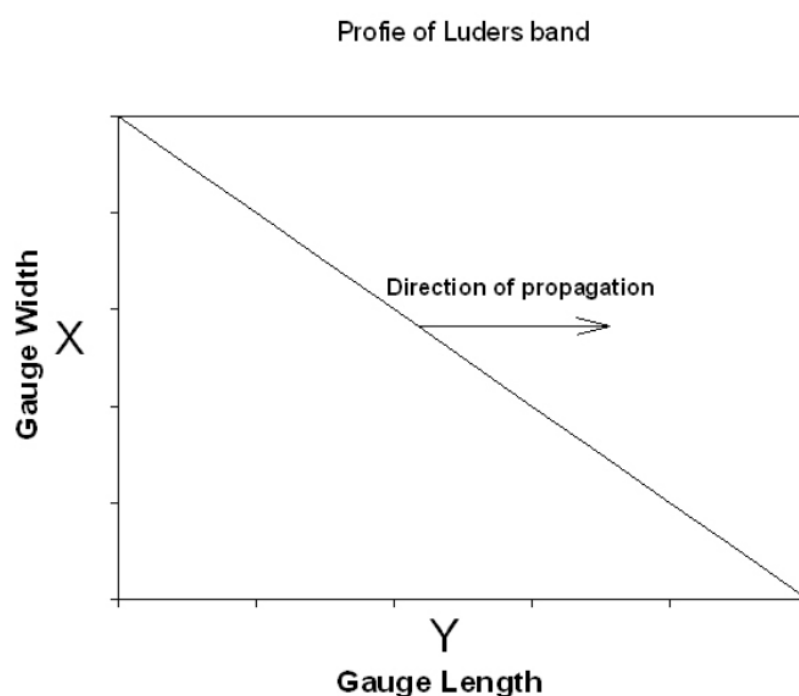


Figure 29: Profile of Lüders band propagating at sheering angle of  $45^\circ$  with the direction of propagation along the gauge length.

The time taken for the band to traverse across the gauge length can also be calculated, assuming nucleation begins on the edge of the gauge length.

Using Pythagoras' formula for velocities:

$$v_{xy} = \sqrt{v_x^2 + v_y^2} \quad (139)$$

where  $v_{xy}$  is the velocity in the x-y direction.

The time taken is simply the overall distance divided by the overall velocity.

Therefore the time taken is:

$$t = \frac{\sqrt{(\Delta x)^2 + (\Delta y)^2}}{\sqrt{v_x^2 + v_y^2}} \quad (140)$$

### 3.5 Zhang model

The model chosen to represent Lüders bands in this report is the Zhang model. It is taken from the original work of Zhang et al[49] and uses the standard constitutive equations of stress-strain dynamics, with multi-axial loading from Estrin et al[50]. The model was originally developed to account for the Portevin-Le Chatelier[6] effect and uses the physics of dynamic strain-ageing or DSA to account for the multiple yielding(serrated behaviour) that occurs during uni-axial testing.

DSA occurs when carbon atoms have enough energy, due to the thermal energy, to move at velocities comparable to the mobile dislocations. The carbon atoms move towards the mobile dislocations and pin them temporarily, thus in the process creating yield points. This process continues and is seen as serrations on the Lüders plateau.

The main function that is responsible for the DSA is Equ.(145), is an oscillatory function that is used to describe the serrated behaviour and whose stability is dependent on the parameters defined within Equ.(144). To translate the model representative of an Al-Mg-Si alloy to ferritic steel, Wenman et al[1] and Graff el al[51] changed the parameters(see table 11) and varied Equ.(144, page 138) slowly in order to keep the solution stable, that is no serrations on the Lüders strain.

A description of the model will now be provided.

The combined strain of the elastic and plastic contribution is written as:

$$\varepsilon_{ij} = \varepsilon_{ij}^e + \varepsilon_{ij}^p \quad (141)$$

where  $\varepsilon_{ij}$  is the combined strain,  $\varepsilon_{ij}^e$  is the elastic contribution and  $\varepsilon_{ij}^p$  is the plastic contribution.

For the yield stress one uses:

$$\sigma_y = D_1 + D_2 \left( 1 - \exp \left( -\frac{\varepsilon_{eq}^p}{D_3} \right) \right) + P_1 C_s \quad (142)$$

where  $\sigma_y$  is the yield stress,  $\varepsilon_{eq}^p$  is the accumulated plastic strain,  $D_2$  and  $D_3$  are constants related to the work hardening curve, but are not strain-rate dependent,  $D_1$  is related to the initial yield stress and defined as:

$$D_1 = \sigma_y(0) - P_1 C_s \quad (143)$$

where  $P_1$  is a constant and  $C_s$  is the pinning solute concentration.

According to Wenman et al[1] the term  $P_1 C_s$  represents the pinning term in Equ.(142).

$C_s$  is defined as:

$$C_s = C_M (1 - \exp(-P_2 T_A^N (\varepsilon_{eq}^p)^\alpha)) \quad (144)$$

where  $P_2$ ,  $\alpha$  and  $N$  are constants,  $C_M$  is the maximum solute concentration and  $T_A$  is the ageing time and is governed by the following first order differential equation[1]:

$$\frac{dT_A}{dt} = 1 - \frac{T_A}{T_W} \quad (145)$$

where  $T_W$  is the time taken for the dislocation to traverse an obstacle(extrinsic). This is defined as:

$$T_W = \frac{\Omega}{\dot{\varepsilon}_{eq}^P} \quad (146)$$

where  $\Omega$  is the effective strain during interaction with obstacle, which is expressed in terms of constants  $\omega_1, \omega_2, \beta$  and plastic strain  $\varepsilon_{eq}^P$ :

$$\Omega = \omega_1 + \omega_2 (\varepsilon_{eq}^P)^\beta \quad (147)$$

and  $\dot{\varepsilon}_{eq}^P$  is the strain-rate defined as:

$$\dot{\varepsilon}_{eq}^p = \dot{\varepsilon}_0 \exp \left( \frac{\sigma_{Mises} - \sigma_y}{SRS} - P_1 C_s \right) \quad (148)$$

where  $\sigma_{Mises}$  is the Mises' stress and SRS is the instantaneous strain-rate sensitivity defined as:

$$SRS = S_1 + S_2(\varepsilon_{eq}^P)^{\frac{1}{2}} \quad (149)$$

Now that a description of the model has been presented, it will now be compared to the tensile data amassed from the tensile testing section and the data from the hole.

### 3.6 Summary

The dynamics of the Sun et al[8] model were revealed by showing that the form of the drag force, when equated to the driving force, produced similar equations as derived by Sun et al. This showed that they describe a steady state i.e. when the acceleration of the dislocations are zero. This model was then incorporated in the Orowan equation(Equ.(90)) and, with the aid of the Bergstrom equation to relate the dislocation density to the strain, an equation of motion was derived that was shown to have the key features of a sigmoidal equation and, therefore, inhomogeneous deformation. Predictions were made due to the nature of the sigmoidal function which will be tested against data in chapter 7, such as the maximum strain and strain-rate.

It was also shown by looking at the structure of the sigmoidal formula, it was possible to relate the Lüders strain to the dislocation density(see Equ.(121)). Equ.(123) from Vetter[47] and Balion et al[48] when substituted into Equ.(121), produced three equations that explicitly related the Lüders strain to the dislocation density, mean-free path and the grain-size. That is Equ.(124), Equ.(125) and Equ.(127).

Equ.(125) showed how a Lüders strain could still vary even if the carbon content is the same. This was attributed to the average mean free path  $S_0$ . The profile of the band was also calculated from knowing how the strain varied with time.

The Zhang model was also presented (contrasting with the simplistic model) and takes into consideration the number of carbon atmospheres coupled with the dislocation dynamics, as it emerged from Hahn[18]. It represents the main characteristics of the Lüders band and, therefore, will be chosen as the main model when comparing the tensile data.

### 3.7 Conclusion

- a) A unique parameter  $\phi$  has been identified from the data of Tsuchida et al[7] that has unique values for each carbon content of ferrite steel. This can then be applied to a stress-strain curve and a Lüders strain can be related to the carbon content.
- b) The dynamics of the Sun et al[8] model describe dislocations in steady-state.
- c) Equ.(71) adequately describes the magnitude of the Lüders strain as a function of carbon content for materials with similar micro-structures.
- d) If the function that describes the mean free-path of the dislocations is reversed to account for inhomogeneous deformation and when  $\omega = \Omega$  and substituted in the Bergstrom equation, the solution is that of Gilman's original equation.
- e) The factors that affect the Lüders strain in ferrite steels are the dislocation density, mean-free path and grain-size assuming the same composition(all elements). Therefore, it follows that if a material with the same composition is heat treated to produce a different micro-structure, then the Lüders strain should be different.
- f) The Zhang model is based on a yield drop model, but does contain the appropriate dynamics to allow for Lüders band. However, there seems to be no direct way of altering the Lüders strain and therefore, factor in the micro-structure.

## 4 Tensile testing

### 4.1 Introduction

The aim of the experiments was to determine how the distribution of carbides would affect the Lüders strain in ferritic steel with constant composition. Carbides with different morphologies were formed via different heat treatments, producing different micro-structures of the material. These micro-structures were ferrite/pearlite, a tempered martensite structure with the as-received structure as an upper bainitic structure, which shall be abbreviated to FP, TM and AR, respectively. The following strain-rates were used:  $\dot{\varepsilon} = 1 \times 10^{-2}$  to  $1 \times 10^{-4}\text{s}^{-1}$ , on each micro-structure.

The same tensile tests were done on a low carbon steel with an abundance of manganese sulphide particles present and an ultra low carbon with trace carbides, which shall be abbreviated to AL and UL, respectively.

The results discussions and conclusions are shown.

### 4.2 Materials and methods

AR is an RPV steel, supplied by Rolls Royce, AL is a low carbon steel with high sulphur and, therefore, manganese sulphide inclusions in clusters supplied as a cylinder(with texture) with 120mm diameter and 1 metre in length and UL is an ultra low carbon steel supplied in billet form at 75 mm<sup>2</sup> face and 1 metre in length.

Table 3: Chemical composition of elements in % wt

Material	C	Mn	N	P	S	Cr	Ni	Cu	Mo
AR	0.17	1.39	0.0093	0.006	0.002	0.14	0.79	0.054	0.56
AL	0.07	1.11	0.0025	0.059	0.312	0.06	0.03	0.02	0.01
UL	0.007	0.05	0.0037	0.003	0.007	0.006	0.17	0.008	0.001

The AR steel went through the following heat treatments to achieve the following micro-structures.

Ferrite-Pearlite structure(FP):

1. Heated at 900<sup>0</sup> C for 30-35 mins
2. Furnace cooled for 24 hours. The resulting material exhibited a hardness 170Hv and the micro-structure was verified by optical microscopy.

Table 4: A summary of the materials and expected micro-structures

Structure	Heat-treatment	Micro-structure
AR	N	Upper-bainite*
FP	Y	Ferrite/pearlite
TM	Y	Tempered martensite•
AL	N	Ferrite/Pearlite <sup>b</sup>
UL	N	Ferrite*

\* Normalised

• With spheroidised carbides

<sup>b</sup> With texture

\* Trace carbon

Upper Bainite(AR): The as-received material was an upper bainitic with a grain-size of  $10 \mu\text{m}$  and a hardness of 227Hv. The hardness, in conjunction with optical and Scanning electron microscopy work, see[52], confirmed the upper bainitic structure.

#### Tempered martensite(TM):

1. Heated at  $900^0 \text{ C}$  for 30-35 mins
2. Water quenched
3. Tempered at  $650^0 \text{ C}$  for 5, 24, 48, 96, 120, 144, 168 and 192hrs

UL and AL structure were hot worked(industrial process unknown) and air cooled with a average grain-size of  $35\mu\text{m}$  and  $40\mu\text{m}$  ,respectively, with pearlitic carbides.



Figure 30: Picture of double-shoulder specimen with a 35mm gauge length.

#### 4.2.1 Specimen geometry

Specimens were cut using an electric discharge machine(EDM), with copper based brass wire is  $250\mu\text{m}$  in diameter, cutting out double-shoulder “dog-bone” design, with 35 mm gauge length, 4mm gauge width, 5mm thickness and a total length of 64mm length, as shown in Fig.30.

#### 4.2.2 Hardness

The hardness was measured using a standard Buehler Vickers hardness machine with 20kg load. Five points were randomly made on blocks that had the same heat treatments as the specimens and then the average value was taken.

Table 5: The hardness of AR FP and TM at 650C

Structure	Time(hours)	Hardness(Vickers)	$\sigma_{lyp}^*$
AR	N/A	217	487
FP	N/A	173	420
TM	5	228	627
TM	120		543
TM	144	192	446
TM	168	162	406
TM	192	138	373

\* At  $\dot{\varepsilon} = 1 \times 10^{-2} \text{ s}^{-1}$  and the yield stress was rounded to the nearest whole number and calculated using Equ.(150)

### 4.3 Procedure

- 1 The specimens were cut out using an electric discharge machine or an EDM, manually polished with 120 grit size silicon carbide paper, auto polished with 250 grit size for 10 mins, depending on the finish, then spray painted using standard Mat-black(non-gloss) and Primer white paint to achieve a speckle pattern finish.
- 2 The specimens were placed in two En24 steel grips(which were also cut from the EDM) and strained uni-axially with a Denison 100kN hydraulic machine in displacement control.
- 3 The strain displacements were recorded using two 5 mega-pixel cameras on Istra 4.D Dantec Digital Image Correlation software with maximum frame rate of 10 frames per-second, in order to track the speckle pattern.  
The stress was measured from analogue channels fed from the Hydraulic machine into the DIC, at the desired strain-rates.
- 4 The data is in the form of an image (see Fig.(31)), then a mask or polygon is mapped over the image and the average strain is calculated across the whole gauge area. The average strain calculated from the mask is taken as the engineering strain and is then substituted into Equ.(150) and Equ.(151) to produce a stress-strain graph, from which

the tensile properties are calculated (see appendix A).

- 5 The local strain is also calculated with the y-component in the tensile direction and the x-component in the compressive direction, during uniaxial tension.

### Digital Image Correlation

The DIC uses pattern recognition software that follows the painted speckles on the specimens and calculates the strain accordingly, as shown in Fig.(31).

The displacement and the force were fed from the hydraulic machine<sup>13</sup>, which were then converted into the true stress and strain, respectively, from the R6 procedure[2]:

$$\sigma_T = \sigma_{eng}(1 + \varepsilon_{eng}) \quad (150)$$

and

$$\varepsilon_T = \ln(1 + \varepsilon_{eng}) \quad (151)$$

where  $\sigma_T$  is the true stress,  $\varepsilon_T$  is the true strain,  $\sigma_{eng}$  and  $\varepsilon_{eng}$  are the engineering stress and strain.

---

<sup>13</sup>The details of which are found in appendix C.

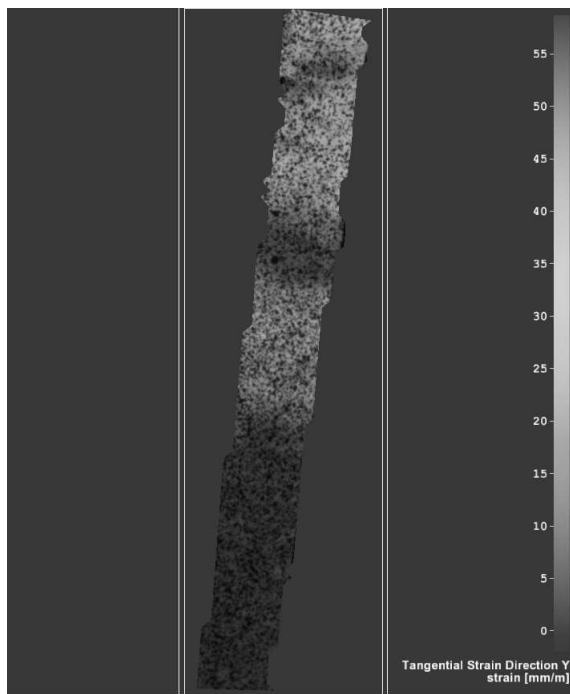


Figure 31: Speckled specimen superimposed over the image generated from the DIC.

#### 4.4 Exponents

It is usual in tensile experiments to measure the following parameters, post yielding. They are the strain-rate sensitivity exponent  $m$  and the stress-rate exponent  $n$ . However, following the method of Sun et al[8] the parameters will be measured at the end of the Lüders strain or when the material has strained a value of  $\varepsilon_L$  at the stress at which inhomogeneous deformation ends and homogeneous deformation begins. Although the value of the exponents should be the same as if measured during homogeneous deformation, as the definition of the Lüders strain is a measure of how long inhomogeneous deformation occurs[44], this only applies to idealised Lüders bands and, consequently, even when the the material has strained the value of  $\varepsilon_L$  there will still be a degree of inhomogeneous deformation.

The tacit assumption made by Sun et al[8] that the calculated values for the aforementioned parameters is representative of the material are incorrect as it assumes inhomogeneous deformation has ceased at the Lüders strain. However, the parameters will give an insight into the nature of the micro-structures, especially for the structures that have the same composition.

The following equations will be used to calculate  $m$  and  $n$ :

$$m = \frac{d \ln(\sigma_{lyp})}{d \ln(\dot{\varepsilon})} \quad (152)$$

$$n = \left( \frac{1 - \frac{d \ln(\varepsilon_L)}{d \ln(\dot{\varepsilon})}}{m} \right) \quad (153)$$

as derived by Sun et al[8].

The parameters in Equ.(152) and Equ.(153) are calculated from stress vs strain-rate and Lüders strain vs strain-rate plots. Tsuchida et al[32] used a standard power-law known as the Holoman parameters to model stress vs strain for homogeneous deformation and applied it to stress vs Lüders strain plots for different grain-sizes and strain-rates. It was shown that the data fitted a power-law whose exponent was denoted as  $u$ . However, there was no explicit relation for  $u$  and therefore no theoretical basis other than the analysis obtained from the numerical values.

It was shown that  $u$  could be calculated from the above parameters by combining the model of Sun et al[8] and Tsuchida et al[7], as shown in the literature review. This has added another equation for  $u$  and a third parameter that will be calculated from the following equation:

$$u = \frac{m}{1 - mn} \quad (154)$$

The physical interpretation of  $u$  will be discussed in section 4.6.

## 4.5 Results

The results presented in this section are:

- Fig.(32) and Fig.(33) show the effect of increasing carbon content on the Lüders strain and the lower yield stress, for all materials in ferrite-pearlite form, as a function of strain-rate.  
The AR and TM structure have been neglected as their micro-structures are upper-bainite and tempered martensite.
- Fig.(34) and Fig.(35) show the effect of heat treatment on the Lüders strain and lower yield stress as a function of strain-rate for all three micro-structures of the RPV steel. That is, AR, FP and TM with the latter having two plots to illustrate the effect of Lüders strain as a function of tempering time. It is evident that it decreases with increasing tempering time.
- Fig.(36) to Fig.(41) show the materials that had positive correlation with both the Lüders strain and lower yield stress as a function of strain-rate, as expected from the literature[8].

- Table 6 shows the calculated values of the exponents  $m$ ,  $n$  and  $u$ .  
The number within the parenthesis represent doubtful results.
- Equ.(155) and Equ.(156) represent the formulae used to calculate  $m$  and  $n$  and Equ.(157) for the exponent  $u$ .

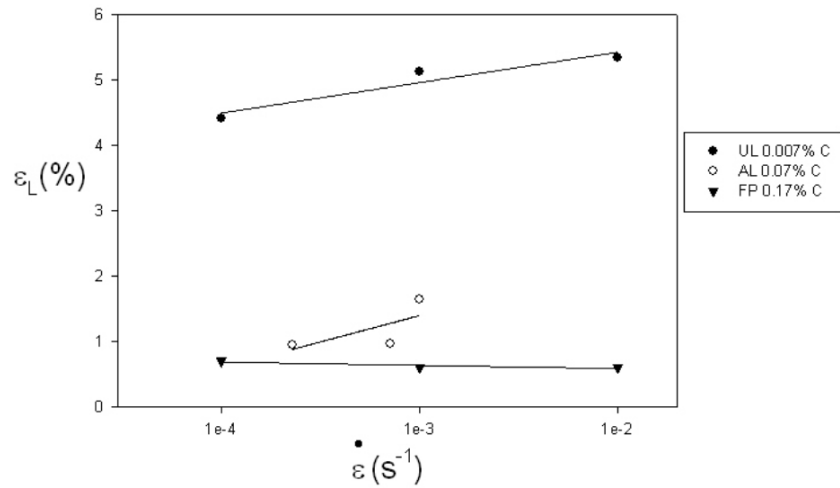


Figure 32: Effect of carbon content on Lüders strain(UL,AL,FP).

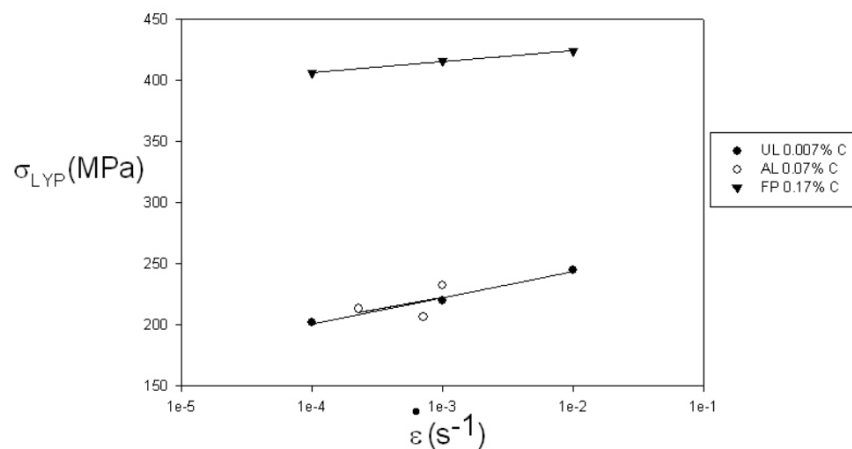


Figure 33: Effect of carbon content on lower yield strength(UL,AL,FP).

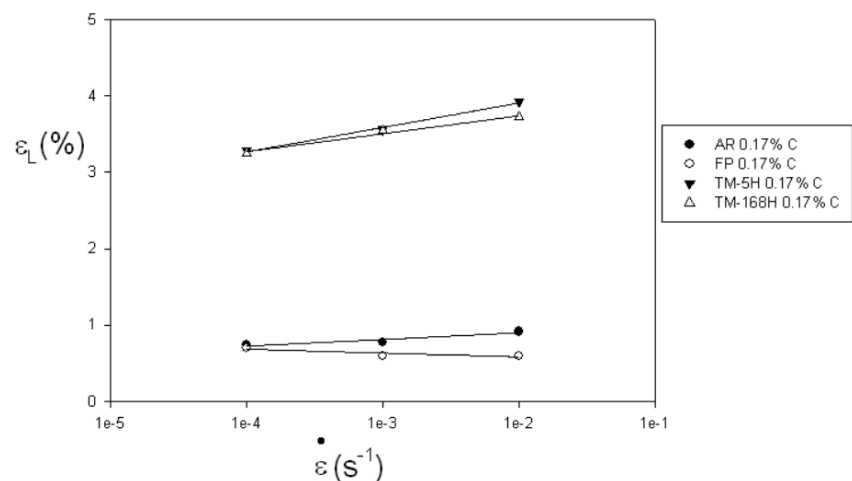


Figure 34: Effect of heat treatment on RPV steel on Lüders strain(AR,FP,TM-5H,TM-168H).

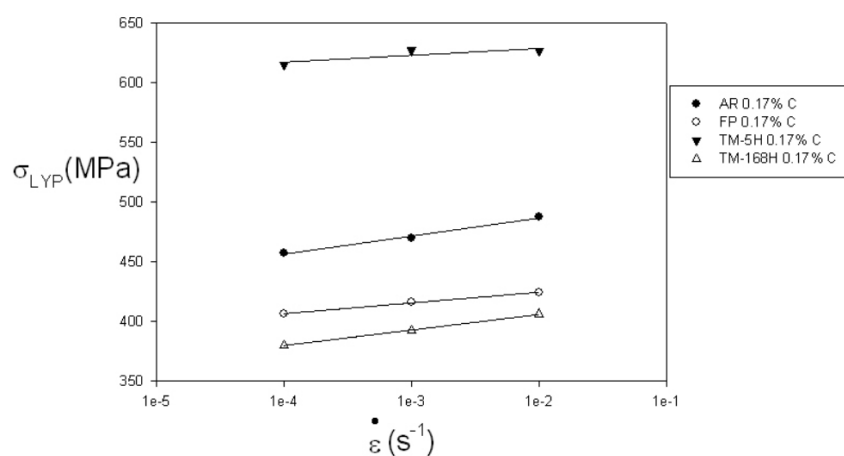


Figure 35: Effect of heat treatment on RPV steel on lower yield stress(AR,FP,TM-5H,TM-168H).

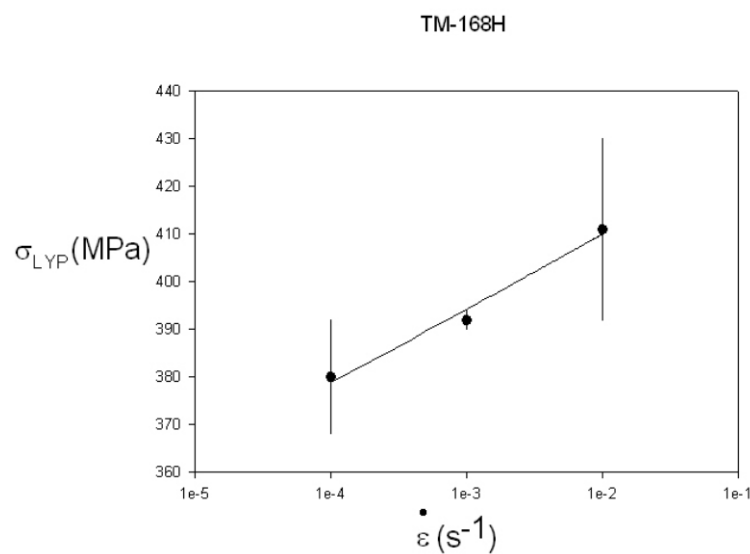


Figure 36: The spread of data of the lower yield stress at strain-rates:  $1 \times 10^{-2}$ ,  $1 \times 10^{-3}$  and  $1 \times 10^{-4} s^{-1}$  of TM-168H structure.

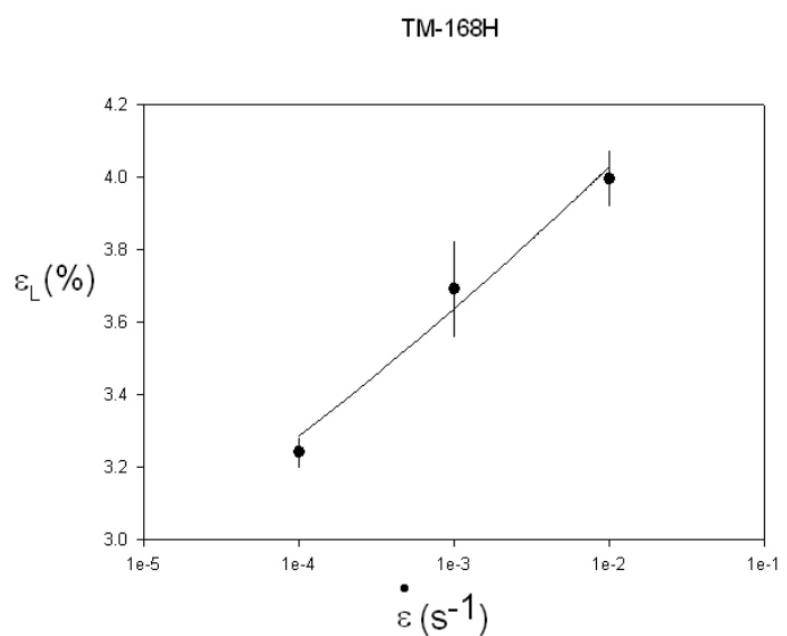


Figure 37: The spread of data of the Lüders strain at strain-rates:  $1 \times 10^{-2}$ ,  $1 \times 10^{-3}$  and  $1 \times 10^{-4}s^{-1}$  of TM-168H structure.

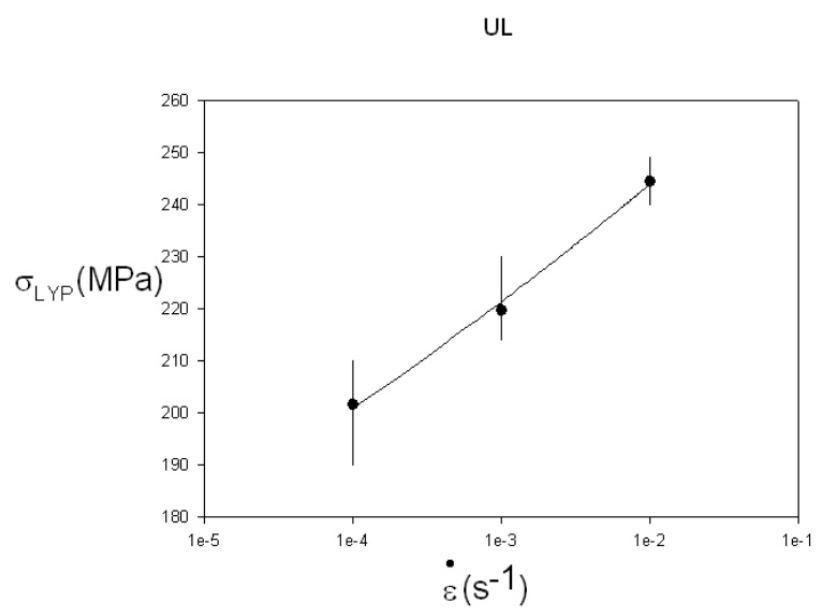


Figure 38: The spread of data of the lower yield stress at strain-rates:  $1 \times 10^{-2}$ ,  $1 \times 10^{-3}$  and  $1 \times 10^{-4}\text{s}^{-1}$  of UL structure.

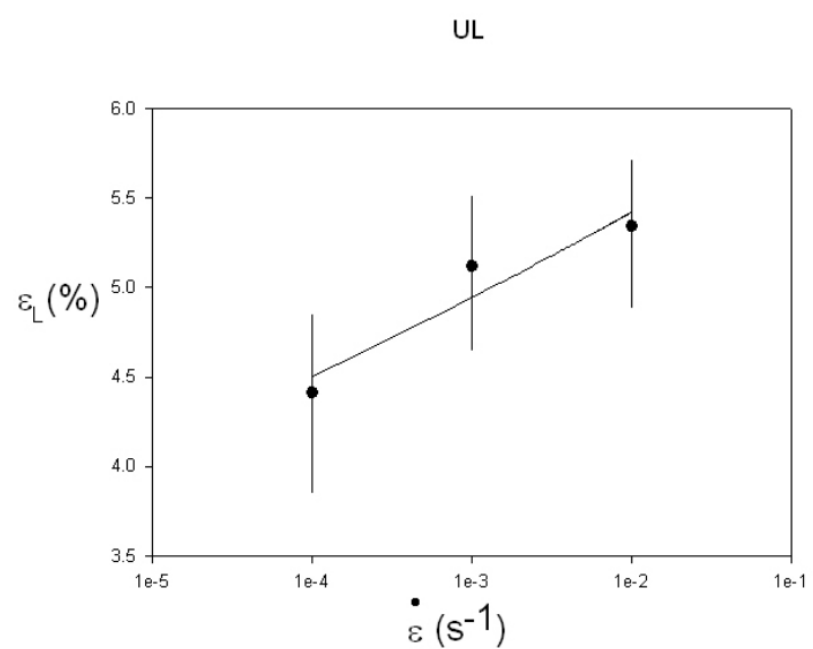


Figure 39: The spread of data of Lüders strain at strain-rates:  $1 \times 10^{-2}$ ,  $1 \times 10^{-3}$  and  $1 \times 10^{-4} s^{-1}$  of UL structure.

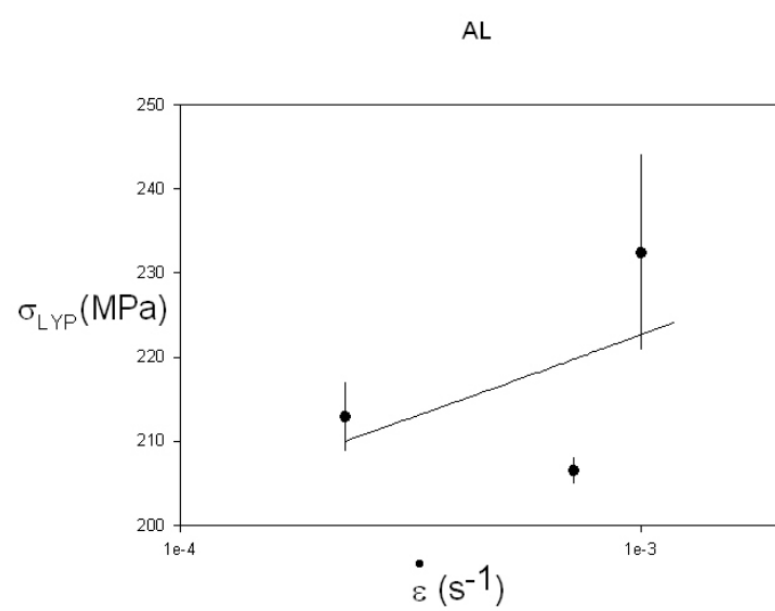


Figure 40: The spread of data of the lower yield stress at strain-rates:  $1 \times 10^{-3}$ ,  $7.14 \times 10^{-4}$  and  $2.28 \times 10^{-4} s^{-1}$  of AL structure.

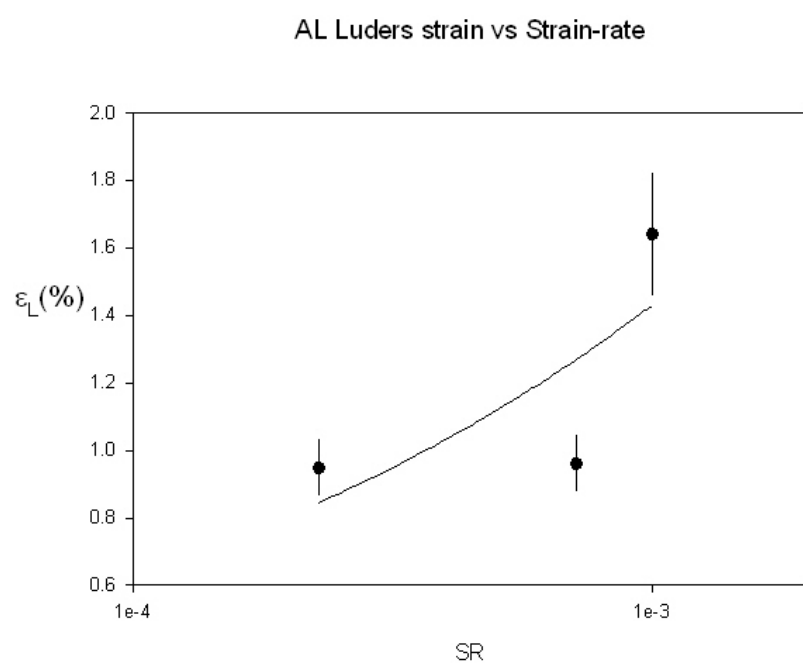


Figure 41: The spread of data of the Lüders strain at strain-rates:  $1 \times 10^{-3}$ ,  $7.14 \times 10^{-4}$  and  $2.28 \times 10^{-4} \text{ s}^{-1}$  of AL structure.

The corresponding values of  $m$ ,  $n$  and  $u$  were calculated from the figures, using the following formulae:

$$m = \frac{d \ln(\sigma_{lyp})}{d \ln(\dot{\varepsilon})} \quad (155)$$

$$n = \left( \frac{1 - \frac{d \ln(\varepsilon_L)}{d \ln(\dot{\varepsilon})}}{m} \right) \quad (156)$$

and

$$u = \frac{m}{1 - mn} \quad (157)$$

with the results shown in table 6.

Table 6: Strain-rate sensitivity( $m$ ) and stress-rate exponent( $n$ ) and  $u$  of AR, TM-5H, TM-120H, TM-144H, TM-168H, UL and AL.

Carbon(%)	Structure	$m$	$n$	$u$
0.17	AR	$1.344 \times 10^{-2}$	70.83	0.28
0.17	FP	$4.1 \times 10^{-3}$	N/A	
0.17	TM-5H	$4.023 \times 10^{-3}$	(237.30)	0.089
0.17	TM-120H	$(-1 \times 10^{-3})$	(-982)	(-0.06)
0.17	TM-144H	$(-3.7 \times 10^{-2})$	(-27.5)	(2)
0.17	TM-168H	$1.71 \times 10^{-2}$	55.59	0.38
0.007	UL	$4.22 \times 10^{-2}$	22.74	1.05
0.07	AL	$3.96 \times 10^{-2}$	16.27	0.11

## 4.6 Discussion

The Lüders strain and lower yield stress increased with increasing strain-rate, as shown in Fig.(32) and Fig.(33) for the ferrite-pearlite structures of UL and AL. This is in agreement with data predicted in the literature[8]. However, the trend was less evident for the FP structure. Only the lower yield stress of the FP structure increased with strain-rate. This is better seen, when looking at the effect of heat treatment on the RPV steel of AR, TM and FP on Fig.(34) and Fig.(35). The Lüders strain did not correlate as well(for the FP) with the strain-rate as the upper-bainite and some of the tempered martensite, because there was evidence of work-hardening within

the Lüders band(shown as an inclined plateau on the stress-strain curve) of the ferrite-pearlite structure. Consequently, the form of the Lüders strain was not as prominent as the upper-bainite and tempered martensite structure.

In Fig.(32) the magnitude of the Lüders strain decreases with increasing carbon content. This agrees with data presented in the literature, as discussed in the literature review under carbon content section 2.4.1. The difference in Lüders strain between micro-structures of the RPV steel is evident(see Fig.(34)). However, the difference only becomes noticeable, when comparing the tempered martensite structure to the ferrite-pearlite and upper bainite structure, as the difference in Lüders strain of the latter two structures(FP and AR) is small. Therefore, a clear dependency between the Lüders strain and the micro-structure with the same composition is evident.

Multiple banding was evident in all of the materials. The standard way of dealing with multiple banding is to divide Lüders strain by the number of bands[53]. However, as shown in table 7, dividing by the number of bands does not reflect the strain in each band. Using digital image correlation or D.I.C software, it was possible to calculate the local strain of the Lüders band at the stress of nucleation as shown in Fig.(42). The result of which is shown as a strain-time(frame number) curve. It is evident, from table 7, that the maximum strain at the peak of the sigmoidal curve is not reduced. In fact, the contrary is more evident. The values of the strain in the first and second band at the beginning of nucleation are greater than the Lüders strain for the AR, TM and UL materials. This shows that dividing by the number of bands does not reflect the localised strain of the bands. Therefore, the relationship:

$$\varepsilon_L = \frac{v_m}{v_L} \quad (158)$$

should be used to measure the Lüders strain and the band velocity irrespective of the number of bands nucleated.

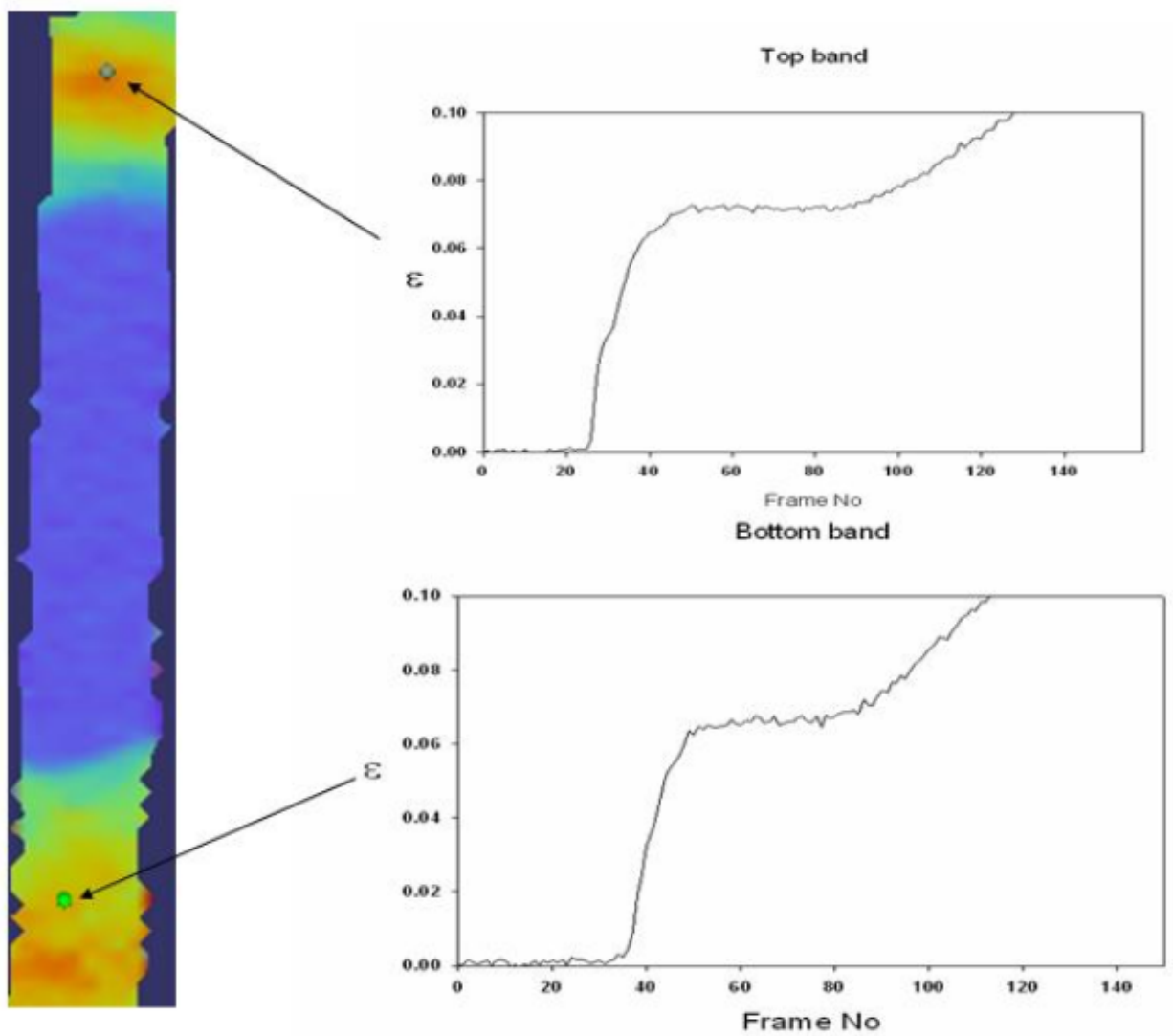


Figure 42: 2 band nucleation using D.I.C software on UL specimen, with the bottom band nucleating first followed by the top band. The local Lüders strain on the top and bottom band are 6.5% and 7%, respectively.

## $\varepsilon_L$ vs Temp time of TM

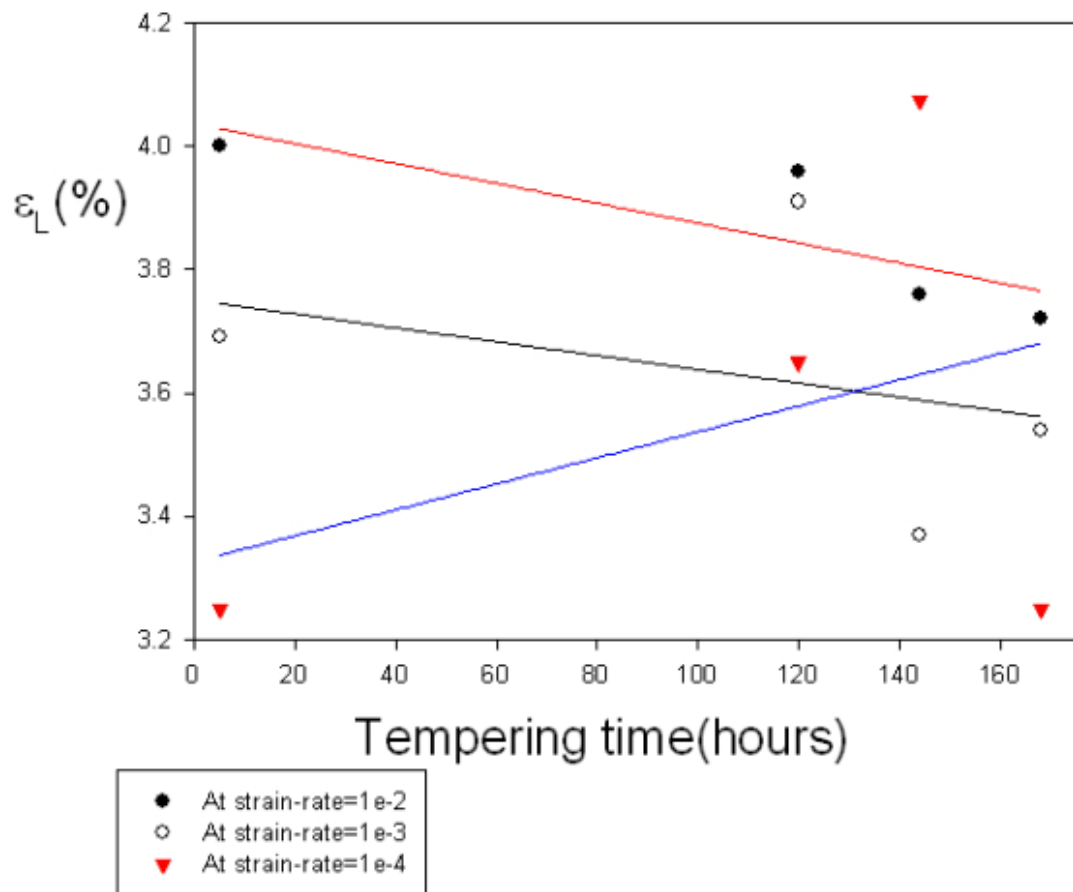


Figure 43: Lüders strain against the tempering time at strain-rates  $1 \times 10^{-2}$   $1 \times 10^{-4} \text{ s}^{-1}$ , where the lines are there purely for illustration to show the trend of the data for each tempering time and are not regression lines.

Table 7: Two band nucleation for the AR, TM-144H and structure at  $\dot{\varepsilon}=1\times 10^{-2} \text{ s}^{-1}$  with  $\varepsilon_f = \frac{\varepsilon_L}{2}$

Structure	Band1(local $\varepsilon_L$ (%))	Band2(local $\varepsilon_L$ (%))	global ( $\varepsilon_L$ )	$\varepsilon_f$
AR-6	1.34	1.33	0.9	0.45
TM144H-2	4.55	4.12	3.47	1.74
UL-3	7.32	6.4	5.52	2.76

The lower yield stress increases with strain-rate for AR, TM-5H, TM-168H, UL and AL(Fig.(35), Fig.(36), Fig.(38) and Fig.(40)), which confirms Hahn's relation of Equ.(53).

The lower yield stress increased with carbon content. Although this is expected as discussed in the literature review, this trend is not as conclusive when comparing the AL steel and the UL steel, despite the former having ten times more carbon content than the latter.

The lower yield stress in the ferrite-pearlite structure of the RPV steel was almost indistinguishable from the upper yield stress(see, table 18, appendix A)) for  $\dot{\varepsilon} = 1 \times 10^{-2} \text{ s}^{-1}$  and to a lesser extent with the lower strain-rates.

It was mentioned in this section, the FP structure during band propagation showed evidence to suggest work hardening was taking place during the propagation of the Lüders band, shown as an inclined plateau. As a result, even when the band began to nucleate, localised homogeneous deformation was taking place, making it difficult to determine precisely when the Lüders band first nucleated and, therefore, the value of the lower yield stress. However, the lower yield stress of the FP structure became more prominent, as the strain-rate decreased. The AR structure also showed evidence of work-hardening during band propagation, although to a lesser extent compared to FP.

The tempered martensite structure behaved similarly to UL steel, by maintaining a reasonably flat plateau during band propagation. As a result, as shown in tables 19-22 of appendix A for the tempered martensite, the upper and lower yield stress were distinguishable and thus easier to determine when the band nucleated. However, not all of the structures obeyed Equ.(53), especially TM-144H, because the value of  $m$  and  $n$  are negative.

The Lüders strain in the tempered martensite decreases as a function of tempering time, generally, for all strain-rates as shown in Fig.(43). This is due to the effect of the increase amount of spheroidized carbides with tempering time. As the material is tempered the dislocation within the

laths rearrange themselves due to the minimization of the surface energy of the material and the production of ferrite grains and spheroidized precipitates. Consequently, the dislocation density as a function of tempering times decreases[54]. As the Lüders strain is related to the dislocation density(see chapter 3), this results in the reduction in Lüders strain.

In table 6 the values calculated for the exponents of TM-120H and TM-144H are surrounded in parenthesis to indicate the doubtful nature of the results. The results are doubtful, because they give negative values for both the strain-sensitivity  $m$  and the stress-rate sensitivity  $n$  and of  $u$  for TM-120H. Although, a negative  $m$  can occur for serrated plateaus or what is prosaically called blue brittle failure, it only occurs at temperatures where the diffusion of the carbon atmospheres is comparable to the dislocation velocity, and as a serrated plateau for the aforementioned tempered martensite structures was not observed and the experiments were conducted at room temperature, below the activation energy of carbon or when the diffusion of carbon is negligible, the results for  $m$  and  $n$  are attributed to the specimens themselves and the sample size. In other words, if more experiments were done,  $m$  and  $n$  should be positive.

The trend in  $m$  could be attributed to the increase in pearlite content with increasing carbon content and the corresponding effects this has on the dislocations and the glide planes. However, the work of Lee et al[55] when looking at the  $m$  as a function of strain-rate for 0.15%, 0.48% and 1.16% carbon steel showed that  $m$  varied almost negligibly with constant strain-rate. Therefore, according to Lee et al[55] despite the large contrast between micro-structures there was negligible dependence of  $m$  on the carbon content, but this occurred for materials that did not exhibit Lüders strain and, consequently, for homogeneous deformation only. In the results in table 6, for  $m$ , show noticeable variation in micro-structure, indicating a micro-structural dependence during inhomogeneous deformation, although further experiments are required. The difference in  $m$  in the as-received RPV steel, for the upper-bainite and ferrite-pearlite structure, is attributed to the different forms of the carbides i.e a fine cementite laths in the upper bainite and coarse iron carbide lammellae in the ferrite-pearlite, but also it could be attributed to the number of, as according to Hahn[18], the higher the initial number of free dislocations the less distinguishable the upper and lower yield stress (see Fig.(19)).

The tempered structure has a higher Lüders strain than the ferrite-pearlite structure and the upper-banite structure with evidence of spheroidised

particles on the grain-boundaries, verified through optical micrograph. This is due to the re-crystallization of the grains from its original martensite form, resulting in the precipitation of carbides on the grain-boundary or to areas of high potential[54]. This trend also agrees with the work of Samuel et al[56], who showed a similar trend of the strain-rate sensitivity for the three structures.

$n$  is expected to increase with carbon content, which is observed in table 6. A method of demonstrating this trend is to consider the standard equation, due to Johnston and Gilman, that relates the velocity of the dislocation to the upper and lower yield stress.

Hahn[18] showed experimentally that the speed of a Lüders band can be related to the dislocation speed, by the following relation:

$$v_l = s v_d \quad (159)$$

where  $v_l$  is the Lüders band velocity,  $s$  is a constant and  $v_d$  is the dislocation velocity.

The speed of a dislocation is related to the yield stress as:

$$v_d = \left( \frac{\sigma_{uyp}}{\sigma_{lyp}} \right)^n \quad (160)$$

or

$$\frac{v_l}{s} = \left( \frac{\sigma_{uyp}}{\sigma_{lyp}} \right)^n \quad (161)$$

Taking the natural log,  $n$  becomes:

$$n = \frac{\ln \left( \frac{v_l}{s} \right)}{\ln \left( \frac{\sigma_{uyp}}{\sigma_{lyp}} \right)} \quad (162)$$

Let  $n_1$  be the stress-rate exponent for a low carbon steel and let  $n_2$  be the stress-rate exponent for a steel with higher carbon content. Dividing  $n_1$  and  $n_2$  gives:

$$\frac{n_1}{n_2} = \left( \frac{\ln \left( \frac{v_{l1}}{s} \right)}{\ln \left( \frac{v_{l2}}{s} \right)} \right) \frac{\ln \left( \frac{\sigma_{uyp2}}{\sigma_{lyp2}} \right)}{\ln \left( \frac{\sigma_{uyp1}}{\sigma_{lyp1}} \right)} \quad (163)$$

Equ.(163) shows that if the difference in band velocity is small compared to the difference in upper and lower yield strength, then the value of  $n$  is

determined by the yield stresses only<sup>14</sup>. Therefore, as  $n_2$  has a higher carbon content than  $n_1$  it follows that the difference in magnitude between upper and lower yield stress of  $n_2$  should be less than the difference of  $n_1$ . That is:

$$\frac{n_1}{n_2} < 1 \quad (164)$$

or

$$n_2 > n_1 \quad (165)$$

This trend is observed as  $n$  increases as a function of carbon content as shown in table 6.

The same argument is difficult to apply to materials with the same carbon content, that is the tempered and upper-bainitic structure, because the carbon content does not play as a dominant part in the magnitude of the Lüders strain as it does in materials with differing carbon content. Although, as it has been demonstrated, the morphology of the carbides affects the Lüders strain.

There is a clear difference of  $n$  between the structures, e.g. TM5H,  $n = 237$ . However, more values from the different tempering times are needed before a definite correlation can be determined. Also the value of  $n$  for the tempered structure of TM5H is quite unrealistic, due to the amount of scatter present on the gradient between the Lüders strain and strain-rate, as only two tensile tests were done for each strain-rate. However, as discussed in the previous paragraph, the trend of an increasing  $n$  with carbon content is nonetheless maintained.

The value of  $u$ , the strain-hardening exponent, was calculated from the derived values of  $m$  and  $n$ . The trend of  $u$  seemed to follow that value of  $m$ . This is to be expected, at least mathematically, from Equ.(157) i.e. for small  $m$  such that  $m \ll 1$ , then  $u \approx m$ .

## 4.7 Conclusion

- a) Lüders strain as a function of micro-structure for materials with the same composition increases from ferrite-pearlite structure(least) to tempered martensite structure(most). Evidence from the observations suggest that not only the carbon content affects the Lüders strain, but

---

<sup>14</sup> $n_1$  and  $n_2$  are assumed to be greater than zero

also the form of the carbides. More specifically, the spherodized iron carbides on the ferrite grain-boundaries produce a higher Lüders strain than the upper bainite and ferrite-pearlite structure. This is due to how the carbides are formed from the martensite during tempering. As the diffusion of the old carbide to form new carbides at regions of high potential, such as dislocations and grain-boundary, this increases the amount of pinning, which leads to a higher upper and lower yield stress than the upper-bainite and ferrite-pearlite structure, whilst reducing the dislocation mean free-path. The tempered structure has a greater Lüders strain, due to the larger dislocation density and smaller grain-size. Consequently, a tempered martensite structure can be as strong as a bainite structure, but have a greater ductility with a larger Lüders strain.

An application of such a possibility, using tempered steel, is to fusion reactors, subject to satisfactory fracture toughness properties[57].

- b) It has been demonstrated that Lüders strain varies as a function of strain-rate in a manner that obeys Equ.(47) and, therefore, agrees with Sun et al[8] equations.

The Lüders strain increases as a function of strain-rate as shown from the UL steel(see Fig.(39)). Having a carbon content of 0.007%, in terms of the dislocation mean free-path, there is little that can impede the motion of the dislocations. Consequently, the only factor that affects the dislocations and can contribute to the Lüders strain is the dislocation density and the rate of dislocation multiplication. It follows that the higher the strain-rate, the higher the release of free dislocation, the higher the yield stress and, therefore, the higher the Lüders strain.

When the amount of carbon increases to 0.17% and the carbides are in an upper-bainite form, although work-hardening occurs during the propagation of the band, the dislocation dynamics as described in the UL carbon material are still maintained. Because they both obey Sun's equations(see Equ.(78) and Equ.(79)), which according to the chapter 3 describe dislocation motion in steady state. It is only when the form of the carbide was in ferrite-pearlite form that the Lüders band was less defined.

- c) The treatment of multiple bands showed that, using DIC, dividing the measured Lüders strain by the number of bands was inadequate

to describe the local strain or Lüders strain upon nucleation, as the value of the strains of each band at nucleation was closer to the overall Lüders strain. Therefore, if multiple banding occurs, treating the resulting Lüders strain as a single band is more representative of the localised strain of the bands than dividing the Lüders strain by the number of bands and using the calculated value as representative of the strains in the material.

- d) The values of  $m$ ,  $n$  and the strain-hardening exponent  $u$  were shown to confirm the relationships of Hahn and Sun et al[8].

$m$  is the gradient of the lower yield stress versus the strain-rate and this agreed with the findings of Sun et al[8], that the value of  $m$  decreases with carbon content.

The value of  $n$ , although not as reliable as  $m$  as there was a lot of scatter, due to the gradient of the Lüders strain and strain-rate, still agreed with the model of Johnston and Gilman that a material with a larger carbon content will have a larger  $n$ .

The value of  $u$  also agreed with data taken from Tsuchida et al[7] and Samuel et al[56], although the latter's work was calculated outside the Lüders range.

- e) The overall effect of the ferrite matrix and each morphology of the carbides showed that a pure ferrite matrix with trace amounts of iron-carbide on the grain will produce an elongated Lüders strain, depending on the strain-rate for a fixed grain-size.

The FP structure of the RPV steel forms a Lüders band that has evidence of work-hardening occurring during band propagation. This is attributed to the simultaneous, high dislocation motion during the movement of the band[58]. Consequently, a ferrite-pearlite structure reduces the effect of discontinuous yielding.

The carbides in the upper-bainite form, fine cementite laths, also shorten the Lüders strain with less work hardening, thus promoting a more continuous band than the ferrite-pearlite structure, but with similar Lüders strain.

The effect of the carbides in spheroidized form lengthens the Lüders band to percentages comparable to the Lüders strain in the ultra low carbon

steel. This is due to the increased dislocation population of tempered martensite compared to its bainite and ferrite counter parts. The increase in dislocation population also results in greater pinning, not only due to the Cottrell pinning, but also attributed to the migration of the carbides to regions of high potential during tempering through void base diffusion. In the process, this relieves the surface tension of the material with the formation of new ferrite grains, also known as recrystallisation process[59].

## 5 Tensile experiment with defect

This section is an extension of the tensile experiment chapter, and following the work of Wenman et al[1] and Zhang et al[6], looking at Lüders bands under biaxial stress conditions.

The work by SINTAP[2] showed that the nucleation of a Lüders band is affected by the thickness of the specimen used. It was also concluded that where Lüders bands occurred in localised regions of large structures, they could be neglected.

The work from SINTAP did not offer any insight as to the optimum configuration of a Lüders band for a structure. Although, according to their findings a thicker material would lessen the effect of Lüders bands, there was no definite threshold and, more importantly, thicker materials can result in greater cost. Therefore, with the dimensions of the thickness of the tensile specimen, holes that were small compared to the size of the gauge length were drilled to determine the effects on a Lüders band that is not confined to the surface but throughout the volume.

Another motivation was to test the versatility of the Zhang model that will be addressed in the modelling chapter and also test the formula derived in appendix C, which showed that the displacement vs load data from the analogue channels that relayed to the DIC could be modelled as a spring system in series. That is:

$$t_y = \frac{\sigma_p}{v} \left( A \left( \frac{1}{k_1} + \frac{1}{k_2} \right) + \frac{l_0}{E} \right) \quad (166)$$

where  $t_y$  is the yield time,  $\sigma_p$  is the proof stress,  $A$  is the cross-sectional area,  $v$  is the cross-head velocity,  $k_1$  is the spring constant of the hydraulic machine,  $k_2$  is the constant measured from the DIC,  $l_0$  is the gauge length and  $E$  is Young's modulus.

### 5.1 Method

A TM-28H or tempered martensite for 28 hours was chosen alongside TM-168H. The tempered structure was chosen, because on average they exhibited the largest Lüders strain of the low alloy RPV steel out of the three microstructures and also to determine whether an increase in volume fraction of spheroidized particles from TM-28H to TM-168H would affect the chances of nucleation of a Lüders band.

A hole of approximate 1.5mm diameter was drilled into the TM-28H steel and 1mm diameter hole was drilled in to the TM-168H steel to look at the effects of reducing the hole size.

The strain-rates at  $1 \times 10^{-3} \text{ s}^{-1}$  initially for the TM-28H, then changed to  $1 \times 10^{-4} \text{ s}^{-1}$  for the TM-168H in order to determine the effect on strain-rate.

The materials were strained with the same equipment as the other tensile experiments.

## 5.2 Results

The following figures show the images taken by the DIC after processing of the images. Fig.(44) shows four points around the circular defect. Of the four points around the circle, two are shown graphically; The two right hand points, point 1 and point 2, as seen in Fig.(45) and Fig.(46), showing no Lüders banding. To see graph of Lüders banding see Fig.(49).

Fig.(47) shows the corresponding stress-strain curve of TM-28H and TM-168H materials, with gauge length of 34mm.

The spatial distribution of local strain across the hole and the gauge width of 4mm and is shown in Fig.(48).

A table showing the predicted time of yield, using Equ.(166) and the actual time is shown in table 8.

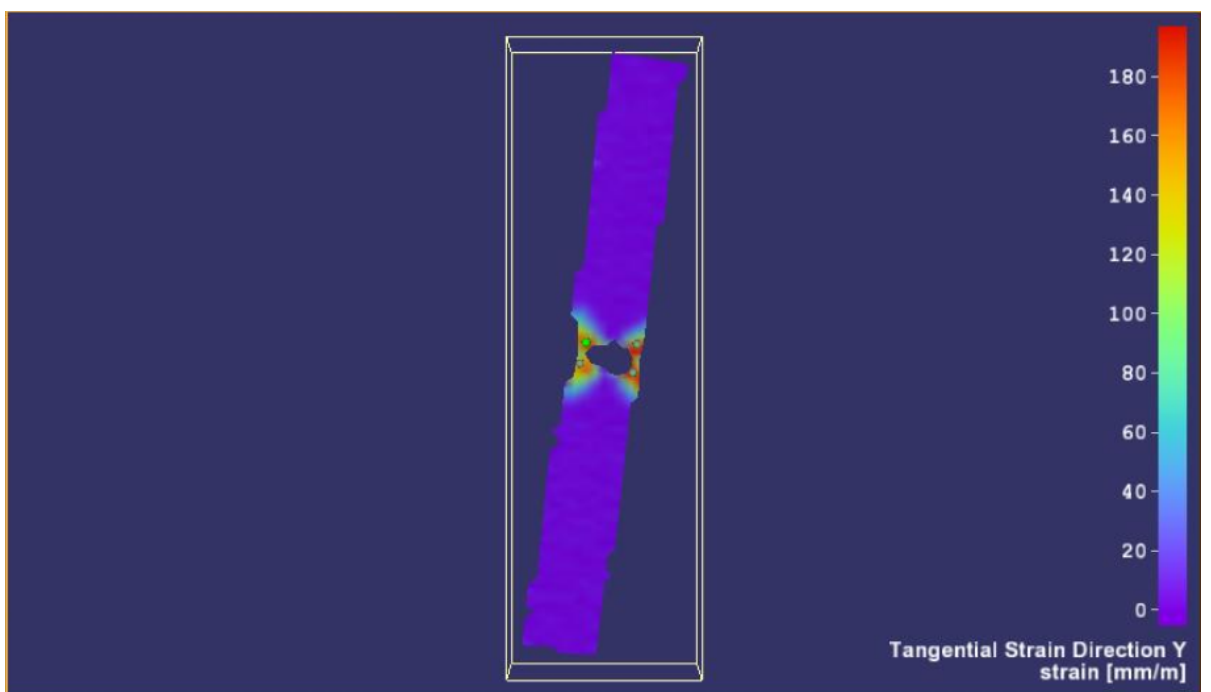


Figure 44: 1.5mm TM-28H hole of tensile specimen taken from the DIC. Points 1, 2, 3 and 4 are clockwise, starting from the top right.

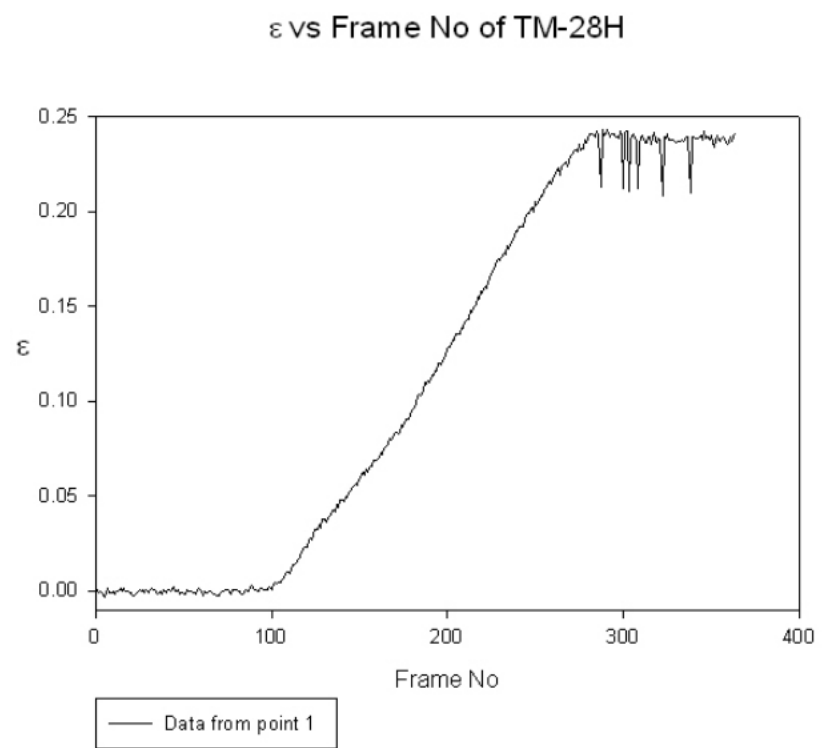


Figure 45: Strain vs Frame number taken from point 1 (top right of circle surrounding the hole of Fig.(44)) indicating no Lüders band.

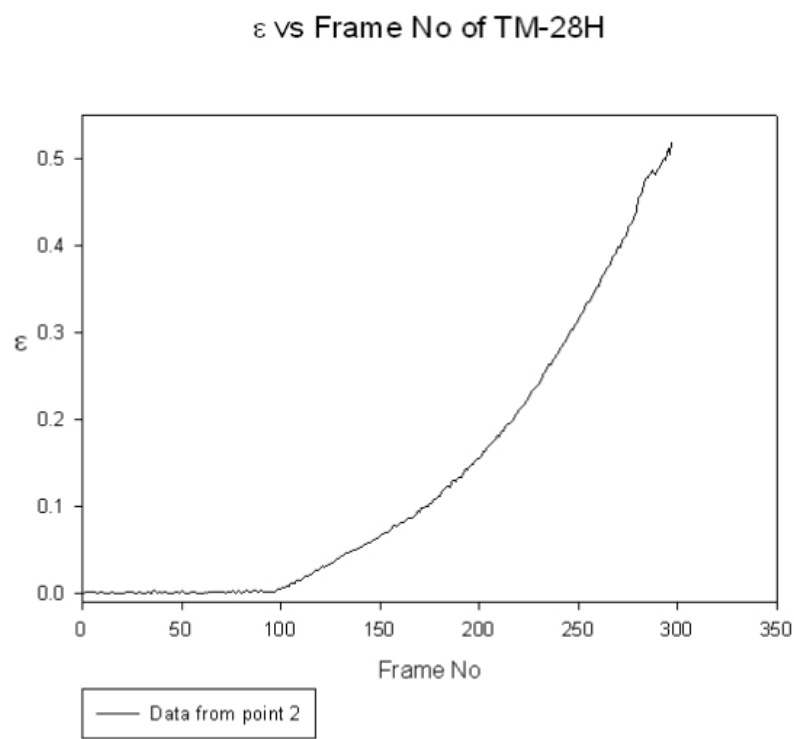


Figure 46: Strain vs Frame number taken from point 2(bottom right of circle surrounding the hole of Fig.(44)), indicating no Lüders band.

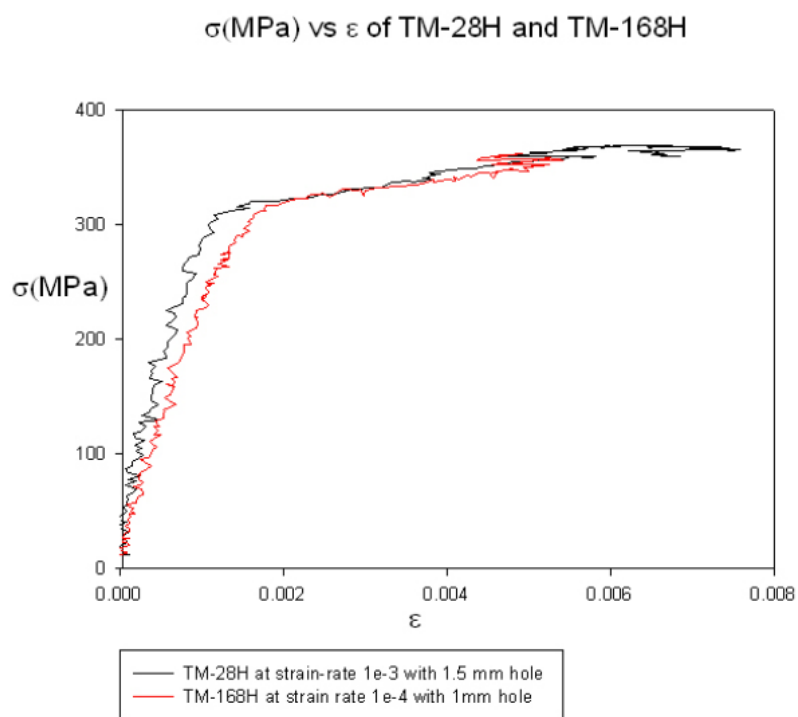


Figure 47: Stress( $\sigma$ ) vs strain( $\varepsilon$ ) curve of TM-28H(black) and TM-168H(red) at strain-rates  $1 \times 10^{-3}$  and  $1 \times 10^{-4} \text{ s}^{-1}$  respectfully.

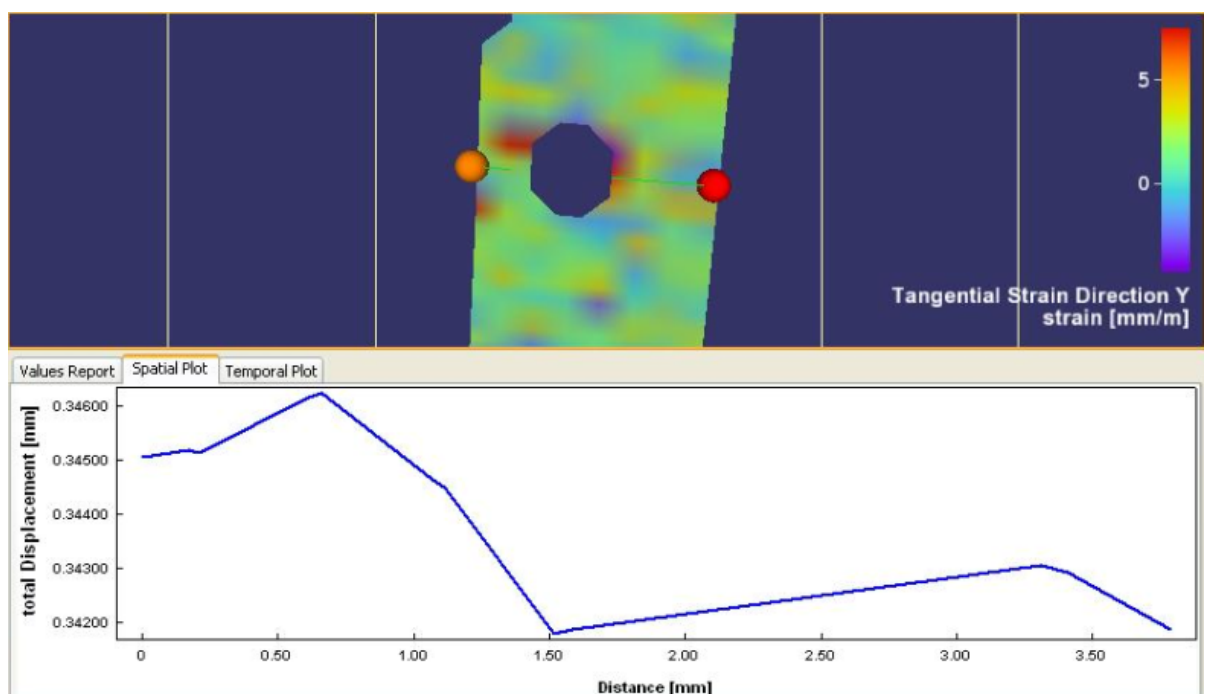


Figure 48: The spatial distribution of the total displacement of TM-168H, showing greater displacement on the left than right. This is due to being located offset to the left.

Table 8: Predicted yield and actual yield time in seconds

Material	Actual $t_y$ (seconds)	$t_{y1}^*$ (seconds)	$t_{y2}^\bullet$ (seconds)	$(t_y - t_{y1})\%$	$(t_y - t_{y2})\%$
TM-168H	100	86	119	28	-15
TM-28H	16	13.2	19	17.5	-16

\* Calculated with a cross-section minus the diameter of the hole

• Calculated assuming no defect in cross-section

### 5.3 Discussion

Fig.(44) shows the distribution of local strain result of a 1.5mm hole taken from the DIC at an applied stress at approximately 300 MPa. The evolution of strain-rate at point one, which is located at the top right, is plotted as a function of frame number in Fig.(45) showing clear evidence that a Lüders band is not present in the strain-displacement profile. A similar behaviour is also observed in Fig.(46), although the work-hardening during plastic deformation is greater. This trend was also observed at points 3 and point 4(top and bottom left), showing clear indications that a Lüders strain, if evident, was too small or rapid to be detected by DIC.

This could be attributed to the stress distribution around a circular hole. The stresses around a circle are greater than the tensile stress. Therefore, the material closer to the hole yielded earlier. This is further substantiated by Fig.(47) that shows the stress-strain curve of both TM-28H and TM168H. The average yield of both of the materials seems to be approximately 300 MPa and the profile of the curves fits a more homogeneous type deformation than what is usually expected from a tempered structure in tensile dominated stress. The overall effect of holes which are small compared to the overall gauge length, seems to change the profile of the stress-strain curve. Therefore, this suggests that localised rapid deformation in a small area can affect the overall structure despite the difference in size. However, it is also noted that while the diameter of the hole is small compared to the gauge length, the diameter is about half of the size of the gauge width. This was the main cause of the material yielding at the rate it did.

The placement of the hole also affected the rate of yielding, because, evident in Fig.(44) and Fig.(48), the placement of the hole was not located in the centre, although the placement of the hole was not contrived, due to the experimental set up and the difficulty in drilling the hold in the centre. Therefore, the side with the smallest cross-sectional area yielded and failed first. This asymmetry could be responsible for the difficulty in detecting Lüders bands for both the TM-28H and TM-168H.

The yield time of nucleation was also tested. The results of which are shown in table 8. It is evident that the actual time of nucleation fell between the  $t_{y1}$ , which was calculated<sup>15</sup> assuming a cross-section with the defect included, but assumed that the effect of including a circular defect was to

---

<sup>15</sup>The values were calculated using Equ.(166), which can be found in appendix C (That is  $k_1$ ,  $k_2$ ,  $l_0$  and  $E$ .).  $\sigma_p$  took the value of the yield stress from Fig.(47) for both structures.

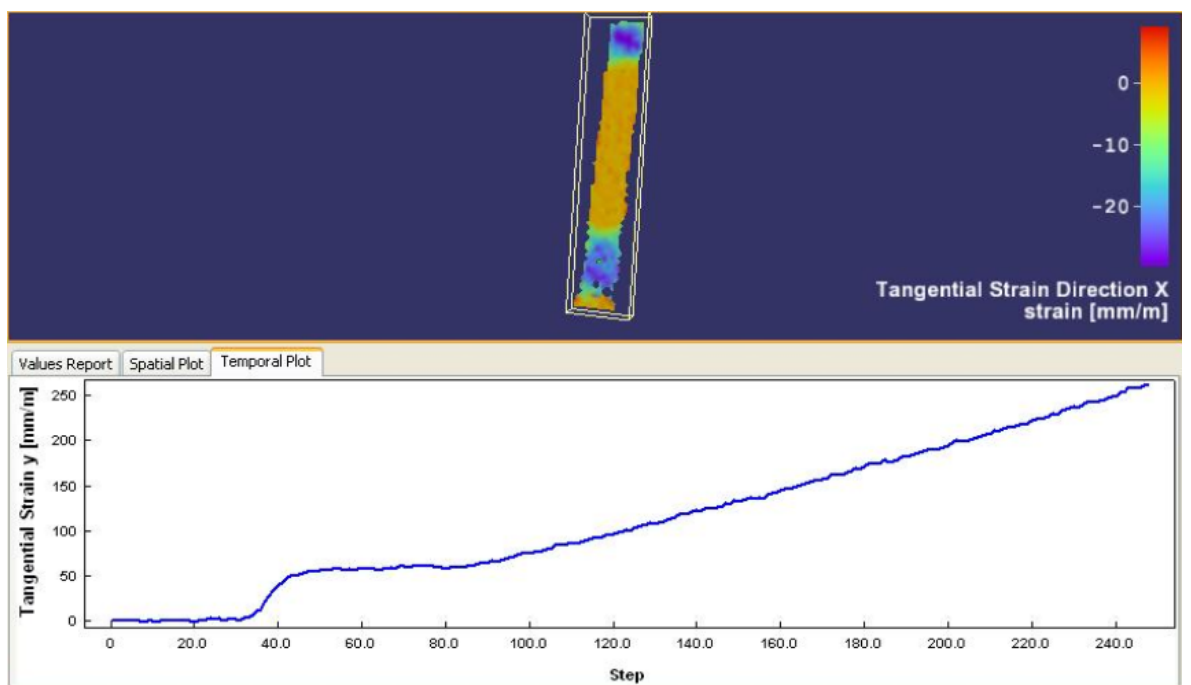


Figure 49: Strain displacement in the y-axis with the point of nucleation location on the tensile specimen of UL-05. Taken from DIC.

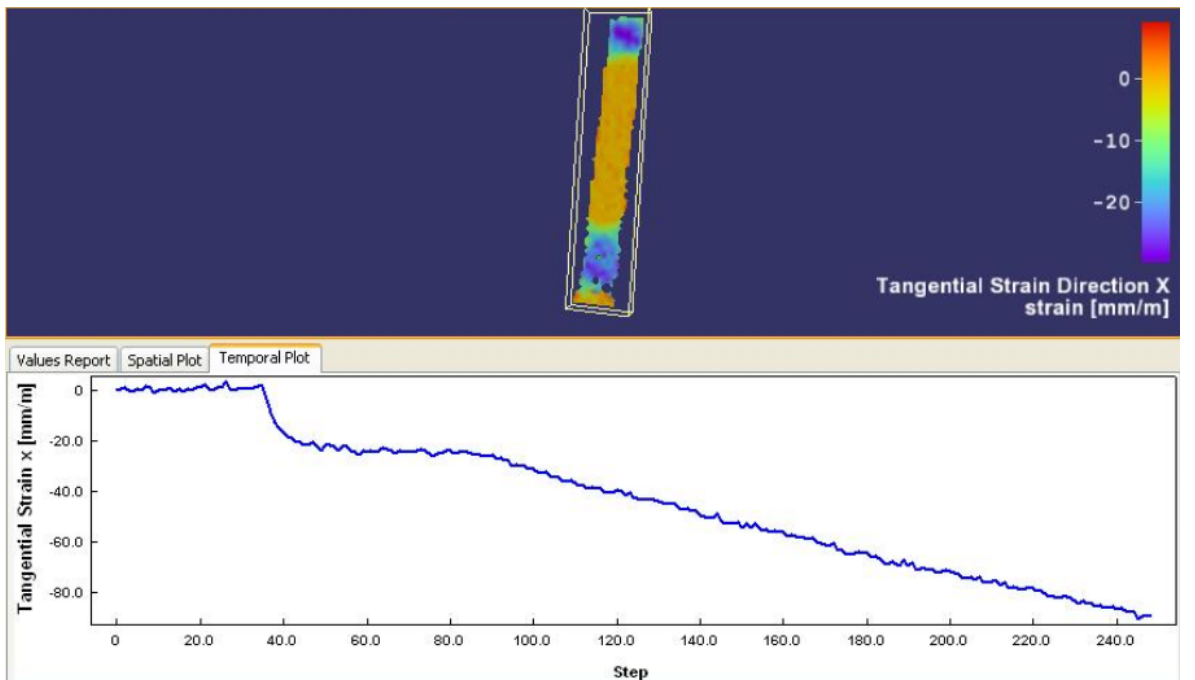


Figure 50: DIC with corresponding strain displacement in the x-axis with dot on compressive specimen(point of nucleation) of UL-05. The maximum strain in the compressive axis is less than the strain in the uniaxial direction or y-axis, see Fig.(49). This confirms the prediction of Equ.(132)(chapter 3) that is  $\varepsilon_y > \varepsilon_x$ . For experimental procedure see section 4.3.

reduce the overall cross-section, and  $t_{y2}$ , which assumed the defect was too small to change the overall cross-section significantly. This was also true when the size of the hole increased to 1.5mm with the TM-28H. Therefore, it is evident that a small structural defect such as the hole behaves in-between the two approximations. That is, reducing the overall cross-sectional area, but not as significantly as the size of the defect minus the overall cross-section.

The flexibility of Equ.(166) derived and shown in appendix C, was also illustrated in table 8. The importance of having a reliable method that can predict the approximate yield time. In the tensile case, as shown in the appendix C, it was shown that the equation worked for pure tensile stress, without defects in the material, with agreement(in the notation of table 8), actual  $t_y = 39$  seconds and  $t_{y1} = 30$  seconds giving error of -23%. This seems large, however this is due to the value of  $k_2$ , which was only calculated for a few experiments and, therefore, further experiments are required to obtain a more representative value of  $k_2$ ;  $k_2$  is interpreted as the spring between the gauge length and the hydraulic machine( $k_1$ ) and is therefore the specimen ends.

It has also been demonstrated that the equation can also be applied to tensile specimens with defects, provided the cross-sectional area is correctly assessed. If not, as shown in table 8, the answers can be either under or over the actual yield time.

The significance of this is not as apparent in tensile experiments using clip gauges, as tensile tests of that type do not demand a resolution as high as DIC. It is only apparent when using camera and frame-rates at high strain-rates, that an algorithm to determine the optimum strain-rate is required. One of the problems with Equ.(166) was choosing a value of  $k_2$ . The final value was based on the average of a few tensile tests, which was about 18 MN/m. Therefore, if Equ.(166) was used for subsequent tests, further experiments are required at different strain-rates and materials in order to obtain a better value of  $k_2$ .

The total spatial distribution of Fig.(48) of TM-168H was taken at the point of nucleation. It shows that the displacement due to the yielding was not homogeneous across the gauge width of the specimen. The result of this is a higher displacement in the thinnest wall, seen on the left of the hole in Fig.(48)

The compressive component(the x-direction), although not plotted in this section, gave no evidence of a Lüders band despite regions of equal tensile and compression. The signature of a Lüders type in the compressive region, is

a symmetric displacement about the x-axis(see, Fig.(49) and Fig.(50)). This also shows the benefit of using DIC as opposed to strain-gauges, because of the resolution that is possible on the surface.

## 5.4 Conclusion

- a) A tempered martensitic structure that has a Lüders strain greater than 3% when strained uniaxially, does not show evidence of a Lüders band(see, Fig.(45) and Fig.(46)) around the hole defect.  
The same was true for both of the tempered structures(TM-28H and TM-168H), showing that despite an increase of spheroidisation on the grains from 28 hours to 168 hours(from the optical micrograph), the nucleation of a Lüders band had a negligible dependence on the spheroidised carbide density.
- b) The effect of a hole was quantified by calculating theoretically the time taken for the material to yield. It was shown that the actual time taken to yield fell between  $t_{y1}$  and  $t_{y2}$  for both 1mm and 1.5mm holes. This showed that the actual effect of holes of this dimension on the tensile specimen reduces the cross-sectional area, but not to an effect where the total reduced cross-section (including a hole) differs significantly from the original cross-section.
- c) The spatial displacement across the gauge length was not homogeneous. This was attributed to the asymmetry of the adjacent thickness of the walls surrounding the hole, which had experienced greater displacement on the left side than the right.
- d) A Lüders band in uniaxial tests will have the same profile in the x-direction due to Poisson's ratio with a reduced Lüders strain, as shown in Fig.(49) and Fig.(50). This confirms one of the predictions of the model derived in chapter 3(see Equ.(131)), that a band propagating in the uniaxial direction will have a similar band profile in the compressive, x-direction.

## 6 Failure Assessment Diagrams(FAD) using R6 code

### 6.1 Introduction

This section aims to answer the following question:

- Is the presence of a Lüders strain beneficial to residual stress<sup>16</sup>?

To fully answer this question this section will be broken down as follows: A brief introduction to the R6 code procedure and how further models can improve upon the original assumptions of the R6 code such as the work done by Mirazee-Sisan et al[4] and Lei et al[42]. This will lead to a report conducted by Structural Integrity Assessment Procedures or SINTAP, which is the European equivalent of the R6 procedure, whose purpose was to determine the safety assessment of the inclusion of Lüders bands.

This will then lead to the work arrived at by Wenman et al[1], presenting the case of a Lüders band being more beneficial in residual stress calculations. Finally, the discussion will be on generating FADs for the AR, TM and FP structure, though of the TM structures only the TM-168H will be shown, as the yield stress is closer to the FP and the AR structure. This will be done at  $\dot{\varepsilon} = 1 \times 10^{-3}\text{s}^{-1}$ .

This will be followed by discussions and conclusions.

### 6.2 R6 code

The safety assessment code or R6 procedure has been in development since 1976[60] and is specifically designed for the assessment of nuclear plant components containing defects. The R6 code is broken into two failure modes: Plastic collapse and fracture.

The R6 code resolves stresses into primary and secondary. Primary stresses are non-equilibrating stress and secondary stresses are equilibrating or residual stresses.

The R6 code consists of evaluating the following parameters:  $L_r$  and  $K_r$  which are the proximity to plastic collapse and proximity to failure by

---

<sup>16</sup>In the case of a RPV, residual stress due to irradiation, thermal gradients etc.

fracture respectively, are defined as:

$$K_r = \frac{K}{K_{frac}} \quad (167)$$

where  $K$  is the stress intensity factor and  $K_{frac}$  is the fracture toughness.

$L_r$  is defined as:

$$L_r = \frac{P}{P_L(\sigma_p)} \quad (168)$$

where  $P$  is the load and  $P_L$  is the crack body stress rigid-plastic limit load at 0.2% strain and the proof stress  $\sigma_p$ <sup>17</sup>.

These parameters coupled with the J-parameter of instability:

$$\frac{\partial J_{app}}{\partial x_i} > \frac{\partial J_{mat}}{\partial x_i} \quad (169)$$

where  $x_i$  a spatial parameter,  $J_{app}$  is the applied  $J$  and  $J_{mat}$ , for plane strain or mode I loading, as:

$$J_{mat}(\Delta a) = \frac{K^2(\Delta a)}{E'} \quad (170)$$

where  $\Delta a$  is the crack extension length and  $E'$  is dependent on the planar stress(plane strain) for which it is defined as:

$$E' = \frac{E}{1 - \nu^2} \quad (171)$$

where  $E$  is Youngs modulus and  $\nu$  is Poissons ratio, which is 0.3 for steel<sup>18</sup>.

$J_{mat}$  is derived from the J-integral, which is defined as[61]:

$$J = \lim_{\Gamma \rightarrow 0} \oint_{\Gamma} \left( W \delta_{ij} - \sigma_{ij} \frac{\partial u_i}{\partial x_1} \right) n_i ds \quad (172)$$

where  $W$  is the strain energy density,  $\sigma_{ij}$  and  $u_i$  are components of stress and displacement,  $\Gamma$  is the contour surrounding the crack tip and  $n_i$  is the normal vector to the path  $ds$ , as shown in Fig.(51).

$J$  is defined as the strain-energy release rate for a crack subjected to monotonic loading[62]. The details of the derivation of the  $J$ -integral and the modified version to account for residual stresses can be found in appendix E.

---

<sup>17</sup>In materials that yield discontinuously  $\sigma_p$  is defined as the lower yield stress or  $\sigma_{lyp}$

<sup>18</sup>For plane stress  $E' = E$

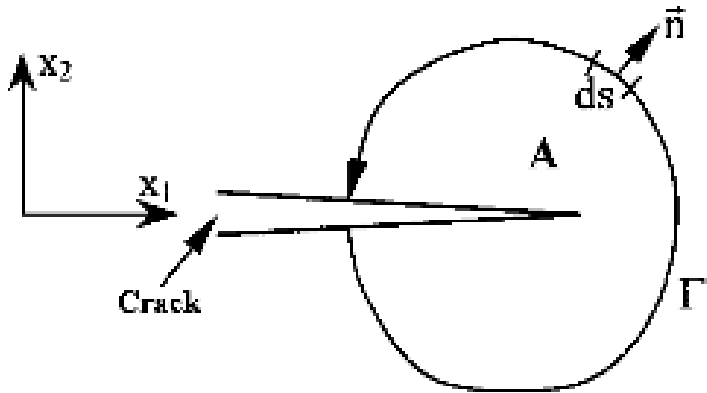


Figure 51: Integration path around the crack tip taken from Lei et al[61].

Budden et al[60] after investigating the development of the R6 code, concluded that major developments in crack or fracture mechanics and finite element(FE) modelling have made the R6 code essential to the nuclear industry; and because the code is always updated, it has become one of the most robust codes or procedures in the nuclear industrial today.

However, work by Mirazee-Sisan et al[4], using  $J_{mod}$  derived by Lei et al[61] to account for residual stresses calculated  $J$  and consequently  $K_{frac}$  and compared to R6(revision IV) standard safety assessment calculations. They calculated the J-integral from standard abaqus calculations that adhered or were derived from R6-procedure, of a crack, and compared their results with a modified form, known as  $J_{mod}$  with the aid of finite element analysis.

This A533B steel, which has 0.23% C[63] was cooled down to -150°C and then subjected to in-plane compression of a 3-point bend specimen of complete loading cycle or abbreviated to CUCF(compression-unload-cool-fracture). FE analysis was done, with the same geometry, as shown in Fig.(52) with the corresponding FE model in Fig.(53).

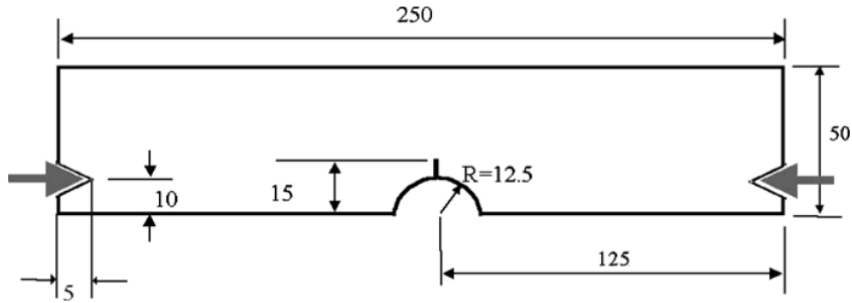


Figure 52: Specimen geometry taken from Mirazee-Sisan et al[4].

It was shown that  $J$ , in its R6 defined form, did not maintain a path independent value as a function of distance from the crack, while  $J_{mod}$  managed to maintain a constant value and thus remain path independent. This was done assuming that there was an initial strain  $\varepsilon_{ij}$  that was not due to primary loading. This allowed for the introduction of residual stress  $J_{mod}$ , the details of which are found in appendix E.

Also when the J-integral is calculated using FE, in all but the simplest of cases, the path enclosing the crack tip is shrunk to almost the origin of the crack tip and as a result does not maintain complete path-independence. The plot of  $J$  as a function distance from the crack tip and  $J_{mod}$  are shown in Fig.(54). It is evident that the value of  $J$  as a function of crack length, when compared to  $J_{mod}$ , while maintaining path independence, are greater than  $J_{mod}$  and, additionally,  $J_{mod}$  maintains complete path independence. Consequently, this resulted in higher values of  $K_r$  compared to  $K_{mod}$ , where  $K_{mod}$  is the calculated  $K_r$  from  $J_{mod}$ .

The degree of conservatism was quantified with the aid of FAD, as shown in Fig.(55). This was done by calculating the the assessment lines of A533B

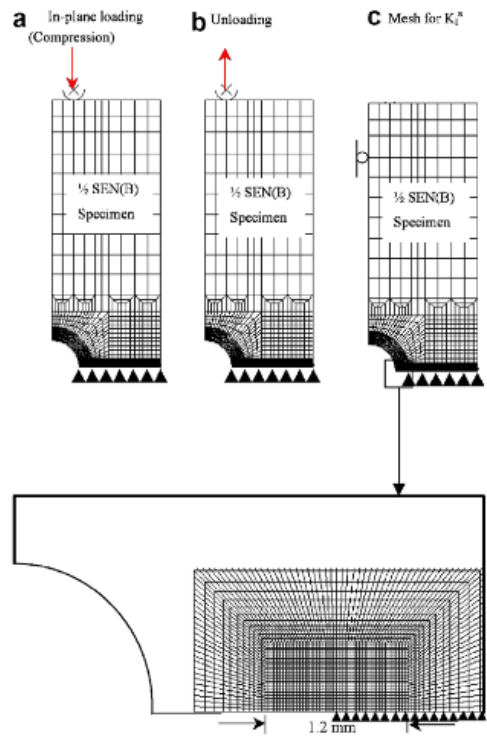


Figure 53: Development of mesh during compression and tension taken from Mirazee-Sisan et al[4].

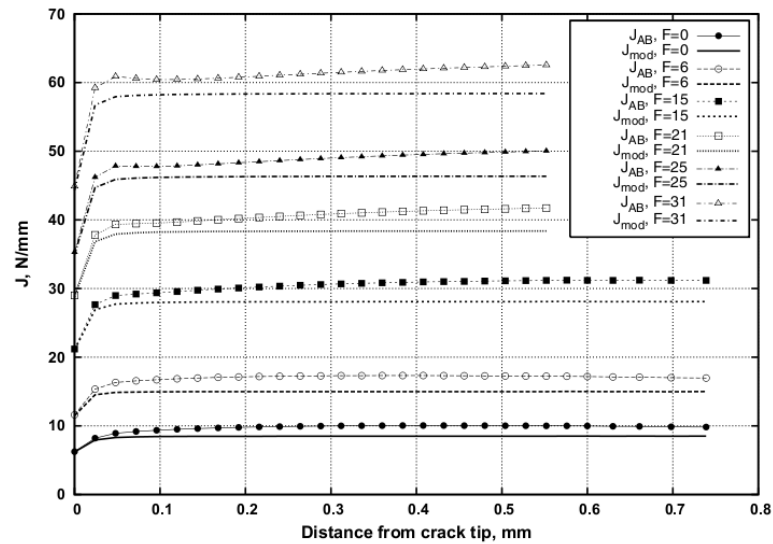


Figure 54:  $J$  as function the distance  $a$  from the crack tip. Taken from Mirazee-Sisan et al[4].

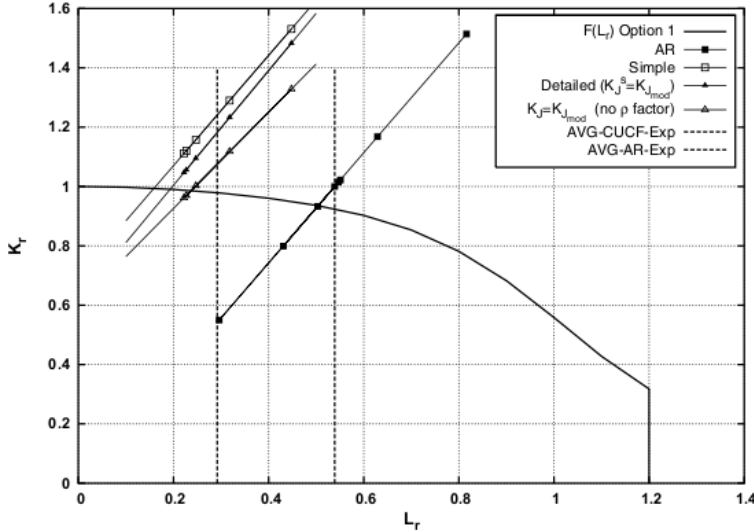


Figure 55: FAD curves for A533B specimens at  $-150^\circ\text{C}$  under primary and secondary stresses by in-plane compression taken from Mirazee-sisan et al[4].

through the following equations:

$$K_r = \frac{K_I^P}{K_{frac}} + \frac{K_I^S}{K_{frac}} + \rho \quad (173)$$

$$L_r = \frac{F_{applied}}{F_{limit}} \quad (174)$$

where  $K_r$  and  $L_r$  were defined at the beginning of the chapter,  $K_I^P$  and  $K_I^S$  are the linear elastic stress intensity factor due to the primary loads and secondary loads, respectively,  $F_{applied}$  is the applied primary load is calculated from the geometry of Fig.(52) of single notch bend:

$$F_{limit} = 0.704 \times \sigma_y \frac{BW^2}{S} \left(1 - \frac{a}{W}\right)^2, \quad 0.18 \leq a \leq 1 \quad (175)$$

where  $\sigma_y$  is the yield stress,  $B$  is thickness,  $W$  is the width,  $a$  is the crack length and  $S$  is the loading span of the specimen.

Also  $\rho$  is a factor that accounts for the interactions in the material such as residual stress and is used for problems or assessment that are material

dependent and is defined as:

$$\rho = \begin{cases} \rho_1 & L_r \leq 0.8 \\ 4\rho_1(1.05 - L_r) & 0.8 < L_r < 1.05 \\ 0 & L_r \geq 1.05 \end{cases} \quad (176)$$

where  $\rho_1$  is determined from:

$$\rho_1 = \begin{cases} 0.1x^{0.714} - 0.007x^2 + 0.00003x^5 & x < 5.2 \\ 0.25 & x > 1.05 \end{cases} \quad (177)$$

where  $x = \frac{K_I^S L_r}{K_I^P}$ .

The degree of conservatism was quantified from taking the ratio of the failure predicted by the standard failure assessment diagram derived from the R6-code( $L_r$ ) and the measured failure( $L_{test}$ )<sup>19</sup>. This was also done for  $K_r$  by calculating the R6  $J$  and comparing to  $K_{jmod}$  from calculating  $J_{mod}$ .

This was also done with  $J_{mod}$  to  $J$  from the R6 code was also calculated from the corresponding K-values of  $K_{mod}$  and  $K_{frac}$  as shown in table 9.

Table 9: Predicted and observed failure modes of A533B taken from Mirazee-Sisan et al[4].

Test condition	$L_r$ at failure	$\frac{(L_r)_{ass}}{(L_r)_{test}}$	Conservatism of R6 code
As-received	0.503	0.93	7%
CUCF, simplified $\rho$	0.161	0.55	45%
CUCF, detailed $\rho$	0.193	0.66	34%
CUCF, $K_r = \frac{K_{jmod}}{K_{frac}}$	0.237	0.81	19%

The degree of conservatism ranges from 7% to 45%.

The work by Mirazee-Sisan et al[4] supports the consensus that a model that has greater detail(see Wenman et al[1]) especially with the application of  $J_{mod}$ , will produce less conservative results, which were up to 45% in some cases.

---

<sup>19</sup>The purpose of using the FAD was for failure prediction, rather than for failure avoidance[4].

CHEMICAL COMPOSITIONS OF TEST PLATES (Wt. %)													
Grade	Thickness (mm)	C	Si	Mn	P	S	Cr	Mo	Ni	Al	Cu	N	Nb
S275J0	25.0	0.130	0.200	1.05	0.018	0.006	-	-	0.030	0.026	0.030	-	0.002
S355J2	25.0	0.160	0.410	1.36	0.012	0.007	0.011	0.001	0.018	0.044	0.004	-	0.030
355 EMZ	25.0	0.089	0.370	1.44	0.009	0.003	<0.020	<0.005	0.510	0.041	<0.020	0.006	0.023
355 EMZ	50.0	0.088	0.360	1.42	0.009	0.003	<0.020	<0.005	0.490	0.042	<0.020	0.006	0.021
450 EMZ	12.5	0.110	0.286	1.44	0.012	0.003	<0.020	<0.005	0.014	0.041	<0.020	0.005	0.003
450 EMZ	25.0	0.093	0.290	1.24	0.015	0.002	0.020	0.140	0.430	0.043	<0.020	0.007	<0.005
450 EMZ	50.0	0.090	0.300	1.24	0.016	0.003	0.030	0.180	0.510	0.039	<0.020	0.008	<0.005
S690Q	12.0	0.140	0.400	1.39	0.013	0.002	0.017	0.002	0.018	0.041	<0.020	-	0.037
S690Q	25.0	0.090	0.410	1.42	0.015	0.002	0.023	0.003	0.022	0.042	0.012	-	0.034
S690Q	40.0	0.130	0.400	1.41	0.012	0.004	0.170	0.150	0.230	0.033	0.140	0.006	0.032
ABR400	12.5	0.130	0.400	1.38	0.013	0.002	0.025	0.003	0.001	0.043	0.008	-	0.037
ABR400	25.0	0.180	0.391	1.39	0.010	0.003	0.131	0.151	0.242	0.036	0.152	-	0.034

Figure 56: Compositions of all steels sued by SINTAP for their experiments[64].

A report by SINTAP[64] or the Structural Integrity Assessment Procedures, which is the European equivalent of the R6 procedure, looked at the assessment or occurrence and significance of yield plateaus in structural steels on behalf of British Steel<sup>20</sup>.

It was shown that the following structural conditions(see table.(10)) for the production and negation of Lüders bands for particular components and crack geometries. Looking at the steel grades of Fig.(56), it is evident that the range of carbon content falls within the range of the materials, UL-AR that were used experimentally in the previous chapter. The most applicable to this chapter is the 450EMZ(0.110% C) steel as it was quenched at 930 °C and tempered at 670 °C for 3 hours and 25 minutes, which is the closest to the least tempered RPV steel or TM-5H investigated in the previous chapter.

The specimens varied from simple tensile specimens to welded and unwelded plates, with varying thickness. The main conclusions drawn from the quench and tempered structured tests were:

---

<sup>20</sup>Now part of Tata Steel.

Table 10: Structural conditions for significant influence of yield plateau taken from[64]

Component and Crack Geometries	Predominately Tensile	Loading	
	Predominately Tensile	Predominately Bending	Equal Tensile and Bending
Thin Wall, Shallow Crack	✓	✗	( )
Thin Wall, Deep Crack	✓	✗	( )
Thick Wall, Shallow Crack	✗	✗	( )
Thick Wall, Deep Crack	✗	✗	( )

✓ Yield Plateau Structurally Significant

✗ Yield Plateau Structurally Insignificant

( ) Significance Uncertain

- a) Lüders bands are less prominent in thicker plates, than thinner, tensile specimens(though no recommendation was made as to the minimum thickness of material to ensure no Lüders strain.)
- b) When constructing the FADs, it was better to use the lower yield stress as the proof stress than the upper yield stress as choosing the upper yield stress or proof stress lead to over-conservatism of the FAD diagram compared to using the lower yield stress.
- c) Materials exhibiting 4-5 % Lüders strain in flat plates, did not exhibit or show a work-hardening curve and thus maintain the plateau, if the elongation of the plate fell to failure within the Lüders strain.

The question of the desirability of a Lüders band, from the SINTAP investigation, was unclear, as the purpose of the report was to address the following criteria :

1. When to assume the presence of a discontinuous yield.

2. Whether the length of the plateau can be estimated from knowledge of the yield strength.

To determine whether a Lüders strain is advantageous was addressed by Wenman et al[1], when comparing standard work-hardening models with Lüders type models and determining which gave the better stress-strain response.

The aim of the work was to determine whether a model that had a Lüders band added, through artificial process, or a more refined model that factored in the physics of the Lüders band, would be less conservative when looking at the stress around a crack.

This was done by first calibrating the models from the data of the tensile test that were used to predict the residual stress distribution from the pre-loaded CT test or experiments.

This was done with four models: a standard isotropic-elastic plastic work hardening model, that is ABAQUS standard; the same model, with Lüders strain; the same model again, but with only the lower yield stress and Lüders strain and, finally, the Zhang model, which models dynamic strain ageing or DSA and is a Cottrell type yield drop model from Zhang et al[6], see Fig.(57).

The material used was 0.25 % C in an as-received form i.e. no heat treatment and cut using and EDM. The tensile specimens were subjected to strain-rate= $1\times10^{-2}$ -  $2.4\times10^{-5}$  s $^{-1}$ , using DIC.

Apart from giving better resolution of the stress-strain curve to strain-gauges, DIC can also detect the strain-distribution around a crack tip during CT tests. This is beneficial(see Fig.(58)) because it makes it more easier to compare with FE models.

The initial parameters of the Zhang model taken from Graff et al[51] were shown to be too small, therefore the parameters were adjusted until the following values were shown to fit the tensile data(see table 11).

The stress-strain predicted by the models are plotted on Fig.(57) for a uni-axial test. A comparison between models shows that for a standard work hardening model(in green) a continuous yield is predicted for a given strain-rate, which is to be expected, in contrast to the Zhang model and the modified work hardening models that predict discontinuous yield.

The plot of element 128 gives some insight as to what happens on a mesh scale, which would be representative of the scale that was measured on DIC.

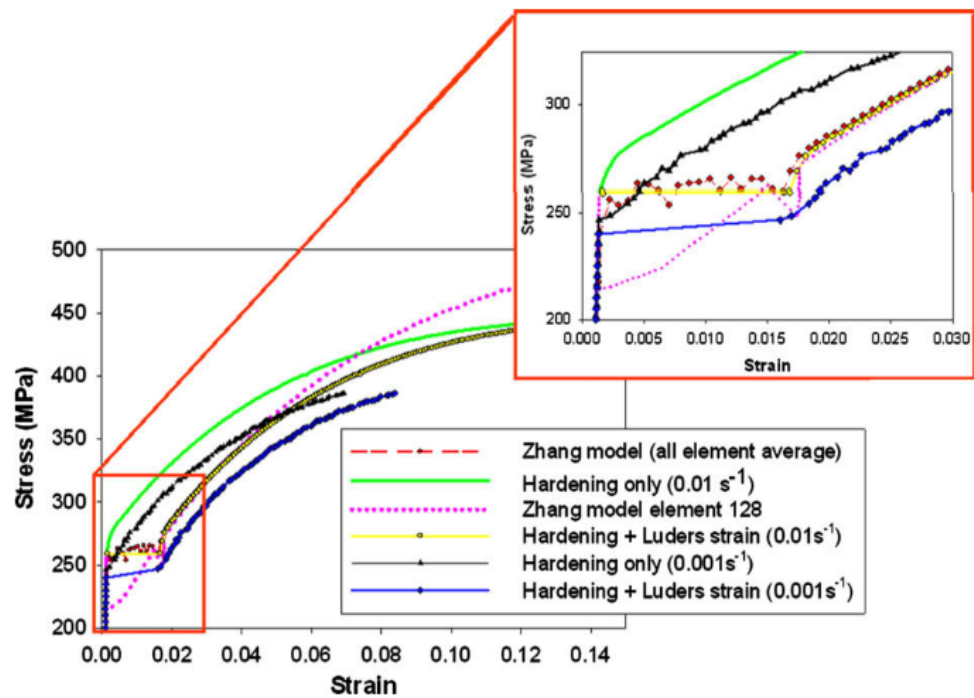


Figure 57: A comparison between the Zhang model with modifying hardening models and experimental data from Wenmen et al([1]).

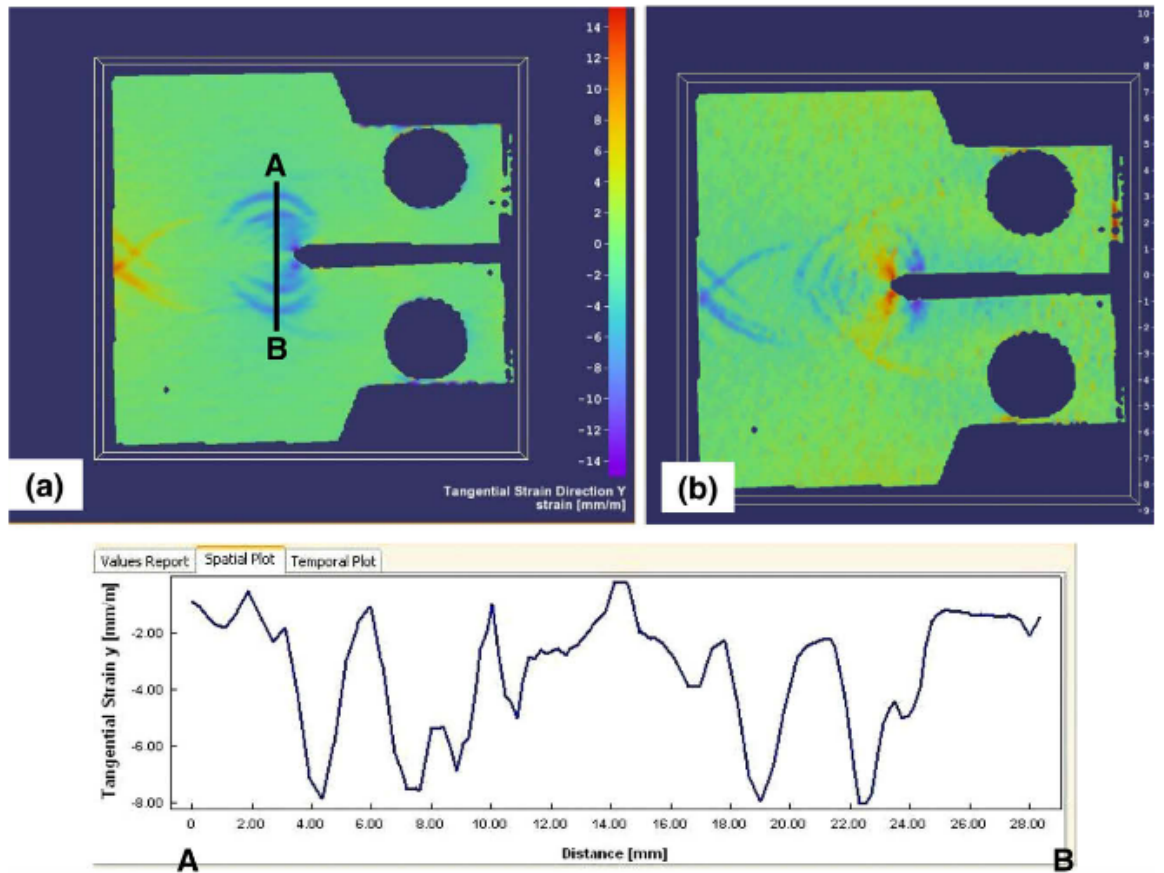


Figure 58: CT test specimen using DIC of (a) loading and (b) unloading, showing the shear strains around the crack tip, with the spatial dependence across the line A-B taken from Wenmen et al[1].

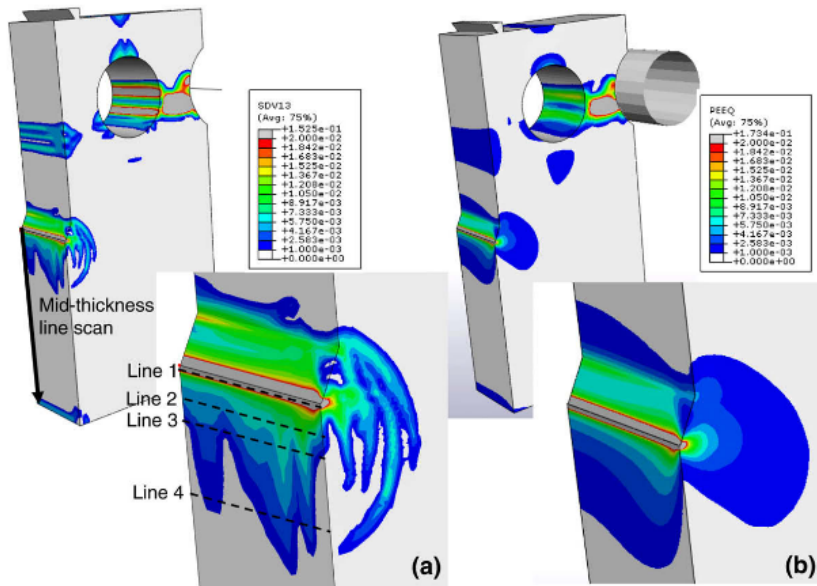


Figure 59: The residual stress distribution predicted from the FE model from the crack tip. Fig(a) shows the stress distribution for the Zhang model and Fig(b) show the stress distribution for the standard work-hardening models at strain-rate  $1 \times 10^{-2} \text{ s}^{-1}$ , taken from Wenman et al[1]. The stress and equivalent plastic strains can be seen on lines 1-4 in Fig.(61).

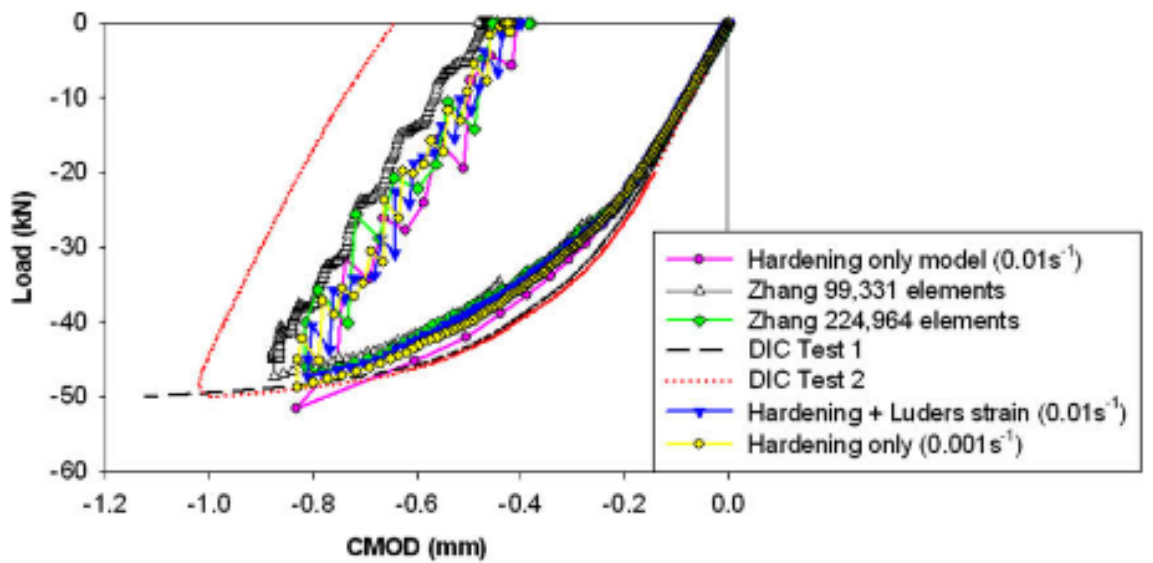


Figure 60: Load vs CMOD or Crack mouth opening displacement plot, in order to determine the type of work-hardening model to use. The hysteresis curve from the Zhang model is smaller than the curve from the data. However the shape is approximately congruent, illustrating that the Zhang model or yield drop model is qualitatively correct. This is also true for the standard work-hardening models, showing that the material does not purely obey a kinematic or isotropic work hardening model, but rather a combination of the former and the latter, as shown for reactor pressure vessel steel in Price[52]. Taken from Wenman et al[1].

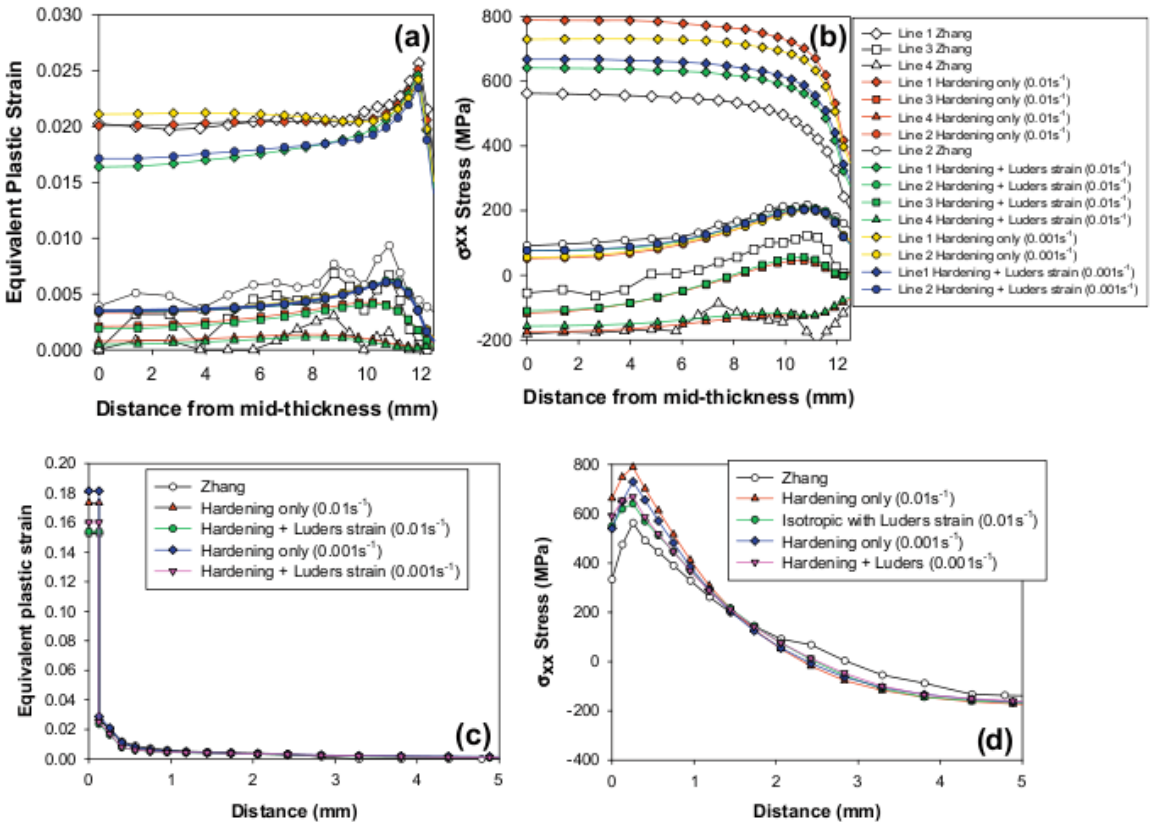


Figure 61: The residual stresses predicted by each model in the x-direction-along the face of the CT specimen. The serrated lines of the Zhang model in plot (a) and (b) are evidence of yield points and, therefore, inhomogeneous deformation(Lüders bands) around the crack region during the loading and unloading of the CT specimen. It is evident that the residual stresses predicted by the Zhang model are consistently less than the other work hardening models, supporting the consensus that a yield drop model will predict lower residual stresses and, therefore, reduce the degree of conservatism. Taken from Wenman et al[1].

Table 11: Values of the parameters used for modelling with the blanks indicating dimensionless quantities, taken from Wenman et al[1].

Parameter	Value	unit
$\dot{\varepsilon}_0$	100	
$D_1$	200	MPa
$D_2$	325	MPa
$D_3$	0.065	
$\omega_1$	$1 \times 10^{-6}$	
$\omega_1$	$1 \times 10^{-5}$	
$N$	1	
$T_A$	4000	seconds
$\alpha$	0	
$\beta$	0.68	
$P_1$	37	MPa
$P_2$	0.001	
$S_1$	12.5	MPa
$S_2$	5	MPa
$C_M$	1	

To determine how a material plastically deforms or work-hardens, crack mouth opening displacement tests(CMOD) are used as shown in Fig.(59), in this case in plane compression and unloading. The results of which are compared to FE models with the same geometry, but with different work-hardening models. That is isotropic or kinematic work-hardening. The results of these are plotted as a form of hysteresis curve(see Fig.(60)); whichever models the CMOD curve most accurately is then used for subsequent modelling of the material.

It is apparent in Fig.(60) that the work hardening models and the Zhang model at least predict the shape of the curve from the data. However, the models and the data only converge below a load of -40kN(see, Fig.(60)). This is due to, at least with the Zhang model, the values chosen from table 11.

This resulted in the production of Lüders band from the Zhang model, but at a lower magnitude due to a lower CMOD curve as seen in Fig.(60).

The corresponding stress distributions around the crack tip are shown in Fig.(61) for lines 1-4 for each model at the chosen strain-rate. It is evident that for the resulting stress distribution of the unloaded CT specimen, a lower residual stress is predicted than the standard work hardening model,

which would be used in the R6 code(see Fig.(61)). The difference between the standard model and the modified form differed by approximately 200 MPa at most, with the general trend showing that the Zhang model seems to produce less conservative values than the work-hardening models that had a Lüders band added.

Although it is clear from the above analysis of Weman et al's work that having a model that describes Lüders bands naturally shows less conservative predictions of the resultant residual stress pattern around the crack tip, it should be noted, due mainly to the limitations of DIC as it can only detect or show strain-displacement, that the stresses were not verified by experiment and therefore any conclusions drawn pertaining to the degree of conservatism in terms of stress should be considered with caution. Consequently, further work into the actual stress distribution around crack tips is needed to substantiate the above analysis.

In conclusion, the work of Wenman et al has shown that the addition of Lüders type model into residual stress models agree to the consensus of this chapter that a more refined model than the standard work-hardening models will produce less conservative results. However,  $\sigma_R$  was predicted with a more refined material model. It does, therefore, also answer the question of whether the addition of a Lüders strain in a material would be beneficial. In the case of structural integrity safety calculations, this would seem to be the case. However, it was also evident that the process by which a Lüders band is added also makes a difference to the overall residual stress calculations from the crack tip.

It was also shown that the process of using uniaxial data to try and determine multi-axial or triaxial stresses in the aforementioned case seems to work only qualitatively. Therefore, this shows that using tensile data alone is inadequate to make realistic residual stress calculations and further work such as x-ray diffraction of the actual stress distribution(see Price[52]) and other non-destructive techniques are required to better calibrate the FE models.

To summarise: It was shown that as the nucleation of a Lüders band relies on tensile dominated regions and that these regions in the SINTAP analysis were shown to be small compared to the material dimensions of thickness, the overall effect of a Lüders band can be treated as the standard codes dictate or neglected completely. That is, assume the material yields discontinuously. However, the analysis of SINTAP did not include residual stresses or the effects of a Lüders band on residual stress.

The work of Wenman et al[1] showed that the inclusion of a Lüders band from the Zhang model[6] compared to other models that have no Lüders band predicted lower residual stresses overall around the crack tip. Therefore, it suggests if further work substantiates the above analysis, Lüders bands may reduce the degree of conservatism by predicting a lower residual stress.

This leads onto the next section of this chapter, which is generating FADs for the micro-structures of the RPV steel, FP AR and TM-168H at a strain-rate of  $1 \times 10^{-3}$ .

TM-168H was chosen, because it has the closest tensile properties to that of the AR and FP micro-structures. This is important as one of the key aims was to determine how the Lüders strain varied with micro-structure. This is achieved by requiring the other tensile properties of the material, such as the yield stress(lower), to be kept as similar as possible,in order to determine the effects of the differing in micro-structure, the effect of which, will be seen in the FADs.

### 6.3 Generating FADs

### 6.4 Method

- The tensile data taken from DIC was truncated by reducing the number of stress-strain points and using extrapolation techniques to complete the curve, because of effects such as scattering of the data, which the software(R-code) would not accept. Therefore, the stress-strain curves developed were an approximation of the stress-strain curve measured from DIC.
- Each region of the stress-strain curve was broken into three, as required, in order to use Equ.(183)-Equ.(188). Subsequently the average of all the sections, elastic region, Lüders region and work-hardening region, were calculated to produce a stress-strain curve that was representative of the average of the specimens used for a given strain-rate for the strain-rate of  $1 \times 10^{-3} \text{ s}^{-1}$ .
- Equ.(183)-Equ.(188) were used to calculate the FAD.  $K_r$  was calculated from  $L_r$ .  $L_r$  was calculated using Equ.,(168), but was modified to calculate the applied stress. That is:

$$L_r = \frac{\sigma_{app}}{\sigma_{lyp}} \quad (178)$$

where  $\sigma_{app}$  is the applied stress taken as the tensile stress and  $\sigma_{lyp}$  is the lower yield stress.

$L_{max}$  or the maximum proximity of plastic collapse is defined, according to the R6 procedure handbook, as[2]:

$$L_{max} = \left( \frac{\sigma_{UTS} + \sigma_{lyp}}{2\sigma_{lyp}} \right) \quad (179)$$

where  $\sigma_{UTS}$  is the UTS stress.

Any values that exceed  $L_{max}$ , when applying Equ.(178), are disregarded.

The following equations were used to construct the FAD: the R6-procedure defines FADs as a composite of four parts<sup>21</sup>:

$$K_r = \begin{cases} f(L_r) & \text{for } L_r < 1 \\ f_{dis}(1) & \text{for } L_r = 1 \\ f_{dis}(1)L_r^{\frac{N-1}{2N}} & \text{for } 1 < L_r < L_r^{max} \\ 0 & \text{for } L_r \geq L_r^{max} \end{cases} \quad (180)$$

where  $K_r$  and  $L_r$  have their usual meaning and  $f(L_r)$  is a characteristic function of the FAD defined as:

$$f_{con}(L_r) = (1 + 0.5L_r^2)^{-\frac{1}{2}}(0.3 + 0.7 \exp(-0.6L_r^6)) \quad (181)$$

where  $f_{con}$  is the characteristic function for continuous yielding.

For discontinuous materials:

$$f_{dis}(L_r) = \left( \frac{E\varepsilon_{ref}}{L_r\sigma_p} + \frac{L_r^3\sigma_p}{2E\varepsilon_{ref}} \right)^{-\frac{1}{2}} \quad (182)$$

where  $f_{dis}$  is the function for discontinuous yielding,  $E$  Young's modulus,  $\varepsilon_{ref}$  is a reference strain and  $\sigma_p$  is the proof stress(taken as the lower yield stress).

---

<sup>21</sup>Three, if the material yields continuously

As an approximation Equ.(182) can be broken down into three equations that characterise the three stages of discontinuous yielding.

For  $L_r < 1$ :

$$f_{dis}(L_r) = (1 + 0.5L_r^2)^{-\frac{1}{2}} \quad (183)$$

For  $L_r = 1$ :

$$f_{dis}(1) = \left( \lambda + \frac{1}{2\lambda} \right)^{-\frac{1}{2}} \quad (184)$$

where  $\lambda$  is defined as:

$$\lambda = 1 + \frac{E\Delta\varepsilon}{\sigma_{lyp}} \quad (185)$$

where  $\Delta\varepsilon$  is defined as the Lüders strain  $\varepsilon_L$ <sup>22</sup>.

For  $1 < L_r \leq L_{max}$ :

$$f_{dis}(L_r) = f_{dis}(1)L^{\frac{N-1}{2N}} \quad (186)$$

where  $N$  has several definitions:

$$N = 0.3 \left( 1 - \frac{\sigma_{lyp}}{\sigma_{UTS}} \right) \quad (187)$$

where  $\sigma_{UTS}$  is the UTS.

If the stress-strain data is known, a more accurate way of calculating  $N$  is:

$$N = \frac{\ln(\frac{\sigma_t}{\sigma_y})}{\ln\left(\frac{\varepsilon_t - \frac{\sigma_t}{E}}{0.002}\right)} \quad (188)$$

where  $\sigma_t$  is the true stress,  $\sigma_y$  is the yield stress,  $\varepsilon_t$  is the true strain and  $E$  is Young's.

The crack body problem considered is a simple block with a 1mm crack defect, plane strain, with constant primary load of 100MPa(tensile, mode one failure).

The fracture toughness for AR steel according to Price[52] calculated at -155°C:

$$K_{frac} = 57 MPam^{\frac{1}{2}} \quad (189)$$

where  $K_{frac}$  is the fracture toughness.

---

<sup>22</sup>When  $\Delta\varepsilon = 0$  then the number of regions reduces to two, which is to be expected

This value will also be taken for the FP structure. The value of  $K_{frac}$  for the tempered martensite structure was initially chosen at  $57 \text{ MPa } m^{\frac{1}{2}}$  to compare with the aforementioned micro-structures. However, according to Firrao et al[65] the value tempered martensite steel with similar micro-structure had values of  $K_{frac} = 89 - 97 \text{ MPa } m^{\frac{1}{2}}$ . Therefore, to give a more realistic assessment of tempered martensite, FADs will be generated for  $K_{frac} = 70, 90$  and  $110 \text{ MPa } m^{\frac{1}{2}}$ .

It is possible to generate FADs for materials with the same tensile properties without Lüders band. Therefore, it can be determined whether it is better to retain a Lüders strain in the region of operation or to lose the Lüders strain through strain-ageing or other methods.

The same method of analysis will be applied to the AR structure, in order to determine whether the presence of a Lüders band would be conducive and, therefore, testing one of the conclusions of the SINTAP investigation(see previous), that a material with less than 2% Lüders strain can be modelled as a material that yields continuously. The strain-rate of the data used is  $1 \times 10^{-3} \text{ s}^{-1}$ .

The following rules are required to be satisfied when entering data in the R6-code software program.

1. The origin (0,0).
2. At least 3 data points have to fall on the elastic part of the curve.
3. At least 1 data pair which has a stress value exceeding the flow stress, defined as half the sum of the mean engineering 0.2% proof stress and the ultimate tensile stress.
4. At least 6 data pairs which fall between the elastic line and the flow stress.
5. The data must be ascending. That is each adjacent value has to be greater than the previous value. Therefore, under the R-code, it is not possible to construct a perfectly flat plateau.

## 6.5 Geometry

The type of geometry used was a thick-walled plate, as shown in Fig.(62) with the boundary conditions imposed on the geometry, to approximate plane strain.

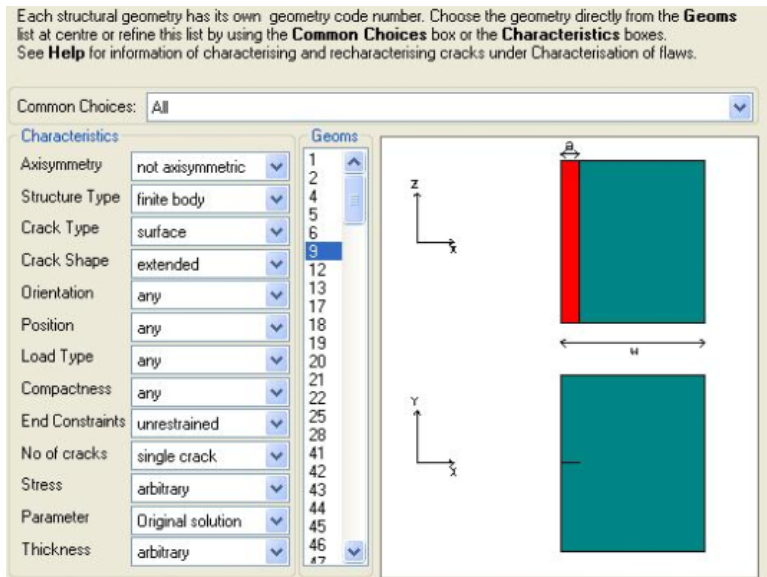


Figure 62: Geometry chosen with constraint choice on geometry.

The following boundary conditions for the plastic behaviour are found on Fig.(63).

The resultant stress distribution for the chosen geometry can be solved analytically with the equations found in the R6-code handbooks, shown graphically in Fig.(64) as a function of wall thickness.

**PLASTIC SELECTION**

Select the required parameters from the boxes below:

Alternative geometry	<input type="text" value="current geometry:9"/>	The equation identifier is:	<input type="text" value="E4P6S"/>
Thickness	<input type="text" value="uniform"/>	Alternative reference (if any):	
Collapse type	<input type="text" value="membrane_only"/>	<input type="text" value="Connors eq 117"/>	
Loading type	<input type="text" value="under_plane_strain_loading"/>	R6 Reference (if any):	
Yield surface	<input type="text" value="derived_from_von_mises_yield_surfac"/>	<input type="text" value="IV.1.5.5-4"/>	
Remote constraint	<input type="text" value="pinned_at_infinity"/>		
Global or local collapse	<input type="text" value="global_everywhere"/>		
Reference	<input type="text" value="all"/>		

Figure 63: Selected parameters for the plastic behaviour.

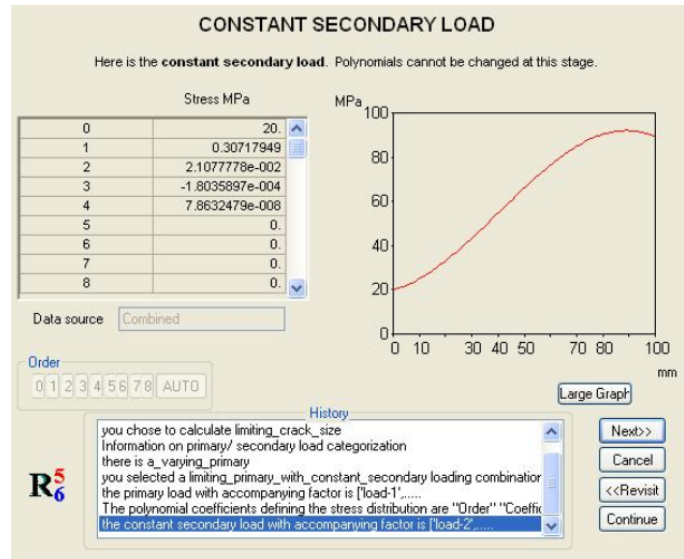


Figure 64: Assumed stress distribution of secondary/residual stress in plate.

## 6.6 Results

- Fig.(65)-Fig.(67) show the initiation of failure on the FAD of AR, FP and TM-168H with the predicted value of  $K_r$  and  $L_r$  at the corresponding Lüders strains.
- Fig.(68)-Fig.(69) show the crack initiation for AR and TM-168H both with a Lüders strain and without a Lüders strain. The results of which are shown in table 13
- Table 12 shows the data from the three micro-structures, with the corresponding Lüders strain in each.  $a_{dis}$  represents the crack length which failure begins or becomes unstable for a material that yields discontinuously.
- Table 13 shows the R-code prediction for a discontinuous material. If it is assumed that it yields continuously with  $a_{con}$  defined as the the crack length at which failure begins or becomes unstable for material that is assumed to yield continuously.
- Table 14 shows different values of  $K_{frac} = 57\text{-}800 \text{ MPa m}^{\frac{1}{2}}$  (see also Fig.(70)), illustrating the regions on the FAD where having no Lüders strain would be beneficial for  $K_{frac}$  less than  $250 \text{ MPa m}^{\frac{1}{2}}$ , and for regions where the presence of a Lüders strain in TM-168H is beneficial, that is for  $K_{frac}$  greater than or equal to  $250 \text{ MPa m}^{\frac{1}{2}}$ .

FAD of AR at Strain-rate=1e-3

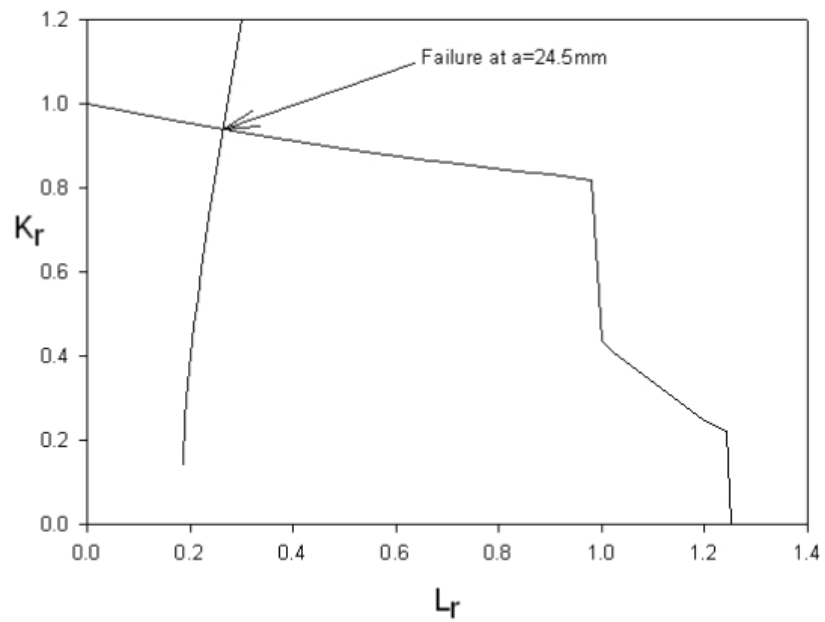


Figure 65: Failure assessment diagram of AR structure at strain-rate  $1 \times 10^{-3} s^{-1}$ , where  $a$  is the crack length. Measured at  $K_{frac} = 57 \text{ MPa m}^{\frac{1}{2}}$  at  $\varepsilon_L = 0.82\%$

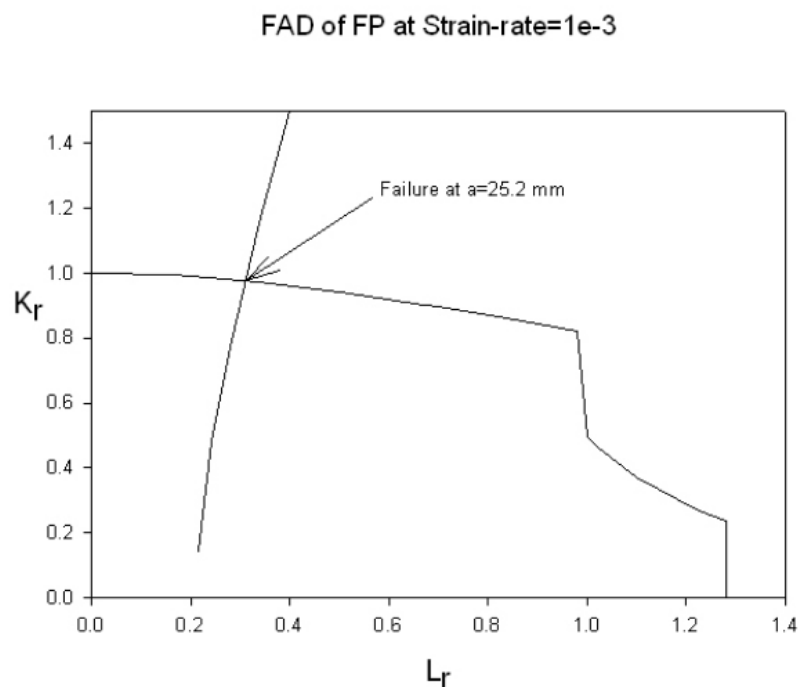


Figure 66: Failure assessment diagram of ferrite/pearlite structure at strain-rate  $1 \times 10^{-3} s^{-1}$ , where  $a$  is the crack length. Measured  $K_{frac} = 57 \text{ MPa m}^{\frac{1}{2}}$  at  $\varepsilon_L = 0.6\%$

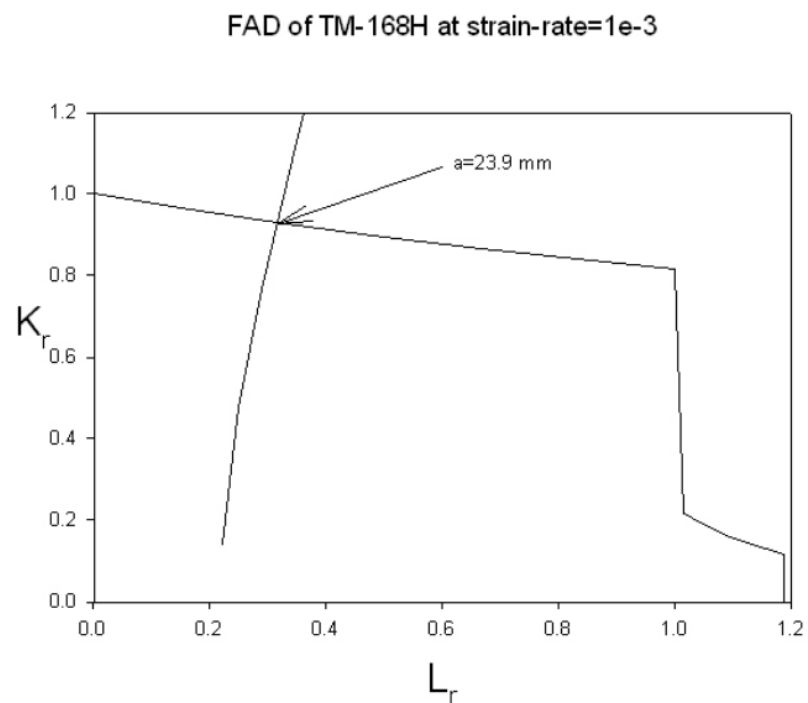


Figure 67: Failure assessment diagram of TM-168H structure at strain-rate  $1 \times 10^{-3} \text{ s}^{-1}$ , where  $a$  is the crack length. Measured  $K_{frac} = 57 \text{ MPa m}^{\frac{1}{2}}$  at  $\varepsilon_L = 3.54\%$

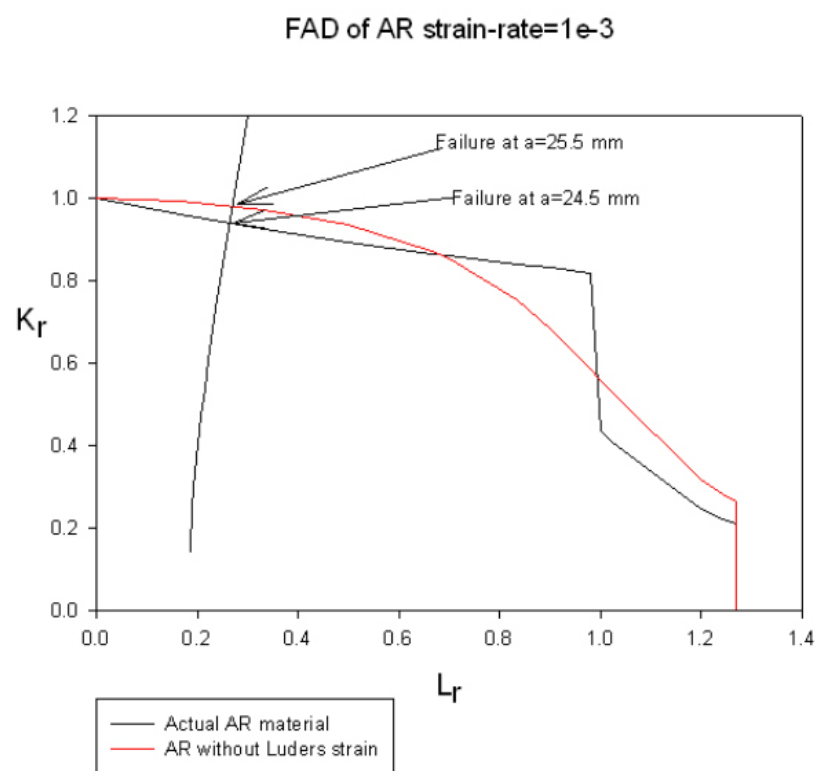


Figure 68: Failure assessment diagram of AR structure with Lüders strain(24.5 mm) without Lüders strain(25.5mm).

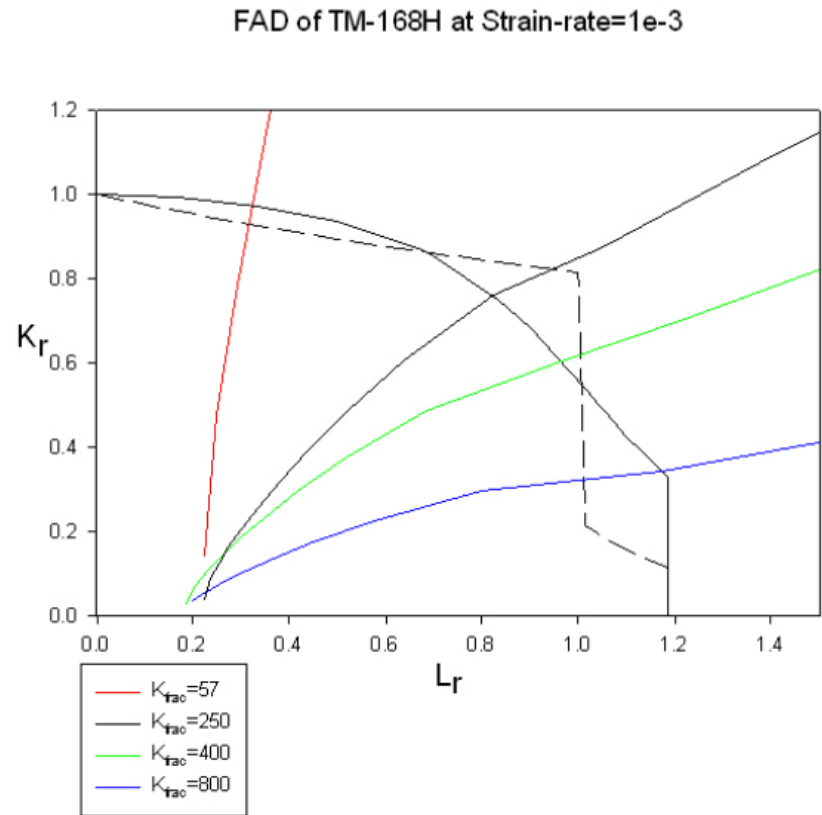


Figure 69: Failure assessment diagram of TM-168H structure at strain-rate  $1 \times 10^{-3} s^{-1}$  varying fracture toughness values and FAD of TM-168H without Lüders strain(dotted line).

Table 12: Failure of AR FP and TM-168H

Micro-structure	$K_{frac}$ (MPa m $^{\frac{1}{2}}$ )	$\varepsilon_L$ (%)	$a_{dis}$ (mm)
AR	57	0.82	24.5
FP	57	0.60	25.4
TM-168H	57	3.54	23.9

Table 13: Failure of AR and TM-168H with Lüders strain( $a_{dis}$ ) and without( $a_{con}$ )

Micro-structure	$K_{frac}$ (MPa m $^{\frac{1}{2}}$ )	$\varepsilon_L$ (%)	$a_{con}$ (mm)	$a_{dis}$ (mm)	$\frac{a_{dis}}{a_{con}}$	Difference(%)
AR	57	0.82	25.3	24.5	0.97	3.2
TM-168H	57	3.54	29.9	28.9	0.95	5

Table 14: Failure of TM-168H for varying fracture toughness(57-800)MPa m $^{\frac{1}{2}}$ 

Micro-structure	$K_{frac}$ (MPa m $^{\frac{1}{2}}$ )	$a_{con}$ (mm)	$a_{dis}$ (mm)	$\frac{a_{con}}{a_{dis}}$	Difference(%)
TM-168H	57	25.13	23.9	0.95	5
TM-168H	70	29.9	28.9	0.97	3
TM-168H	90	35.6	34.2	0.96	4
TM-168H	110	40	39	0.98	2
TM-168H	250	53.3	55.2	1.04	-4%
TM-168H	400	59	60	1.02	-2%
TM-168H	800	62	59.1	0.95	5%

## 6.7 Discussion

The following figures(see Fig.(65)-Fig.(67)) show the FADs for the three micro-structures. The Young's modulus for each micro-structure was calculated from the average of each tensile test and, as the Young's modulus is strain-rate independent at nominal strain-rates or has negligible dependence, the average value was taken from all strain-rates for each micro-structure.

The FADs constructed for each micro-structure show a small difference between initiation of crack failure for the same fracture toughness. This shows that the difference in micro-structure between AR, FP and TM-168H is quite negligible. However, this is only in the regime for the chosen fracture toughness.

A comparison of AR with its no Lüders strain counter part, with TM-168H was also done and shown in table 13. It is evident that AR and TM-168H with no Lüders strain predicts values of  $a_{con}$  that are greater than  $a_{dis}$ . This indicates that an upper-bainitic structure and a tempered martensite structure with no Lüders strain would be more beneficial as it predicts failure occurring later than with a Lüders strain, by 3% and 5% respectively. Mirazee-Sisan et al[4], as shown in table 9, quantified the degree of conservatism of the R6-code by calculating variables such as  $K_r$  at failure from experiment and comparing them to the R6-code prediction. As these experiments were not done and are the focus of future work, the degree of conservatism was quantified through the ratio between  $a_{dis}$  and  $a_{con}$  and then subtracted from 100% to find the difference in percentage instead. Therefore, in the AR and TM-168 micro-structure, removing the Lüders strain and, if the tensile properties will remain the same, will reduce the degree of conservatism in the domain of FAD.

The regions that a Lüders strain or the presence of a Lüders strain is beneficial is for  $K_{frac} \approx 250\text{MPa m}^{\frac{1}{2}}$  and over for TM-168H( see table 14). The amount of conservatism peaks at around -4%. This indicates that it would be desirable to have a Lüders strain at  $K_{frac} = 250\text{MPa m}^{\frac{1}{2}}$ . Further work needs to be done on TM-168H, such as the experiments by Mirazee-Sisan et al[4] for TM-168H to obtain accurate value of  $K_{frac}$ . This could reduce the current limit of  $250\text{MPa m}^{\frac{1}{2}}$ .

The above analysis shows that the degree of conservatism depends on the point of operation on the FAD, though for  $K_{frac} > 250\text{MPa m}^{\frac{1}{2}}$ . having a Lüders strain is desirable at -155 °C.

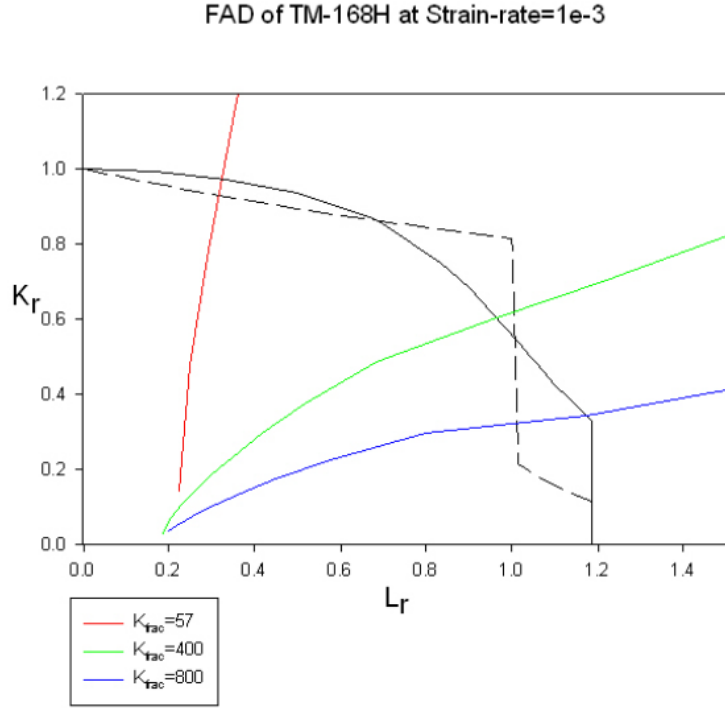


Figure 70: The value of  $K_{frac}$  for 57, 400 and 800 MPa  $m^{\frac{1}{2}}$

## 6.8 Conclusion to FADs

- a) In terms of crack initiation, there is little difference between micro-structures for the same fracture toughness. Therefore, micro-structure alone, at least in the above analysis has negligible effect on crack initiation<sup>23</sup>.
- b) The difference between the constructed FAD of AR and AR without a yield stress, in terms of crack length initiation, was about 5% (see table 13). The difference in length was taken to be a measure of conservatism to quantify the difference in FADs, although it was also evident from the shape of the FADs that the amount of conservatism would depend on the region of operation of the FAD.
- c) TM-168H or the tempered martensite structure, as shown in table 13, had two comparisons similar to AR, without a Lüders strain. It was shown that for different values of  $K_{frac}$ , despite having a Lüders strain

---

<sup>23</sup>Assuming no difference in fracture toughness

of 3.5%, were comparable to AR. This shows that a Lüders strain irrespective of size, does not make a substantial difference to the point of crack initiation, at least in the regions shown on Fig.(67).

- d) Having a Lüders strain for the assumed value of  $K_{frac} = 57 \text{ MPa m}^{\frac{1}{2}}$  for all micro-structures indicates that removing the Lüders strain would be beneficial and reduce conservatism. This also applies to values up to  $K_{frac} = 110 \text{ MPa m}^{\frac{1}{2}}$  at  $-155^\circ\text{C}$ .

Although the values up to  $K_{frac} = 110 \text{ MPa m}^{\frac{1}{2}}$  were calculated for TM-168H it can be generalised to AR and FP as the difference in FAD is small compared to the effect of increasing  $K_{frac} = 57$  to  $K_{frac} = 110 \text{ MPa m}^{\frac{1}{2}}$

## 7 Modelling Analysis

The model derived in chapter 3 is tested against some of the data and key parameters such as the dislocation velocity  $v_d$ , the maximum strain-rate  $\dot{\varepsilon}_{max}$ , the mean free path  $S_0$  and the dislocation density  $\rho_{max}$  will be calculated. Lesser known parameters as a result of the theory will also be calculated such as the immobilization term  $\Omega$ , the constants  $\Lambda$  and  $\gamma$  and the average time for the dislocations to unpin  $\tau$ .

The constants that will be allowed to remain constant are the Taylor factor  $\hat{m}$  and the Burger's vector  $b$ .

### 7.1 Method

The method used for the tensile experiments and equipment used is outlined in chapter 4.

As discussed above, the following parameters will be calculated.

- $v_d$ -The dislocation velocity within the band.
- $S_0$ -The mean free path of the dislocations
- $\dot{\varepsilon}_{max}$ -Maximum strain-rate within the band.
- $\rho_{max}$ -The maximum dislocation density within the Lüders band
- $\Omega$ -Remobilization term
- $\Lambda$  and  $\gamma$ -Parameters
- $\tau$ -The average time for the dislocations to become unpinned during propagation

With  $\hat{m} = 2$  and  $b = 2.5 \times 10^{-10} \text{ m}$ <sup>24</sup>.

The only parameter that will be calculated externally is the dislocation velocity through Nilsson et al[66]. That is:

$$v_d = 1.7 \times 10^{-5} (\dot{\varepsilon}_{nom})^{0.6} m \text{ s}^{-1} \quad (190)$$

---

<sup>24</sup>The values of  $b$  and  $\hat{m}$  were taking from Bergstrom et al[5] and are considered average values for steel. Therefore, it is assumed that the length of the dislocations for all the material used are the same.

where  $\dot{\varepsilon}_{nom}$  is the nominal strain-rate.

The above correlation was done for 0.03% C[66], therefore in its current form, it is not representative of the materials under consideration. Consequently, Equ.(190) requires modification. This is done by substituting  $\dot{\varepsilon}_{nom}$  for the maximum strain-rate within the Lüders band of each material  $\dot{\varepsilon}_{max}$ .

The following formulae were used to calculate the following quantities, based on the work from chapter 3.

$$S_0 = \frac{v_d}{\gamma \hat{m}} \quad (191)$$

$$\dot{\varepsilon}_{max} = \frac{\gamma}{4\Omega} \quad (192)$$

$$\rho_{max} = \frac{\hat{m}\varepsilon_L}{4bS_0} \quad (193)$$

$$\Omega = \frac{1}{\varepsilon_L} \quad (194)$$

$$\tau = \frac{\Lambda + 1}{\Lambda\gamma} \ln(\Lambda + 1) \quad (195)$$

while  $\Lambda$  and  $\gamma$  are obtained from curve fitting.

## 7.2 Results

1. Table 15 shows the calculated values of the aforementioned parameters, with additional terms  $\varepsilon_c$  for the localised strain on the curve and  $\tau_{acc}$  which is the time taken for the Lüders band to propagate, which were obtain from Fig.(71)-Fig.(74).
2. Fig.(71)-Fig.(74) show the model curve of Equ.(108) against the data at strain-rate of  $1 \times 10^{-3} \text{s}^{-1}$ , showing good correlation between experiment and theory.

Table 15: The calculated values of the material parameter  $\Omega, \gamma, \Lambda, \rho_{max}, S_0, \varepsilon_L, \dot{\varepsilon}_{max}, v_l, v_d, \tau$  and  $\tau_{acc}$ 

Material	$\Omega$	$\gamma(s^{-1})$	$\Lambda$	$\rho_{max}(m^{-2})$	$S_0(\mu\text{m})$	$\varepsilon_c(\%)$	$\varepsilon_L(\%)$	$\dot{\varepsilon}_{max}\text{s}^{-1}$	$v_l(\text{m/s})$	$v_d(\text{m/s})$	$\tau(\text{s})$	$\tau_{acc}(\text{s})$
AR	79	0.75	399	$2 \times 10^{13}$	1.2	1.23	0.83	$2.28 \times 10^{-3}$	$4.21 \times 10^{-3}$	$4.5 \times 10^{-7}$	8	8.4
	24	0.54	196	$3 \times 10^{13}$	2.9	4.21	3.5	$5.63 \times 10^{-3}$	$1 \times 10^{-3}$	$7.8 \times 10^{-7}$	9.8	10
TM-168H	79	1.28	1122	$2.3 \times 10^{13}$	1.1	1.261	1.46	$5.23 \times 10^{-3}$	$2.4 \times 10^{-3}$	$7.3 \times 10^{-7}$	5.5	6
	17.5	0.66	620	$3.8 \times 10^{13}$	3	5.73	5.51	$8.46 \times 10^{-3}$	$6.35 \times 10^{-4}$	$9.7 \times 10^{-7}$	9.74	10.2

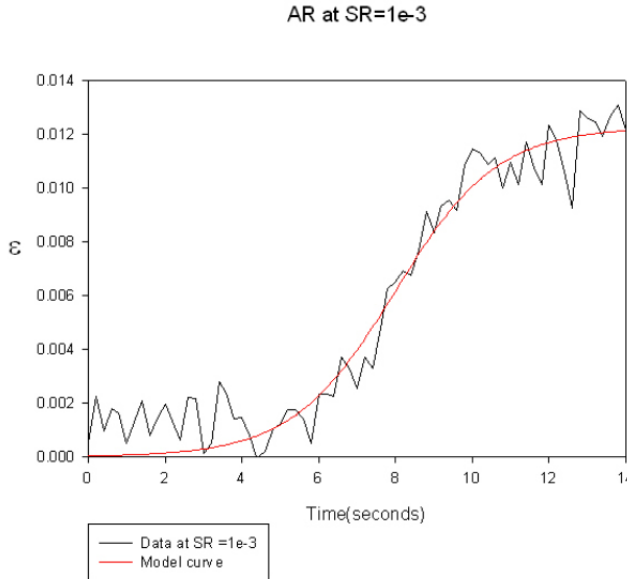


Figure 71: Strain-time curve of AR with model curve in red and data in black at strain-rate  $1 \times 10^{-3} \text{ s}^{-1}$

### 7.3 Discussion

The model has been applied to materials with different micro-structures and compositions. That is, an upper-bainitic structure (AR), tempered martensite structure(TM-168H), ferrite with some pearlite structure(AL) and pure ferrite with almost negligible amount of carbon present(UL).

The model shows good correlation with the UL structure, as shown in Fig.(74) and  $R^2$ (correlation strength) of 0.99. This is to be expected, at least from the view of the theory, as it was assumed the exponential factor according to Gilman[45] that the small strain displacement within the Lüders band and the frictional effect of the dislocations during band propagation was of first order<sup>25</sup>.

There is also good correlation for materials of higher carbon content, such as the mild steel with the manganese sulphide particles(see Fig.(73)). This shows that although the carbon content is ten times the amount of the UL-steel and, additionally, with iron-carbide on the grain-boundaries and manganese sulphide particles in abundance, the overall effect is still of first order i.e. obeys Equ.(108).

The model also correlates well with the steel of AR and TM-168 micro-structures.

---

<sup>25</sup>First order friction refers to the approximation Gilman[45] made, when deriving an equation of the form of Equ.(87)(see chapter 3). It was that  $df \approx -fd\varepsilon$ , where  $f$  is the fraction of mobile dislocations lost in the Lüders band during band propagation

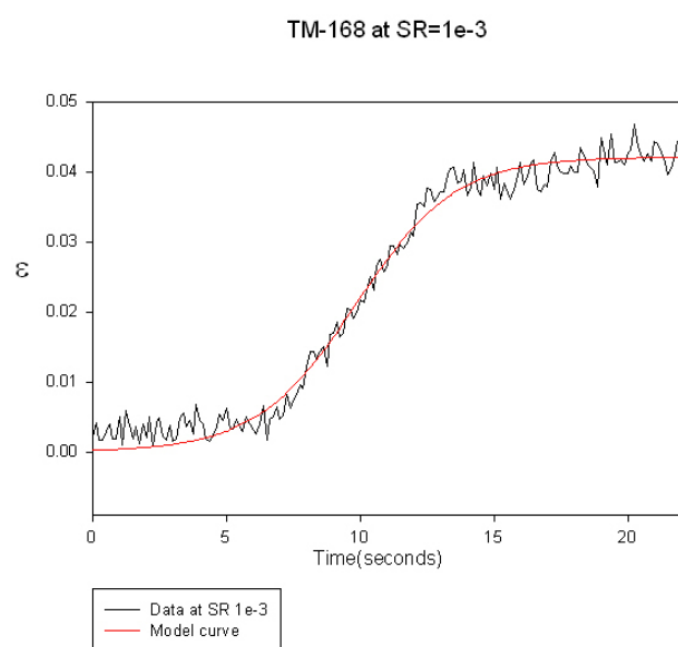


Figure 72: Strain-time curve of TM-168H with model curve in red and data in black at strain-rate  $1 \times 10^{-3} \text{ s}^{-1}$

AL at SR=1e-3

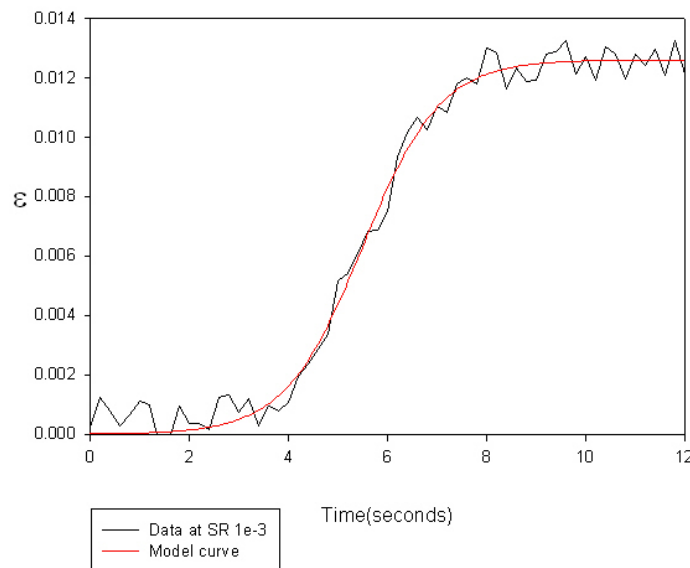


Figure 73: Strain-time curve of AL with model curve in red and data in black at strain-rate  $1 \times 10^{-3} \text{ s}^{-1}$

UL at SR=1e-3

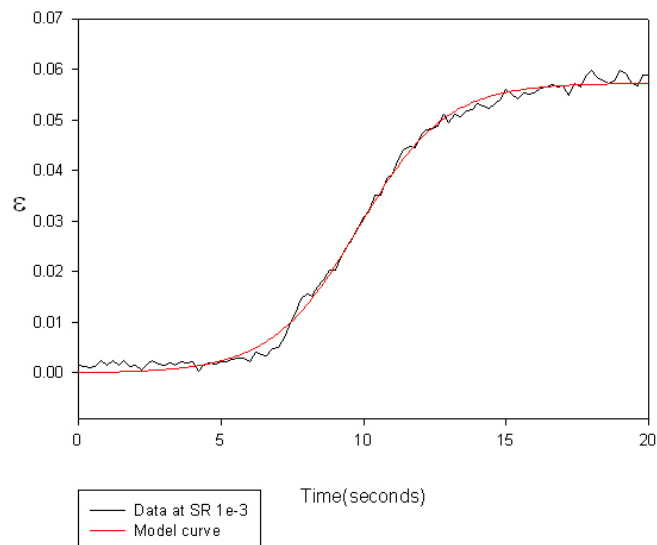


Figure 74: Strain-time curve of UL with model curve in red and data in black at strain-rate  $1 \times 10^{-3} \text{ s}^{-1}$

AR structure is an upper-bainitic structure in contrast to its tempered martensite counter-part, the TM-168H. Despite the different tensile properties(see appendix A) with tables of the tensile results for AR and TM-168H, such as yield stress and ultimate tensile stress, the shape of the Lüders band and the dynamics that govern the shape, due to Equ.(108), are quite similar. This shows that the approximation of first order friction on the dislocations(Gilman[14]) is justifiable. To what extent the model can be used or what amount of carbon content is required to prevent a sigmoidal type shape is uncertain. A possible answer will be discussed in the latter part of this section.

Table 15 shows in more detail the calculated variables as a result of the curve fitting to the data. It is evident that the numbers, for the dislocation density are credible and expected for steel[5]. However, this was at the expense of large mean free-paths. A credible number according to Bergstrom[5] is approximately  $S_0 \approx 1 \times 10^{-7}$ m, but this gives dislocation values, according Equ.(193), of about  $\rho \approx 10^{15}$ . This is too large for strain-rate  $1 \times 10^{-3}$  s $^{-1}$ . This can be resolved by calculating the dislocation velocity directly through experiment. As the Equ.(191) was used for the mean free-path and is dependent on the dislocation velocity, an accurate value of the dislocation velocity during band propagation would produce a mean free-path that is more representative of the materials in table 15. It is evident that the variation of  $\gamma$  does not vary significantly with the micro-structure, apart from its value in AL.

The grain-size of the different micro-structures seems not to affect  $\gamma$ , this is evident from the range of grain-sizes from UL which has a grain size of approximately 40μm to AR of 10μm. It must therefore be the structure within the grains i.e how the carbides are distributed.

However, as shown in Fig.(71)-Fig.(74), the micro-structure of the differing materials has managed to maintain approximately similar profiles, albeit scaled differently because of the size of the Lüders strain. Therefore, this shows that the effect of the carbides does not alter the profile of the curve and, therefore, does not change  $\gamma$  significantly between AR, TM-168 and UL. Consequently, as the AL is the only material out of the tested materials that has manganese sulphide particles, it is reasonable to suggest that the presence of the manganese sulphide particles are responsible for the significant increase of  $\gamma$  with respect to the other materials.

The term  $\gamma$  is interpreted as the frequency of the Lüders band with units

of  $\text{s}^{-1}$  from:

$$\tau \propto \frac{1}{\gamma} \quad (196)$$

The magnitude of the Lüders strain was the largest for the UL structure and the TM-168H structure. They also have the largest maximum dislocation density. This is attributed simply to Equ.(124) which states that  $\rho_{max}^{\frac{1}{2}} \propto \varepsilon_L$ . Consequently, from the data, it is reasonable to suggest that the larger the Lüders strain, assuming comparable mean free paths, the larger the dislocation density. Although, it should be noted that other factors such as the grain size, micro-structure and rate of dislocation multiplication can also effect or contribute to the number of free dislocations being released.

The difference of Lüders strain between AR and TM-168H can not be attributed to the carbon content alone, because they have the same composition. Therefore, it is a micro-structural dependence. It was stated in the chapter 4, as a consequence of the model, that if the compositions are similar and the grain-sizes are assumed similar, then the difference in Lüders strain is attributed to the mean free path parameter  $S_0$ . However, it was tacitly assumed that the dislocation density would be similar. In the case of table 15 it is evident that  $S_0$  is smaller in the upper-bainite structure than TM-168H. Yet, the Lüders strain in TM-168H is still larger than AR. This is explained through the difference of the maximum dislocation density.

The value of the maximum dislocation density for TM-168H is  $3 \times 10^{13} \text{ m}^{-2}$ , while for AR it is  $2 \times 10^{13} \text{ m}^{-2}$ , which gives a difference in dislocation density of  $1 \times 10^{13} \text{ m}^{-2}$ . It is the additional amount of  $1 \times 10^{13} \text{ m}^{-2}$  in the confines of the model that gives TM-168H its additional Lüders strain.

The dislocation velocity was calculated using Equ.(190). To have a more representative value for the dislocation velocity of each material the maximum strain-rate in the Lüders band was taken instead of the nominal or tensile strain-rate, because the value of the dislocation velocity for each material would have been the same, which is incorrect.

The dislocation velocity is greatest in the UL, followed TM-168H and AR. Not surprisingly, this trend is also observed in the band velocity, showing a clear correlation between the Lüders velocity  $v_l$  and the dislocation velocity  $v_d$ . Such a relation can be derived from Equ.(192) and from the definition of  $v_l$ , that is:

$$v_l = \frac{v_m}{\varepsilon_L} \quad (197)$$

where  $v_m$  is the machine velocity.

Equ.(192) in terms of the Lüders strain can be written as:

$$\dot{\varepsilon}_{max} = \frac{\gamma \varepsilon_L}{4} \quad (198)$$

substituting Equ.(197) into Equ.(198) and the definition of  $\gamma$  i.e.  $\gamma = \frac{v_d \hat{m}}{4S_0}$ , one obtains:

$$v_l = \frac{\hat{m} v_d v_m}{4S_0 \dot{\varepsilon}_{max}} \quad (199)$$

or

$$v_l \propto v_d \quad (200)$$

that is the velocity of the Lüders band is proportional to the dislocation velocity. This agrees with the observation made by Hahn[18].

$\varepsilon_c$  was defined as the local strain in the model plateaus. It is evident that  $\varepsilon_c$  agrees with the measured Lüders strain.  $\varepsilon_c$  could possibly be a better representation of the Lüders strain, as the value of the Lüders strain is usually measured by eye and therefore lacks rigour. The procedure of measuring  $\varepsilon_c$  is much more thorough and agrees with the interpretation of the theory that the Lüders strain, locally, is a measure of the strain required to free the dislocations for a given region.

It is tacitly assumed in this model that the form of the sigmoidal curve or shape remains constant through time, when travelling as a wave. In other words it is assumed that there is no dampening, during the propagation of the Lüders band. However, as shown in Fig.(75) of the tensile specimen taken from DIC and the corresponding strain-time(frame number) profiles of each of the Lüders bands(Fig.(76) and Fig.(77)), the sigmoidal curve does flatten and therefore  $\varepsilon_c$  reduces in value and is less than  $\varepsilon_L$ . Consequently, if dampening is significant then the local value of  $\varepsilon_c$  could not be taken as a measure of the Lüders strain and an additional function, say  $f(x)$ , would be coupled to Equ.(108) to take into account the flattening the curve as it propagates. To determine such a function, many values would have to be taken across the gauge length, resulting in figure such as Fig.(76) and Fig.(77), and the measured values of  $\varepsilon_c$  for each band would be plotted against the distant that the strain-time curves were measured and through curve fitting the form of  $f(x)$  could be determined. The average time calculated from Equ.(109) is shown to be in good agreement with the observed time for the band to propagate across the region of interest.

It was stated, according to Bergstrom[5], that the definition of  $\tau$  is the time taken for immobilized dislocations to remobilize and is related to the

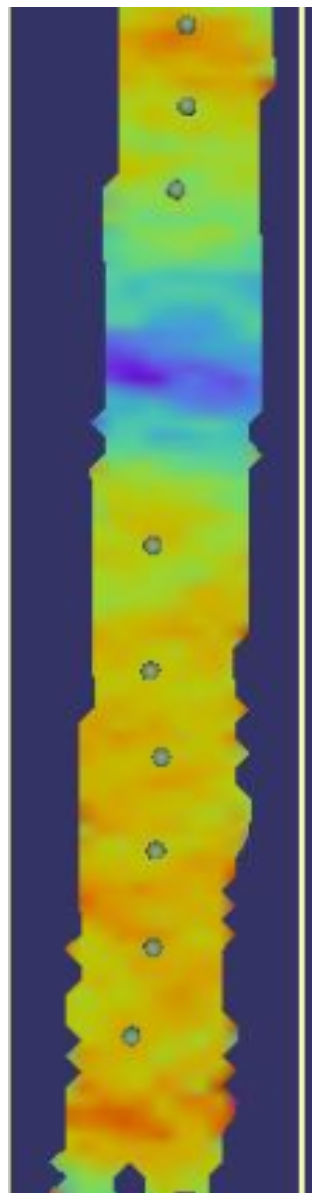


Figure 75: Tensile specimen taken from DIC software, showing points 1-5 of the first band, starting from the bottom and ending at the top of the first band (the longest band) and points 1-3 of the second band (starting from the top of the second band and ending end at the bottom of the second band (the smallest band) of UL-05 at strain-rate  $1 \times 10^{-2} \text{ s}^{-1}$ .

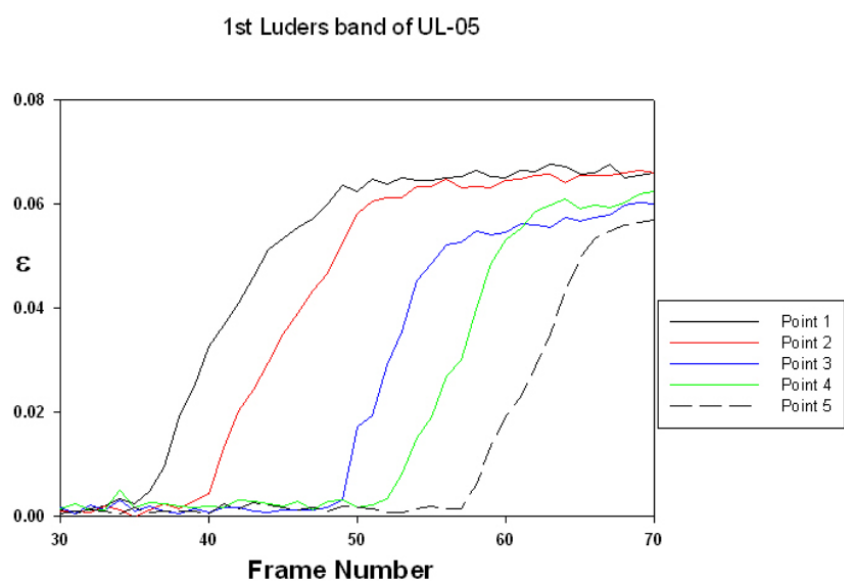


Figure 76: Points 1-5 of the first Lüders band nucleated at the bottom of the tensile specimen, see Fig.(75) with point 1 starting from the bottom, shows a reduction in the Lüders strain as it propagates to the last point on the first band. This characteristic of dampening.

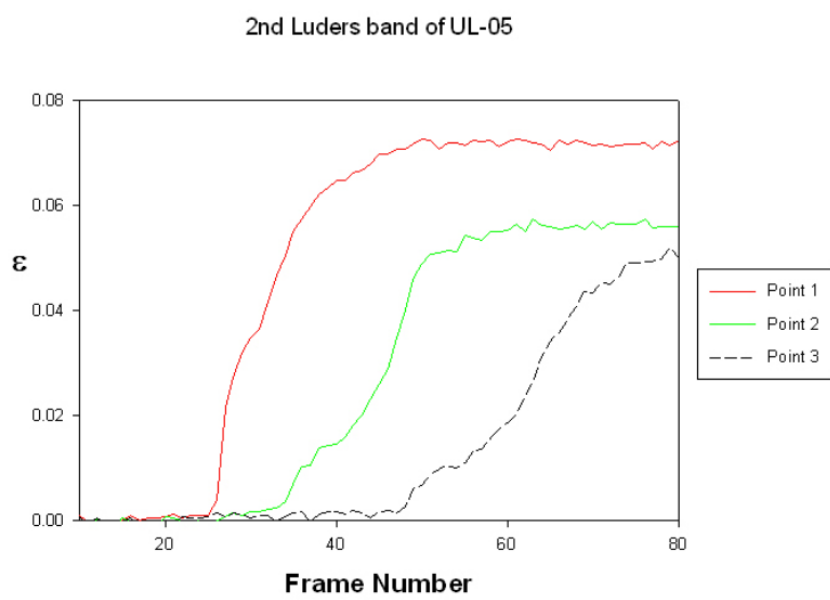


Figure 77: Points 1-3 of the second Lüders band(nucleated at the top) of UL-05 have strains that are less than the first band, because nucleation occurred later and therefore at a lower stress. However, dampening is evident in the second band, too.

remobilization parameter  $\Omega$ . According to table 15  $\tau$  is the average time taken for the band to propagate across a given area. Therefore, this shows that time averaging the dislocation density of Equ.(106) is equivalent to time averaging the strain on the curve. It also shows that, if Bergstrom's interpretation of  $\tau$  is correct, then the most dominant mechanism for a remobilized pinned dislocation, is the release of the dislocations from the carbon atmospheres.

It was stated earlier in the discussion that it was not clear as to what extent in terms of carbon content a sigmoidal profile would remain. A possible answer to this can be seen from the definition of  $\tau$ (Equ.(112)). That is

$$\tau = \frac{\Lambda + 1}{\Lambda} \frac{\ln(\Lambda + 1)}{\gamma} \quad (201)$$

Also looking at Equ.(108) and taking the strain when  $t=0$  gives:

$$\Lambda + 1 = \frac{1}{\varepsilon_i \Omega} \quad (202)$$

where  $\varepsilon_i$  is the initial strain.

Since  $\Omega$  is the reciprocal of the Lüders strain(Equ.(119)), the following is obtained:

$$\Lambda + 1 = \frac{\varepsilon_L}{\varepsilon_i} \quad (203)$$

noting that generally from the data of table 15  $\frac{\Lambda+1}{\Lambda} \approx 1$  and substituting  $\Lambda + 1$  back into the Equ.(201) gives:

$$\tau \approx \frac{1}{\gamma} \ln \left( \frac{\varepsilon_L}{\varepsilon_i} \right) \quad (204)$$

Therefore, when  $\tau$  is zero it will correspond to carbon contents, where  $\frac{\varepsilon_L}{\varepsilon_i} \approx 1$ .

$\Omega$  in the literature review has been regarded as a constant of about 5 for typical ferrite steel[5]. It is evident in table 15 that the values of  $\Omega$  are not in agreement with the literature. However, the values quoted in the literature are for the general case of  $\omega \neq \Omega$ , where  $\omega$  is dependent on the micro-structure of the material. As the values of  $\omega$  can be up to 271 for ferrite steel[5], it is not surprising that the values calculated for  $\Omega$  in table 15 are between these the values of 5 and 271, as only the special case was considered i.e.  $\omega = \Omega$  in the derivation in chapter 3 . The value of  $\Omega$  taken from the literature was shown by Bergstrom to be both strain-rate and temperature dependent. Therefore, it is evident that under certain conditions the value

of  $\Omega$  can be greater than 5. For example, at 77K for copper it is about 6[47]. Also,  $\Omega$  calculated in the literature was for homogeneous deformation and, therefore, not representative of values within a Lüders band. Consequently, it is reasonable to suggest that the values of  $\Omega$  in table 15 are representative of Lüders bands, until further research is done on specifically calculating  $\Omega$  within the Lüders band.

## 7.4 Conclusion

- a) The strain-time curve of a Lüders band is approximately sigmoidal and has the same form for all materials tested. This shows that the amount of carbon content makes little difference to the profile of the band, in the range of carbon content tested.
- b) The model works for all the materials tested. This is indicated by the correlation strength range of  $R^2 = 0.99 - 0.98$ . Further, it shows that the dislocation dynamics in all the materials, irrespective of the different micro-structures, are similar. Consequently, the increased precipitate density with carbon content does not impede the dislocations to a high degree such that the obstacles behave more as voids.
- c) The inclusion of manganese sulphide clusters speed up the Lüders band and in the process, shorten the Lüders strain compared with a material of the same composition without manganese sulphide clusters. This is shown when looking at  $\gamma$  for the materials in table 15.
- d) The dislocation density is larger for the TM-168H and the UL, because they have the largest Lüders strain. This explains why within the model, the Lüders strain is larger in the TM-168 than AR for the same composition, despite the mean free path of AR being less than TM-168H. This shows that the effect of the dislocation density on the Lüders strain for different micro-structures is more dominant than the effect of the mean free-path, which is due to a smaller grain-size.
- e) The time taken for the Lüders strain to propagate through a given area can be calculated from  $\tau$ . Bergstrom[46] interpreted Equ.(109) as the time take for immobilized dislocations to move from the carbon atmosphere. If this is assumed to be correct, then the time taken for the propagation of the band can be assumed to be a measure of the time

take for the dislocation to free themselves from the carbon atmospheres and, therefore, validates the assumption of interpreting  $\rho_0 = 0$ .

- f) The profile on the band contrary to the model dampens during propagation. This results in a flattening of the curve as a function of distance across the gauge length, represented as a function( $f(x)$ ). This opens the possibility of each material having a unique function  $f(x)$ , dependent on the dampening and, therefore, characteristic of the micro-structure of the material.
- g) The velocity of the Lüders band is linearly related to the dislocation velocity, see Equ.(199). This was also observed by Hahn[18].

## 8 Modelling of the tensile and hole defect

The following chapter will show the comparison of the Zhang model outlined in chapter 3 with the tensile data, taken from the experiments on AR at  $1 \times 10^{-2}$  and  $1 \times 10^{-3} \text{ s}^{-1}$  and the data taken from chapter 5 for biaxial stresses that were tested on TM-28H structure having a 1.5 mm hole and TM-168H with a 1mm hole.

It was shown through the data of chapter 5 that difference in tensile properties such as yield point were small. It was concluded in the same chapter that the amount of precipitates due to the increased spheroidization made little difference to the overall tensile properties of the stress-strain curve of the tensile specimen with the circular defect(see Fig.(47)). Therefore, in this chapter the model will only be applied to the TM-28H data, because of the similarities between TM-28H and TM-168H.

### 8.1 Method

The Finite element or FE model used the ABAQUS 6.9 code with the standard ABAQUS vumat packaging for the work-hardening with the subroutine for the Lüders plateau(see appendix G).

It was stated in the description of the Zhang model that, when applying the model to mild steel that some of the parameters were adjusted to fit the tensile data. This was also done for the TM-28H steel, because the values in table 16 did not produce the observed yield point. The method of the modelling of the tensile experiments are described in section 4.3.

The size of the mesh for the tensile experiment was about 6850 elements with hexagonal elemental type. For a simple geometry this is adequate as meshes with greater sizes cost more computer time and did not produce different results significantly from the tensile data presented in this chapter.

The specimen was set to pull a total of 3.5mm with total number of 100 frames to obtain a strain-rate of  $1 \times 10^{-2} \text{ s}^{-1}$  and  $1 \times 10^{-3} \text{ s}^{-1}$  for AR with the following boundary conditions:

- Constrained on one side, known as encastre.
- Eight lines of concentrated force nodes applied at the end of the model, not the constrained side.
- The displacement of the force was dynamic explicit.

Table 16: Values of the parameters used for AR and TM-28H modelling with the blanks indicating dimensionless quantities.

Parameter	Value	unit
$\dot{\varepsilon}_0$	100	
$D_1$	500	MPa
$D_2$	325	MPa
$D_3$	0.065	
$\omega_1$	$1 \times 10^{-6}$	
$\omega_1$	$1 \times 10^{-5}$	
$N$	1	
$T_A$	4000	seconds
$\alpha$	0	
$\beta$	0.68	
$P_1$	37	MPa
$P_2$	0.001	
$S_1$	12.5	MPa
$S_2$	5	MPa
$C_M$	1	

## 8.2 Results

- Fig.(78) shows a comparison of the stress-strain predicted by the Zhang model at strain-rate  $1 \times 10^{-2} \text{ s}^{-1}$  and  $1 \times 10^{-3} \text{ s}^{-1}$  (shown in red and black, respectively) and the stress-strain curves from AR at the same strain-rates (shown in black and green, respectively). The value of the parameter  $D_1$ , which was interpreted as the lower yield point, was set 500 MPa.
- Fig.(79) shows the point of necking in the specimen.
- Fig.(80) shows the specimen geometry with a hole cut inside. The hole is placed in the centre, contrary to the position of the holes in the experiment, which were not in the centre.
- Fig.(81) shows the stress-strain curve as calculated from the model of Fig.(80). The yield stress is reduced from the initial value of  $D_1 = 635$  to just under 400MPa. Also showing a UTS of over 500 MPa.
- Fig.(82) shows the elements taken at the top of the hole to determine

whether a Lüders type strain-time curve or signature was evident. The result is shown in Fig.(83) for 18 of the elements. It is evident that the majority of the curves of the left portion of the graph deform homogeneously, while the form of deformation of the curves on the right is less clear.

- Fig.(84) is taken from the same model as Fig.(82), but for elements on the left side of the hole. The elements are plotted in Fig.(85) which shows homogeneous deformation similar to Fig.(45) and Fig.(46)(see chapter 5) with a higher magnification in Fig.(86).
- Fig.(87) shows the point of yielding at frame 116, which corresponds to approximately 16 seconds. It is evident that the model of Zhang produces a similar effect in Fig.(80), because it is yielding in the expected areas.

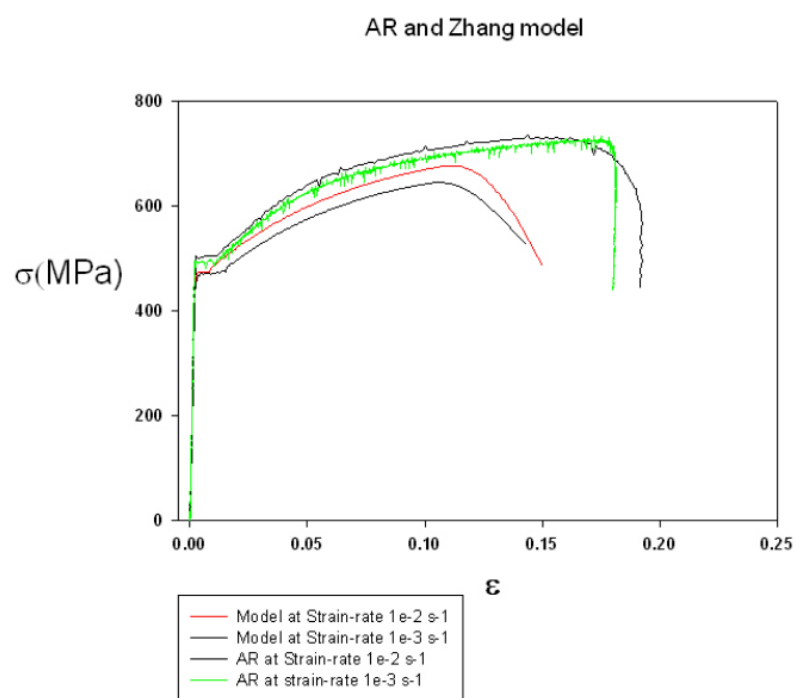


Figure 78: Comparison of the Zhang model with AR at strain-rate  $1 \times 10^{-2} \text{ s}^{-1}$  and  $1 \times 10^{-3} \text{ s}^{-1}$  with parameter  $D_1 = 500 \text{ MPa}$  compared with the model data at the same strain-rates.

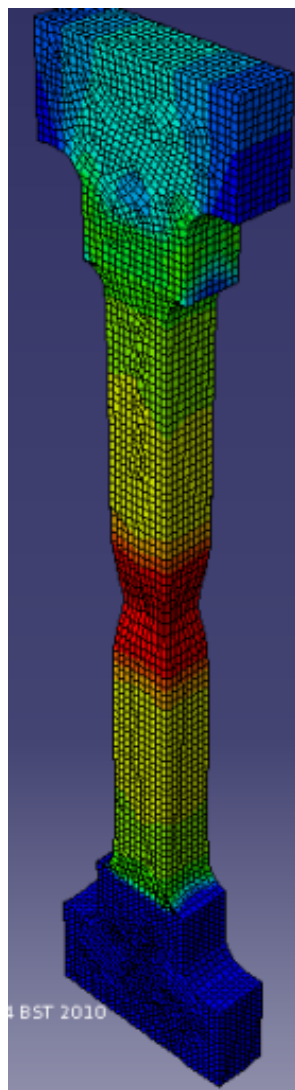


Figure 79: Zhang model at point of necking, showing key feature of dislocation pile up on grain-boundary.

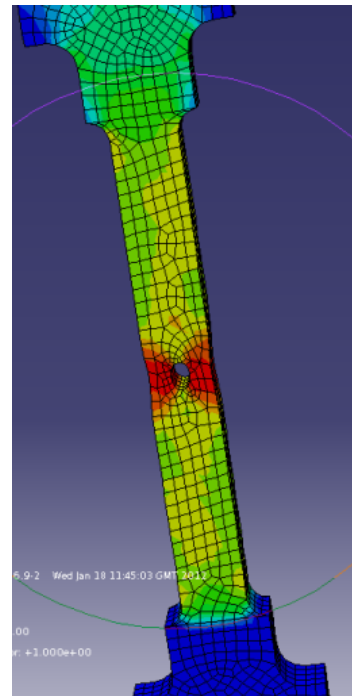


Figure 80: Point of yield of 1.5mm hole with  $D_1 = 635$  at time at point of yielding.

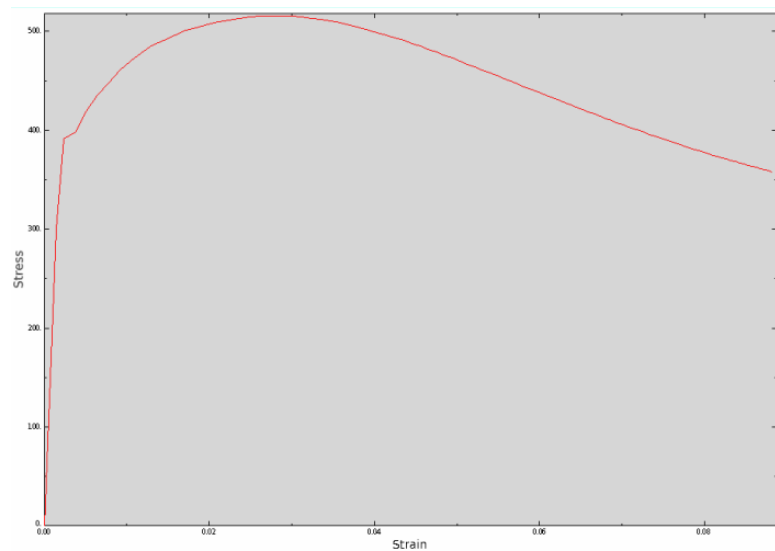


Figure 81: Calculated stress-strain-curve of Fig.(80).

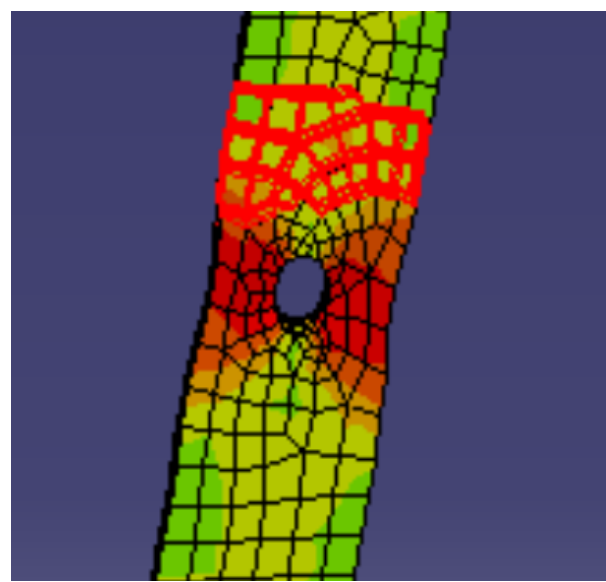


Figure 82: Elements taken from top of hole of TM-28H model plotted in Fig.(83).

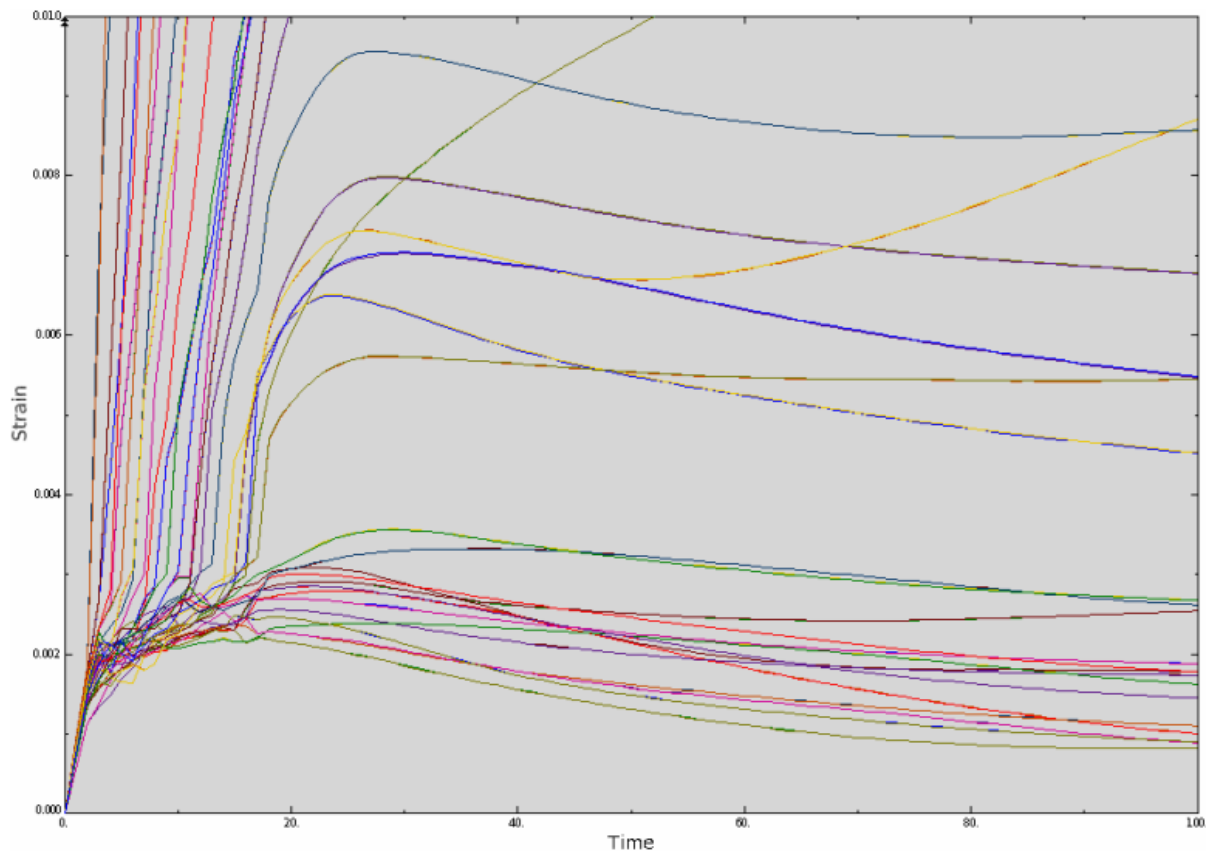


Figure 83: Strain vs time(in seconds) for approximately 18 elements around the elements in Fig.(82) at strain-rate  $1 \times 10^{-3} \text{ s}^{-1}$  on the top.

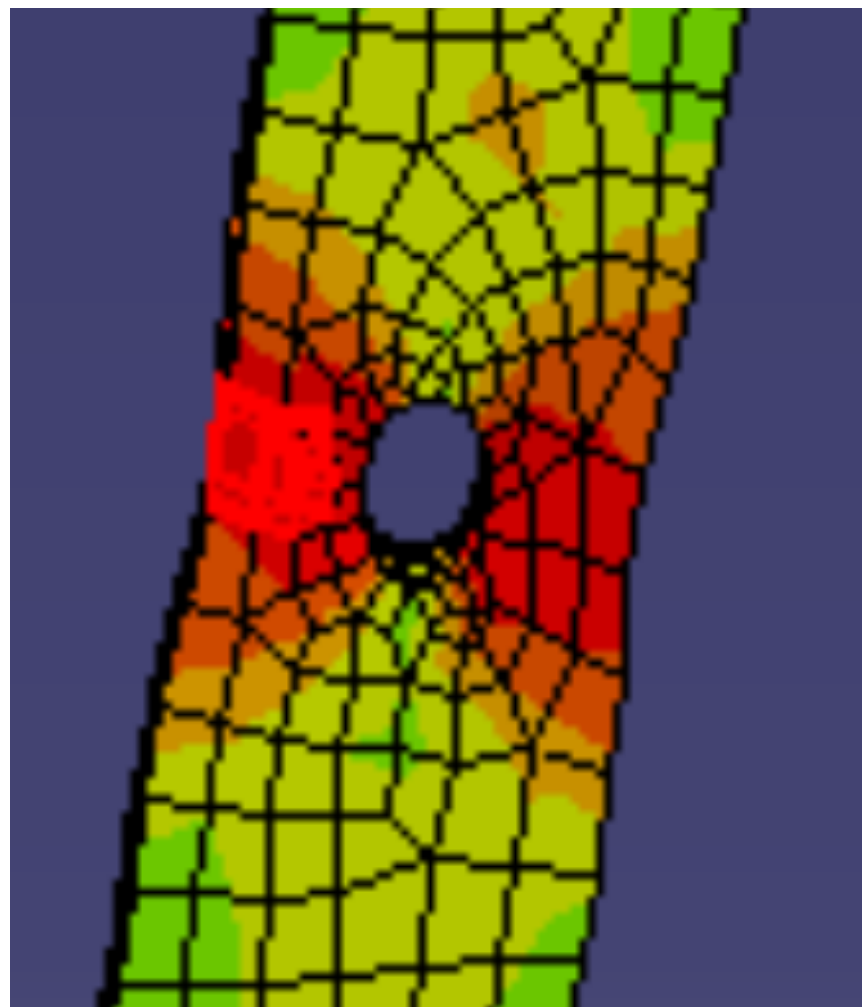


Figure 84: Elements taken from the left of hole of TM-28H model plotted in Fig.(85).

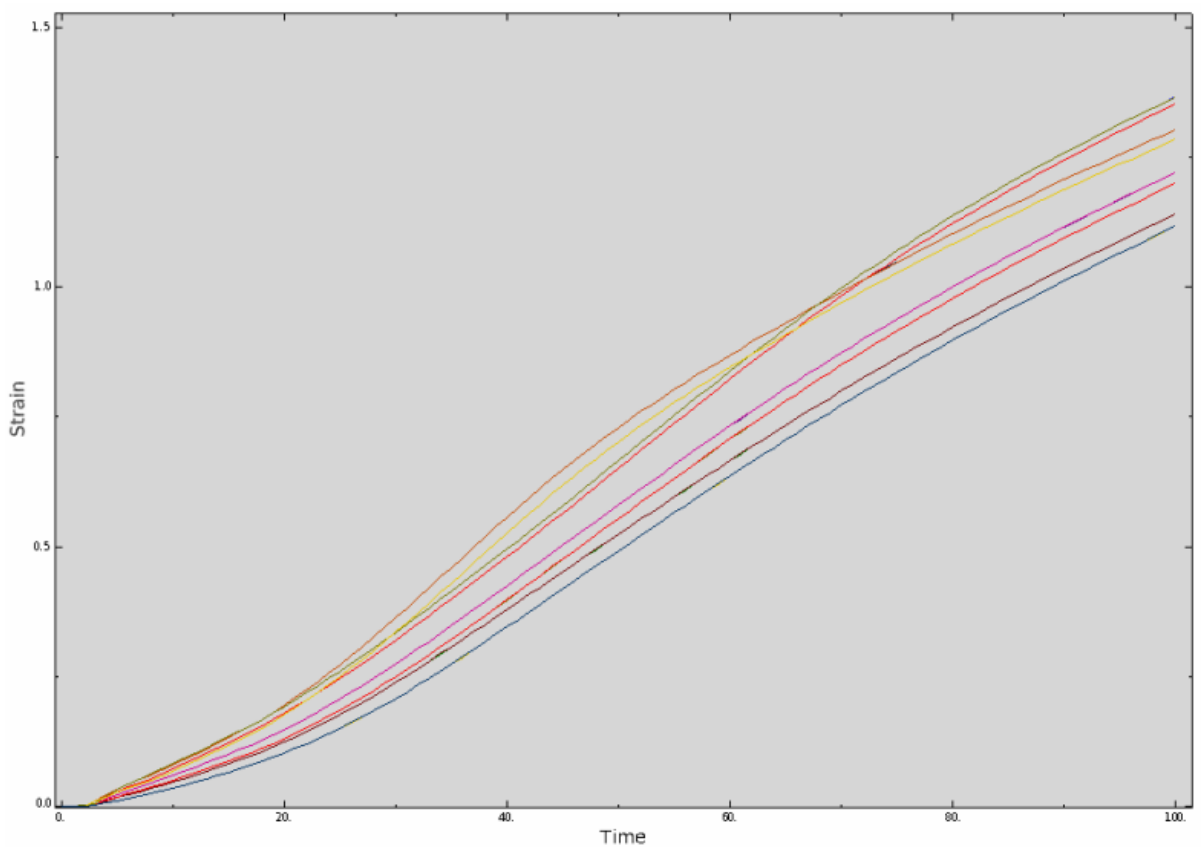


Figure 85: Strain vs time(in seconds) for approximately 10 elements around the elements in Fig.(84) at strain-rate  $1 \times 10^{-3} \text{ s}^{-1}$ .

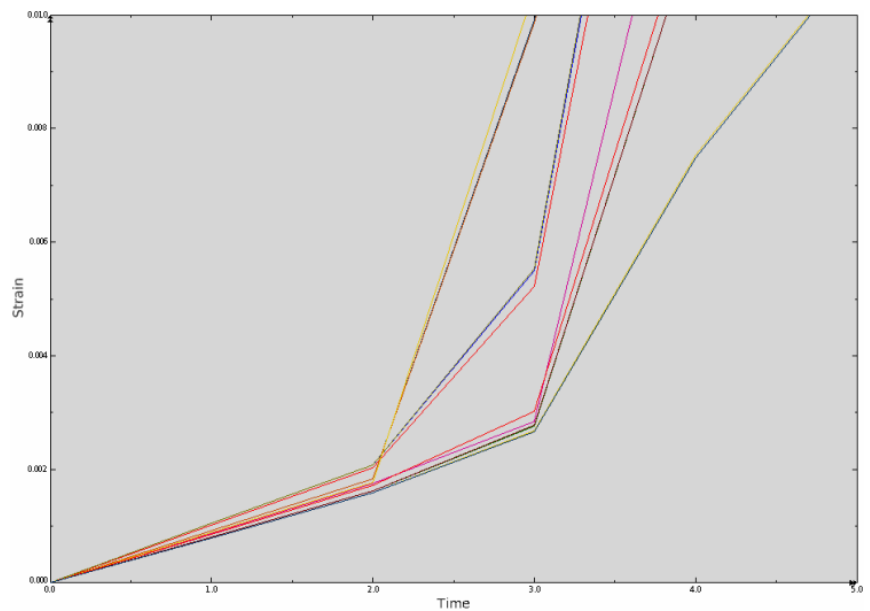


Figure 86: Magnification of Fig.(85) indicating no evidence of a Lüders band or sigmoidal strain-time curve.

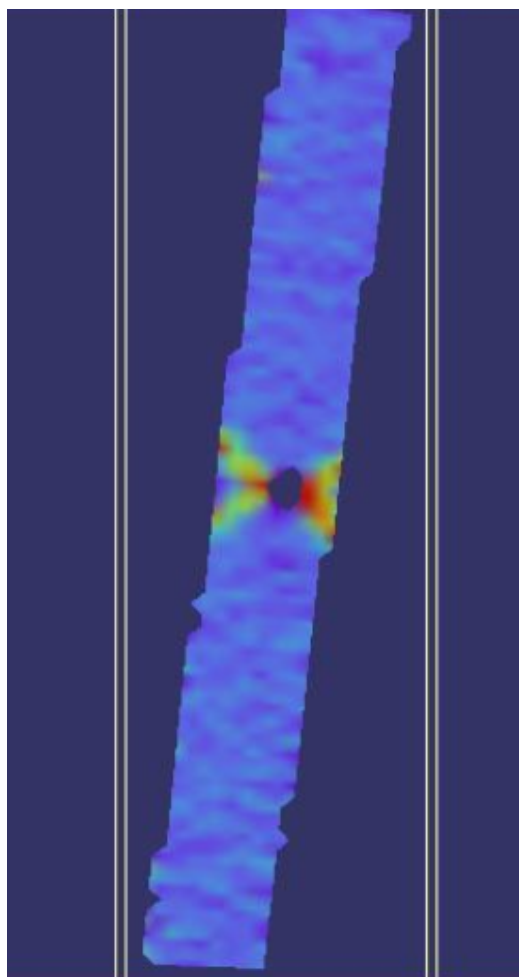


Figure 87: Point of nucleation for TM-28H

### 8.3 Discussion

The Zhang model has been compared to low alloy steel of the AR and TM-28H micro-structures of RPV steel. The former was compared to the tensile data, while the latter was compared to the tensile data with a circular defect.

The model compared to the tensile data of AR at  $1 \times 10^{-2} \text{ s}^{-1}$  produces all the characteristics of the stress-strain curve uniaxially of a specimen with the experimented geometry (see Fig.(78)). However, although the value  $D_1$  was set to the same lower yield stress as AR from the data, it is evident that the model curve(red) predicts a lower overall yield stress and consequently a lower Lüders strain, as the Lüders strain is related to the yield stress. The UTS of the model is also less than the UTS of AR. This shows that the model parameters of table 16, which took the same values when modelling AR TM-28H apart from  $D_1$ (as it had to be adjusted to account for the yield stress) did not describe the Lüders strain and work-hardening correctly. Consequently, the parameters need to be adjusted to get a more reflective stress-strain curve.

The strain-rates at  $1 \times 10^{-2} \text{ s}^{-1}$  and  $1 \times 10^{-3} \text{ s}^{-1}$  are shown in Fig.(78), illustrating that most of the tensile properties of the stress-strain curve decrease with strain-rate such as the UTS and yield stress. However, the Lüders strain does not follow the trend contrary to observation and standard theory. That is, the Lüders strain increases with the strain-rate. The cause is attributed to computation error within the model and the code, though a transition from  $1 \times 10^{-2}$  to  $1 \times 10^{-3}$  should not produce difficulty for the model as the strain-rate is adjusted in the ABAQUS program and not the subroutine of appendix G. Therefore, the reduction in Lüders strain is considered as an anomaly and not reflective of the model's ability to handle different strain-rates.

Although the Zhang model in the stress-strain graph of Fig.(78) did not produce the correct tensile properties of AR, the model did produce the characteristic stress-strain curve of a material that has a Lüders strain up until necking (see Fig.(79)). Therefore, given enough time for experimentation, as demonstrated by Wenman et al[1] in chapter 6, the model could produce the correct stress-strain curve. However, the only concerns would be the work-hardening rate as it uses standard vumat work-hardening package of ABAQUS(see appendix G) and producing the correct Lüders strain. The work-hardening model does not factor in micro-structure or grain-size and the Lüders strain can not be controlled directly from the model or it requires

the adjustment of many parameters to alter the Lüders strain at the expense of altering the tensile properties of the material, such as the UTS and yield point.

The Zhang model was also compared to a tempered structure of TM-28H with the only parameter in the model  $D_1$  altered to the lower yield stress of TM-28H shown visually in Fig.(80).

The stress-strain curve produced by the model predicted a reduction in yield stress, when compared to the stress-strain curve produced without the defect (see Fig.(78) and Fig.(81)). This agreed with experiment, though the predicted yield stress was just below 400 MPa, while the actual yield stress was closer to 300 MPa. Also, the model predicted a Lüders strain with a degree of work-hardening, this is evident from the Lüders strain plateau which is inclined( see Fig.(81)). However, the stress-strain curve of the TM-28H (see Fig.(47)) did not show evidence of a Lüders strain and, therefore, inhomogeneous deformation. This is due to the positioning of the hole in the specimen. In the model the positioning of the hole in the centre and therefore was not off-set. Further work is required to quantify how accurately the stress-strain curve predicted in Fig.(81) is to the tensile test with a circular defect.

The model did agree with experiment that around the hole there was no clear evidence of a Lüders band and, therefore, no inhomogeneous deformation around the hole. This is evident in Fig.(85) and with further magnification of Fig.(86) that the deformation strain-times curves are similar to experiment. However, at the top of the hole the elements show that homogeneous deformation is not dominant(see Fig.(82) and Fig.(83)) or the form of deformation is not constant unlike Fig.(86). This is attributed to the positioning of the elements as some are more exposed to the largest areas of yield, that is from the left and right side of the hole, while others are less exposed in the same time. This results in a delay with the curves on the right side of Fig.(83) yielding later. Although the trend of the curves can be explained in terms of a delayed yielding, the variation or shape of the curve can not be explained. This degree of variation in the experiment of TM-28H was not observed. It could be a purely geometrical property of the meshes themselves. Further work is needed, possibly with finer meshes. A finer mesh could minimize geometric effects as the meshes would be more homogeneous, than the current mesh size.

## 8.4 Conclusion

- a) The Zhang model produces the correct stress-strain curve qualitatively for AR and TM-28H, though the latter can not be established presently, because of the experimental technique. Further experiments with smaller holes that are placed at the centre, are required. This shows that there is potential for the Zhang model to be used in most configurations, depending on the geometry of the defect, a sufficient mesh size is required to minimize geometric effects, as shown in this chapter.
- b) The adjustment of the parameters are required, at possibly several strain-rate, before they can be representative of a material. This is due to the complicated nature of the parameters and the number of parameters that need adjusting. However, once a suitable calibration has been established as shown in the work of Wenman et al[1] the model can translate onto multi-axial problems.
- c) The model showed that there was no evidence of a Lüders band around a hole. This is agreement with the findings of digital image correlation. Therefore, the lack of sensitivity of the DIC as being a possible cause of no Lüders band being observed, can be eliminated. This was discussed as a possibility in chapter 5 to account for the absence of a Lüders band.
- d) The nucleation of a Lüders band requires considerable tensile stress/s-strain component in the uniaxial direction in order to nucleate. Even in regions that seemed to be more tensile-based than compressive, the nucleation of the band was not detected. Therefore, if Lüders bands are to be studied multiaxially, it is important that the configuration is such that there are regions of high tensile stress(see Wenman et al [1] chapter 6) otherwise the compressive components will dominate and therefore reduce the chance of nucleation.

## 9 General discussion

The primary objective of this work was to understand the mechanism of the formation and propagation of Lüders bands, from which it would be determined whether the addition of a Lüders band in Nuclear safety structural integrity codes, like the R6-procedure and the European counter part SINTAP, would be beneficial and, therefore, reduce the degree of conservatism in secondary or residual stress calculations.

The following discussion will outline in detail how this task was achieved or to what extent, highlighting and elucidating on the main conclusions drawn from the previous chapters. General conclusions will be made with the objective of determining future work.

The subsections will consist of a theoretical, experimental and modelling parts.

### 9.1 Theoretical

The main conclusion drawn from the literature review was the Lüders strain as a function of carbon content was incorrectly correlated without considering the effect of the micro-structure with same composition. The work of Song et al[24] gave a general explanation in terms of quantifying the micro-structure or change in micro-structure by the additional work-hardening that would be required to move a dislocation with respect to a structure with no precipitates. It followed that the larger the difference in stress, the higher degree of precipitates, which would be reflected in the micro-structure.

However, as shown in chapter 3, when an empirical approach was attempted to find a unique parameter that would relate the Lüders strain to the carbon content, a new parameter  $\phi$  defined as:

$$\phi = \frac{\frac{d\sigma_{ly}}{d\varepsilon_L}}{d\sigma_{ly}} \quad (205)$$

which, instead of the work hardening alone, was found to have a unique value for the carbon content of each material in the data of Tsuchida et al[7]. Consequently, from assuming an inverse relation between the lower yield stress and the Lüders strain an explicit relation of the Lüders strain and carbon content was derived. That is:

$$\varepsilon_L = \frac{a}{1 + bC} \quad (206)$$

The above equation was applied to the data of Tshuchida et al[7] and extended to the data of Song et al[24], though the latter had a micro-structure that was an ultra fine grained steel with fine cementite particles on the grain. However, a plot of the equation(see Fig.(26)) predicted approximately the size of the Lüders strain of Song et al[24]. This indicated that inhomogeneous deformation in a ferrite-pearlite structure and fine cementite structure are similar; as Equ.(206) makes the assumption that the micro-structures between different carbon contents of materials are similar.

The above equation can be used as a precursor to a more accurate description of the Lüders strain against carbon content.

A theoretical model combining the work of Sun et al[8], Bergstrom[5] and Gilman[45] produced a simple model that gave an analytical solution that accounted for the sigmoidal curve and, consequently, the Lüders band.

It was conceded that the model was simplistic in nature and made some assumptions, such as the variability of the parameter  $\Omega$  and proposed that the initial dislocation density was zero. However, further analysis showed that the aforementioned assumptions were permissible as the interpretation of  $\rho_0 = 0$  was equivalent to re-writing the modified form of the Gilman equation as:

$$\rho - \rho_0 \exp(\Omega\varepsilon) = \frac{m}{bS_0} \varepsilon \exp(-\Omega\varepsilon) \quad (207)$$

The result of which produced a dislocation density that only referred to the number of dislocations freed from pinning and the corresponding multiplication of those, as the model implicitly assumes a Johnston-Gilman type multiplication mechanism.

Although the model was simplistic in nature, it did derive new relationships between the Lüders strain and the mean free-path that is an inverse relationship. The change in Lüders strain for the same composition, but different micro-structure could be explained by allowing the amount of the precipitates to determine the size of the mean free path of the dislocations. This, in the process, was also substantiated from the work of Song et al[24] and combined the effect of the additional precipitates to work-hardening effect on the mean free path and, consequently, on the Lüders strain.

Other relations were also derived that related the Lüders strain to the dislocation density from which was shown, by using an Equ.(126) due to Bailon et al[48], that the Lüders strain was related to the grain-size through

a Hall-Petch type relation, that is:

$$\varepsilon_L \propto d_{grain}^{-\frac{1}{2}} \quad (208)$$

where  $\varepsilon_L$  is the Lüders strain and  $d_{grain}$  is the grain-size.

The validity of the above relation was confirmed from the data of Tsuchida et al[7] with Lüders strain against grain-size at constant strain-rate and temperature(see Fig.(27)).

This showed that the Lüders strain increases with the number of dislocations freed by the reduction in grain-size. Consequently, the larger the number of dislocations freed, the smaller the grain-size, the greater number of pinning and, therefore, the larger the Lüders strain as a result of those dislocations being freed during band propagation.

A new formula that related the Lüders velocity to the dislocation velocity was shown to be a linear relation that agreed with the observations of Hahn[18].

This has the advantage of obtaining the dislocation velocity from merely knowing the average mean free path of the dislocation velocity, the maximum strain-rate within the Lüders band and the speed of the Lüders band.

It was also shown that Gilman's original equation is merely a special case of the Bergstrom model and to have a more realistic model would require to take the general case, which will be expanded upon in the future work section.

## 9.2 Experimental

The main materials used in the tensile experiments were the RPV steel with 0.17% C and an upper-bainite structure, compared with a ferrite/pearlite 0.07% C steel with manganese sulphide particles and an ultra low 0.007% C steel.

It was evident that the tempered martensitic structures had a larger yield point and ductility than upper-bainitic RPV steel. It was also shown that the tempered martensitic steel had a larger Lüders strain for a given strain-rate. This led to the conclusion that if a Lüders band was desirable in a structure, then a tempered martensitic structure would be more beneficial than an upper-bainite steel.

However, the practicalities of quenching an RPV without inducing residual stresses would be difficult and would require a more gradual form of quenching, such as air hardening.

At the time of conducting the experiments on the tensile testing chapter, it was the consensus[53] that two band nucleation should be treated as a scalar problem i.e. divide the total Lüders strain by the number of bands to obtain the Lüders strain of the material. However, using DIC or digital image correlation, it was shown that it was better to take the value of the measured Lüders strain on the corresponding stress-strain curve, as it was more representative of the local strain within the two bands, than simply dividing the total Lüders strain by the number of the bands.

The parameter  $u$  was for the first time, taken from Tsuchida et al[7], given a theoretical basis by being combined with Sun et al[8]. This parameter  $u$  was calculated for the different micro-structures and shown to be comparable to the parameter strain-rate sensitivity  $m$ . The work of Tsuchida et al[7] showed that  $u$  was equivalent to a work-hardening exponent at the end of a Lüders band. However, it was not expressed in terms other parameters and therefore it was unclear as to precisely what  $u$  depended upon. The amalgamation of Sun et al[8] model with the aforementioned showed that  $u$  could be expressed in terms of more familiar parameters, such as the strain-rate sensitivity exponent  $m$  and the stress-rate sensitivity exponent  $n$ . It was possible to calculate  $u$  from the tensile experiments performed in chapter 4 and this showed that  $u$  was equivalent to  $m$ , if  $m \ll 1$ . This was evident in the data as the trend of the size of  $u$  followed that of  $m$ .

The insight of  $u$  is an explicit relation for the Lüders strain and has filled some of the gaps of the Tsuchida et al[7] original equation:

$$\varepsilon_L = \left( \frac{\Delta}{K'u} \right)^{u^{-1}} \quad (209)$$

where  $K'$  is a constant unique to the material and  $\Delta$  is considered a universal constant whose significance was not fully understood or clarified by Tsuchida et al[7].

The new form looks as follows:

$$\varepsilon_L = \left( \frac{\Delta l_0 (1 - mn)}{kDC^n m} \right)^{\frac{1-mn}{m}} \quad (210)$$

and therefore the constant  $\Delta$  is expressed in material constants that can be obtained from experiment.

The tensile data from appendix A showed that the Lüders strain decreases as a function of tempering time. This was also evident in the other tensile

properties such as the yield stress and UTS. The reason for this trend was attributed to the reduction in dislocation density during tempering time. Consequently, a tempered structure can be altered to a specific requirement. For example, if it is desirable to have a yield point that is higher than the RPV steel but have a ductility that is greater than the RPV steel and, additionally, if a Lüders strain is required (especially through methods done by Mirazee-Sisan et al[4] and Wenman et al[1] that the optimum Lüders strain is established for residual stress), then it would be possible to design the tempered steel accordingly.

One of the major design problems as discussed above in this section is quenching a large structure such as an RPV without inducing residual stresses. Solutions exist such as air-hardening, which would quench the steel gradually enough that martensite is produced, whilst ensuring minimal production of residual stress.

Further tensile tests were conducted on a TM-28H steel and TM-168H steel at strain-rate  $1 \times 10^{-3}$  and  $1 \times 10^{-4} \text{ s}^{-1}$  with holes of 1.5mm and 1mm drilled into tensile specimen.

It was shown that around the defect, even in tensile dominated regions, there was no evidence of Lüders strain (see Fig.(45) and Fig.(46)). This indicated that the nucleation of a Lüders band is particular to tensile dominated stress and the slightest degree outside tensile dominated stress can affect the possibility of nucleation significantly.

It was also shown that the role a defect has in terms of the effect on the overall cross-sectional area is between that of assuming the hole has a negligible affect on the cross-section and that of assuming it reduces the cross-section entirely. This was concluded from the time taken for the TM-28H and TM-168H to yield.

It was also shown that the TM-28H and the TM-168H yield at approximately the same stress, despite the difference in tensile properties (see appendix A). Therefore, this shows that the difference in spheroidised particle density of TM-28H and TM-168H, does not significantly affect the material properties under a multiaxial stress condition.

### 9.2.1 FAD

Chapter 6 used the tensile data from chapter 4 at a strain-rate of  $1 \times 10^{-3} \text{ s}^{-1}$  for the AR, FP and TM micro-structures; of the tempered structures TM-168H was chosen because it was important to choose a tempered structure

that resembled the tensile properties of AR and FP at strain-rate of  $1 \times 10^{-3} \text{ s}^{-1}$ .

It was shown that the FADs of AR and TM-168 when contrasted with the same FAD without a Lüders strain included, showed that reducing the Lüders strain produced less conservative predictions in terms of crack initiation of failure or  $a_{con} > a_{dis}$  for a fracture toughness of  $57 \text{ MPa m}^{\frac{1}{2}}$ , which was calculated at  $-155^\circ\text{C}$ [52].

Table 12 showed that the prediction for crack initiation as a function of micro-structure did not change significantly for the aforementioned fracture toughness value. This indicates that in the region of operation there is small difference between upper-bainitic, ferrite-pearlite and tempered martensite structure with similar yield point.

Regions that are favourable to have a Lüders strain were explored and it was shown for TM-168H that a fracture toughness greater than  $250 \text{ MPa m}^{\frac{1}{2}}$  showed that a Lüders strain reduced the amount of conservatism by 4%, assuming the ratio of crack lengths can be considered as a measure of conservatism.

The work of Miazee-Sisan et al[4], SINTAP[2] and Wenman et al[1] was reviewed to propose the consensus that a model that had more detail about the material, such as yield point and residual stress distribution would reduce the degree of conservatism when compared to the standard R6-code handbook or procedure. Wenman went further by concluding that a material with a Lüders strain would reduce the amount of residual stress predicted compared to standard work-hardening models and work-hardening models with Lüders strains artificially added. However, the work from the FADs showed the antithesis of this was true at the brittle stage of the material. That is, for the AR and TM-168H material, assuming the material yielded continuously gave higher values of the crack-initiation than the FAD constructed from the tensile data.

### 9.3 Modelling

The theoretical model constructed from chapter 3 and the Zhang model introduced in the same chapter were compared to some of the tensile data.

The theoretical model was compared to all materials apart from the FP structure, because of the high degree of work-hardening occurring within the Lüders band. This made correlation difficult and was subsequently neglected from the final results of table 15.

It was shown that the model equation(Equ.(108)) correlated well with the data, having an average  $R^2 = 0.99$  for all the materials. This showed that model, despite the assumption that the dislocations were subjected to first order friction only(see Gilman[45]) was valid even up to a carbon content of 0.17%C. This indicated that the obstacles on the glide plane of the dislocation do not affect the dislocation motion significantly and possibly acted more as voids than barriers.

It was hypothesised from the work described above that the condition for which a sigmoidal profile would not occur and, consequently, no Lüders band would be from:

$$\tau \approx \frac{1}{\gamma} \ln \left( \frac{\varepsilon_i}{\varepsilon_L} \right) \quad (211)$$

where  $\tau$  is the time taken for the Lüders band to propagate a given region,  $\varepsilon_i$  is the initial strain and  $\varepsilon_L$  is the Lüders strain.

When the above equation is approximately zero, then  $\varepsilon_i \approx \varepsilon_L$ . This value could then be substituted into Equ.(206) and the corresponding carbon content could be calculated. This has implications in material design if it was required to know the threshold percentage of carbon content for which Lüders bands could not form.

Table 15 showed that the dislocation density was greater for the TM-168H than the AR micro-structure. Although the AR had a lower mean free-path, and according to the analysis of chapter 3 and the work of Song et al[24] a lower mean free path would result in a higher Lüders strain, the dislocation density was large enough to dominate the effect of the mean free-path such that the Lüders strain was greater for the tempered structures. Equ.(127) can add further insight into this by showing that a larger dislocation density corresponds to a smaller grain-size. This is evident between the micro-structures on table 15, where the TM-168H has a grain-size of  $5.2\mu\text{m}$  to the grain-size of AR which is  $10\mu\text{m}$ .

The presence of the manganese sulphide particles had a dramatic effect on the quantity  $\gamma$  which has units of  $\text{s}^{-1}$  and can be thought of as the frequency of the Lüders band. The result of this was that the band velocity would be faster than in the same material without the presence of manganese sulphides. This can be inferred from table 15 by looking at the effect from the other materials on  $\gamma$  that had only ferrite-pearlite precipitates. A faster Lüders band gives a shorter Lüders strain, as the band velocity is inversely related to the Lüders strain and also the band velocity is proportional to  $\gamma$ .

The Zhang model was compared to the RPV steel, specifically the AR micro-structure. It was shown that the Zhang model accounted for the yield point and Lüders strain, but as a result of calibrating the variables to fit the parameters from table 11, the ultimate tensile stress and consequently the work-hardening prediction was affected. This resulted in the model predicting necking prematurely compared to the actual work-hardening and UTS.

The Zhang model can adequately describe AR steel, if the model parameters are determined by experiment. Therefore, the failure of the Zhang model to fit the tensile data of AR precisely is due to lack of rigour in determining the constants or parameters of table 15, rather than a reflection of the model. However, there was no direct way of controlling the Lüders strain exactly on the Zhang model. Increasing the parameter  $D_1$ , which has been defined as the Lüders yield or possibly flow stress, as it was the altering  $D_1$  that produced comparable yield stress, increased the Lüders strain, but only slightly. The Zhang model was also applied to the tensile data taken from DIC with the hole defect. It was evident that the Zhang model at least qualitatively produced what was expected. For example, the mesh cells around the hole(see Fig.(85)) showed conclusively that no Lüders bands nucleated in the uniaxial direction. This is in agreement with experiment.

This shows the flexibility of the Zhang model, both for CT experiments(see Wenman et al[1]) and for geometries with defects. If the parameters are calculated correctly, the Zhang model has the potential to model more complicated geometries, such as reactor pressure vessels and might be one of the few methods that are available at the moment to model a material accurately if a Lüders strain is present.

## 10 Conclusion

This Chapter will consist of the main conclusions from the thesis. Conclusions that warrant further investigation will be elaborated on in the future work chapter.

- a) The Lüders strain has a clear dependence on the micro-structure. This was evident in the literature review and through the experiments conducted through the work. The reason for the dependence is three-fold; Dislocation density, the mean free path and the grain-size. If any of these variables are changed or if one is significantly greater than the other, then the Lüders strain will be dependent on it.
- b) The Lüders strain in the confines of the CT experiments reduces the amount of residual stress. The extent of which has only been conducted for that particular geometry, however it was clear that the Zhang model described the material more accurately than the other work-hardening models. Additionally, a Lüders strain that is calculated from an independent model, such as Zhao model, produces less conservative results in residual stress predictions than a work-hardening model with a Lüders strain artificially added, which is the current method in R6 procedure.
- c) The results from the FADs suggest that removing the Lüders strain from an upper-bainite structure and a tempered martensite structure can be more beneficial in terms of prevention of crack initiation failure than the presence of a Lüders strain and, therefore, reduces the amount of conservatism, assuming the same fracture toughness values.
- d) The nucleation of a Lüders band is heavily dependent on the amount of tensile stress available. If the total stress is resolved, then the chances of a Lüders band nucleating or producing a magnitude that is comparable to the pure tensile Lüders strain is small. Therefore, in material with structural defects that exhibit a Lüders band(depending on the size of the defect and structure)it can be assumed that the material does not exhibit Lüders bands. This is substantiated by the findings of SINTAP discussed in chapter 6. However, the conclusion is not exhaustive and therefore further work is required, especially residual stress calculations with CT specimens of different micro-structures with the same composition

- e) A tempered martensitic structure gives higher yield stress than the current micro-structures of RPVs, namely the upper-bainite structure. The advantages is that a tempered structure can be manipulated accordingly to produce a desired specification, especially if an optimum Lüders strain is desirable.  
Further work, such as the practicalities of building tempered martensite structures of RPV sizes is necessary, especially when it comes to designing RPVs with specific properties in the relation to Lüders bands.
- f) The addition of manganese sulphide particles has the effect of increasing the speed of the Lüders band and, therefore, rate of inhomogeneous deformation, whilst reducing the Lüders strain relative to a material with the same composition without manganese sulphide particles.  
Further work such as the effect of precipitates in general on Lüders band is warranted to build a better understanding of how precipitates can improve or exacerbate the effects of a Lüders band, especially on residual stress.
- g) A value that uniquely defines the carbon content in Tsuchida et al[7] is a dimensionless parameter  $\phi$ , from which an explicit relation between the Lüders strain and carbon content is derived.  
Further work is required, such as conducting experiments with different carbon contents that have similar grain size and micro-structures at constant strain-rate, as any relationship derived from the data between the Lüders strain and carbon content will implicitly make the assumption that the micro-structures between the materials are similar. However, if it is shown that different micro-structures handle inhomogeneous deformation similarly, then all similar micro-structures can also be included.
- h) Assuming  $\omega = \Omega$  in the Bergstrom equation[5] produces dislocation density that describes deformation in Lüders band, when Taylor expanded to the second order to produce the corresponding strain-time curve that was produced from the digital image correlation. Also the model worked for all micro-structures, not including the ferrite-pearlite or FP micro-structure due to work-hardening within the band, despite the simplicity of the model.
- i) The Zhang model describes all the features of the Lüders band, when

modelling tensile tests. However, the approach of calibrating the model purely from tensile data in order to use the same values for more complicated geometries does not seem to match experiment quantitatively(see Wenman et al[1]). This was also evident when looking at defects in materials. Therefore, a better method is required or additional parameters are required in the Zhang model.

- j) A Lüders band can reduce the degree of conservatism within a material, from the work of Wenman in residual stress calculations around a crack tip, but it can also increase the degree of conservatism, too, as shown in the FADs for all the AR and TM. Therefore, to determine whether a Lüders strain will reduce the degree of conservatism, the process is twofold: The region of operation on the FAD diagram must be in regions where a Lüders strain is beneficial, as shown in chapter 6 and secondly, residual stress calculations based on CT experiments on the chosen material are required, in order to determine, the difference in residual stress from assuming the material behaves continuously and a yield drop model, such as Zhang model.

## 11 Future work

The Chapter will be on the future work. The main points from the conclusion chapter that warranted further work will be elaborated on, proposing ways which they could be achieved.

- a) Further work needs to be done into explicitly relating the Lüders strain with carbon content, while maintaining constant composition. Other material variables that can affect the Lüders strain such as grain size and the micro-structure, which has been identified and quantified in this thesis. If the algorithm which was used in chapter 3 is used to identify the quantity  $\phi$ , they would allow more accurate correlations between Lüders strain and the carbon content. Ultimately, one would want to derive a master curve from carbon contents of different morphologies and micro-structures.
- b) The model derived in Chapter.(3) produced good correlation with the data taken from DIC. However the model was quite simplistic as a result of assuming  $\omega = \Omega$ , but it did produce the Gilman equation in the process.

The proposed method of improving the model, as stated above, would be to simply solve it for the general case while maintain the fixed value of  $\Omega$ . This could then be compared to the simplistic model and would quantify to what extent the simplistic model is valid. This could improve the equations derived from the simplistic model that related the Lüders strain to the dislocation density, mean free path and the grain-size.

Bergstrom et al[5] developed another equation that factored in the proportion of tempered martensite and ferrite for dual-phase steels, for materials that did not exhibit Lüders bands. The form of the Bergstrom equation was modified accordingly to:

$$\frac{d\rho}{d\varepsilon} = \frac{1}{f_0 + (f_1 - f_0) \exp(-r\varepsilon)} \left[ \frac{\hat{m}}{b(s_0 + (s_1 - s_0) \exp(-\omega\varepsilon))} - \Omega\rho \right] \quad (212)$$

where  $f_1$  and  $f_0$  are volume fractions,  $s_0$  and  $s_1$  initial and final mean free-paths,  $r$  is a rate material parameter and the rest have their usual meaning.

If the same procedure is done, that is reversing the function that describes the mean free path, then one would have a model that accounts for the amount of ferrite and precipitate in the grain for a propagating Lüders band.

- c) The effects of precipitates on dislocations is well established[53], however the full effects on Lüders bands in general have not. It has not been fully realised whether Lüders bands are desirable in a material, especially in RPVs.

CT tests for potential materials with and without precipitates are required to determine the effect they have on the Lüders strain and the corresponding residual stress. From the work in this thesis, the addition of sulphide particles suggests a reduction in Lüders strain and according to Wenman et al[1] the Lüders strain is related to the amount of the reduction of residual stress compared to standard work hardening models. This is easily realised by thinking of the yield point as a delay phenomena and the strain uniaxially can be thought of as the time[44]. Therefore, the larger the Lüders strain the longer the time delay and the bigger the difference between a material that is deforming homogeneously and the material that is still in the Lüders strain. As a result, by the time the Lüders strain has strained  $\varepsilon_L$  the stress value will be less than that of the material that is deforming homogeneously.

The argument assumes that the residual stress is tensile dominated. However, to fully understand the nature of Lüders band more research into Lüders bands with precipitate dependence is necessary.

- d) The irradiation of a Lüders band in RPVs can be further investigated using the R6 code, in conjunction with DIC.

The work done on the FADs did not take into consideration the effect of irradiation on the micro-structures. The R6-code can easily do irradiation calculations to simulate RPV conditions, from which it can be determined how long it would take the material to fail upon a certain dose limit. Such calculations are warranted, because to fully determine whether a tempered structure could be a credible alternative to the current upper bainite structure, irradiation tests are necessary.

Using DIC it would be possible to look at the strain-time curves and to validate the simple theoretical model developed in chapter 3. This would determine whether the profile of the Lüders strain is still sig-

moidal and, subsequently, adjusting the model to fit the data. This is also true for the improvement of the Zhang model. If the parameters of the Zhang model were adjusted to account for the tensile tests from irradiated material, then, although the values of the parameters at first, might seem unrealistic, further work or even a better model could account for the values of the parameters and thus produce a working model that accounts for the effects of irradiation on the Lüders strain.

- e) If it is shown through the suggestions above that the tempered martensite structure is more beneficial than the upper bainite structure, then the next task would be to determine how a tempered structure of RPV size could be quenched and tempered without the induction of residual stresses. Presumably through the addition of 1% Mo, for example. A possible solution to this is to air harden the material.

## A Appendix-Data from tensile tests

Table 17: The results for the as-received or AR, upper bainitic structure.

Structure	$\sigma_{uyp}$ (MPa)	$\sigma_{lyp}$ (MPa)	UTS(MPa)	$\varepsilon_L$ (%)	$\dot{\varepsilon}$	Notes
AR-RPV-4	491	488	N/A	1.00	$1 \times 10^{-2}$	2-bands
AR-RPV-5	483	472	N/A	1.02		2-bands
AR-RPV-6	505	502	730	0.9030		2-bands
Average	493	487.3	730	0.974		
AR-RPV-1	444	441	N/A	0.861	$1 \times 10^{-3}$	2 bands
AR-RPV-3	482.6	481.4	N/A	0.758		2 bands
AR-RPV-7	490	487	725	0.828		
Average	472.2	469.8	725	0.816		
AR-RPV-2	476	466	N/A	0.741	$1 \times 10^{-4}$	
AR-RPV-8	460	455	580	0.825		
AR-RPV-9	454	450	644	0.777		
Average	463.3	457	612	0.781		

Table 18: The results of FP, ferrite-pearlite structure.

Structure	$\sigma_{uyp}$ (MPa)	$\sigma_{lyp}$ (MPa)	UTS(MPa)	$\varepsilon_L$ (%)	$\dot{\varepsilon}$	Notes
FP-1	424	424	N/A	0.6	$1 \times 10^{-2}$	
FP-2	420	416	N/A	0.6	$1 \times 10^{-3}$	
FP-3	410	406	N/A	0.7	$1 \times 10^{-4}$	

Table 19: The results of TM-5H(for 5hours), tempered martensitic structure.

Structure	$\sigma_{uyp}$ (MPa)	$\sigma_{l_{yp}}$ (MPa)	UTS(MPa)	$\varepsilon_L$ (%)	$\dot{\varepsilon}$	Notes
TM-5H-1	650	620	N/A	4.07	$1 \times 10^{-2}$	
TM-5H-4	657	633	N/A	3.92		
Average	653.5	626.5		4.00		
TM-5H-2	652	619	N/A	3.56	$1 \times 10^{-3}$	
TM-5H-6	645	635	N/A	3.82		
Average	648.5	627		3.69		
TM-5H-3	638	610	N/A	3.28	$1 \times 10^{-4}$	
TM-5H-6	635	620	N/A	3.2		
Average	636.5	615		3.245		

Table 20: The results of TM-120H(for 120hours), tempered martensitic structure.

Structure	$\sigma_{uyp}$ (MPa)	$\sigma_{l_{yp}}$ (MPa)	UTS(MPa)	$\varepsilon_L$ (%)	$\dot{\varepsilon}$	Notes
TM-120H-1	555	545	695	4.12	$1 \times 10^{-2}$	
TM-120H-2	548	540	685	3.79		
Average	545.5	542.5	690	3.96		
TM-120H-3	575	530	683	4.26	$1 \times 10^{-3}$	
TM-120H-4	560	550	680	3.56		
Average	567.5	540	681.5	3.91		
TM-120H-5	560	537	673	3.45	$1 \times 10^{-4}$	
TM-120H-6	591	554	668	3.84		
Average	575	545	670.5	3.65		

The next set of tables show the ultra-low carbon steel or UL and the mild steel, defined A-L. A-L stands for the longitudinal face, as it was originally cut from a cylindrical bar.

Table 21: The results of TM-144H(for 144hours), tempered martensitic structure.

Structure	$\sigma_{uyp}$ (MPa)	$\sigma_{lyp}$ (MPa)	UTS(MPa)	$\varepsilon_L$ (%)	$\dot{\varepsilon}$	Notes
TM-144H-1	440	434	600	4.05	$1 \times 10^{-2}$	2-bands
TM-144H-2	470	458	614	3.47		
Average	455	446	607	3.76		
TM-144H-3	491	463	637	3.83	$1 \times 10^{-3}$	Starts from centre
TM-144H-4	462	444	588	2.9		
Average	476.5	453.5	612.5	3.37		
TM-144H-5	482	467	611	4.19	$1 \times 10^{-4}$	
TM-144H-6	445	440	595	3.96		
Average	463.5	453.7	603	4.075		

Table 22: The results of TM-168H(for 168hours), tempered martensitic structure.

Structure	$\sigma_{uyp}$ (MPa)	$\sigma_{lyp}$ (MPa)	UTS(MPa)	$\varepsilon_L$ (%)	$\dot{\varepsilon}$	Notes
TM-168H-1	393	382	544	3.93	$1 \times 10^{-2}$	
TM-168H-2	446	430	565	3.5		
Average	419.5	406	554.5	3.72		
TM-168H-3	390	390	532	3.55	$1 \times 10^{-3}$	Mask broke
TM-168H-4	404	394	546	3.52		
Average	397	392	539	3.54		
TM-168H-5	380	368	520	3.67	$1 \times 10^{-4}$	Mask broke
TM-168H-6	396	392	N/A	2.84		
Average	388	380	520	3.25		

Table 23: shows the results of UL(0.007% C).

Structure	$\sigma_{uyp}$ (MPa)	$\sigma_{lyp}$ (MPa)	UTS(MPa)	$\varepsilon_L$ (%)	$\dot{\varepsilon}$	Notes
UL-1	320	240	N/A	5.8	$1 \times 10^{-2}$	2-bands
UL-2	260	248	480	4.9		
UL-3	310	240	400	5.52		2-bands
UL-4	290	250	420	5.62		
UL-5	280	245	390	4.88		2-bands
Average	292	244.6	422.5	5.34		
UL-6	223	215	390	5.2	$1 \times 10^{-3}$	
UL-7	270	230	390	5.51		
UL-8	263	214	400	4.65		2-bands
Average	252	219.7	393.3	5.12		
UL-9	222	205	376	4.85	$1 \times 10^{-4}$	
UL-10	262	210	380	4.53		
UL-11	253	190	360	3.86		
Average	245.7	201.7	356.7	4.41		

Table 24: The results of AL(0.07% C).

Structure	$\sigma_{uyp}$ (MPa)	$\sigma_{lyp}$ (MPa)	UTS(MPa)	$\varepsilon_L$ (%)	$\dot{\varepsilon}$	Notes
AL-1	265	244	N/A	1.82	$1 \times 10^{-3}$	
AL-2	240	221	N/A	1.46		
Average	252.5	232.5		1.64		
AL-3	225	205	N/A	1.04	$7.14 \times 10^{-4}$	
AL-4	217	208	N/A	0.88		
Average	221	206.5		0.96		
AL-5	229	217	N/A	1.03	$2.28 \times 10^{-4}$	
AL-6	217	209	N/A	0.87		
Average	223	213		0.95		

## A.1 Additional results

The next set of results are considered doubtful. However, they have been added for completeness.

Table 25: The results of TM-120H(for 120hours), tempered martensitic structure.

Structure	$\sigma_{uyp}$ (MPa)	$\sigma_{l_{yp}}$ (MPa)	UTS(MPa)	$\varepsilon_L$ (%)	$\dot{\varepsilon}$	Notes
TM-120H-7	518	506	704	3.02	$1 \times 10^{-2}$	
TM-120H-8	554	511	N/A	2.92		
Average	536	509	704	2.97		
TM-120H-9	516	489	698	2.88	$1 \times 10^{-3}$	
TM-120H-10	531	491	694	3		
Average	524	490	639	2.94		

Table 26: The results of TM-192H(for 192hours), tempered martensitic structure.

Structure	$\sigma_{uyp}$ (MPa)	$\sigma_{l_{yp}}$ (MPa)	UTS(MPa)	$\varepsilon_L$ (%)	$\dot{\varepsilon}$	Notes
TM-192H-1	394	373	536	2.38	$1 \times 10^{-2}$	
TM-192H-2	378	376	572	3.12		
Average	386	375	554	2.75		
TM-192H-3	387	374	538	3.87	$1 \times 10^{-3}$	
TM-192H-4	388	376	563	3.21		
Average	388	376	563	3.21		
TM-192H-5	386	377	551	3.54	$1 \times 10^{-4}$	

## B Optical micrographs

This appendix consists of some micro-graphs taken of the tempered martensite structure for different tempering times.

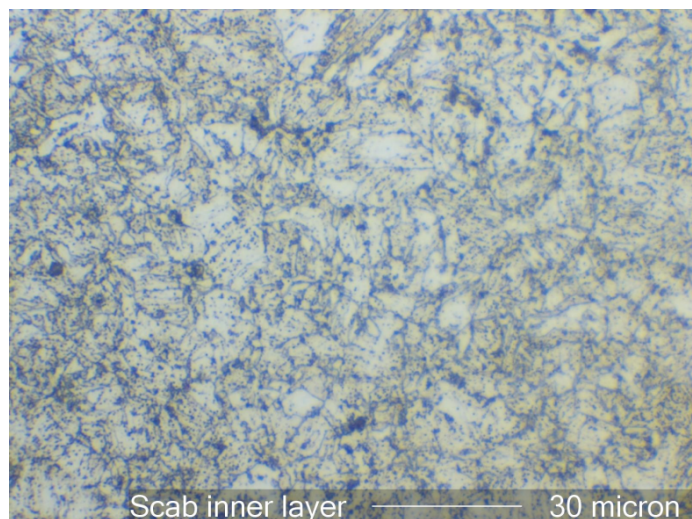


Figure 88: Grain structure of TM-120H at 500 magnification

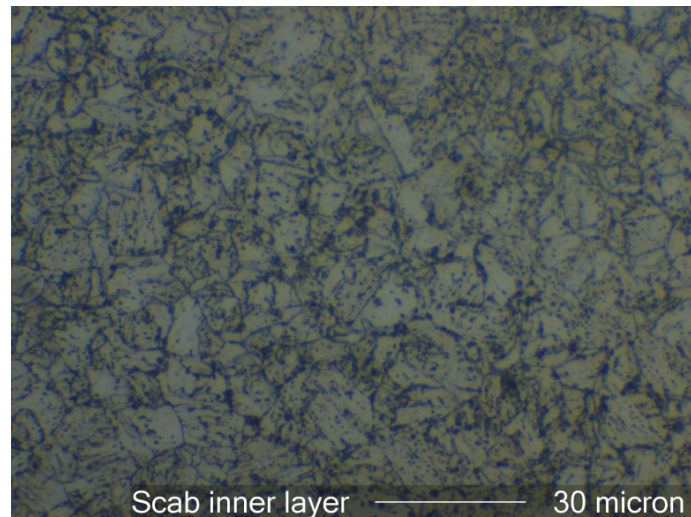


Figure 89: Grain structure of TM-144H at 500 magnification

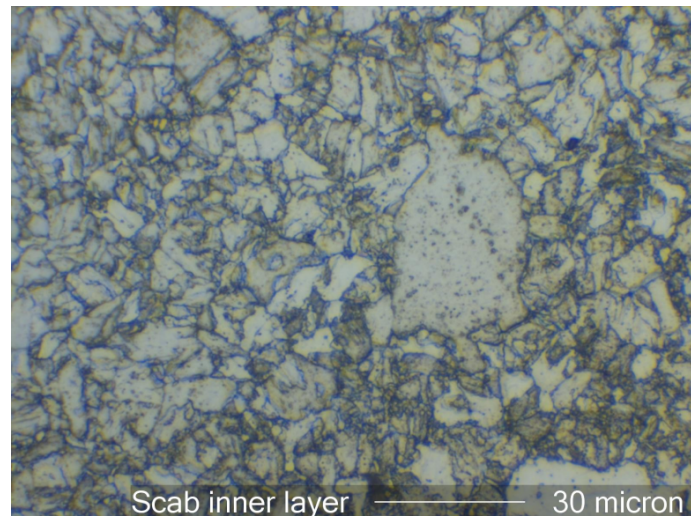


Figure 90: Grain structure of TM-168H at 500 magnification

## C Appendix-Time dependent yield prediction

### Abstract

It is shown that in the load vs frame graph taken from low carbon ferritic steel 0.07%C, measured by the D.I.C through analogue channels, is analogous to a two spring system in series; with the application of predicting the time taken to reach the elastic limit. This is interpreted from the value of the spring constant calculated from fig.91 when compared to the theoretical value of a two spring system in series. The spring constant is then used to calculate the time taken for a mild carbon steel(0.07% C), to reach its elastic limit.

The displacement of a tensile machine within the elastic limit, is described by the following equation:

$$vt = \frac{\sigma A}{k} + \Delta x \quad (213)$$

where  $v$  is the cross-head velocity,  $t$  is the time,  $A$  is the cross-sectional area of the specimen,  $k$  is a spring constant and  $\Delta x$  is the change in specimen length.

In the elastic limit,  $\Delta x$  is related to the strain thus:

$$\varepsilon = \frac{\Delta x}{l_0} \quad (214)$$

where  $\varepsilon$  is the strain and  $l_0$  is the gauge length of the specimen.

Substituting Equ.(214) into Equ.(213) and using Hooke's law for stress and strain, Equ.(213) becomes:

$$vt = \frac{\sigma A}{k} + \frac{\sigma l_0}{E} \quad (215)$$

where  $E$  is Young's modulus.

For a two spring system in series, Equ.(215) becomes:

$$vt = \sigma A \left( \frac{1}{k_1} + \frac{1}{k_2} \right) + \frac{\sigma l_0}{E} \quad (216)$$

where  $k_1$  is the spring constant of the piston and  $k_2$  is a spring connected from  $k_1$  to the specimen.

Resolving for  $k_2$ , one obtains:

$$k_2 = \frac{\sigma k_1 A E}{k_1 ((E v t - \sigma l_0) - \sigma A E)} \quad (217)$$

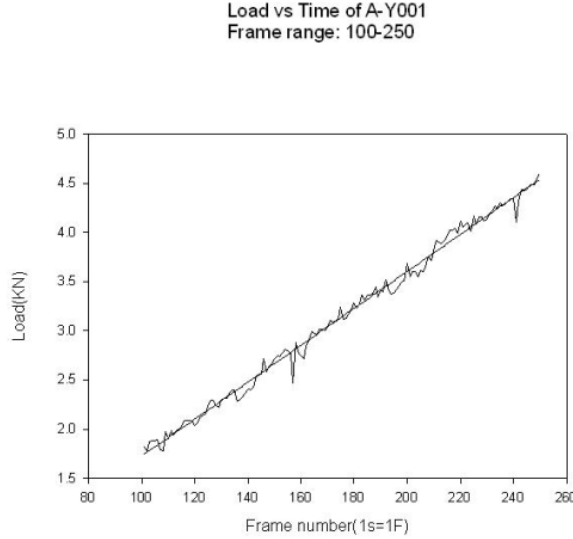


Figure 91: Load vs frame number of 0.007%C ferritic steel, pulled at strain-rate  $2.85 \times 10^{-6} s^{-1}$

## C.1 Method

Let  $k'$  take the value of the spring constant calculated from Fig.(91), which was calculated through the following method: the D.I.C(digital image correlation) was directly connected to the hydraulic machine, through analogue channels. The amount of voltage corresponding to load and extension were noted and calibrated. Fig.(91) shows a section of the plot obtained from the low carbon steel pulled at a strain-rate of  $2.85 \times 10^{-5} s^{-1}$  which gave a cross-head velocity of  $v=1 \times 10^{-6} m/s$ . The corresponding yield point was  $\sigma_y = 230 \text{ MPa}$ .

The derivative or gradient of Fig.91 is in N/Frame, while the actual stiffness of a spring is expressed in N/m. To convert between N/m and N/frame, one uses the fact that the frame rate and time of this experiment was 1:1 thus  $N/\text{frame} = N/\text{time}$ . Then using the fact the velocity of the specimen was constant and that the distance is related to the time:

$$dx = vdt \quad (218)$$

where  $v$  is the cross-head velocity.

one obtains:

$$\frac{dF}{dt} = v \frac{dF}{dx} \quad (219)$$

or:

$$k' = \frac{\frac{dF}{dt}}{v} \quad (220)$$

## C.2 Results

The value of  $k'$  described from Fig.(91) was  $k' = 18.78 \text{ MN/m}$ .

Comparing to the value calculated in Equ.(221), where  $k_1=600 \text{ MN/m}$ ,  $E=210 \text{ GPa}$ ,  $t \approx 250 \text{ s}$  at elastic limit,  $\sigma_y=230 \text{ MPa}$ ,  $v=1 \times 10^{-6} \text{ m/s}$ ,  $l_0=3.5 \times 10^{-2} \text{ m}$  and  $A=20 \times 10^{-6} \text{ m}^2$  gives:

$$k_2 = \frac{5.796 \times 10^{23}}{2.667 \times 10^{16}} = 21.73 \text{ MN/m} \quad (221)$$

Thus the predicted value and the experimental value are in good agreement. It is therefore shown that  $k'$  is interpreted as  $k_2$ .

Having shown that the Denison tensile machine behaves like a two spring system in series, the time taken for a material to reach its elastic limit at a different strain-rate and with a mild steel specimen will now be calculated.

The geometry of the mild steel specimen was identical to the low carbon steel specimen and thus had the same cross-sectional area, with 0.07% C, a yield point  $\sigma_y=216 \text{ MPa}$  and cross-head speed  $v=8.3 \times 10^{-6} \text{ m/s}$ .

The time taken for yield from Equ.(217):

$$t_y = \frac{\sigma_y}{v} \left( A \left( \frac{1}{k_1} + \frac{1}{k_2} \right) + \frac{l_0}{E} \right) \quad (222)$$

which gives

$$t_y = \frac{216 \times 10^6}{8.3 \times 10^{-6}} (9.86 \times 10^{-13} + 1.67 \times 10^{-13}) = 29.97 \approx 30 \text{ s} \quad (223)$$

the specimen sample reached the elastic limit at  $t=39 \text{ s}$ .

The predicted and the actual time are in agreement, which is to be expected if  $k_2$  is regarded as a constant.

## C.3 Conclusion

A simple method for determining the time of a material reaching its elastic limit was provided. Through the concept that a hydraulic piston with grips is analogous to a two spring system in series, it was possible to predict where the specimen would begin to yield.

## D Appendix-Digital Image Correlation.

This appendix will describe the digital image correlation or DIC technique that has been used on the tensile experiments. The amount of data taken from DIC and the information that can be taken from it has been illustrated through the experimental chapter and subsequent modelling chapters that went with it. However, although the benefits of DIC were mentioned in the FAD and hole chapter and the technique was discussed in the tensile experiment chapter, they were only mentioned briefly. Therefore, this appendix will elucidate those points with the mathematics and corresponding algorithms responsible for the observed strains and displacements presented in the previous chapters.

For stress-strain analysis the following hardware is used:

- 2 Q-400 5 mega-pixel cameras mounted onto a tripod.
- High Intensity Light Emitting display or HILED-Designed to provide high intensity equivalence to high intensity lamps, usually red, but without the heating environment.
- The HILED is powered by HU-4XB power supply with with a knob that alters the intensity of the monochromatic light.
- These are fed into a standard Dell computer with the Istra 4.2 software.

The process of DIC from obtaining the images can be separated into the following processes.

1. Obtaining image: the elements and pixels
2. Correlation Algorithm: How the computer calculates the optimum residuum value.
3. Calibration.

### D.1 Obtaining image

The principle of DIC uses a stochastic technique as shown in the Fig.(92).

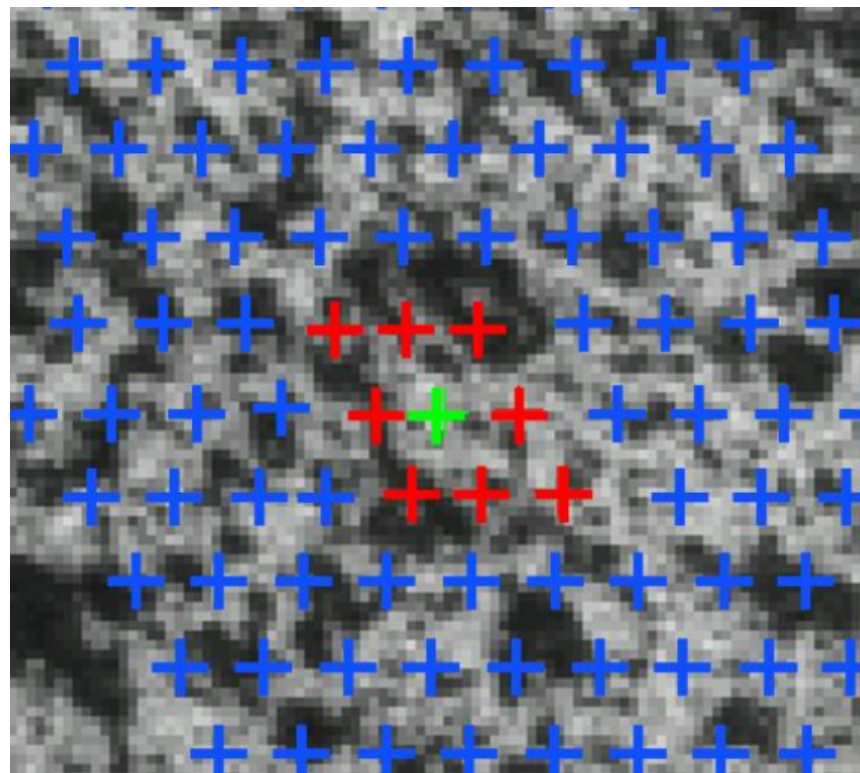


Figure 92: Stochastic technique with the red crosses indicating displacement, while the blue crosses represent non-displaced elements take[67].

## D.2 Correlation Algorithm

The correlation algorithm of DIC is based on the following equation:

$$R = \min_{a_0, \dots, a_7, g_0, g_1} \sum_{x,y} \|G_2(x, y) - G_T(x, y)\| \quad (224)$$

where  $R$  is the residuum parameter,  $a_0, \dots, a_7$  are affine transformations defined as:

- $a_0$  and  $a_4$  are translations.
- $a_1$  and  $a_6$  are stretching.
- $a_2$  and  $a_5$  are shear.
- $a_3$  and  $a_7$  are distortion.

and

$$G_T(x, y) = g_0 + g_1 G_1(x_t(x, y), y_t(x, y))$$

$$x_t(x, y) = a_0 + a_1 x + a_2 y + a_3 x y \quad (225)$$

$$y_t(x, y) = a_4 + a_5 x + a_6 y + a_7 x y$$

Once the affine transformations have been calculated, the residual parameter is calculated with an optimum value dependent on the size and type of calibration target<sup>26</sup>. This value varies with different size calibration targets as shown in Fig.(93).

## Processing

Fig.(94) shows a typical set-up of DIC when capturing the stresses and strains on a surface.

The angle of the cameras depending on the scale of the object varies between 40-60°. This range is chosen as it is important that the measured displacement on each camera is approximately equal.

---

<sup>26</sup>For example, a residuum value of 0.3-0.5 is consider optimum for the calibration target used in the tensile experiments conducted on a gauge length of 35mm

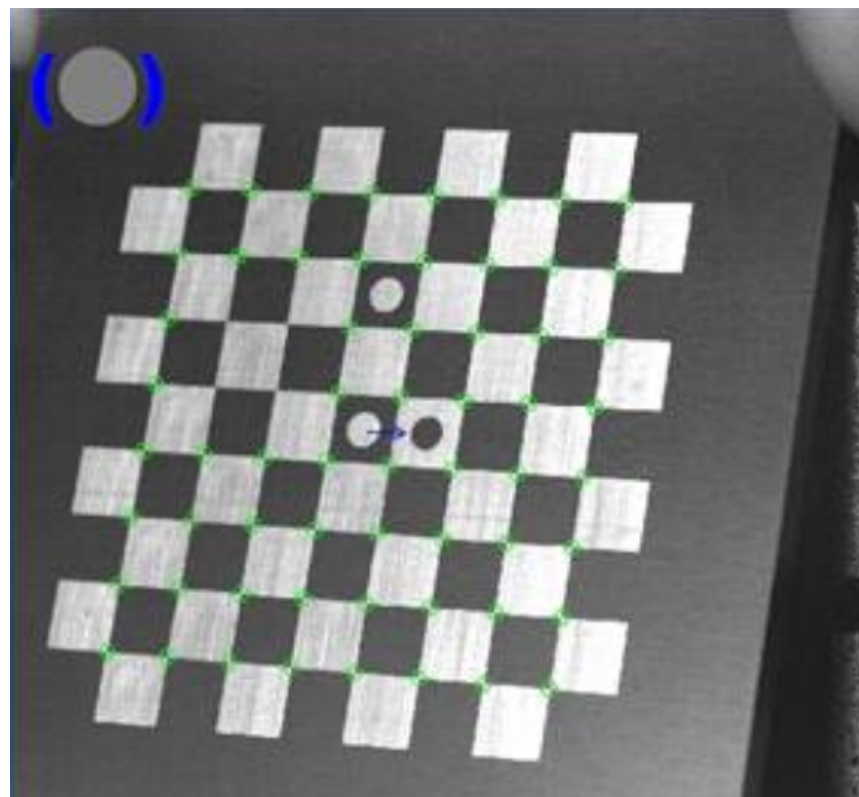


Figure 93: Aluminium calibration target where the green dots are the tracking dots, taken from[67].



Figure 94: Two 5-mega-pixel camera mounted on a tripod facing the object of interest. Taken from [67].

Once the image is captured, for efficiency, a mask is drawn around the area of interest and the images are compiled accordingly. Deformation and contour are calculated from the Lagrangian strain tensor:

$$\varepsilon_{ij} = \frac{1}{2} \left( \frac{\partial u_i}{\partial x_j} + \frac{\partial u_j}{\partial x_i} + \sum_{l=1}^3 \frac{\partial u_l}{\partial x_j} \frac{\partial u_l}{\partial x_i} \right) \quad (226)$$

where  $u$  is the spatial component in the  $i, j$ , whose components can be extracted accordingly from the data.

A description of the digital image correlation has been shown with the main parameters and procedure that is required to obtain the images and data presented in the previous chapters.

It is clear that with modelling requiring more precision from experiment, especially in the case of Wenman et al[1] where the parameters were calculated from tensile experiment, non-destructive processes such as DIC are needed and archaic methods such as extensometers are becoming obsolete. Therefore, technology like DIC will become more abundant in later experiments in the future.

## E Appendix-J-integral

In this Appendix, as discussed in the FAD chapter, the J-Integral will be discussed in further detail.

It will be shown how the J-integral is path independent, with limitations of the J-integral discussed and it will be shown from the work of Lei et al[61] how it can be modified to account for residual stress. A further modification will be proposed, by the author, using a similar approach by Lei et al to account for Lüders strain.

The J-integral written in its full form is written as[61]:

$$J = \lim_{r \rightarrow 0} \oint_{\Gamma} \left( W \delta_{ij} - \sigma_{ij} \frac{\partial u_i}{\partial x_1} \right) n_i ds \quad (227)$$

where  $W$  is the strain energy density,  $\sigma_{ij}$  and  $u_i$  are components of stress and displacement,  $\Gamma$  is the curve surrounding the crack tip and  $n_i$  is the normal vector to the path  $ds$ , as shown in Fig.(51).

A full proof of the path independence of the J-integral can be found in Rice[62] due to its originator. Therefore, the following proof will be a simplified proof with the focus on understanding rather than rigour.

To show that the integral is path independent requires the use of Green's theorem, which is a special case of Stoke's theorem. It states that:

$$\oint_{\Gamma} (L dx - M dy) n_i ds = \int \int \left( \frac{\partial M}{\partial x} - \frac{\partial L}{\partial y} \right) dx dy \quad (228)$$

where  $L$  and  $M$  are functions.

Equ.(227) with the application of using Green's theorem, Equ.(228) becomes:

$$J = \int_A \left( \frac{\partial W}{\partial x_1} - \sigma_{ij} \frac{\partial \varepsilon_{ij}}{\partial x_1} \right) dA \quad (229)$$

The term with the strain comes from the definition of strain in terms of spatial displacement and conservation of linear momentum. That is:

$$\varepsilon_{ij} = \frac{1}{2} \left( \frac{\partial u_j}{\partial x_i} + \frac{\partial u_i}{\partial x_j} \right) \quad (230)$$

where  $u_i$  and  $u_j$  are spatial displacements.

And conservation of linear momentum[68]:

$$\nabla \bullet \sigma = 0 \quad (231)$$

As the system is in static equilibrium.

It is then simple to show that the first partial derivative containing  $W$  in Equ.(229) can be re-written using the chain-rule:

$$\frac{\partial W}{\partial x_1} = \frac{\partial W}{\partial \varepsilon_{ij}} \frac{\partial \varepsilon_{ij}}{\partial x_1} = \sigma_{ij} \frac{\partial \varepsilon_{ij}}{\partial x_1} \quad (232)$$

When substituted back into Equ.(229) the net result is zero. A corollary of a closed path is that it is path independent.

The J-integral does not account for residual or second order stresses. This is a problem, because a significant number of engineering problems concern with the distribution and redistribution of residual stress. Therefore, in order to use  $J$ , the integral has to be modified to account for residual stress, although its path independence or integral does not reduce to zero.

Lei et al[61] using the gauge invariance of the J-integral under linear transformation modified Equ.(227) by introducing a concept of pre-strain.

It was assumed that at equilibrium minus loading there was an initial strain of  $\varepsilon_{ij}^0$ , which meant the total strain displacement was the sum of two components instead of one. That is:

$$\varepsilon_{ij}^T = \varepsilon_{ij}^m + \varepsilon_{ij}^0 \quad (233)$$

where  $\varepsilon_{ij}^T$  is the total strain displacement,  $\varepsilon_{ij}^m$  is the mechanical strain and  $\varepsilon_{ij}^0$  is the new initial strain to account for residual stress.

When the new strain displacement is substituted back into Equ.(227) the form of the integral becomes:

$$J = \lim_{\Gamma \rightarrow 0} \oint_{\Gamma} \left( W \delta_{ij} - \sigma_{ij} \frac{\partial u_i}{\partial x_1} \right) n_i ds + \int_A \sigma_{ij} \frac{\partial \varepsilon_{ij}^0}{\partial x_1} dA \quad (234)$$

It is easy to show that the above equation is path independent with similar analysis shown above.

The success of Equ.(234) is provided in the FAD chapter and as Sissan et al[4] and Sherry et al[69]. The invariance of J-integral under linear transformation can be taken advantage of by allowing for many arbitrary initial strains( as shown with Lei et al) and still maintain the path independence.

Therefore, it is proposed that another strain be added, that accounts for the Lüders strain called  $\varepsilon_{ij}^{0L}$ . Consequently, the initial strain of Lei et al  $\varepsilon_{ij}^{0P}$  will be made of two components.

$$\varepsilon_{ij}^0 = \varepsilon_{ij}^{0P} + \varepsilon_{ij}^{0L} \quad (235)$$

where  $\varepsilon_{ij}^{0P}$  is the plastic contribution and  $\varepsilon_{ij}^{0L}$  is the elasto-plastic contribution.

When substituted back into Equ.(234) it becomes:

$$J = \lim_{\Gamma \rightarrow 0} \oint_{\Gamma} \left( W \delta_{ij} - \sigma_{ij} \frac{\partial u_i}{\partial x_1} \right) n_i ds + \int_A \sigma_{ij} \left( \frac{\partial \varepsilon_{ij}^{0P}}{\partial x_1} + \frac{\partial \varepsilon_{ij}^{0L}}{\partial x_1} \right) dA \quad (236)$$

The details of the finite element method to solve and use Equ.(234) can be found in Lei et al[61]. As Equ.(236) is similar to Equ.(234), then the same FE element method can be used.

## F Appendix Lüders strain carbon content

This appendix will use the equations developed in chapter 3 and provide a more rigorous approach, with the intention of deriving a relationship between the Lüders strain and the carbon content without presupposing or assuming a relationship between the stress-strain, as done in chapter 3(see Equ.(68)) as suggested from the data of Winlock[23].

There will be several assumptions made regarding how the precipitates increase with carbon content and, consequently, the mean free path of the dislocations based upon the results of the thesis and literature review.

It is assumed that the main contributions to the effect of Lüders strain on the carbon content are the mean free-path and the surface area of the precipitates.

### F.1 Theory

The above assumptions are reasonable as it is assumed that the other factors affecting the Lüders strain, such as grain-size and the micro-structure are constant, because the eventual objective of this appendix is to quantify the effect of carbon content on the Lüders strain only and therefore keeping the main-factors discussed in the previous chapters constant. The morphology of the ferrite-pearlite structure is also assumed constant and increases homogeneously as the carbon content increases.

The goal is to solve the following equation

$$\frac{d\varepsilon_L}{dC} = \frac{d\varepsilon_L}{dS} \frac{dS}{dC} \quad (237)$$

where  $\varepsilon_L$  is the Lüders strain,  $C$  is percentage mass of carbon and  $S$  is the mean path.

Further:

$$\frac{dS}{dC} = \frac{dS}{dr} \frac{dr}{dC} \quad (238)$$

where  $r$  is the average radius of the precipitates.

It is assumed that from the findings of Song et al[24] that the amount of carbon content is proportional to the surface area of the precipitates, and therefore, assuming circular precipitates<sup>27</sup>:

$$C = N\rho\pi r^2 \quad (239)$$

---

<sup>27</sup>Although the analysis hence is not restricted to circular precipitates

with

$$\frac{dr}{dC} = \frac{1}{2\pi N \rho_{car} r} \quad (240)$$

where  $\rho_{car}$  is the surface density of the precipitates, with dimensions  $\frac{1}{m^2}$ , as  $C$  is considered dimensionless and  $N$  is the number of precipitates on the surface, which conforms to the boundary condition,  $C=0$  when  $r=0$ .

To find the  $\frac{dS}{dr}$  use the following equation:

$$\frac{dS}{dr} = \frac{dS}{d\sigma_L} \frac{d\sigma_L}{dr} \quad (241)$$

where  $\sigma_L$  is the lower yield.

To obtain  $\frac{dS}{d\sigma_L}$ , the following relates the stress to the dislocation density[5]:

$$\sigma_{ly} = \sigma_0 + \delta G b \rho^{\frac{1}{2}} \quad (242)$$

where  $\delta$  is a dimensionless quantity,  $G$  is the shear modulus,  $b$  is the Burger's vector and  $\sigma_0$  is a constant.

Substituting Equ.(242) and differentiating with respect to  $S$  gives:

$$\frac{d\sigma_{ly}}{dS} = -\frac{K_{car}\delta G b}{S^2} \quad (243)$$

It is difficult to find a stress relation between the yield point and the increase in ferrite-pearlite radius, because most work is concerned with material with constant composition. There are also many mechanisms that contribute to the yield stress, such as cohesive hardening and the Orowan mechanism. However, this analysis, it is assumed that the ferrite-pearlite interacts with the Lüders band collectively such that the ratio between the radius of the precipitates and the lamallae spacing is  $\frac{r}{L} \gg 1$ . Therefore, the precipitates are assumed to be continuous(ferrite-pearlite). The mechanism that interacts with continuous precipitates is called dislocation cutting.

The sheer stress responsible is:

$$\tau = \frac{\pi r \Xi}{bw} \quad (244)$$

where  $r$  is the average radius of the precipitate,  $\Xi$  is average the surface energy,  $b$  is the burgers vector and  $w$  is the average spacing between pinning points, assumed the same for each carbon content.

Bo et al[69] related the shear stress to the yield stress as:

$$\sigma_L = \hat{m}\tau = \vartheta r \quad (245)$$

where  $\sigma_L$  is the lower stress and  $\hat{m}$  is the Taylor factor and  $\vartheta = \frac{\hat{m}\pi\Xi}{bw}$  for simplicity.

Where the yield stress to the lower yield point and taking the derivative and substituting it into Equ.(241) gives the following:

$$\int \frac{dS}{S^2} = -\frac{K_{car}\vartheta}{\delta Gb} \int dr \quad (246)$$

to get:

$$S = \frac{K_{car}\delta Gb}{\vartheta r} \quad (247)$$

having imposed the boundary condition, when  $r = 0$ ,  $S = \infty$ . Or when there are no precipitates, the mean free path of the dislocation is infinite, which is feasible according to Modi et al[70].

Therefore, Equ.(238) becomes:

$$\frac{dS}{dC} = -\frac{K_{car}\delta Gb}{\vartheta r^2} \frac{1}{2N\pi\rho_{car}r} = -\frac{M}{r^3} \quad (248)$$

where  $M = \frac{K_{car}\delta Gb}{\vartheta} \frac{1}{2N\rho_{car}\pi}$ .

To obtain the strain dependence as a function the mean free path, use the following equation from chapter 3:

$$S = S_{car} \exp(\omega_{car}\varepsilon_L) \quad (249)$$

where  $S_{car}$  indicates that it is the same for all materials and likewise for  $\omega_{car}$ .

Taking the derivative of the above equation and substituting with Equ.(248) into Equ.(237) gives:

$$\frac{d\varepsilon_L}{dC} = -\frac{1}{S_{car}\omega_{car} \exp(\omega_{car}\varepsilon_L)} \frac{M}{r^3} \quad (250)$$

substituting  $r$  for  $C$  from Equ.(237) gives:

$$\int \exp(\omega_{car}\varepsilon_L) d\varepsilon_L = \frac{M(2\pi N\rho)^{\frac{1}{2}}}{S_{car}\omega_{car}} \int C^{-\frac{3}{2}} dC \quad (251)$$

with solution:

$$\exp(-\omega_{car}\varepsilon_L) = 2AC^{\frac{1}{2}} + B \quad (252)$$

where  $A = \frac{M(2\pi N\rho)^{\frac{1}{2}}}{S_{car}}$ .

For simplicity impose boundary condition  $\varepsilon_L \rightarrow \infty \Rightarrow C = 0 \Rightarrow B = 0$ . Therefore, the above equation becomes:

$$C^{\frac{1}{2}} = \frac{\exp(-\omega_{car}\varepsilon_L)}{2A} \quad (253)$$

or

$$\varepsilon_L = -\frac{\ln(2AC^{\frac{1}{2}})}{\omega_{car}} \quad (254)$$

Now that the strain has been related to the carbon content, it is straight forward to find the stress-strain relationship, by using the following equation (from Equ.(242)):

$$\sigma_L = \sigma_0 + \frac{K_{car}\delta Gb}{S} \quad (255)$$

where  $\sigma_0$  is a constant of integration.

$S$  is related to the carbon content through Equ.(247). That is:

$$S = \frac{K_{car}\delta Gb(2N\pi\rho_{car})^{\frac{1}{2}}}{\vartheta C^{\frac{1}{2}}} = \frac{I}{C^{\frac{1}{2}}} \quad (256)$$

where  $I = \frac{K_{car}\delta Gb(2N\pi\rho_{car})^{\frac{1}{2}}}{\vartheta}$  for simplicity.

Substituting into Equ.(255) gives:

$$\sigma_L = \sigma_0 + \frac{K_{car}\delta GbC^{\frac{1}{2}}}{I} \quad (257)$$

For the strain, substituting Equ.(253)

$$\sigma_L = \sigma_0 + \frac{K_{car}\delta Gb \exp(-\omega_{car}\varepsilon_L)}{2AI} \quad (258)$$

Interestingly, Equ.(257) is similar to a result derived by Fleischer[71] using a more sophisticated method. That is:

$$\tau \propto C^{\frac{1}{2}} \quad (259)$$

where  $\tau$  has its usual meaning. However, using Equ.(245) to relate the sheer stress to the yield stress the above relation becomes:

$$\sigma_L \propto C^{\frac{1}{2}} \quad (260)$$

It seems that although the method of derivation was simplistic and only assumed that the most dominant mechanism of dislocation propagation was cutting, the final result for the stress and carbon content, is of the form similar to more sophisticated models.

Equ.(253), Equ.(257) and Equ.(258) will be curve fitting against the data of Winlock[23] at three different strain-rates:  $1.72$ ,  $1.4 \times 10^{-3}$  and  $1.75 \times 10^{-5} \text{ s}^{-1}$ , respectively.

## F.2 Method

The aforementioned equations can be re-written in the following way:

$$C^{\frac{1}{2}} = B_0 \exp(-\omega_{car}\varepsilon_L) \quad (261)$$

where  $B_0 = \frac{1}{2A}$

$$\sigma_L = \sigma_0 + A_0 C^{\frac{1}{2}} \quad (262)$$

where  $A_0 = \frac{K_{car}\delta Gb}{2AI}$ .

and thus:

$$\sigma_L = \sigma_0 + A_0 B_0 \exp(-\omega_{car}\varepsilon_L) \quad (263)$$

The objective is, therefore, to determine the values of  $\sigma_0$ ,  $A_0$  and  $B_0$  and  $\omega_{car}$  from which the other values defined in this appendix can be calculated. However, the purpose of the appendix was to show that the resulting equations from the assumptions made during the derivation match the data and, therefore, it is for future work to check the validity of the numbers. Although, clearly if the values of  $A_0$ ,  $B_0$  and  $\sigma_0$  are credible then one would expect the other terms with the aforementioned to be also credible.

Starting from Equ.(261) the values of  $B_0$  and  $\omega_{car}$  are calculated from the data, then the value of  $\sigma_0$  and  $A_0$ , subsequently, these values are combined and plotted against the lower yield point and Lüders strain of the same data (The carbon range 1.03-0.06% C).

### F.3 Results

- Fig.(95) shows the a plot of the carbon content to the power of a half against the Lüders strain. It is evident that the curve shifts as function of strain-rate, however the form of the curves are still congruent, indicating that the shape or trend is maintained.
- Fig.(96) shows a plot of the lower yield stress against carbon content. It is evident that the curve fitting of Equ.(262) fits well of the data for all strain-rates.
- Fig.(97) shows a plot of the lower yield stress against Lüders strain. This time the equations were plotted from the values of  $\sigma_0$ ,  $A_0$  and  $B_0$  and  $\omega_{car}$ , showing that Equ.(261) and Equ.(262) translate well and, therefore, can predict the lower yield stress against Lüders strain.

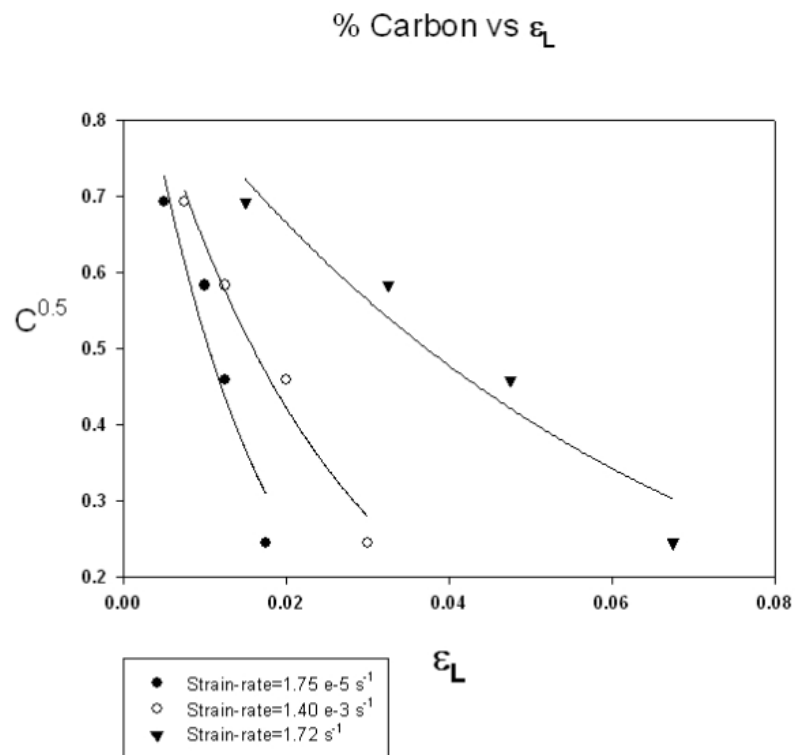


Figure 95: Curve fitting of Equ.(261) for the carbon content vs Lüders strain at different strain-rates. Data taken from Winlock[23].

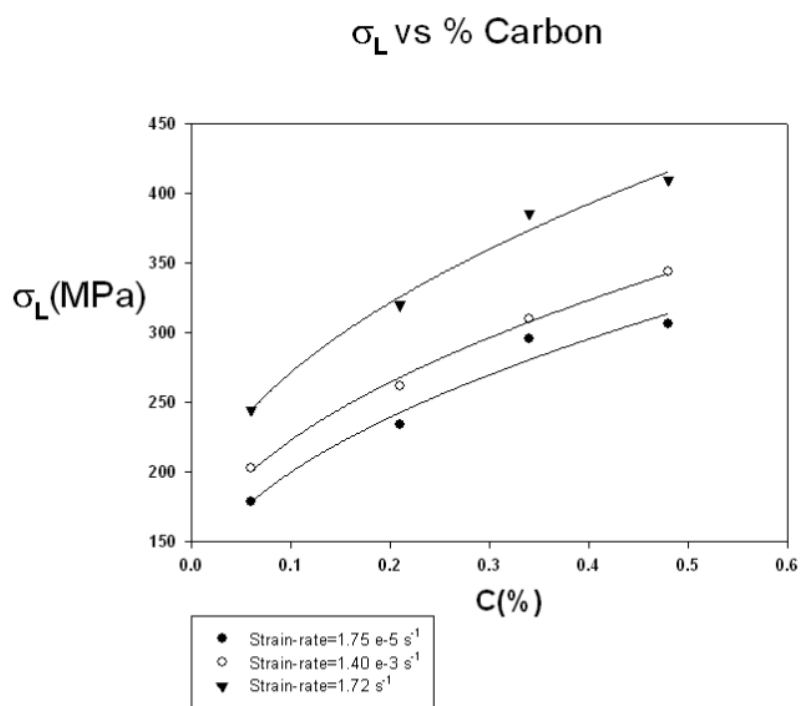


Figure 96: Curve fitting of Equ.(262) of the lower yield stress vs carbon content at different strain-rates. Data taken from Winlock[23].

### $\sigma_L$ vs $\varepsilon_L$

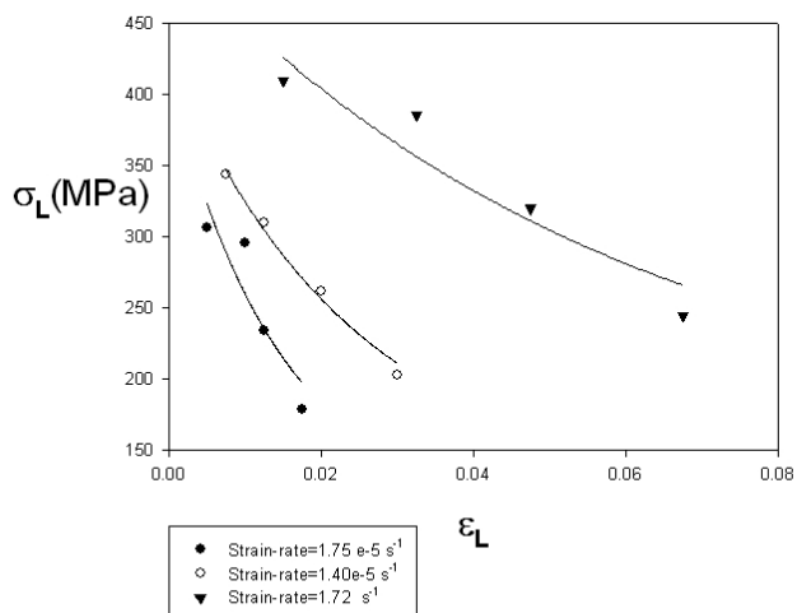


Figure 97: Curve fitting of Equ.(263) for the carbon content vs Lüders strain at different strain-rates, with combined values calculating from Fig.(95) and Fig.(96) Data taken from Winlock[23].

## F.4 Summary

To summarise: It has been shown, using basic assumption on how the Lüders band interacts with the precipitates, that equations relating the key variables such as the Lüders strain and lower yield stress can be related to the carbon content and agree with the data, contrasting with the method of derivation in chapter 3 which was less rigorous. Although, due to the basic assumptions, the equations predicted should be qualitatively correct at best, it was shown that they agreed with the data very well and also managed to produce some relations that are already known in the literature, which were derived from more sophisticated methods, such as Equ.(255). This shows that when modelling a Lüders band through precipitate interactions, in this case the carbon content, interactions such as Orowan mechanism and dislocations bending etc, can be, to an approximation, neglected. However, clearly, to have the most realistic or reflective model, all the contributions are required.

Further work could make more realistic boundary conditions, such as  $r = r_{max} \Rightarrow C = C_{max}$ , which if factored into the above equations could calculate approximately when the Lüders strain finishes. Also, the boundary condition for the mean free path and the radius of the precipitates. Instead of setting  $S = \infty$  at  $r = 0$ , one could set  $S = S_{max}$  when  $r = r_{max}$ , which would coincide with  $r = r_{max} \Rightarrow C = C_{max}$ .

## F.5 Conclusion

In conclusion, a model making basic assumptions about the interaction between a Lüders band and the precipitates has been shown. Although, simple compared to most dislocation models, it managed to produce consistent results for all strain-rates and when collectively used to predict the plot of the lower yield point and Lüders strain, it was shown (from the values of  $\sigma_0$ ,  $A_0$  and  $B_0$  and  $\omega_{car}$ ) that the curves of Equ.(263) fitted the data. However, the model assumed that the precipitates were continuous or that the ratio between the lamaellae spacing and the radius of the precipitates was considerably greater than one. Clearly, the lamaellae spacing should be factored in and it is hoped in future work that a more holistic model similar to the above approach can be executed and thus produce a better model.

## G Subroutine

File: /tmp/LD\_vumat\_mm(1).f

```
VUMAT(NBLOCK,NDIR,NSHR,NSTATEV,NFIELDV,NPROPS,LANNEAL,
* STEPTIME,TOTALTIME,DT,CMNAME,COORDMP,CHARLENGTH,
* PROPS, DENSITY, STRAININC, RELSPININC, TEMPOLD,
* STRETCHOLD,DEFGRADOLD,FIELDOLD,STRESSOLD, STATEOLD,
* ENERINTERNOLD, ENERINELASOLD, TEMPNEW, stretchNew, DEFGRADNEW,
* FIELDNEW,
! Write only variables
* stressnew, statenew, enerinternnew, enerinelasnew)
INCLUDE 'vaba_param.inc'
CHARACTER*80 cmname
DIMENSION props(nprops),density(nblock),coordMp(nblock,*),
*charlength(nblock),strainInc(nblock,ndir+nshr),
*relSpinInc(nblock,nshr), tempOld(nblock),
*stretchOld(nblock,ndir+nshr),
*defgradOld(nblock, ndir+nshr+nshr),
*fieldOld(nblock,nfieldv),stressOld(nblock,ndir+nshr),
*stateOld(nblock,nstatev),enerInternOld(nblock),
*stretchNew(nblock,ndir+nshr),
*defgradNew(nblock,ndir+nshr+nshr),
*fieldNew(nblock,nfieldv), enerinelasold(nblock), tempnew(nblock),
*stressNew(nblock,ndir+nshr), stateNew(nblock, nstatev),
*enerInternNew(nblock), enerinelasNew(nblock),S(NDIR+NSHR)
!-----
! ISOTROPIC VUMAT WITH STRAIN AGEING
! Mark Wenman 09.10.07
!-----
! Define local variables
INTEGER J, nblock
REAL*8 E, NU, G, LAMBDA, TRACE, H, SMEAN, SMISPR, ERATEO
* SYIELD, DDEQPLAS, DEQPLAS, SY, RHS, DENOM, P1, CS, SRS
* S(NDIR+NSHR),DEPLAS(NDIR+NSHR),DEELAS(NDIR+NSHR),D1,D2,D3
* W1, W2, ALPHA, BETA, P2, N, CM, omega, DTA, TA, TW, DUMMY, VM
* S1, S2, EQPLAS
DATA TA /4000.d0/
DATA CS /1.d0/
E = PROPS(1)
NU = PROPS(2)
! Input parameters from Zhang for Dynamic strain ageing of Al alloy
! YIELD = PROPS(3)
! ERATEO = 2.3D-7
! D1 = 38.03D6
! D2 = 29.94D6\begin{appendices}
! D3 = 5.6D-2
! W1 = 3.6D-5
! W2 = 2.16D-3
! ALPHA = 0.44D0
! BETA = 0.68D0
! P1 = 18.D0
! P2 = 3.91D0
! N = 1.d0/3.d0
! CM = 2.D0
! S1 = 0.41D6
```

```

!      S2 = 2.91D6
!Input parameters from Graff for a mild steel that shows luders behaviour
  ERATE0 = 100.D0
  D1 = 170.D0
  D2 = 315.D0
  D3 = 7.5D-2
  W1 = 1.D-6
  W2 = 1.D-5
  ALPHA = 0.D0
  BETA = 0.68D0
  P1 = 40.D0
  P2 = 0.001D0
  N = 1.D0
  CM = 1.D0
  S1 = 12.5D0
  S2 = 5.D0
File: /tmp/LD_vumat_mm(1).f
!Calculate Lame's constants lambda and shear modulus (G)
  LAMBDA = (E*nu)/((1.D0 + nu)*(1.D0 - 2.D0*nu))
  G = E/(2.D0*(1.D0 + nu))
! STATE VARIABLES FOR ISOTROPIC HARDENING in 3D
!SDV(1) = EELAS(1)
!SDV(2) = EELAS(2)
!SDV(3) = EELAS(3)
!SDV(4) = EELAS(4)
!SDV(5) = EELAS(5)
!SDV(6) = EELAS(6)
!SDV(7) = EPLAS(1)
!SDV(8) = EPLAS(2)
!SDV(9) = EPLAS(3)
!SDV(10) = EPLAS(4)
!SDV(11) = EPLAS(5)
!SDV(12) = EPLAS(6)
!SDV(13) = (EQPLAS + DEQPLAS)
!SDV (14) = TA
!SDV (15) = CS
!SDV (16) = TW
!SDV (17) = DEQPLAS
!Start the vectorised block of elements vector length = NBLOCK
  DO J=1, NBLOCK
!Elastic predictor stress
!in VUMAT shear strains are stored as true strains so no divide by 2 necessary
  TRACE = STRAININC(J,1) + STRAININC(J,2) + STRAININC(J,3)
  STRESSNEW(J,1:NDIR) = STRESSOLD(J,1:NDIR) + LAMBDA*TRACE +
*           2.D0*G*STRAININC (J,1:NDIR)
  STRESSNEW(J,NDIR+1:NDIR+NSHR) = STRESSOLD(J,NDIR+1:NDIR+NSHR) +
*           2.D0*G*STRAININC (J,NDIR+1:NDIR+NSHR)
!Set elastic and plastic strains assuming elastic behaviour.
  STATENEW(J,1:NDIR+NSHR) = STATEOLD(J,1:NDIR+NSHR) +
*           STRAININC(J,1:NDIR+NSHR)
  STATENEW(J,NDIR+NSHR+1:2*(NDIR+NSHR)) =
*           STATEOLD(J,NDIR+NSHR+1:2*(NDIR+NSHR))
  STATENEW(J,2*(NDIR+NSHR)+1) = STATEOLD(J,2*(NDIR+NSHR)+1)
!Calculate the hydrostatic or mean stress (SMEAN)
  SMEAN = SUM(STRESSNEW(J,1:NDIR))/3.D0
!Calculate the deviatoric predictor stresses S
  S(1:NDIR) = STRESSNEW(J,1:NDIR) - SMEAN

```

```

S(NDIR+1:NDIR+NSHR) = STRESSNEW(J,NDIR+1:NDIR+NSHR)
!Use the deviatoric stress to calculate the von mises predictor stress SMISPR.
    vm = s(1)**2+s(2)**2+s(3)**2 + 2*s(4)**2 + 2*s(5)**2 + 2*s(6)**2
    smispr = sqrt((3.d0/2.d0)*vm)
!Setup the old value of eqplas
    if (totaltime .LE. 1.d-20)then
        stateold(J,2*(NDIR+NSHR)+1) = 0.d0
    end if
    EQPLAS = STATEOLD(J,2*(NDIR+NSHR)+1)
!Calculate the old yield stress
    IF      (STATEOLD(J,2*(NDIR+NSHR)+1) .LE. 0.D0) THEN
        TA = 4000.D0
        CS = 1.d0
    ELSE
        TA = STATEOLD(J,2*(NDIR+NSHR)+2)
        CS = CM*(1-EXP(-P2*(TA**N)*(EQPLAS + DEQPLAS)**alpha))
    END IF
    SYIELD = D1 + D2*(1-EXP((-EQPLAS)/D3)) + P1*CS
!
    SYIELD = D1 + H*STATEOLD(J,2*(NDIR+NSHR)+1)! Linear hardening
!
    VUMAT MUST BE ELASTIC AT TIME = ZERO
!Check for yield
File: /tmp/LD_vumat_mm(1).f
If (totaltime .gt. 0.d0) then
    IF (SMISPR.GE.SYIELD) THEN
        DEQPLAS = 0.D0
    !!Start calculation with ageing tshows theime TA = 1000secs otherwise use old value of TA.
        IF      (DEQPLAS .LE. 0.D0
                .AND. STATEOLD(J,2*(NDIR+NSHR)+1) .LE. 0.D0) THEN
        *
            TA = 4000.D0
            CS = 1.d0
        ELSE
            TA = STATEOLD(J,2*(NDIR+NSHR)+2)
            CS = CM*(1-EXP(-P2*(TA**N)*(EQPLAS + DEQPLAS)**alpha))
        END IF
!!!
!!! Can use do - end do statement in fortran 90 with EXIT command.
!!! Loop uses newton's method to solve for change in DEQPLAS.
!
    DO
        SY = D1 + H*STATEOLD(J,2*(NDIR+NSHR)+1)! Linear hardening
        SY = D1 + D2*(1-EXP(-(EQPLAS)/D3)) + P1*CS
!Calculate the strain rate sensitivity
        SRS = S1 + S2*(SQRT(EQPLAS))
!Calculate the strain increment omega that occurs when all dislocations overcome obstacles
        OMEGA = W1 + W2*STATEOLD(J,2*(NDIR+NSHR)+1)**BETA
        !
        OMEGA = 3.d-4
!!Calculate the dynamic value of the solute concentration CS.
        CS = CM*(1-EXP(-P2*(TA**N)*(EQPLAS + DEQPLAS)**alpha))
        !
        RHS = DT*ERATE0*EXP((SMISPR - SY)/SRS - P1*CS) - DEQPLAS
        RHS = ERATE0*EXP((SMISPR - SY)/SRS - P1*CS) - DEQPLAS
        !
        DENOM = (-D2/(D3*SRS))*ERATE0*DT
        !
        DENOM = (-D2/(D3*SRS))*ERATE0
        !
        DUMMY = (SMISPR - SY)/SRS - P1*CS - (EQPLAS + DEQPLAS)/D3
        !
        DUMMY = EXP(DUMMY)
        !
        DENOM = DENOM*DUMMY - 1.D0
        !
        DENOM = DENOM*DUMMY
        DDEQPLAS = RHS/DENOM

```

```

        if (ABS(DEQPLAS) .LT. 1.d-12) exit
!
!      IF (ABS(DDEQPLAS).LT.1.0D-5*DEQPLAS) EXIT
!      DEQPLAS = DEQPLAS - DDEQPLAS
!      DEQPLAS = ERATE0*EXP((SMISPR - SY)/SRS - P1*CS)
!      if (deqplas .gt. 1d-5) then
!          deqplas = 1d-5
!      end if
!! Avoid a divide by zero if deqplas is very small then set deqplas to some small quantity
!      END DO
!Calculate the waiting time TW
!      IF (DEQPLAS .LE. 1.D-30) THEN
!          DEQPLAS = 1.d-15
!      END IF
!      TW = omega/deqplas
!Calculate the change in the ageing time TA (DTA).
!      DTA = 1 - TA/TW
!      TA = TA + DTA
!      if (DTA .LT. 0.d0) then
!          TA = TA + DTA
!      end if
!      if (TA .LT. 0.d0) then
!          TA = 0.d0
!      end if
!      =  TA
STATENEW(J,2*(NDIR+NSHR)+2) = SMISPR
STATENEW(J,2*(NDIR+NSHR)+3) = TW
STATENEW(J,2*(NDIR+NSHR)+4) = DEQPLAS
STATENEW(J,2*(NDIR+NSHR)+5) = CS
STATENEW(J,2*(NDIR+NSHR)+6) = DTA
STATENEW(J,2*(NDIR+NSHR)+7)
!! Calculate changes to plastic and elastic strains
DEPLAS(1:NDIR+NSHR) = 1.5D0*DEQPLAS*S(1:NDIR+NSHR)/SMISPR
DEELAS(1:NDIR+NSHR) = STRAININC(J,1:NDIR+NSHR) -
File: /tmp/LD_vumat_mm(1).f
*                      DEPLAS(1:NDIR+NSHR)
! Calculate the new state variables.
STATENEW(J,1:NDIR+NSHR) = STATEOLD(J,1:NDIR+NSHR) +
*                          DEELAS(1:NDIR+NSHR)
STATENEW(J,NDIR+NSHR+1:2*(NDIR+NSHR)) =
STATEOLD(J,NDIR+NSHR+1:2*(NDIR+NSHR)) +
*
*                          DEPLAS(1:NDIR+NSHR)
STATENEW(J,2*(NDIR+NSHR)+1) = STATEOLD(J,2*(NDIR+NSHR)+1) +
DEQPLAS
!Calculate the new stress tensor
TRACE = SUM(DEELAS(1:NDIR))
STRESSNEW(J,1:NDIR) = STRESSOLD(J,1:NDIR) + LAMBDA*TRACE +
2.D0*G*DEELAS(1:NDIR)
*
STRESSNEW(J,NDIR+1:NDIR+NSHR) = STRESSOLD(J,NDIR+1:NDIR+NSHR) +
2.D0*G*DEELAS(NDIR+1:NDIR+NSHR)

```

```

*
END IF
end if
!Set state variables for elastic behaviour
if (SMISPR.LT.SYIELD) THEN
  STATENEW(J,2*(NDIR+NSHR)+2) = TA
  STATENEW(J,2*(NDIR+NSHR)+2) = STATEold(J,2*(NDIR+NSHR)+2)
  STATENEW(J,2*(NDIR+NSHR)+3) = SMISPR
  STATENEW(J,2*(NDIR+NSHR)+4) = STATEold(J,2*(NDIR+NSHR)+4)
  STATENEW(J,2*(NDIR+NSHR)+5) = 0.d0
  STATENEW(J,2*(NDIR+NSHR)+6) = CS
  STATENEW(J,2*(NDIR+NSHR)+6) = STATEold(J,2*(NDIR+NSHR)+6)
  STATENEW(J,2*(NDIR+NSHR)+7) = STATEold(J,2*(NDIR+NSHR)+7)
end if
!
!      if (J .eq.1) then
!      *      open(2,file='C:\abaqus\temp\mark\luders work\l_vumatout.txt',
!      access = 'append')
!      write(2,600)totaltime, smispr, sy, syield, srs, solute
! 600      format(6(e10.4,1X))
!      close(2)
!      end if
END DO
RETURN
END

```

## References

- [1] Wenman M and Chard-Tuckey P, “Modelling and experimental characterisation of the Luders strain in complex loaded ferritic steel compact tension specimens,” *Materials Science and Engineering*, vol. A526, pp. 156–165, 2009.
- [2] Revision 4, “Assessment of the structure of the integrity of structures containing defects.,” *British energy/EDF energy*, vol. SINTAP/BS/19, pp. 1–14, 2011.
- [3] Haubenreich P N and Engel J R, “Experience with the molten-salt reactor experiment,” *Nuclear applications and technology*, vol. 8, pp. 118–136, 1970.
- [4] Mirzaee-Sisan A, Truman C.E, Smith D J and Smith M C, “Interaction of residual stress with mechanical loading in a ferritic steel,” *Engineering Fracture mechanics*, vol. 74, pp. 2864–2880, 2007.
- [5] Bergstrom Y, Granbom Y and Sterkenburg D, “A dislocation based theory for the deformation hardening behaviour of DP steels: Impact on martensite content and ferrite grain-size,” *Journal of Metallurgy*, vol. 2010, pp. 1–16, 2010.
- [6] Zhang Y.T Qiao J.L and Ao T, “Modelling Simulations,” *Science and Engineering*, vol. 15, pp. 147 – 156, 2007.
- [7] Tsuchida N Yomota Y Nagai K and Fukaura K, “A simple relationship between Luders elongation and the work hardening rate at lower yield stress.,” *Scripta Materialia*, vol. 54, pp. 57–60, 2006.
- [8] Sun H B, Yoshida F, Ohmori M and Ma X, “Lüders bands in steel,” *Materials Letters*, vol. 57, pp. 4535–4539, 2003.
- [9] Conrad H and Schoeck G, “Cottrell locking and the flow stress in iron,” *Acta Metallurgica*, vol. 8, no. 11, pp. 791 – 796, 1960.
- [10] LüdersW *Polytechnisches Journal*, vol. 155, pp. 18–22, 1860.
- [11] Cottrell A.H and Bilby B.A, “Dislocation theory of yielding and strain ageing of Iron,” *Physical society*, vol. 62, pp. 49–61, 1948.

- [12] McAdams D J and Mess R W *Trans Society Test Materials*, vol. 43, p. 661, 1943.
- [13] Zhao J Z, De A K and Cooman B C , “Kinetics of cottrell atmosphere formation during strain aging of ultra-low carbon steels,” *Materials Letters*, vol. 44, no. 6, pp. 374 – 378, 2000.
- [14] Gilman J J and Johnston W G, *Dislocations in Lithium Fluoride Crystals*, vol. 13 of *Solid State Physics*. Academic Press, 1962.
- [15] Smallman R.E and Ray J, “Modern physical metallurgy and materials engineering,” *Bishop*, pp. 157 – 160, 1999.
- [16] Haasen P and Hesse J, “Dislocation Density and flow stress of NaCl and LiF,” *National physical Laboratory*, vol. 1, pp. 138 – 143, 1963.
- [17] Johnston W G, “Effect of impurities on the flow stress of lif crystals,” *Journal of Applied Physics*, vol. 33, no. 6, pp. 2050–2058, 1962.
- [18] Hahn G T, “A model for yielding with special reference to the yield-point phenomena of iron and related bcc metals,” *Acta Metallurgica*, vol. 10, no. 8, pp. 727 – 738, 1962.
- [19] Wilson D V and Russell B, “The contribution of precipitation to strain ageing in low carbon steels,” *Acta Metallurgica*, vol. 8, no. 7, pp. 468 – 479, 1960.
- [20] Dalby W.E, “Load-Extension diagrams taken with the optical Load-extension Indicator,” *Royal society Proc*, vol. 88, pp. 281 – 288, 1913.
- [21] Kuroda M, “On the origin of the yield-point phenomena of soft steel,” *IPCR*, vol. 34, pp. 1528 – 1630, 1938.
- [22] Haasen P, “Physical Metallurgy,” *Cambridge Press*, pp. 67 – 219, 1980.
- [23] Winlock J, “The influence of the rate of deformation on the tensile properties of some plain carbon sheet steels,” *Journal of metals*, vol. 197, no. 6, pp. 797–803, 1953.
- [24] Song R, Ponge D and Raabe D, “Improvement of the work hardening rate of ultra fine grained steels through second phase particles,” *Scripta Materialia*, vol. 52, no. 11, pp. 1075 – 1080, 2005.

- [25] *Mechanical Metallurgy*. McGraw-Hill book company, 1988.
- [26] Blakemore J.S and Hall E.O, “Blue-brittle behaviour of mild steel,” *Iron and steel institute*, vol. 204, pp. 817 – 820, 1966.
- [27] Honeycombe R K and Bhadeshia H K D H, “Steels: Micro-structure and properties,” *Metallurgy and Materials science Edward Arnold*, vol. 2nd edition, p. 19, 1995.
- [28] Fisher J C and Rogers H C, “Propagation of Lüders bands in steel wires,” *Acta Metallurgica*, vol. 4, no. 2, pp. 180 – 185, 1956.
- [29] Butler J, “Luders propagation in low carbon steels,” *J Mech Phys Solids*, vol. 10, pp. 313–334, 1962.
- [30] Kocks U F, “Kinetic of non-uniform deformation,” *Progress in Material Science*, vol. 82, pp. 185 – 239, 1981.
- [31] Balokhonov R.R and Romanova V.A, “Numerical modelling of the thermo-mechanical behaviour of steels with allowance for the propagation of luders bands,” *Journal of Applied Mechanics and Technical Physics*, vol. 48, pp. 743 – 750, 2007.
- [32] Tsuchida N, Masuda M, Harada Y, Fukaura K Tomota Y and Nagai K, “Effect of ferrite grain-size on tensile deformation behaviour of a ferrite-cementite low carbon steel,” *Materials Science and Engineering*, vol. 488, pp. 446–452, 2008.
- [33] Imamura J, Hayakawa H and Tadami T, “Contribution of local strain-rate at Lüders band front to grain size dependence of Lower yield stress in iron,” *The Iron and steel institute of Japan*, vol. 11, pp. 191 – 204, 1971.
- [34] Honeycombe R.W.K and Bhadeshia H.K.D.H, “Steels,” *Metallurgy and Materials Science*, vol. 3rd, pp. 242 – 296, 1995.
- [35] Hutanu R, Clapham L and Rogge R B , “Intergranular strain and texture in steel Lüders bands,” *Acta Materialia*, vol. 53, no. 12, pp. 3517 – 3524, 2005.

- [36] Turner P A and Tom C N, “A study of residual stresses in zircaloy-2 with rod texture,” *Acta Metallurgica et Materialia*, vol. 42, no. 12, pp. 4143 – 4153, 1994.
- [37] Pang J W L, Holden T M, and Mason T E, “The development of intergranular strains in a high-strength steel,” *Journal of Strain Analysis*, vol. 332, no. 5, pp. 373 – 383, 1998.
- [38] Dunne F P E, Rugg D and Walker A, “Length scale-dependent, elastically anisotropic, physically-based hcp crystal plasticity: Application to cold-dwell fatigue in ti alloys,” *International Journal of Plasticity*, vol. 23, no. 6, pp. 1061 – 1083, 2007.
- [39] Sun H B, Yoshida F, Ohmori M and Ma X, “Effect of strain rate on Lüders band propagating velocity and Lüders strain for annealed mild steel under uniaxial tension,” *Materials Letters*, vol. 57, no. 29, pp. 4535–4539, 2003.
- [40] Magd E, “Mechanical properties at high strain-rates,” *Journal De Physique*, vol. 4, pp. 149 – 170, 1994.
- [41] Itabashi M and Kawata K, “Carbon content effect on high-strain-rate tensile properties for carbon steels,” *International Journal of Impact Engineering*, vol. 24, no. 2, pp. 117–131, 2000.
- [42] Lee W. S and Liu C.Y, “The effect of temperature and strain rate on the dynamic flow behaviour of different steels,” *Materials Science and Engineering*, vol. 426, no. A, pp. 101 – 113, 2006.
- [43] Iroh M, Yoshida F, Yamashita Y and Ohmori M, “Finite element analysis for non-uniform yielding processes in mild steel plates under stretching,” *Japan Society Mechanical Engineering-International Journal*, vol. 35, no. 1, pp. 70 – 77, 1992.
- [44] Schlipf J, “Phenomenological approach to Lüders bands,” *Journal of Materials Science*, vol. 21, pp. 4111 – 4116, 1986.
- [45] Gilman J J, “Microdynamics of Plastic flow at constant stress,” *Journal of Applied Physics*, vol. 36, pp. 2772–2777, 1965.

- [46] Bergstrom Y, “A correlation between the mean free path of dislocation motion and the grown-in dislocation density.,” <http://www.plastic-deformation.com/>, pp. 1–2, 2010.
- [47] Vetter R, “Dislocation mean free path in Copper at 77K,” *Scripta Metallurgica*, vol. 12, pp. 69–73, 1978.
- [48] Bailon P J and Dorlot M J, “The relationships between stress, grain-size and dislocation density in Armco iron at room temperature,” *Material Science and Engineering*, vol. 8, pp. 288–298, 1971.
- [49] Zhang S, McCormick G P and Estrin Y, “The morphology of Portevin-Le Chatelier Bands: Finite element simulation Al-Mg-Si,” *Acta Materialia*, vol. 49, pp. 1087–1094, 2001.
- [50] Estrin Y, Krausz A S and Krausz K, “Unified constitutive laws of plastic deformation,” *Academic press New York*, p. 69, 1996.
- [51] Graff S, Forest S and Strudel J L , “Strain localisation phenomena associated with static and dynamic strain ageing in notched specimens: experiment and finite element simulations ,” *Materials Science and Engineering*, vol. A387-389, pp. 181–185, 2004.
- [52] Price A, “Fracture behaviour of ferritic steel under the action of combined residual and mechanical loading.,” *Nuclear Department Technical Memorandum*, vol. 989, pp. 1–153, 2008.
- [53] Hall E O, “Yield point phenomena in metals and alloys.,” *Plenum*, vol. 10, pp. 32–33, 1970.
- [54] Honeycombe and H. K. D. H. Bhadeshia, “Steels: Micro-structure and properties,” *Metallurgy and Materials science Edward Arnold*, vol. 2nd edition, 1995.
- [55] Lee W S and Liu C Y, “The effects of temperature and the strain-rate on the dynamic flow behaviour of different steels,” *Materials Science and Engineering*, vol. A 426, pp. 101–113, 2006.
- [56] Samuel H F, Daniel D and Sure O, “Further investigations on the micro-structure and mechanical behaviour of granular bainite in a high

- strength, low alloy steel: Comparison of Ferrite-Pearlite and Ferrite-Martensite structure,” *Materials Science and Engineering*, vol. 92, pp. 43–62, 1987.
- [57] Cadoni E, Dotta M, Forni D and Spatig P, “Strain-rate behaviour in tension of the tempered martensitic reduced activation steel Eurofer97,” *Journal of Nuclear Materials*, vol. 414, pp. 360–366, 2011.
- [58] Han Z, Luo H and Wang H, “Effects of strain-rate and notch on acoustic emission during tensile deformation of a discontinuous yielding material,” *Materials Science and Engineering A*, vol. A528, pp. 4372–4380, 2011.
- [59] Higgins R A, “Materials for the engineering technician,” *Hodder and Stoughton*, p. 125, 1986.
- [60] Budden P J, Sharples J K and Dowling A R, “The r6 procedure: recent developments and comparison with alternative approaches,” *International Journal of Pressure Vessels and Piping*, vol. 77, no. 14-15, pp. 895 – 903, 2000.
- [61] Lei J, O’Dowd and Webster G A, “Fracture mechanics analyst of a crack in a residual stress field,” *International Journal of fracture*, vol. 106, pp. 195–216, 2000.
- [62] Rice J R, “A path independent integral and the approximate analysis of strain concentration by notches and cracks,” *J*, vol. 35, pp. 379–386, 1968.
- [63] Sluys Van der Alan W, Piascik R and Zawierucha R, “Effects of the environment on the initiation of crack growth,” *ASTM international*, p. 211, 1997.
- [64] Banister C A , “The assessment of the occurrence and significance of yield plateaus in structural steels,” *British steel/Chorus group*, vol. SINTAP/BS/19, pp. 1–14, 1999.
- [65] Firrao D, Mattels P and Vasello M, “Fracture toughness of plastic-mould steels: dependence upon heat treatment and microstructure.,” *Politecnico di Torino*, pp. 1–6, 2004.

- [66] Nilsson S, Lagneborg R and Sandsrom R, “A method to determine the mobile dislocation density in low carbon steels,” *Metal Science*, vol. 9, pp. 223–225, 1975.
- [67] Dantec, “Q-400: DIC introduction and training,” *Dantec dynamic*, pp. 1–23, 2008.
- [68] Spiegel R M, “Theoretical mechanics,” *Schaum*, pp. 224–252, 1967.
- [69] Sherry A H, Turski M, Wilkes M A, Beardsmore D W, Withers P J and Bouchard P J, “The development of a compact specimen to study the influence of residual stresses on fracture,” *Engineering structural integrity assessment*, pp. 341–348, 2002.
- [70] Modi OP, Deshmukh N, Mondal D P, Jha AK, Yegneswaran and Kahaira H K, “Effect of interlamellar spacing on the mechanical properties of 0.65% C steel,” *Materials Characterisation*, vol. 46, pp. 347–352, 2001.
- [71] Fleischer R L *Journal of applied physics*, vol. 33, p. 3504, 1962.